AIAA
SP-069-1994

Special Project

Contemporary Models of the Orbital Environment

AIAA
SP-069-1994

Special Project Report

Contemporary Models of the Orbital Environment

Robert A. Skrivanek, Editor

Abstract

The six papers included in this Special Report were presented at the AIAA Aerospace Sciences Meeting in January 1994. They provide state-of-the-art knowledge about ionospheric, radiation, neutral density, space debris, and thermal environments. The papers will be employed in the development of standard models for these aspects of the orbital environment.

Published by
American Institute of Aeronautics and Astronautics
370 L'Enfant Promenade, SW, Washington, DC 20024

Printed in the United States of America

CONTENTS

Foreword

The Air Force and NASA co-leaders of the Space Technology Interdependency Group (STIG) have noted recently that more effort is needed to encourage the application of available knowledge toward specifying and modeling the interaction and effect of the space environment on space systems. This need exists despite the significant amount of progress that has been achieved mutually by both organizations in measuring and modeling the physical and chemical properties of near Earth space.

Our ability to measure, understand, and specify the detailed characteristics of the space environment has improved steadily since the first simplified measurements were made using research balloons and sounding rockets. The lead agencies for sponsoring and performing many of the these measurements have been the US Air Force and NASA. Each of these agencies has had its own requirements and priorities for obtaining the various specific measurements of the space environment. Through the years each has accumulated a comprehensive collection of data sets and models.

This information, as it was being collected, analyzed, and assembled, has been used by the spacecraft design groups in government agencies and industrial concerns throughout the United States. Hundreds of military and civilian satellites, designed and built for both research and operational purposes, have benefited from this evolving data over the last 30 years.

The space environment data that was used by these satellite designers has not always been easily accessible nor easily understood. In most cases the data or models were generated by scientists who were driven more by their desire to understand particular geophysical phenomena than they were to develop an engineering guide or translate a space measurement into a systems design standard. Generally speaking, the space scientists have been very successful. We are still surprised occasionally by a new space environment measurement, but by and large, space scientists have provided us with an excellent understanding of near Earth space that may well continue to be refined, but is not likely to change dramatically.

As mentioned, the co-leaders of the Air Force/NASA group concerned with the interdependency of their space programs feel that more effort is needed to encourage the interaction between NASA and Air Force working level scientists and the hands-on space systems engineers in industry and government that design, build, and operate space systems. A technical meeting, at which a series of survey papers describing the characteristics of available empirical and theoretical models in select areas of interest to the space systems community seemed to be a reasonable approach. It was decided that a well-attended, national, AIAA meeting, with its diverse participation that include some scientists, as well as a large number of engineers and managers from industry and government, would provide a very appropriate forum.

I had the privilege of being asked to organize one technical session for the 1994 Aerospace Sciences Meeting. In this session, a small group of scientists, each well established and respected in his field, would present the characteristics of available on-orbit space environment models. The speakers would describe which models were appropriate under which conditions, what assumptions were made within a particular model, and the effect of these assumptions on the model's product. The session contained six papers and attracted an audience twice as large as expected. The consensus of the audience was that the presented material was interesting, useful to the engineering community, and that the program should be expanded to include additional types of space data and models the following year.

This publication, based on the papers in that session, is another step toward facilitating the availability of space environment data and models to the designers and builders of civilian and military space systems. While this material addresses a limited number of topics, it is comprehensive and up to date for the specific areas covered and should of use of the space systems community.

IONOSPHERIC MODELS

H. C. Carlson, Jr.
USAF Phillips Laboratory
Hanscom AFB, MA

R. W. Schunk
Utah State University
Logan, UT

R. A. Heelis
University of Texas at Dallas
Richardson, TX

Sa. Basu
USAF Phillips Laboratory
Hanscom AFB, MA

Abstract

We seek here to provide a frame of reference for assessing the present status of ionospheric modeling, and for determining which models may best serve a particular user need. This choice depends not only on the geographic region, and time of concern (post analysis, nowcast, forecast), but on the accuracy required by the user, and the ionospheric parameters of greatest concern.

Introduction

Development of ionospheric models has been a preoccupation of scientists and engineers for some decades. The continuing interest of the engineers (communications, surveillance) has been motivated by continuing improvement of commercial and military systems dependent on the ionosphere as a component of the total system. This in turn has generated recurring need for further accuracy and refinement of ionospheric modeling, specification, and prediction capability, as rf systems saw recurring advances to meet ever more stringent demands. The continuing interest of scientists has been motivated by the rapid pace of discovery of different regions of the global ionosphere, controlled by very different physical processes. Furthermore, many global regions exhibit a character often driven by coupling to often very remote regions of space, by a rich complex of interactive mechanisms.

In the earliest days empirical and climatological models were adequate for many purposes. Greater accuracy was afforded, at least for over-head or nearby specification, by adding local measurement for real time scaling or calibration of the empirical statistical model. Today this is still true for certain applications, and for some regions of the globe it is difficult to improve on this approach. For many purposes however, particularly those involving larger sectors of the global ionosphere, physical models are the only way to achieve the accuracies required by the needs of today. This is true not only as a particularly effective way of identifying mechanisms controlling ionospheric behavior, but for practical applications as well. For the latter purposes, the trend is now clearly towards models driven by real time data. To enhance operating speed, and reduce computational cost, these are often streamlined to the form of analytic or semi-empirical models. These then also form the basis of predictive models, where the challenge is to break beyond the realm of prediction by persistence.

Governing processes: For even simple models, the minimum set of parameters required as input to drive the model are: solar activity, geomagnetic activity, time of day (in general both universal and local time), season, and latitude (in general both geomagnetic and geographic). To achieve accuracies of tens of percent or better in electron density requires periodic input of measured ionospheric parameters, with crucial dependence on correlation distances and times.

Figure 1 shows a representative midlatitude ionospheric profile, demonstrating some common nominclature. F region plasma typically has chemical lifetimes of hours and is dominated by transport between production and loss; lower altitude plasma has chemical lifetimes of minutes and less, and is dominated by local production (solar radiation and energetic particles) and chemical recombination.

Quite different morphologies and physical processes distinguish between equatorial, midlatitude, near auroral, and polar cap ionospheric conditions. For instance, the equatorial ionosphere is characterized by strongly enhanced peak electron densities roughly 10-

20 degrees either side of the equator (the Appleton anomaly). These occur on many, but not all days, depending on a variable equatorial electric-field-driven upward transport term. Midlatitude ionospheric electron densities exhibit: strong seasonal variations due in large part to changing upper atmospheric composition; and considerable day to day variability due largely but not solely to variable vertical transport driven by variable horizontal upper atmospheric winds and electric fields. Auroral ionospheric electron densities may be anomalously enhanced in the E region by particle production, and depleted in the F region by velocity dependent chemical loss rates. Because polar ionospheric F region plasma (with typical lifetimes of hours) commonly has anti-sunward horizontal transport velocities of order a km/s, the p[olar cap is characterized by large plasma densities which typically come from source regions thousands of km away. This ionospheric transport is driven by forces originating in the solar wind, and transmitted via interaction through the magnetosphere. Consequently, the character of the polar ionosphere is critically dependent on the interplanetary magnetic field (IMF). The IMF, particularly its vertical component, in fact dominates the polar cap ionospheric electrodynamics and energetics, and threrby its plasma densities, thermal structure, and composition.

Despite these complexities, physical models of ionospheric electron densities, when driven by real time data, can produce real time global models with nominal accuracies of a few tens of percent, within correlation distances less than about a thousand km, and correlation times of a fraction of an hour.

Approaches to modeling: Empirical or statistical models have been widely used over the last decade, based on a large body of measurements, binned by known dependent parameters, and generally analytically fit. The most comprehensive of these is the International Reference Ionosphere, the IRI. It provides a model of the global distribution of electron density , ion composition, and electron and ion temperature and drift. Empirical models also exist for ionospheric high latitude convection, plasma structuring, auroral particle precipitation, and field aligned currents.

Physical models are very effective research tools for identifying missing physical processes and mechanisms controlling ionospheric behavior, and for applications are generally the best way to extrapolate and interpolate between direct measurements of desired parameters. Ab initio calculations grow steadily more accurate as increasingly comprehensive global data sets and refined models are iterated. The model usually solves the continuity, momentum, and energy equations for the electrons and ions, as a function of altitude along curved magnetic field lines, to derive plasma densities, flow velocities, temperatures, and composition.

Analytical models can make much of the power of physical models available to a much broader community of users than otherwise economically feasible. An extensive set of physical model outputs is fit by sets of relatively simple analytic functions, tagged to key parameters, so that the "physical model data" can be more quickly and easily accessed, using a much smaller and less expensive computer.

Real time data driven models are the next logical step, combining the above capabilities. These are already on line, with significantly enhanced capability scheduled for the near future, based on ground based active and passive radio sensors and satellite in situ and remote sensors.

User needs: A major model selection criterion is user or system requirement. What accuracy is needed, for which ionospheric parameters, over what sector of the globe, for what time frame, and with what turnaround time. For system applications, the nature of the rf system for which the ionosphere must be specified is a crucial consideration. An HF communication system is concerned with the bottomside ionosphere, where photochemistry is important, and the height and magnitude of the peak electron density, determined by the balance between photochemistry and vertical transport. The ionospheric span of concern can exceed transcontinental distances. A transionospheric propagation

system depends on the total electron content along the radio line of sight, for which vertical transport, topside thermal balance, and ion composition (for topside scale height) are significant concerns. Radar ranging and satellite tracking may be concerned with a relatively local ionospheric area. Our discussion of these systems has dwelled upon the bulk ionospheric densities.

In sharp contrast, VHF, UHF, and even EHF communications systems using satellites are influenced primarily by spatial structure in the ionosphere, of scale sizes of order a km. These can lead to fades in intensity and phase sufficiently great as to compromise or disrupt communications or radar imaging at these frequencies. Statistical models serve system designers, allowing them to define fade margins, diversity techniques in space, frequency, or time, and other design criteria to avoid or compensate for this scintillation effect. Empirical models, or data driven real time models allow more sophisticated means for dealing with these effects. Such effects are of concern at equatorial latitudes after sunset, near auroral latitudes, and in the polar cap at sunspot maximum. GPS accuracies and even loss of lock are at issue. Different requirements may be best met by monitoring, or empirical or data driven physical models.

Options range from models that can run on a PC, to a workstation, to only a Cray or Cray equivalent. They can be regional or global, tailored to one or several parameters.

Global Ionospheric Models

Empirical Models: A number of empirical climatological ionosphere models are in use, the best known being the International Reference Ionosphere (IRI) (Rawer and Bilitza, 1989), the Bent model (Llewellyn andd Bent, 1973), and the Chiu model (Chiu, 1975). The former two use the International Consultative Committee of Radioscience (CCIR) or International Union ofRadio Science (URSI) coefficients to specify the peak density and altitude of the F and E region; the latter uses its own databases. These models are computationally fast, but suffer accuracy limitations where data is sparse.

IRI: The IRI is the standard ionospheric model established and updated by a joint working group of the Committee on Space Research (COSPAR) and the URSI. Based on a large volume of ground and space based data, IRI provides a global representation of electron density, electron and ion temperature, ion composition and drift from 60 to 2000 km, for all local times, seasons, and levels of solar activity during magnetically quiet conditions. Since initiated several editions have been released: IRI-78, IRI-80, IRI-86, IRI-90 (IRI-94 is in preparation). Improvements and updates are guided by new data at annual workshops.

The IRI electron density profile is normalized to the F2 peak density and altitude in the topside and F region, and to the E peak density and height in the E region and D region. The model includes an F1 ledge and an E region valley for the specific conditions under which these features are most likely to occur. The representation of E and F peak parameters in the IRI is derived from the ionosonde-based global maps recommended for use by the CCIR. The IRI-90 includes the new URSI-88 model maps for F2 peak density, as these give better values over oceans where the model uses theoretically calculated values of F region peak electron densities and heights (Rush et al, 1984), while CCIR values are favored and used over land.

The IRI verticle electron density profile is segmented in the topside, bottomside, F1, intermediate, valley, E, and D regions (Figure 2a). The IRI electron temperature profile fitted to satellite in situ data based global models at 300, 400, 600, 1400, and 3000 km (Figure 2b). Fit to the CIRA-86 neutral temperature at 120 km, they are shaped by incoherent scatter radar data between these points. Ion tempeatures are between the electron and neutral gas temperatures. Topside ion composition is based on satellite data.

Physical Models: Physical or first-principle models have been used for nearly three decades to elucidate the fundamental processes that operate in the various ionospheric regions. With this approach, one typically solves the continuity, momentum, and energy

equations for the electrons and ions either as a function of altitude or along curved geomagnetic field lines in order to calculate the plasma densities, flow velocities, and temperatures. An advantage of this approach is that the different chemical and transport processes can be studied separately so that their quantitative effects can be assessed. However, the conservation equations correspond to a set of coupled, nonlinear, time-dependent, partial differential equations and, hence, numerical techniques and supercomputers are generally required in order to obtain the desired ionospheric parameters. Because of the inherent complexity of the physical ionospheric models, the initial models were regional, i.e., separate models were developed for the equatorial (*Anderson*, 1981; *Chan and Walker*, 1984), mid-latitude (*Stubbe*, 1970; *Schunk and Walker*, 1973; *Roble*, 1975; *Young et al.*, 1980), and high-latitude (*Schunk et al.*, 1975; *Knudsen et al.*, 1977; *Quegan et al.*, 1982) regions of the ionosphere. Later, a fully global ionospheric model was constructed (*Sojka and Schunk*, 1985), and then self-consistent coupled ionosphere-thermosphere models were developed (*Fuller-Rowell et al.*, 1987; *Rees and Fuller-Rowell*, 1987; *Roble et al.*, 1988).

Depending on the ionospheric model, different input parameters are needed in order to characterize the effect of the magnetosphere and thermosphere on the ionosphere. Pure ionospheric models require a specification of the neutral gas densities, temperatures, and winds. In the equatorial region, the electrodynamic drifts are needed, while at high-latitudes all of the models require a specification of the plasma convection and particle precipitation patterns. Also, all of the models need information on the downward electron and ion heat fluxes through the upper boundary as well as information on the protonospheric exchange flux. For the coupled ionosphere-thermosphere models, the neutral gas parameters are calculated self-consistently, but additional inputs are required. Specifically, the tidal and gravity waves traveling up from the mesosphere must be specified, and the escape flux of nitric oxide across the lower thermospheric boundary is a free parameter.

For global studies, the input parameters required by the ionospheric models must be specified all over the globe as a function of time. Since such extensive data sets are rarely available, it is not surprising that by far the bulk of the physical modelling efforts have been based on 'empirical' or 'statistical' model inputs. Empirical models have been developed to describe magnetospheric (convection) electric fields (*Heelis*, 1984; *Heppner and Maynard*, 1987), auroral particle precipitation (*Spiro et al.*, 1982; *Hardy et al.*, 1985), neutral composition and winds (*Hedin*, 1987, 1988), and equatorial (dynamo) electric fields (*Richmond et al.*, 1980). Typically, the empirical models are based on data collected over an extended period of time from many ground-based sites, rocket campaigns, or satellites. The data are synthesized, binned with the aid of appropriate indices, and then fitted with simple analytical expressions. As a consequence, the empirical models represent average conditions, not instantaneous patterns. Therefore, ionospheric simulations based on time-stationary empirical inputs describe ionospheric climate and not ionospheric weather.

USU Time-Dependent Model of the Global Ionosphere: The USU ionospheric model describes the 3-dimensional time-dependent evolution of the global ionosphere at altitudes between 90 and 1000 km. The numerical model yields density distributions for electrons and six ion species (NO^+, O_2^+, N_2^+, O^+, N^+, He^+) as a function of latitude, longitude and altitude on a prespecified spatial grid (*Schunk*, 1988; *Sojka*, 1989). The model also calculates the isotropic electron temperature and the ion temperatures both parallel and perpendicular to the geomagnetic field on the same spatial grid. The model outputs the global density and temperature distributions at specified times. The model was constructed to take account of numerous physical and chemical processes, including field-aligned diffusion, cross-field electrodynamic drifts, thermospheric winds, polar wind escape, energy-dependent chemical reactions, neutral composition changes, ion production due to EUV radiation and auroral electron precipitation, thermal conduction, diffusion-thermal heat flow, and a host of local heating and cooling mechanisms. The

model also takes account of the offset between the geomagnetic and geographic poles.

The USU model of the global ionosphere is based on an Euler-Lagrange hybrid numerical scheme. For the mid-high latitude region, the ion continuity, momentum, and energy equations are solved as a function of altitude using a fixed spatial grid, while for the equatorial region the ion equations are solved along the magnetic field (**B**) from one hemisphere to the conjugate hemisphere on a fixed spatial grid. In all latitudinal domains, the plasma flux tubes are allowed to convect through a moving neutral atmosphere in a direction perpendicular to **B** due to magnetospheric, corotational, and dynamo electric fields. The three-dimensional nature of the model is obtained by following many flux tubes of plasma while keeping track of their positions at all times. This approach has the advantage over a purely Eulerian scheme, which requires fixed grid points in latitude and longitude, because more flux tubes can be placed in the high latitude regions where sharp horizontal gradients are expected, such as near the auroral oval and main trough.

The ionospheric model requires several inputs. The main 'global' inputs are the neutral densities, temperatures and winds; the magnetospheric and equatorial electric field distributions; the auroral electron precipitation pattern; the downward electron heat flux through the upper boundary; and the protonospheric exchange flux. Typically, empirical or statistical models are used for the required atmospheric and magnetospheric inputs, but in this case the calculated ionospheric parameters pertain to the climatology of the region. For storm and substorm simulations, the temporal variation of the magnetospheric and atmospheric inputs must be specified.

The continuity, momentum, and energy equations correspond to a set of nonlinear, second-order, partial differential equations. The equations are first linearized in time and then finite differences are used for the spatial and temporal derivatives. The resulting coupled algebraic equations are solved with standard matrix inversion techniques. A 4 km spatial step is used in the vertical direction and the time step typically varies from 10 to 100 seconds as a given flux tube follows a specified trajectory. The high-latitude region above 50° North is usually modelled with 500 flux tubes of plasma if empirical plasma convection and particle precipitation patterns are used (climatology modelling). For storm and high resolution studies, 1000-3000 flux tubes are used.

At the lower boundary (90 km), the different ion species are assumed to be in chemical equilibrium and, hence, the boundary ion densities are obtained simply by equating local sources and sinks. Likewise, the ion and electron temperatures at the lower boundary are obtained by equating local heating and cooling rates. At the upper boundary (1000 km), a protonospheric exchange flux is specified for O^+ and the fluxes of the other ion species are assumed to be negligibly small. The upper boundary conditions on the ion and electron temperatures are a specification of the downward heat fluxes through this boundary.

The results from the first fully-global ionospheric model are shown in Figure 3, where contours of N_mF_2 are plotted versus magnetic latitude and MLT. The calculations are for solar maximum ($F_{10.7} = 170$), June solstice, quiet geomagnetic activity ($K_p \approx 2$, $Ap = 12$) and southward interplanetary magnetic field ($B_z < 0$, $B_y = 0$) conditions. The left panel shows a global snapshot at 0300 UT, while the right panel is for 1500 UT. In the summer (northern) hemisphere, the densities at high latitudes are fairly uniform and the auroral oval is not very apparent owing to the fact that the bulk of the high latitude ionosphere is sunlit in summer and the auroral ionization source is weak during quiet geomagnetic activity. In the winter hemisphere, on the other hand, there is a large density variation at high latitudes. Clearly evident are ionization enhancements in the auroral region and a mid-latitude electron density trough that is situated just equatorward of the auroral oval. Note that the main trough covers all longitudes at 1500 UT, a feature that is common in the Southern Hemisphere in winter. The lower N_mF_2 values in the winter hemisphere occur because the bulk of the high-latitude region is in darkness and the auroral

oval is more apparent because the weak auroral ionization source does not have to compete with ionization due to solar EUV radiation.

In the equatorial ionosphere, Appleton ionization peaks are clearly visible at night, but not during the day. The lack of Appleton peaks during the day can be traced to the adopted equatorial electric field pattern. For this study, the electric field values given by *Richmond et al.* (1980) were adopted. However, this model appears to inaccurately specify the phase of the upward **E x B** drift because the Appleton anomaly is typically present during the day. Note the slight asymmetry in the Appleton peaks at 1500 UT, which is a consequence of both the neutral wind and the favorable magnetic field geometry at this UT.

UCL Coupled Ionosphere-Thermosphere Model: The first fully-coupled, self-consistent, ionosphere-thermosphere simulations were conducted by the group at the University College, London (UCL), but these initial simulations were restricted to the polar regions (*Fuller-Rowell et al.*, 1987). This coupled model was developed by combining the UCL global thermosphere model and the University of Sheffield model of the high-latitude ionosphere (*Quegan et al.*, 1982). The UCL global thermosphere model is based on a numerical solution of the nonlinear equations of continuity, momentum, and energy for the neutral gas. The model calculates global distributions of the vector wind, temperature, density, and composition of the upper atmosphere as a function of time. In a given simulation, the atmosphere is divided into a 3-dimensional grid containing geographic latitude, longitude, and pressure level. An Eulerian approach is used in that the grid system is fixed to the rotating Earth. Spherical polar coordinates are used with a 2° resolution in latitude, 18° in longitude, and 15 levels in log pressure (one level for each scale height). The altitude domain varies from 80 to about 500 km. The equations are solved with an explicit time-stepping numerical technique with a one minute time resolution.

The thermosphere model contains all of the processes thought to be important. The momentum equation takes account of horizontal and vertical advection, gravity, curvature and Coriolis effects, horizontal pressure gradients, horizontal and vertical viscosity, and ion drag. The nonlinear energy equation includes energy advection, the transfer of energy between internal-kinetic-potential energy, horizontal and vertical heat conduction due to both molecular and turbulent processes, heating via UV and EUV radiation, cooling by infrared radiation, and ion-neutral frictional heating.

The high-latitude ionospheric model developed by *Quegan et al.* (1982) is an Euler-Lagrange hybrid model that is very similar to the high-latitude part of the USU global ionospheric model. The only appreciable difference is that in the *Quegan et al.* (1982) model the molecular ions are assumed to be in chemical equilibrium at all altitudes. The *Quegan et al.* (1982) model also includes H^+, but this ion is not important for ionosphere-thermosphere coupling studies. Since the UCL thermosphere model relates to a grid system that is fixed to the Earth and the Sheffield ionosphere model is tied to moving plasma flux tubes, a considerable effort was required to link the two separate models. Note that the Sheffield ionosphere model is used at geomagnetic latitudes within 35° of the poles. At the middle and low latitudes, the *Chiu* (1975) semiempirical description of the electron density is used.

The coupled ionosphere-thermosphere model requires the same magnetospheric inputs as the USU global ionosphere model. Specifically, the model must be supplied with plasma convection and auroral precipitation patterns, the downward electron heat flux through the upper boundary, and the polar wind escape flux. In addition, the coupled model requires a global specification of the tidal and gravity wave forcing at the lower boundary as well as a global specification of the downward transport of nitric oxide through the bottom boundary.

Figures 4a and 4b show the first results obtained with the UCL coupled ionosphere-thermosphere model. Figure 4a shows a

snapshot of the calculated mean molecular weight and neutral wind vectors at 0600 UT in the (summer) Southern Hemisphere, while Figure 4b shows the corresponding electron density distribution and neutral wind vectors. In this initial study, only the high-latitude regions were self-consistently coupled and the simulation was for high solar activity ($F_{10.7}$ = 185), December solstice, a magnetic activity level of $K_p \approx 3$, and southward IMF ($B_z < 0$, $B_y < 0$) conditions. Note that the ionosphere and thermosphere are strongly coupled for these geophysical conditions and, as a consequence, the neutral wind pattern in the dusk sector is similar to the imposed plasma convection pattern (not shown). With regard to the electron density, one would expect a fairly uniform distribution over the polar region if the strong ionosphere-thermosphere coupling was ignored because the entire polar cap is sunlit at 0600 UT. However, ion-neutral frictional interactions lead to neutral gas upwellings and O/N_2 composition changes, which, in turn, lead to O^+ depletions via the $O^+ + N_2$ Æ $NO^+ + N$ reaction. As a consequence, a hole develops in the O^+ density distribution in the polar cap due to ion-neutral coupling.

Ion-neutral coupling also has a important effect on the ion temperature at high latitudes, but has relatively little effect on the electron temperature. Typically, at *F*-region altitudes, the ion temperature is tied to the neutral gas temperature, which can change due to a change in the global energy input. The ion temperature can also change due to a localized heat input from ion-neutral frictional interactions, and to a lesser extent from coupling to the electrons. The physics controlling the electron temperature, on the other hand, is different. It is controlled by heating from photoelectrons and auroral electrons, thermal conduction, and cooling due to the coupling with the ions. The net result is that ionosphere-thermosphere coupling has an important effect on the electron/ion temperature ratio at high latitudes.

NCAR Global Ionosphere-Thermosphere Model: The National Center for Atmospheric Research (NCAR) scientists developed the first fully global model of the coupled ionosphere-thermosphere system (*Roble et al.*, 1988). The model is based on a self-consistent numerical solution of the coupled continuity, momentum, and energy equations for the ions, electrons, and neutrals. The model calculates global density distributions for N_2, O_2, O, $N(^4S)$, $N(^2D)$, NO, N_2^+, O_2^+, NO^+, N^+ and O^+ as well as neutral winds and temperatures (neutral, ion and electron). Unlike the UCL and USU models, which are Euler-Lagrange hybrid models, the NCAR coupled model is an Eulerian model. A grid system fixed to the rotating Earth is used. The grid spacing is 5° in latitude and longitude and there are 24 pressure levels in the vertical direction from 97 to about 500 km. The basic physics and chemistry contained in the model are very similar to that in the UCL and USU models, and hence, the details will not be repeated. Likewise, the magnetospheric inputs (convection, precipitation, heat flux, protonospheric exchange flux) and tidal and gravity wave inputs are the same as described for the other models.

The first results from the NCAR fully-coupled, global, ionosphere-thermosphere model are shown in Figures 5a and 5b (*Roble et al.*, 1988). The top panel of Figure 5a shows contours of f_oF_2 (~ 300 km) over the globe at 1900 UT for solar minimum and equinox conditions, while the bottom panel shows contours of the electron density at about 120 km. The corresponding self-consistent neutral gas temperatures and wind vectors are shown in the top panel of Figure 5b. The bottom panel of Figure 5b contains contours of the MSIS-86 empirical model of the neutral atmosphere (*Hedin*, 1987). The simulation shown in these figures corresponds to a steady state (or diurnally reproducible) solution for the adopted geophysical conditions. With regard to the magnetospheric inputs, the cross-polar cap potential was 60 kV and the auroral particle power input was 11 GW. A southward IMF, 2-cell convection pattern was adopted. Tidal forcing from the lower atmosphere was also taken into account.

The electron density calculated by the model exhibits features that are in general agreement with measurements. In the *F*-region on the dayside, the Appleton anomaly is clearly

visible via density peaks in the equatorial region that lie on either side of the magnetic equator. On the nightside at mid-latitudes, ionization troughs exist in both the northern and southern hemispheres. Also, in the auroral zones, enhanced electron densities occur owing to auroral electron precipitation. Note, however, that only the large-scale structure of the ionosphere was modelled. This is also evident in the contours of electron density at *E*-region altitudes (120 km). At this altitude, photochemical equilibrium prevails, and therefore, elevated electron densities exist on the sunlit side and in the auroral oval where ionization occurs. Note the sharp drop in the electron density near the terminator (–15° longitude). With regard to the self-consistent atmospheric parameters, the neutral wind pattern at *F*-region altitudes is similar to that calculated in previous studies, with a diurnal component at low- and mid-latitudes and enhanced winds at high latitudes caused by momentum forcing from plasma convection. Also, the calculated neutral temperatures on the dayside are in very good agreement with the MSIS-86 temperatures. However, on the nightside, the midnight (105° longitude) temperature bulge at the equator calculated by the model appears to be too large in comparison with the MSIS-86 values. This discrepancy is related to the strength of tidal forcing (*Roble et al.*, 1988).

Analytic or Semi-empirical models: Analytic or semi-empirical models offer the accuracy and realism of the physical or first principles models, but the computational speed and ease of the empirical models. Anderson and his co-workers have made major advances in this area over the past decade, for calculation of electron density profiles (EDP), including: SLIM (Anderson et al, 1987), FAIM (Anderson et al, 1989), and PIM, the streamlined version of PRISM (Anderson et al, 1993) that gives global ionospheric specification in the absence of the global set of real time data needed to drive PRISM.

SLIM: A semi-empirical Low-latitude ionospheric Model, SLIM, calculates EDPs from 180-1000 km, with a fine resolution grid (2 degrees latitude, half hour time) within 24 degrees of the dip equator. This was motivated by severe underestimates of topside electron density scale-heights and total electron density content (TEC) by empirical models. Assuming Chapman-like profiles, sets of coefficients were then generated to allow computationally fast reproducing of these accurate profiles, leading to greatly improved EDPs and TECs near the equator. SLIM is a set of functions and coefficients that reproduce 9 sets of theoretically calculated low latitude EDPs for three seasons (equinox and both solstices), and three levels of solar activity (F 10.7 of 70, 125, 185, for low, moderate, and high activity. For each latitude/time point the profiles are given by six parameters and the modified Chapman expression.

FAIM: The Fully Analytic Ionospheric Model, FAIM, provided improvement to users of the Chiu model, by altering the low latitude portion of the Chiu model to reproduce the significantly more accurate SLIM profiles, and somewhat modifying the height of the F region EDP peak (Hmax) to improve its accuracy. It thereby extended the SLIM capability into the midlatitude ionosphere. The Chiu model has been extensively used to (computationally quickly) empirically represent the low and mid latitude ionosphere. Rather than generating EDPs from sets of coefficients, as SLIM, it has the added convenience of representing the needed coefficients as analytic functions of local time and latitude. FAIM embraced this approach, and provided software that was different from the Chiu model only in ways fully transparent to the user. However, the FAIM software modified the maximum height and shape of the F layer to better fit actual data. (The peak F region electron density was good at midlatitudes for both Chiu and FAIM.) As FAIM well reproduces the SLIM results at the equator, it both extends and supplants SLIM.

PIM: The Parameterized Ionospheric Model, PIM, seeks to make the results of a large number of high quality theoretical model runs available to a wide range of users, in a convenient readily accessible form. High accuracy is afforded for minimal computor resource requirements. The models used to generate the EDPs for PIM were the: Utah State Three Dimensional Ionospheric Model (Sojka and Schunk, 1985) for high latitudes;

the mid and low latitude F region model of Anderson et al (1989); and the E region model of Jasperse (1986). The grid resolution is 2 degrees latitude, a half hour time, 5 to 100 km altitude, longitude as required. EDPs are for three seasons (equinox and both solstices), three solar activities (F 10.7 of 70, 140, 210), and three magnetic activity levels (Kp of 1, 3+, and 6; i.e. quiet, moderate, active). Thie PIM is based on the Parameterized Real-time ionospheric Specification Model (PRISM), which has been recently validated and found to give impressively low RMS errors in global values of peak F region densities, generally between 10 and 20% (Figure 6). Driven by realistic data, PIM should give quite useful global EDPs.

Ionospheric Electrodynamics

Above about 130 km altitude the distribution of ionization is strongly controlled by the motion of charged particles parallel and perpendicular to the magnetic field. The motions of the plasma parallel to B are most effectively specified in numerical simulation models of the ionosphere which require the external forcing to be specified. In addition to forcing by the neutral atmosphere and the solar EUV radiation, the presence of electric fields is also an important consideration.

Most ionospheric simulation models that describe the plasma above an altitude of about 150 km assume that the plasma moves in the direction ExB in response to an applied electric field. Thus the ion drift perpendicular to the ambient magnetic field and the electric field can be treated similarly. In order to specify the electric field for use in plasma simulation models or to specify the plasma motion itself it is convenient to divide the ionosphere into low and middle latitudes generally described as the plasmasphere and higher latitudes associated with the auroral zone and polar regions.

At low and middle latitudes the large scale electric fields affecting the bulk plasma characteristics are generated internally by the dynamo action of neutral winds at low altitudes. The electric fields themselves map along the Earth's magnetic field lines and pervade the entire plasmasphere. Most of our information about these low and middle latitude electric fields have come from extensive studies of ground based data obtained from incoherent scatter radars distributed around the globe. As expected the observed ion drifts are periodic in nature and a qualitative description of their behavior in local time is usually specified by fourier decomposition of the zonal and meridional components. The response time of the ionospheric plasma to these drifts is quire long; of order tens of minutes; and thus a specification of the drift velocity with 10-20 minute time resolution is sufficient for most purposes.

Near the equator models for the electric field are obtained from the Jicamarca observatory [Fejer et al, 1990]. Figure 7 shows the variation of the zonal and meridional ion drifts obtained from this data base. These drifts show a strong diurnal component with the drifts being up and toward the west during the day and down and to the east at night. Such motion is easily reconciled with similar diurnal oscillations in the lower atmosphere from which the electric fields originate. In addition to this basic sinusoidal variation throughout the day there exist additional features near sunrise and sunset that result from the interactions between the ions and neutral particles in the F-region. There are significant changes in this diurnal pattern that are dependent on solar activity and magnetic activity and a large enough data base is available to quantitatively specify them. These drifts are largely independent of altitude until one reaches heights at the equator that are in excess of 2000 km or so, at which point the dipole magnetic field lines enter the lower atmosphere at middle latitudes and the neutral wind generator changes character.

At middle latitudes observations are available from ground based observatories in Puerto Rico and Japan. The local time variations of the drifts observed from these stations have also been quantitatively described by a fourier decomposition [Ganguly et al, 1989, Oliver et al., 1993]. Examples of the average patterns from each of these sites are shown in Figure 8. Note first that a semi-diurnal component exists in these local time signatures consistent with a change in the neutral wind driver. There are also significant enough dif-

ferences between these two data sets to suggest that a longitudinal dependence may exist in this latitude region. Longitudinal dependencies are even more apparent in the highest latitude regions of the middle latitude zone. In this region the offset between the geographic and geomagnetic poles produces a longitude dependence in the high latitude influence. This is most easily seen in Figure 9 where the local time distribution of the zonal ion drift observed at St Santin [Blanc and Ameyanc, 1973] and a Millstone Hill [Wand et al, 1983] can be compared. Again, the local time distributions of these drifts are quantitatively specified by a fourier decomposition or by using basis splines. In this region of the ionosphere the underlying quiet time drift is similar to that seen at the lower latitude stations but s significant 24 hour variation with an amplitude dependent on magnetic activity is also present.

It is quite common practice in ionospheric simulation models to assume that the zonal and meridional drifts can be specified independently using the models generated from various data sets and cited earlier. It should be noted however that the global electric field existing over time scales of many hours must be curl free and thus derivable from a global electrostatic potential distribution. Attempts to reconcile the observations from different locations on the globe and to produce a global electrostatic potential distribution for the low and middle latitude region have been undertaken. Richmond et al [1980] provide such a quantitative model that adequately describes many of the large temporal scale features in the data. There are however significant departures between local models and the global model near sunrise and sunset and in specification of the magnetic and solar activity dependencies.

At high latitudes the electric field that pervades the ionosphere results largely from the interaction between the solar wind and the magnetosphere. This results in an electric field distribution that can change on time scales of a few minutes and that is strongly dependent on the interplanetary magnetic field orientation and the solar wind speed as well as magnetic and solar activity. In this high latitude region of the ionosphere the magnetic field lines are almost straight and the ionospheric electric field is most easily specified by a global electrostatic potential distribution. Knowledge of this distribution has been assembled both from ground based data that must assume that temporal changes are small over periods of less than 24 hours and from spacecraft observations that must assume that solar activity and seasonal changes are small over time scales of many months. Data from both these sources show that the direction of the interplanetary magnetic field (IMF) has the most profound effect on the global potential distribution. When the IMF is directed southward a two-cell convection pattern pervades the high latitude regions with flow directed antisunward at the highest latitudes and sunward return flow at lower latitudes collocated with the auroral zone. The orientation of the IMF specified by the sign of By has the most dramatic effect on the geometry of the pattern [e.g. Heppner and Maynard, 1987], while the product of Bz and the solar wind speed determine the magnitude of the equipotential lines that describe the plasma flow [Reiff and Luhmann, 1986]. Figure 10 shows empirical representations of high latitude convection pattern obtained from satellite observations by Heppner and Maynard [1987]. Notice that the potential distribution is characterized by a local maximum on the dawnside near 0600 hrs magnetic local time and a local minimum on the duskside near 1800 hrs magnetic local time. The difference between these two values, typically referred to as the polar cap potential drop is a parameter controlling the distribution of the potential around an approximately circular line called the polar cap boundary which separates the antisunward flow from the sunward flow. It can be seen that the effect of the IMF By is largely to change the geometrical configuration of the convection cells inside the polar cap and some of the details of the flow geometry near local noon. All data sources generally reflect these same features in the electrostatic potential distribution. Numerical models of the distribution, suitable for use in plasma simulation routines or in convective flow studies are constructed by either by utilizing mathematical expressions that reproduce the observed features [Hairston and Heelis, 1990; Sojka et al, 1986] or by spherical harmonic fits to average data obtained

from spacecraft [Rich et al, 1990] and from ground based radars [Foster, 1983; Holt et al, 1987]. Each of these approaches has advantages and disadvantages dependent on the required task. Data driven models specify only the configuration for a limited set of IMF conditions with assumptions required to produce smooth transitions between these states. These models usually specify only the potential a specified grid points with numerical interpolation and differentiation required to deliver the ion drift velocity at any give location. Mathematical models can deliver the ion drift velocity at any given point and are usually driven by interplanetary magnetic field inputs allowing the potential distribution to be specified for any give state. However, they may be incapable of representing a given observation unless care is taken to ensure that this is a property of the chosen mathematical functions [Hairston et al., 1990].

When the IMF has a significant northward component ($|Bz|/|By|>0.6$) the two cell convection pattern deteriorates and large scale features frequently become difficult to specify. Quantitative models providing a numerical representation of the pattern are available for specific conditions [Rich et al., 1990, Sojka et al. 1986] but it is generally dangerous to assume that they will successfully mimic any particular observation or that the plasma distributions obtained when they are incorporated into simulation models will yield results compatible with observations. There is clearly more work required in this area, both in understanding and in producing adequate models of the observations.

One technique meeting with some success in addressing a numerical characterization of the potential distribution from a distribution of observations is the so-called assimilative mapping of ionospheric electrodynamics (AIME)[Knipp et al, 1990] procedure. Here a variety of space based and ground-based observations can be incorporated with the condition that they should all be compatible with a divergence free current. The global potential distribution that satisfies this condition and fits the data in a least squares sense can be specified numerically on a local time and latitude grid. This information can be obtained under a variety of different conditions so that representative pictures of the convection pattern are available to be used in numerical plasma simulation models.

The references cited above provide sources for numerical models for the drift motion of ionospheric plasma at low medium and high latitudes. Most of the models are adequate for describing the large scale behavior of the plasma and the changes in this behavior that are effected by parameters like solar activity, season and magnetic activity. Many models do not and cannot describe the plasma motion on small spatial or temporal scales so that caution should be applied in interpreting these models or the outputs for this purpose.

Ionospheric Scintillation Models

Turbulence often develops in the ionosphere and, as a result, electron density structures are formed with horizontal scales varying from tens of kilometers to tens of meters. When radio waves from satellites traverse a turbulent ionosphere, the waves get scattered by the electron density structures and a pattern of varying amplitude and phase is developed at the observer's plane. In the presence of a relative motion between the satellite, the ionosphere and the observer, this pattern sweeps past the observer's antenna, and random fluctuations of signal amplitude and phase as a function of time are recorded. This is known as the ionospheric scintillation. (Arons, 1977; Basu et al, 1987).

Scintillations cause the received signal amplitude to be enhanced and to fade at a fast rate. When the fades due to the ionospheric scintillation exceed the signal margin of the satellite receiving system, the signal randomly becomes buried in noise, bit errors occur which may render the message unintelligible. In addition to satellite communication links, modern navigation receivers using the Global Positioning System (GPS) at 1.2/1.6 GHz become vulnerable to loss of phase lock in strongly scintillating environment. Ionospheric scintillations introduce fluctuations in radar cross-section (RCS) and thereby degrade the ability of a radar to detect targets. In the presence of scattering, the integrated sidelobe ratio may be increased to impair the resolution of space based radars. The top

panel of Figure 11 shows the antenna pattern of a 16-element array with element spacings of 10 m operating at a frequency of 1 GHz. The next two panels illustrate that in the presence of 100 km turbulent layer in the ionosphere with increasing turbulent strengths ($C_s = 10^{20}$ and $C_s = 10^{22}$), the fringe visibility is progressively degraded to reduce the image resolution (Rino et al, 1983). Such turbulent levels may indeed be encountered in the equatorial anomaly regions (nominally 15° N and 15° S magnetic latitudes in the post-sunset hours).

Since scintillations are related to the kilometer scale variations of the total electron content of the ionosphere, systems become most stressed in regions where turbulence develops in an environment of high electron content. Figure 12 shows the global distribution of worst-case scintillation at L-band corresponding to GPS transmissions during the solar maximum (left panel) and the solar minimum periods (right panel) (Basu et al, 1988). The figure is organized in magnetic co-ordinate system so that the central latitude circle is the magnetic equator and the extreme left and right meridians represnt respectively the noon and midnight magnetic meridians. The drastic reduction of scintillation in the right hand panel is attributed to nearly a factor of ten reduction of F-region electron density during the solar minimum period. The left hand panel shows that the equatorial region becomes very disturbed after sunset and the strongest scintillating region is located at 15° N and 15° S magnetic latitudes but not at the magnetic equator. These are the so-called equatorial anomaly locations where the electron density is enhanced due to the transport of ionization from the magnetic equator by an upward drift and diffusion of ionization along magnetic field lines.

At high latitudes, scintillations in the auroral region is a nighttime event but, within the polar cap scintillations can be observed at virtually all local times. During the solar maximum period, GPS navigation systems become most vulnerable in the equatorial anomaly regions but are also stressed within the polar cap. Figure 13 provides a two-frequency comparison of system effects due to scintillation and total electron content in the auroral region. The parameters listed in Figure 13 may be scaled for the equatorial and polar cap regions by considering that the F-region electron density within the polar cap and the equatorial anomaly regions are higher than the auroral region by a factor of about 5 and 20 respectively and assuming that the small scale structuring factor is identical in all regions.

WBMOD Scintillation Model: The empirical WBMOD (Secan et al, 1987) ionospheric scintillation model is a computer coded global model of ionospheric scintillation. The model was based on amplitude and phase scintillation measurements of VHF and UHF radio transmissions from the Defense Nuclear Agency's Wideband satellite. The observational results were integrated in the framework of the phase screen theory. The model was complemented by theoretical studies and other experimental investigations of the ionosphere. The limitations of the model in the equatorial region were caused by a limited number of stations clustered close to the magnetic equator and only two fixed local times of observations caused by the sun-synchronous nature of the orbit. These limitations have recently been removed by infusing the model with Phillips Laboratory's long-term geostationary satellite scintillation data.

When the user specifies environmental conditions (date, universal time, sunspot number and planetary magnetic index), the model provides a table of phase and amplitude scintillation index, phase spectral strength and phase spectral slope at any frequency for any geographic location of the station and the satellite. Figure 14 shows an example of the model output adapted to a particular application. The user specified the environmental conditions as listed in the header of the diagram and asked for a plot of the amplitude scintillation index, S_4, at a satellite frequency of 1.541 GHz, in the form of a contour diagram. The satellite at a geosynchronous altitude was moved over a specified lat - long grid. The requested dimension of the plot covers a geographic latitude grid of 40° N to 40° S and longitude swath of -180° to +180° on which the magnetic equator and magnetic

latitudes of +20 and -20 are to be indicated. Figure 14 shows the presence of scintillation between 0° and 60° longitude corresponding to local times of 20h to 00 h and the scintillations to be strongest near the anomaly locations.

The model should be used to determine scintillations at frequencies above 100 MHz and for satellite altitudes above 700 km. The WBMOD model is implemented in standard FORTRAN 77 with a few standard VAX/VMS extensions.

Physical Model of Scintillation: A physical model of scintillation is being developed by coupling a physics based model of electron density in the F-region of the ionosphere with plasma instability theories. The large scale electron density structures so determined are infused with small scale irregularities with prescribed spectrum and irregularity amplitude. Radio waves at any frequency are allowed to traverse the turbulent ionosphere and the scattering theory is used to determine the signal distortions or scintillations in the received signal.

The framework for such a physical model in the polar cap region is illustrated in Figure 15. The diagram illustrates the two states of the polar ionosphere. When the z-component of the interplanetary magnetic field is southward, large scale patches of ionization are transported into the polar cap from the high mid-latitude ionosphere. As illustrated in the botttom right panel, these patches develop small scale irregularities through the operation of the gradient drift instability mechanism. The Utah State University's (USU) Time Dependent Ionospheric Model (TDIM) has been run to generate large scale patches of ionization. The gradient drift instability mechanism operated on the these patches indicate growth times of the order of tens of minutes. The patches when perturbed with 5 - 10 % irregularity amplitudes are found to develop the observed levels of scintillation within the polar cap. Scintillation models have not been formulated for the other state of the ionosphere, as illustrated in the left hand panel of Figure 15. This is because sun-aligned arc related scintillations are less intense than patch related events.

Similar physical models of scintillation for the equatorial region are also being developed in the framework of post-sunset enhancement of electric fields in the ionosphere, and development of Rayleigh Taylor instability.

Such models of scintillation can be driven by input parameters related to the physical parameters of the ionosphere and hence are suitable candidates for future forecast models. Further, these models can be used to determine scintillation at any frequency and even for satellite to satellite propagation within the ionosphere.

References

Aarons, J.,Equatorial Scintillations: A Review, *IEEE Trans. Antennas Propag.*, AP-25, 729, 1977.

Anderson, D. N., Modeling the ambient, low latitude F region ionosphere–a review, *J. Atmos. Terr. Phys., 43*, 753-762, 1981.

Anderson, D. N., M. Mendillo, and B. Herniter, A semi-empirical low-latitude ionosphere model, *Radio Sci., 22*, 292, 1987.

Anderson, D. N., J. M. Forbes, and M. Codrescu, A fully analytical, low-latitude ionospheric model, *J. Geophys. Res., 94*, 1520, 1989.

Basu, S., E. MacKenzie, Su. Basu, E. Costa, P. F. Fougere, H. C. Carlson, and H. E. Whitney, 250 MHz/GHz scintillation parameters in the equatorial, polar, and auroral environments, *IEEE Journal on Selected Areas in Communications*, SAC-5, 102, 1987.

Basu, S., E. MacKenzie, and Su. Basu, Ionospheric constraints on VHF/UHF communication links during solar maximum and minimum periods, *Radio Sci.*, 363, 1988.

Blanc, M., Magnetospheric convection effects at mid-laitudes I, St. Santin observations, *J. Geophys. Res., 88*, 211, 1983.

Chan, H. F., and G. O. Walker, Computer simulations of the ionospheric equatorial anomaly in East Asia for equinoctial, solar minimum conditions, Part I: Formulation of model, *J. Atmos. Terr. Phys., 46*, 1103-1112, 1984.

Chiu, Y. T., An improved phenomenological model of ionospheric density, *J. Atmos. Terr. Phys., 37*, 1563-1570, 1975.

Fejer, et al, Average vertical and zonal F-region plasma drifts over jicaamarca, *J. Geophys, Res., 96*, 13901, 1991.

Fuller-Rowell, T. J., D. Rees. S. Quegan, R. J. Moffett, and G. J. Bailey, Interactions between neutral thermospheric composition and the polar ionosphere using a coupled ionosphere-thermosphere model, *J. Geophys. Res., 92*, 7744-7748, 1987.

Hairston, M. R., and R. A. Heelis, Model of the high latitude ionospheric convection pattern during southward IMF using DE 2 data, *J. Geophys. Res., 95*, 2333, 1990.

Hardy, D. A., M. S. Gussenhoven, and E. Holeman, A statistical model of auroral electron precipitation, *J. Geophys. Res., 90*, 4229-4238, 1985.

Hedin, A. E., MSIS-86 Thermospheric Model, *J. Geophys. Res., 92*, 4649-4662, 1987.

Hedin, A. E., N. W. Spencer, and T. L. Killeen, Empirical global model of upper thermosphere winds based on Atmosphere and Dynamics Explorer satellite data, *J. Geophys. Res., 93*, 9959-9978, 1988.

Heelis, R. A., The effects of interplanetary magnetic field orientation on dayside high-latitude ionospheric convection, *J. Geophys. Res., 89*, 2873-2880, 1984.

Heppner, J. P., and N. C. Maynard, Empirical high-latitude electric field models, *J. Geophys. Res., 92*, 4467-4489, 1987.

Knipp et al, Electrodynamic patterns for September 1984, *J. Geophys. Res., 94*, 16913, 1989.

Knudsen, W. C., P. M. Banks, J. D. Winningham, and D. M. Klumpar, Numerical model of the convecting *F2* ionosphere at high latitudes, *J. Geophys. Res., 82*, 4784-4792, 1977.

Quegan, S., G. J. Bailey, R. J. Moffett, R. A. Heelis, T. J. Fuller-Rowell, D. Rees, and R. W. Spiro, A theoretical study of the distribution of ionization in the high-latitude ionosphere and the plasmasphere: First results on the mid-latitude trough and the light-ion trough, *J. Atmos. Terr. Phys., 44*, 619-640, 1982.

Rawer, K. and Bilitza, Electron density profile description in the International Reference

Ionosphere, *J. Atmos. Terr. Phys., 51,* 781-790, 1989.

Rees, D., and T. J. Fuller-Rowell, A theoretical thermosphere model for CIRA, *Adv. Space Res., 7,* (10)185-(10)197, 1987.

Richmond, A. D., M. Blanc, B. A. Emery, R. H. Wand, B. G. Fejer, R. F. Woodman, S. Ganguly, P. Amayenc, R. A. Behnke, C. Calderon, and J. V. Evans, An empirical model of quiet-day ionospheric electric fields at middle and low latitudes, *J. Geophys. Res., 85,* 4658-4664, 1980.

Rino, C. L., R. C. Livingston, N. B. Walker, and M. D. Cousins, The effects of naturally occuring propagation disturbances on discrete focused arrays, *Final AFGL Rep.*, SRI International, CA 94025, March, 1983.

Roble, R. G., The calculated and observed diurnal variation of the ionosphere over Millstone Hill on 23-24 March 1970, *Planet. Space Sci., 23,* 1017-1030, 1975.

Roble, R. G., E. C. Ridley, A. D. Richmond, and R. E. Dickinson, A coupled thermosphere/ionosphere general circulation model, *Geophys. Res. Lett., 15,* 1325-1328, 1988.

Rush, C. M., M. PoKempner, D. N. Anderson, J. Perry, F. G. Stewart, and R. Reasoner, Maps of foF2 derived from observations and theoretical data, *Radio Sci., 19,* 11083, 1984.

Schunk, R. W., A mathematical model of the middle and high latitude ionosphere, *PAGEOPH, 127,* 255-303, 1988.

Schunk, R. W., and J. C. G. Walker, Theoretical ion densities in the lower ionosphere, *Planet. Space Sci., 21,* 1875-1896, 1973.

Schunk, R. W., W. J. Raitt, and P. M. Banks, Effect of electric fields on the daytime high-latitude *E*- and *F*-regions, *J. Geophys. Res., 80,* 3121-3130, 1975.

Secan, J. A., E. J. Fremow, and R. E. Robins, A review of recent improvements to the WBMOD ionospheric scintillation model, Effect on the ionosphere of communication, navigation and surveillance systems, edited by J, Goodman, 607-616, U.S. Printing Office, Springfield, VA, 1987.

Sojka, J. J., Global scale, physical models of the *F*-region ionosphere: A review, *Rev. Geophys., 27,* 371-403, 1989.

Sojka, J. J., and R. W. Schunk, A theoretical study of the global *F*-region for June solstice, solar maximum, and low magnetic activity, *J. Geophys. Res., 90,* 5285-5298, 1985.

Sojka, J. J., C. E. Rasmussen, and R. W. Schunk, An interplanetary magnetic field dependent model of the ionospheric convection electric field, *J. Geophys. Res., 91,* 1281, 1986.

Spiro, R. W., P. H. Reiff and L. J. Maher, Precipitating electron energy flux and auroral zone conductances: An empirical model, *J. Geophys. Res., 87,* 8215, 1982.

Stubbe, P., Simultaneous solution of the time dependent coupled continuity equations, heat conduction equations, and equations of motion for a system consisting of neutral gas, and electron gas, and a four component ion gas, *J. Atmos. Terr. Phys., 32,* 865-903, 1970.

Young, E. R., D. G. Torr, P. Richards, and A. F. Nagy, A computer simulation of the midlatitude plasmasphere and ionosphere, *Planet. Space Sci., 28,* 881-893, 1980.

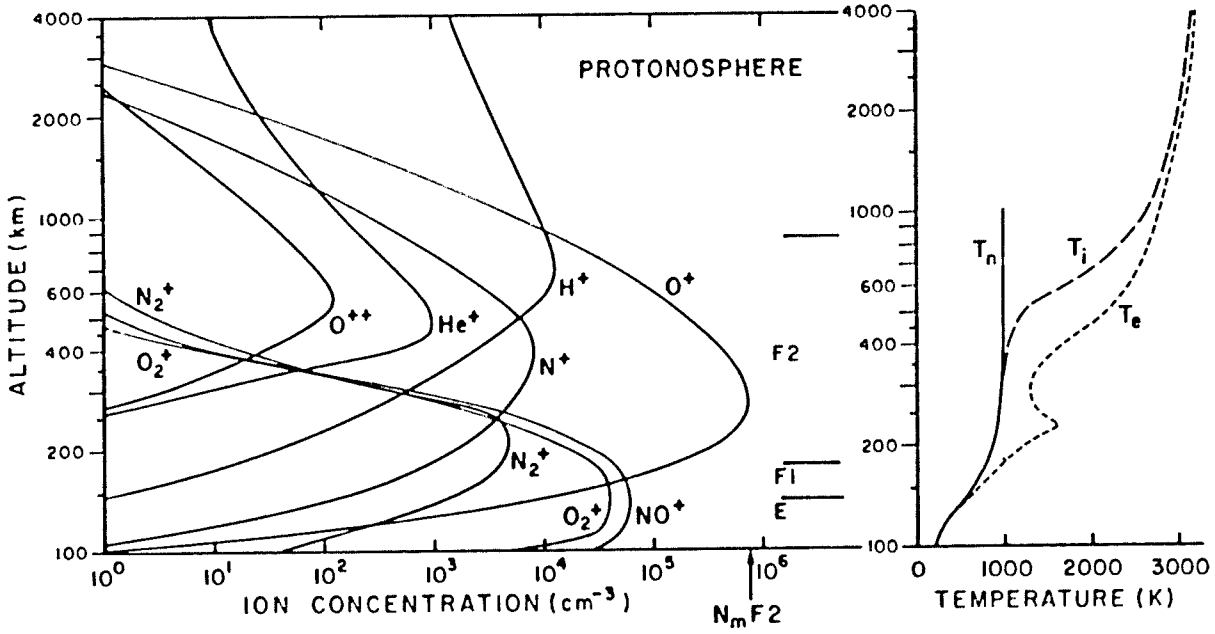

Figure 1a. Representative Midlatitude Ionospheric Profile

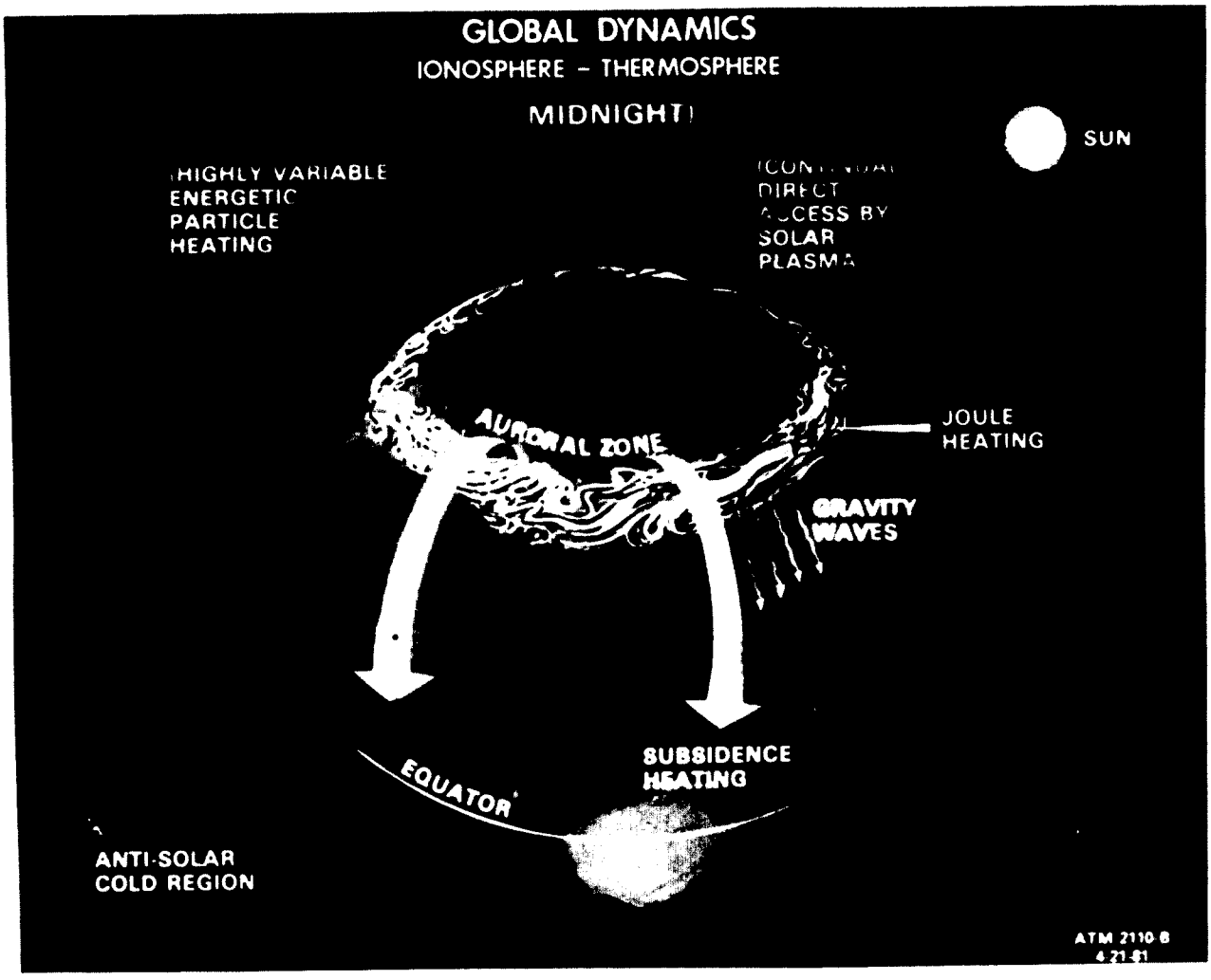

Figure 1b. Global Dynamics of Ionosphere-Thermosphere

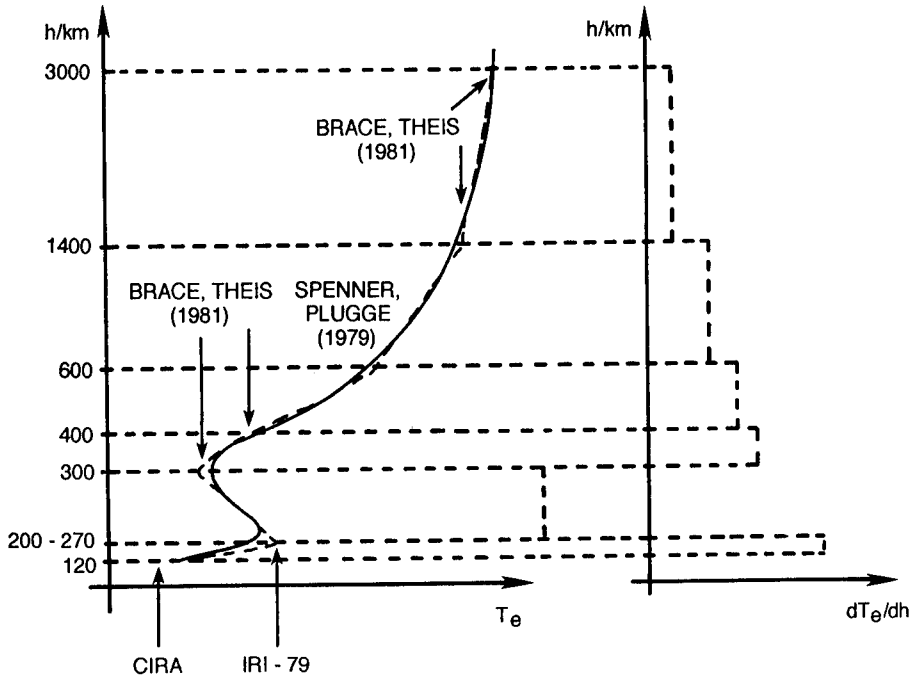

Figure 2a. Buildup of IRI Electron Density Profile

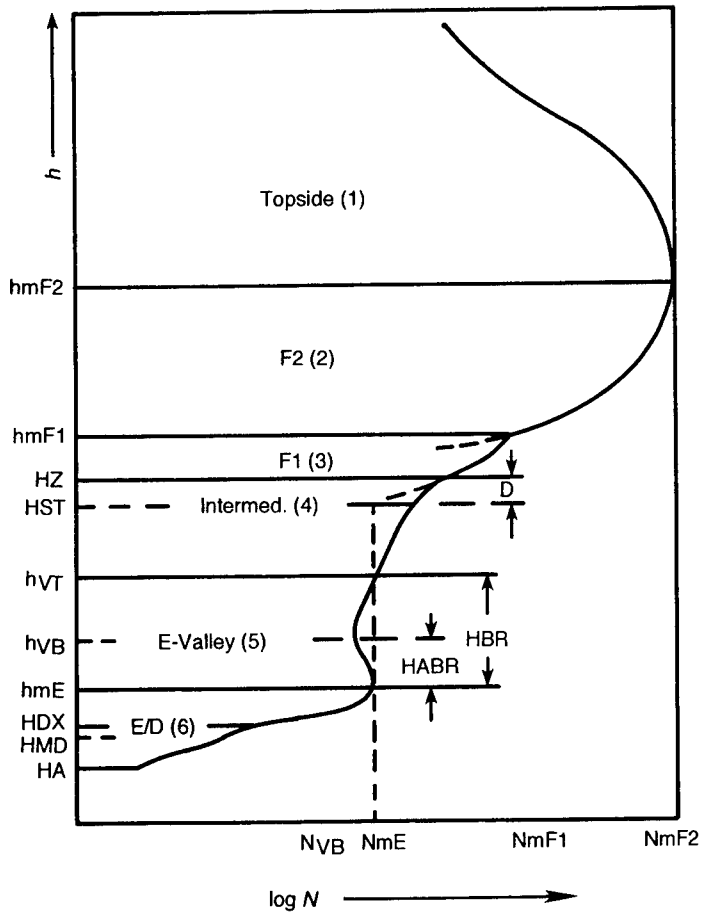

Figure 2b. Buildup of IRI Electron Temperature Profile

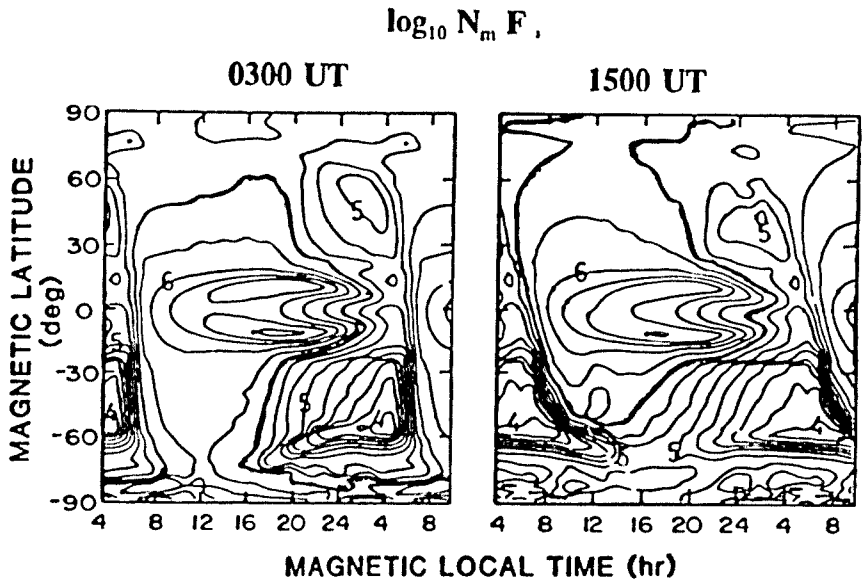

Figure 3. First Fully Global Ionosphere Model

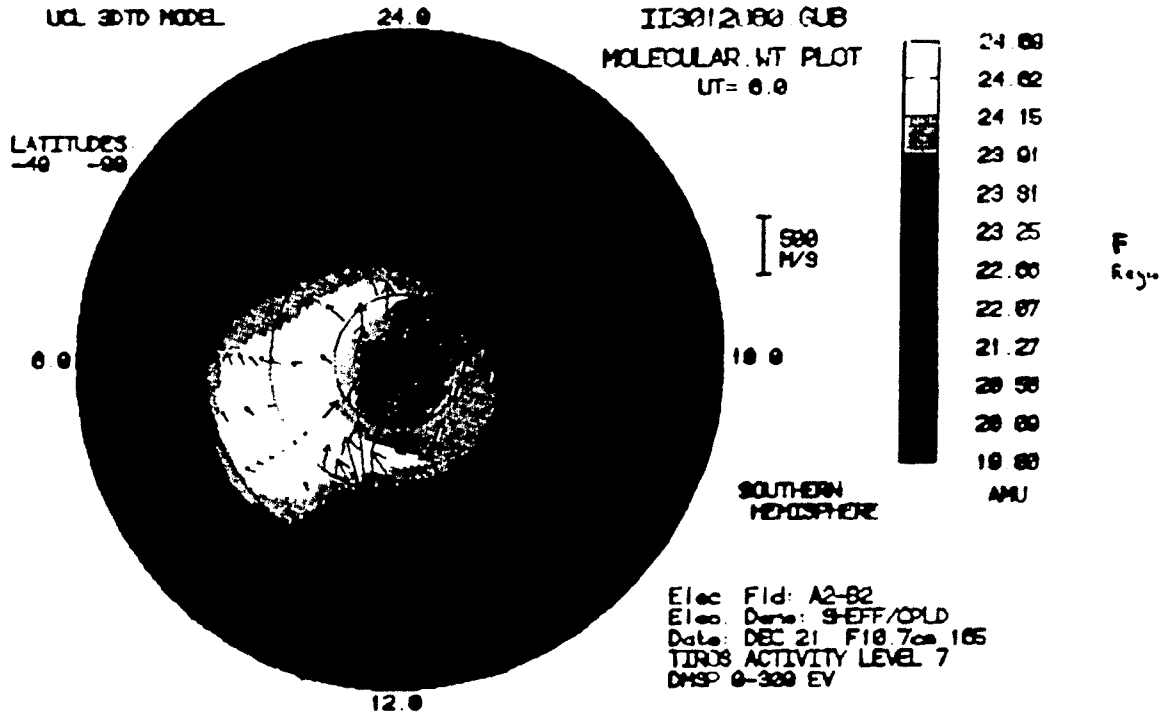

Figure 4a. UCL Coupled Ionosphere-Thermosphere Model (calculated mean molecular weights)

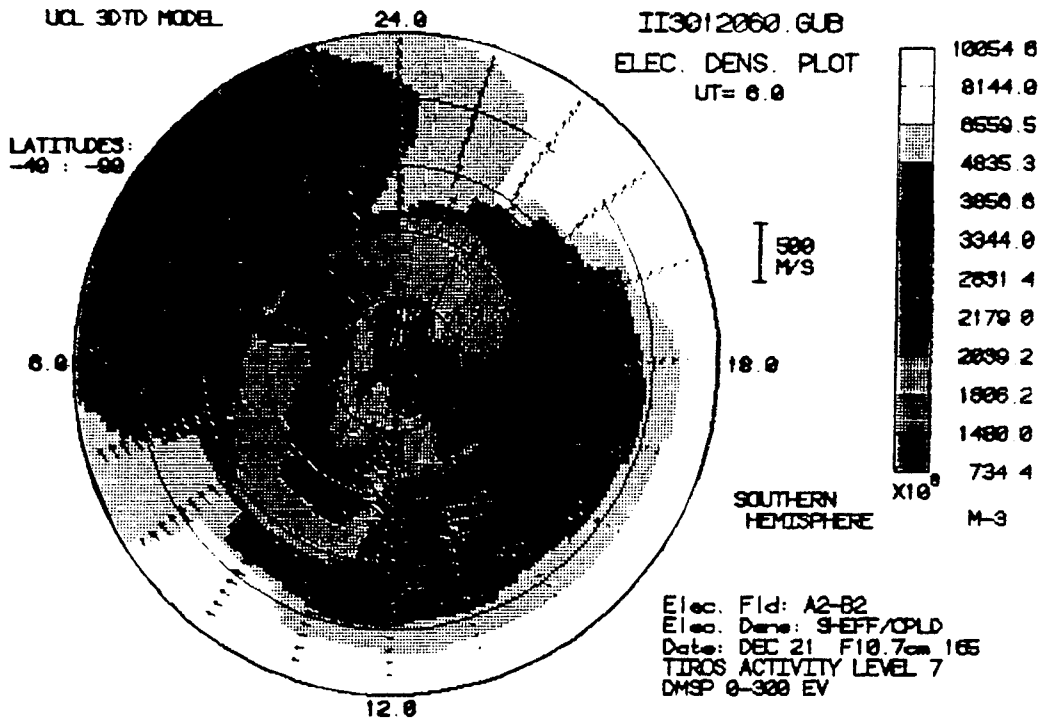

Figure 4b. UCL Coupled Ionosphere-Thermosphere Model (electron density)

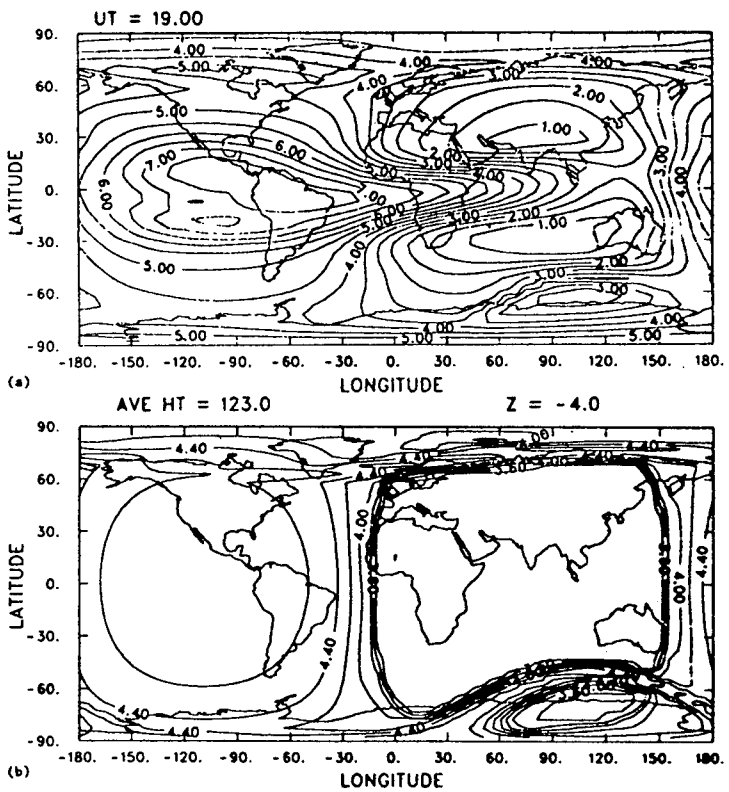

Figure 5a. NCAR Fully-Coupled,Global Ionosphere-Thermosphere Model (f_0F_2 and electron density)

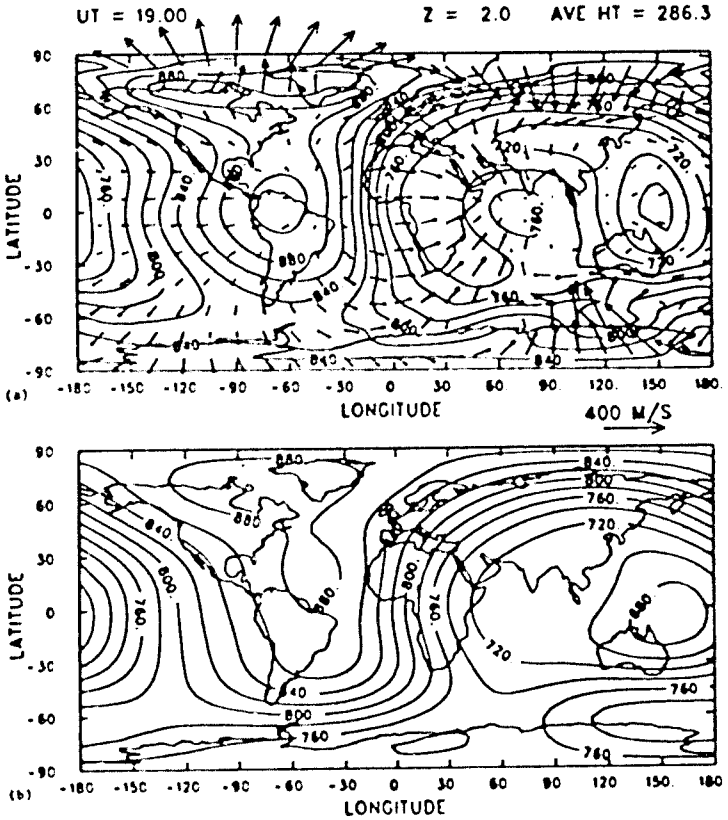

Figure 5b. NCAR Fully-Coupled,Global Ionosphere-Thermosphere Model (temperature-wind and meutral atmosphere plots)

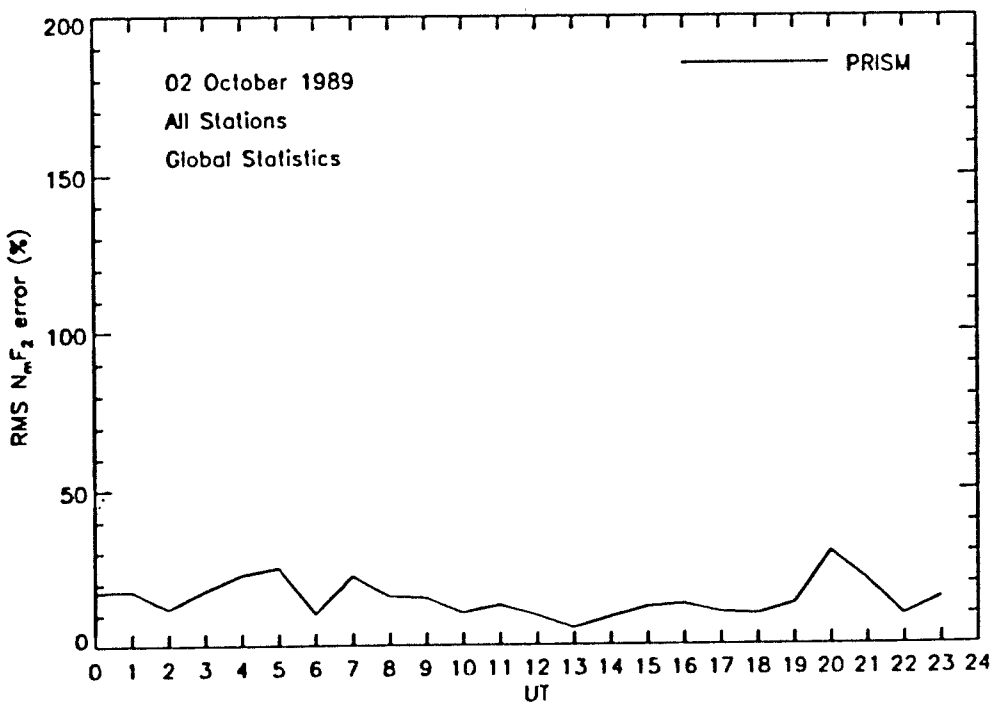

Figure 6. RMS N_mF_2 Errors (%) for PRISM and ICED

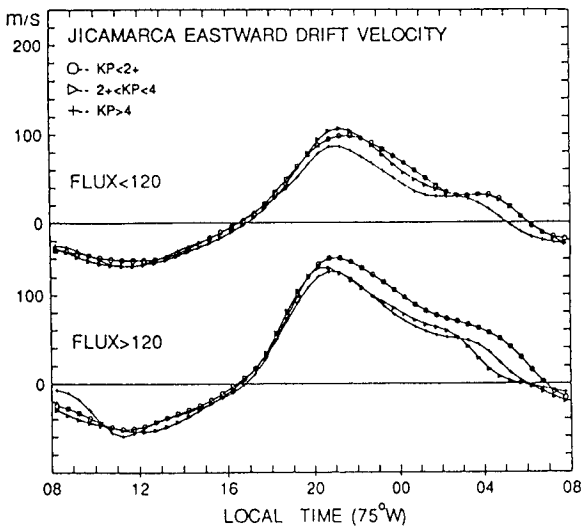

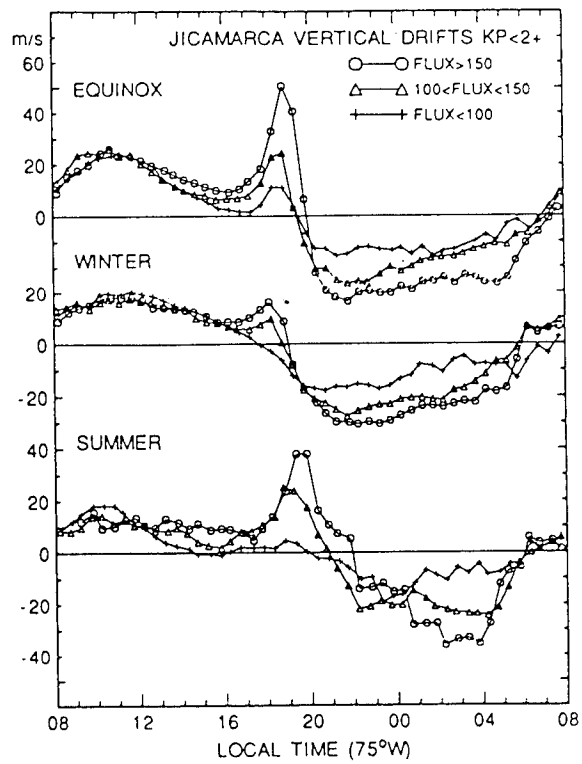

Figure 7. Ion Drift Data (near equator)

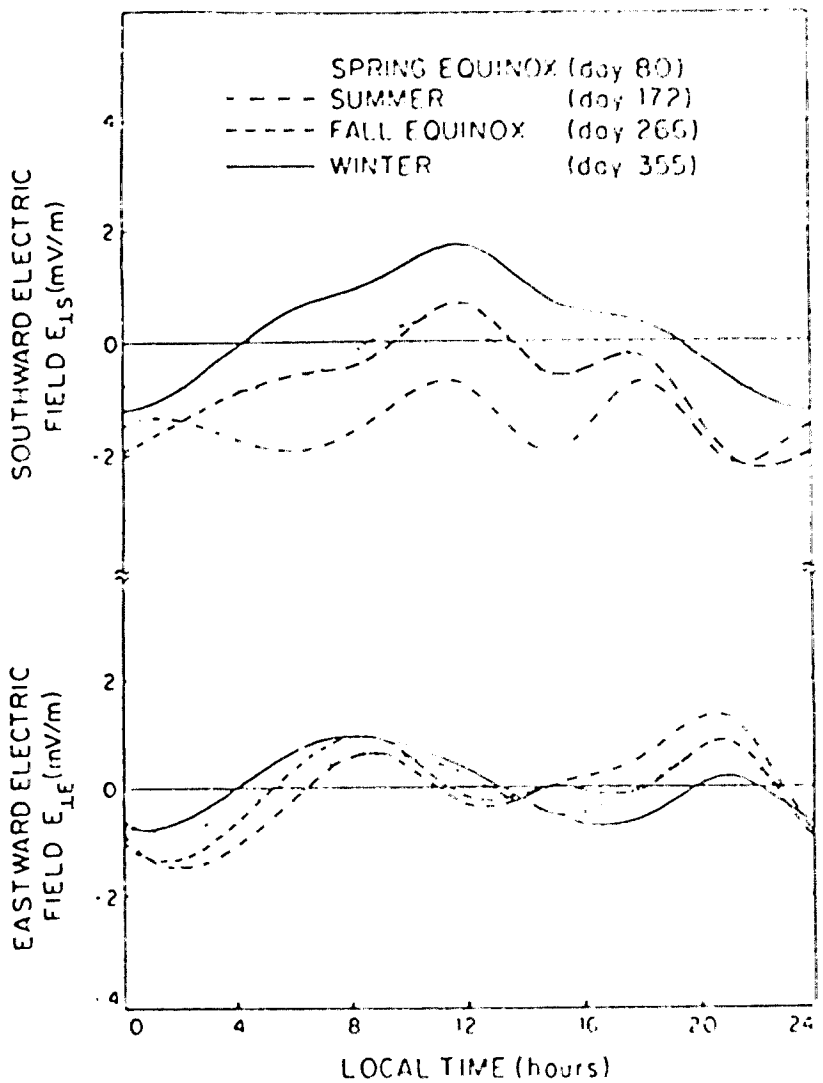

Figure 8. Ion Drift Data (Arecibo, PR)

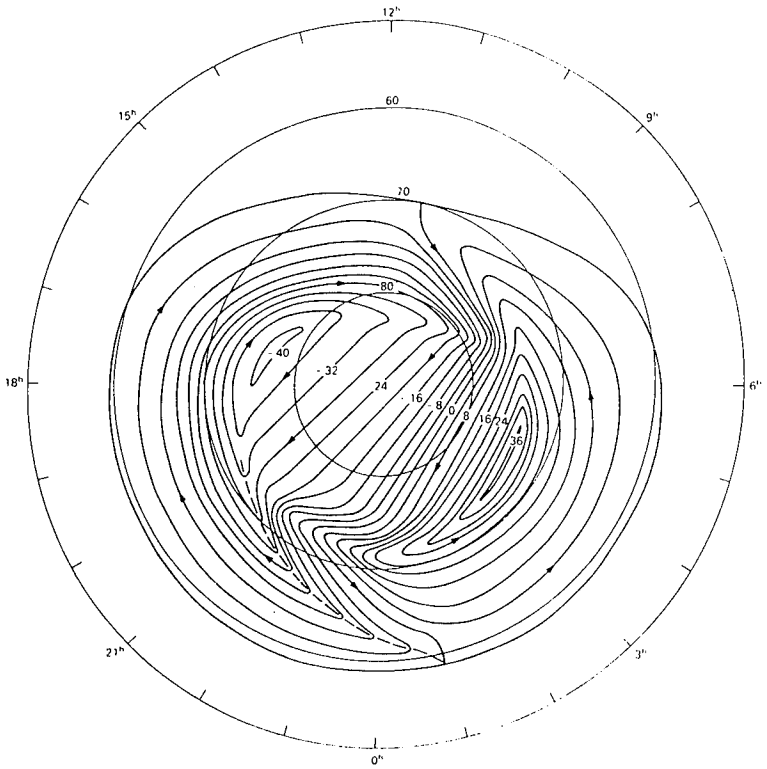

By Positive Northern Hemisphere

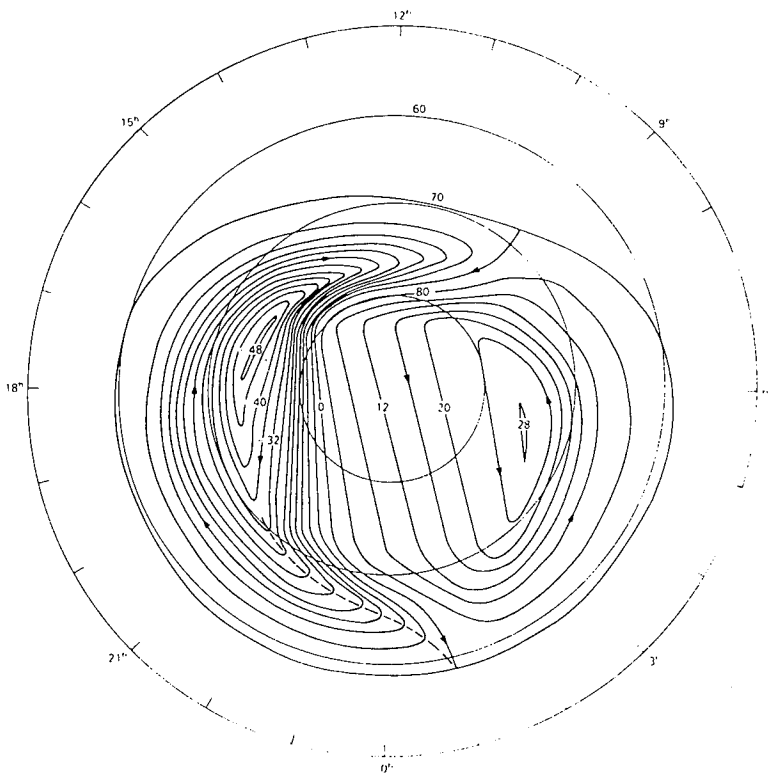

By Negative Northern Hemisphere

Figure 9. Ion Drift Data (Millstone Hill)

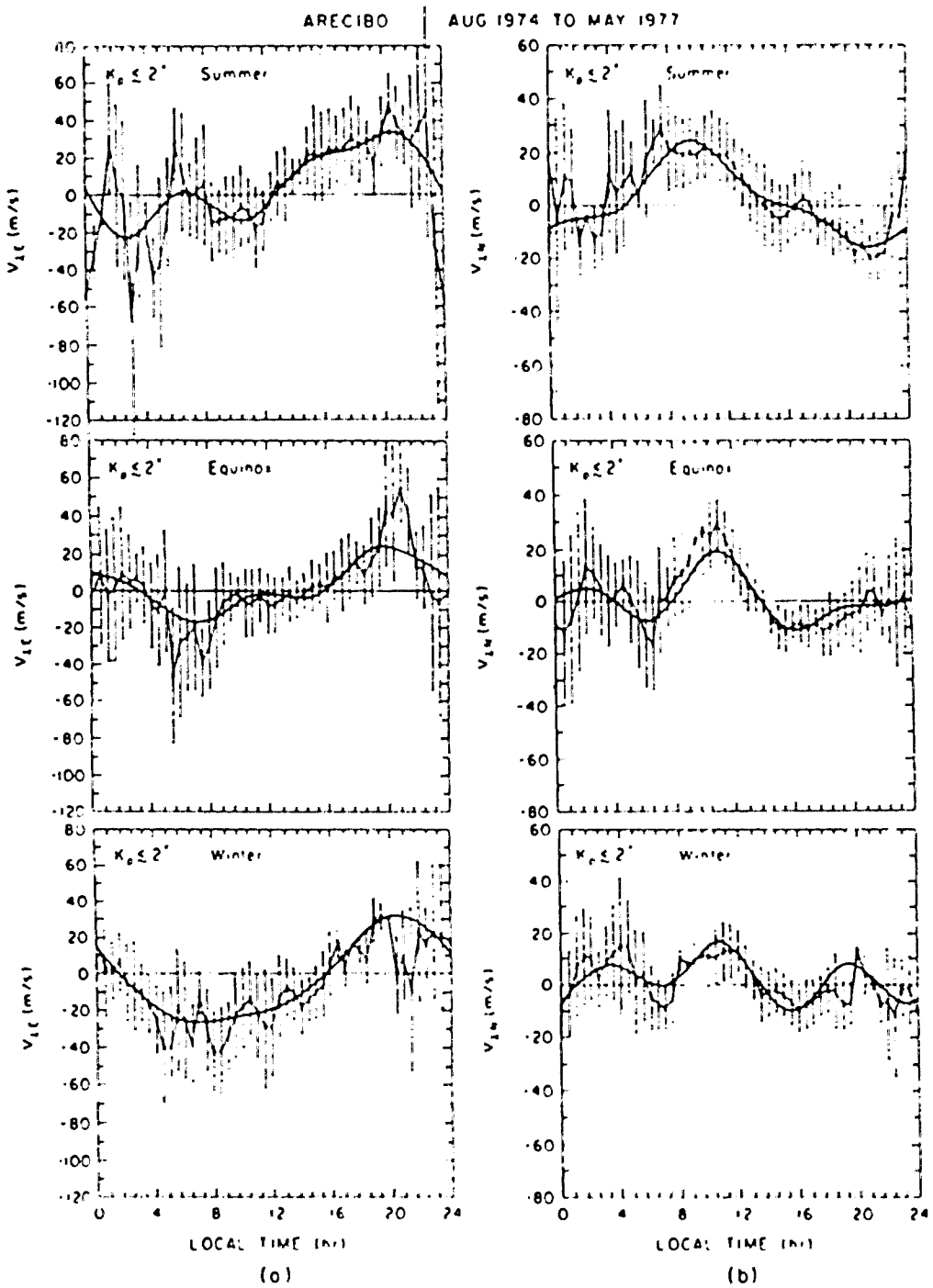

Figure 10. Electric Field Convection Patterns with Southware IMF

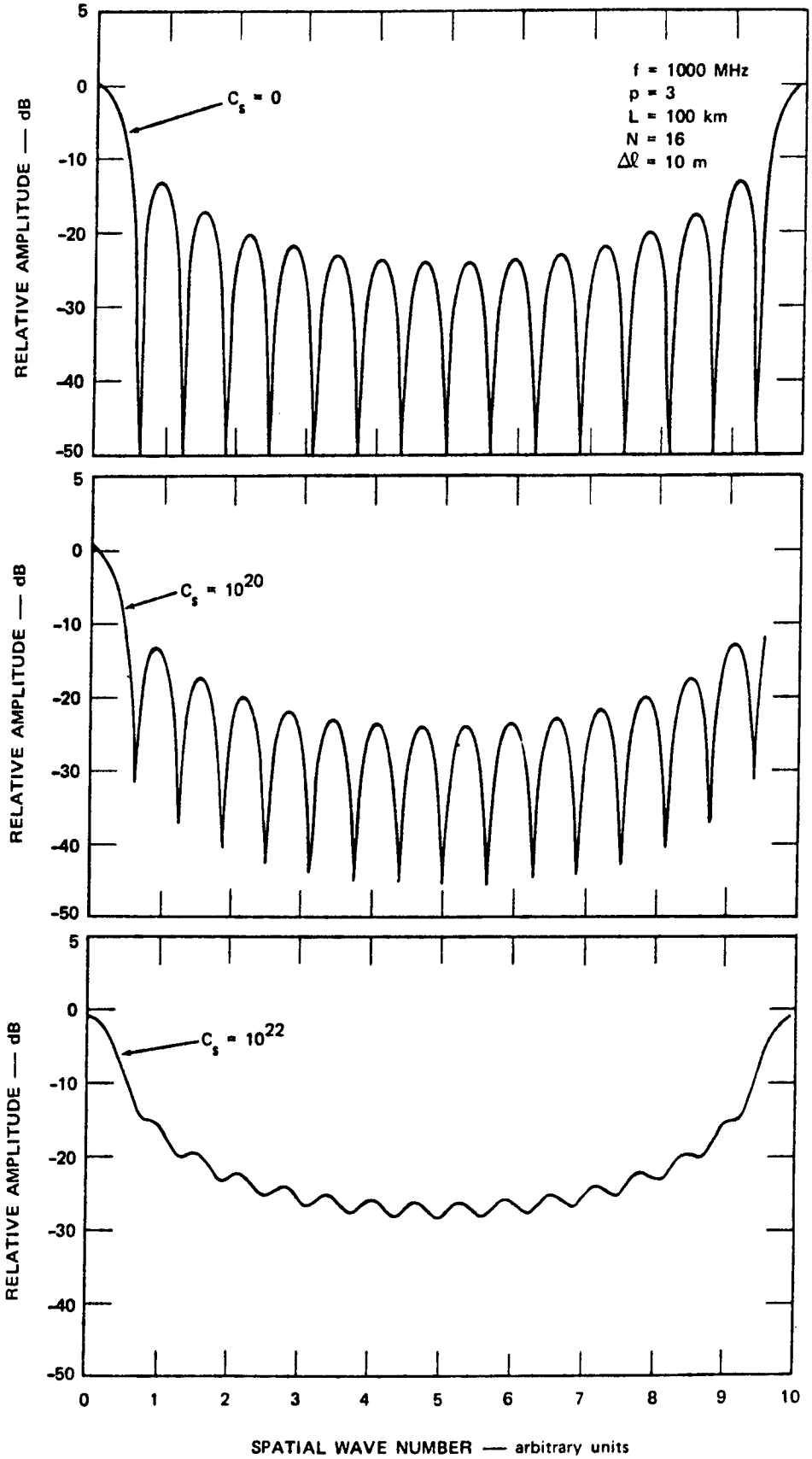

Figure 11. Degradation of Linear DFA Pattern

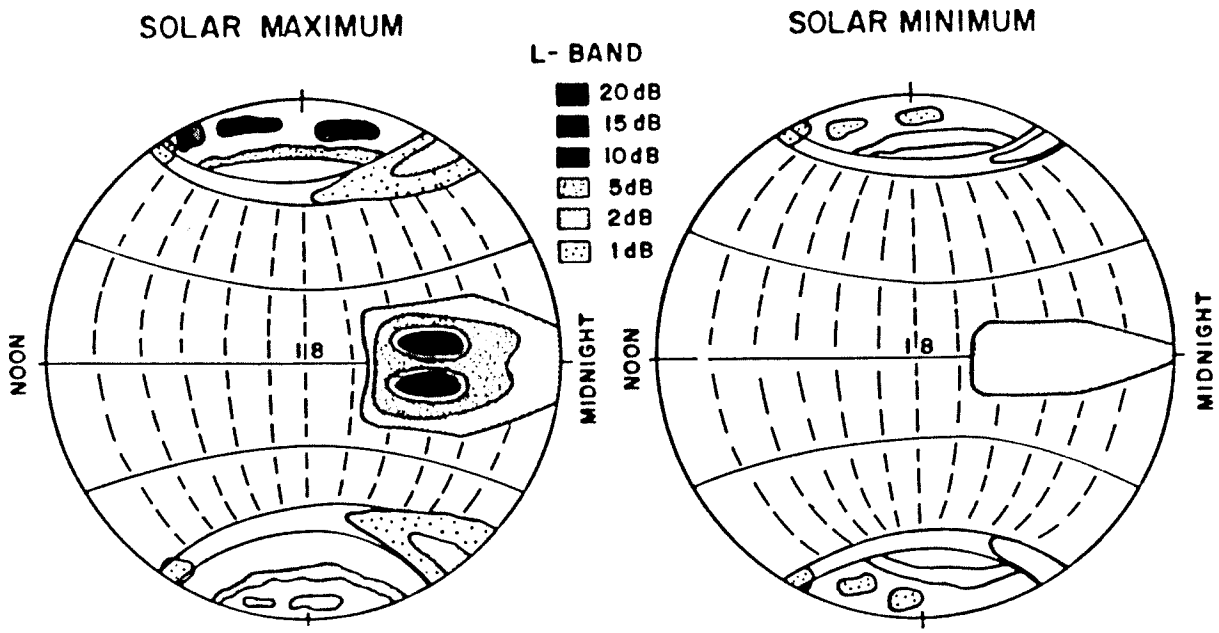

Figure 12. Global Distribution of Worst Case Scintillation

IONOSPHERIC FADING PARAMETERS

LOCATION: AURORAL/SUB-AURORAL

FREQUENCY	1 GHz	250 MHz
INTENSITY SCINTILLATION	2 dB	15 dB
PHASE SCINTILLATION (RMS OVER 90 SEC)	1.5 RAD	6 RAD
DECORRELATION TIME	0.5 SEC	0.2 SEC
PHASE RATE	0.05°/500 μSEC	0.2°/500 μSEC
GROUP DELAY AT 10° ELEVATION (SUB-AURORAL)	200 NANOSEC	3.2 μSEC
RANGE ERROR (SUB-AURORAL)	60 METERS	1 KM
FARADAY ROTATION/TWO WAY AT 10° ELEVATION (SUB-AURORAL)	50°	800°
FARADAY LOSS TWO-WAY	4 dB	TOTAL

Figure 13. Comparison of Scintillation and Total Electron Content

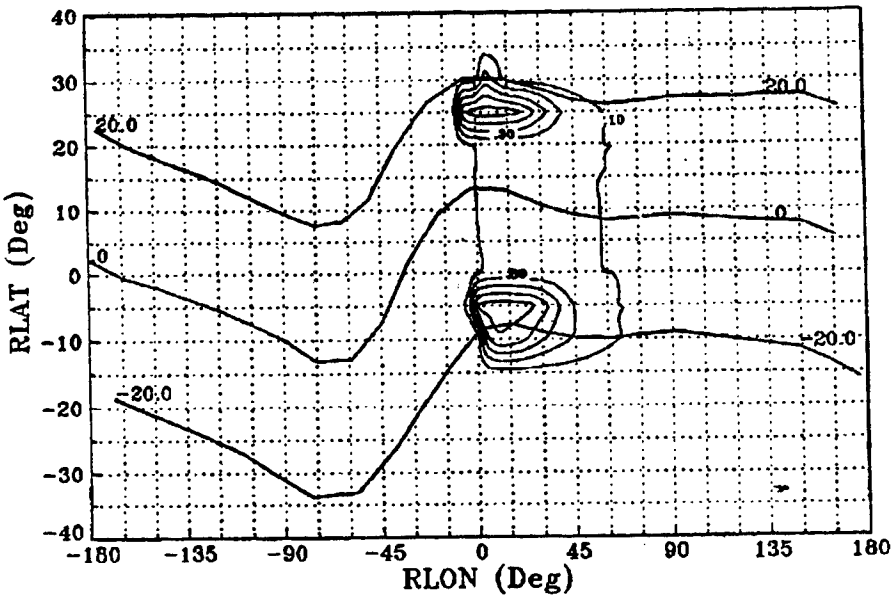

Figure 14. Adapted Use of WBMOD Scintillation Model

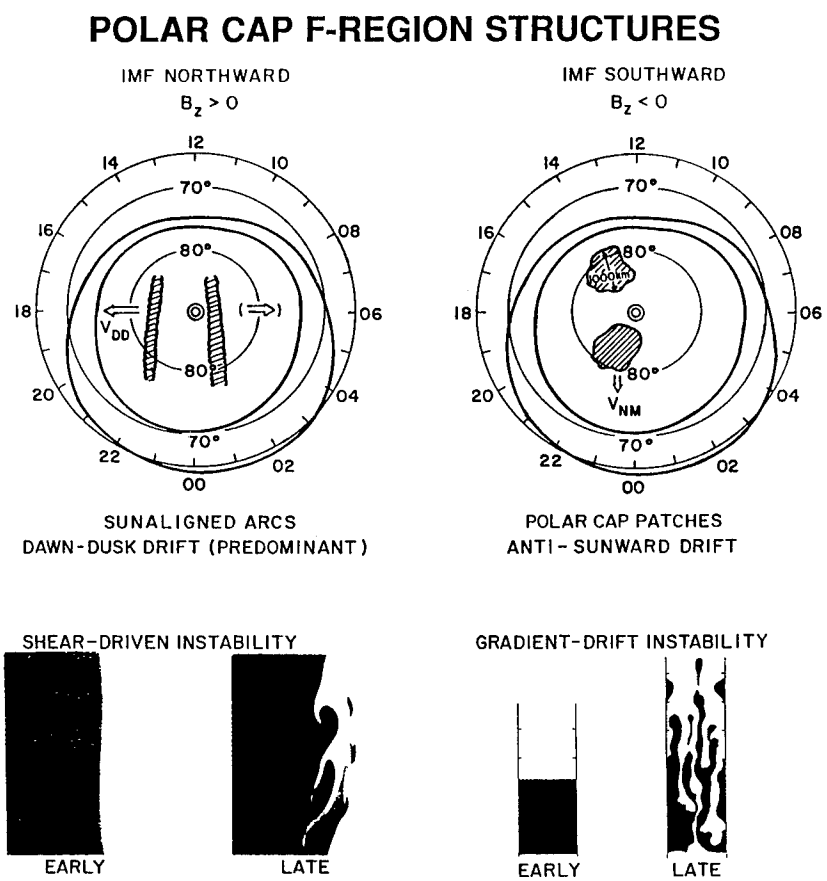

Figure 15. Polar Cap F-Region Structures

THE SPACE RADIATION ENVIRONMENT

Henry B. Garrett
The Jet Propulsion Laboratory,
California Institute of Technology
Pasadena, CA 91109

Daniel Hastings
Department of Aeronautics and Astronautics
Massachusetts Institute of Technology
Cambridge, MA 02139

Abstract

Space radiation has become a primary consideration in the design of modern spacecraft. This paper addresses one aspect of the radiation problem, namely the particulate radiation environment, by reviewing the current models of that environment. Particular emphasis is on the Earth's trapped radiation belts and on the solar flare proton environment as these are the primary environments of concern in estimating spacecraft dosage. Solar flare heavy ions and Galactic Cosmic Rays will also be covered as these environments are of special importance to single event upset modeling—a major concern for the new generation of microelectronics. In addition, models of neutrons and other interplanetary radiation environments will be discussed.

Introduction

As electronic components have grown smaller, drawn less power, and increased in complexity, their enhanced sensitivity to space radiation and its effects has become a major source of concern for the spacecraft designer. The objective of this paper will be to address one aspect of this problem, the radiation environment, by reviewing the high energy particulate environments. For each environment, a model will be presented and briefly reviewed. The paper, while not intended as a detailed review of each radiation environment, should serve as an introductory reference to the current available models and to this interesting and important field of space science and spacecraft design.

The high energy particle radiation environment considered here consists of electrons with energies greater than 100 KeV, protons or neutrons with energies greater than 1 MeV, and heavy ions with energies above 1 MeV/nucleon. The populations are characterized in terms of their kinetic energy, charge state (or lack thereof), and composition. Unlike photons which travel uniformly at the speed of light, particles can vary in velocity from a few m/s up to a sizable fraction of the speed of light in the case of cosmic rays. The discussion will be divided into four families of radiation based on these characteristics:

1) Trapped radiation;
2) Galactic Cosmic Rays which consist of interplanetary protons, electrons, and ionized heavy nuclei;
3) Protons and other heavy nuclei associated with solar proton events;
4) Neutrons (primarily Cosmic Ray Albedo Neutrons or CRAN particles).

The first two sources are treated typically as background environments whereas the third is very random and highly time dependent varying on scales of minutes to hours. The fourth is a secondary population because the relatively short lifetime of neutrons severely limits any solar produced fluxes at 1 AU or beyond. Each type of radiation has a characteristic spectrum and preferred interaction mode with matter that supports this simple division.

Trapped Radiation

Given its importance, the first environment to be discussed is the Earth's trapped radiation. Discovered by J. Van Allen and his collaborators on Explorer I, trapped radiation at the Earth consists principally of energetic protons and electrons, with lesser percentages of heavy ions such as O^+, contained in toroidal belts by the Earth's magnetic field. This toroid is commonly known as the

"Van Allen belt(s)"[1] and consists of (at least) two zones: a low altitude zone, or "inner belt"; and a high altitude zone, or "outer belt". The inner belt extends from ~100s of km to ~6,000 km in altitude and is populated by high-energy (~10s of MeV) protons and high energy (1-10 MeV) electrons, while the outer belt, up to 60,000 km in altitude, is predominately high energy electrons. Schematics of the radiation flux contours for the Van Allen belts are presented in Fig. 1[2] for the AE/AP models. The detailed mechanism by which particles are entrapped in the belt regions is not well understood. The primary source is also not clearly identified although albedo neutrons are considered an important source of the intense proton and electron fluxes in the inner belts. The outer belt, in contrast, may be primarily due to the entrapment of low-energy solar wind plasma by the geomagnetic field followed by local acceleration. Observations of abundance ratios in the outer belts imply both terrestrial and interplanetary sources. Once captured, the motions of the charged particles in the Earth's magnetic field are governed by the Lorentz force.

The trapped radiation environment also exhibits temporal variations. The inner belt zone, because of the dominance of the Earth's main field, is relatively stable. Most temporal variations in this population occur as the solar cycle proceeds and the Earth's neutral atmospheric density at a given altitude changes causing variations in the altitude at which radiation particles can mirror without being scattered. In contrast, the outer belt, which is more influenced by the Earth's highly variable geomagnetic tail, experiences much greater temporal fluctuations. The electron concentration in the outer zone may experience temporal fluctuations as large as a factor of 1000. Fortunately, most of the physical damage caused by the trapped radiation is largely attributable to the long-term cumulative (or integral) dose received by the spacecraft rather than the instantaneous fluctuations of the radiation.

Geomagnetic Field

Any discussion of a trapped radiation belt model must be presented in the context of the corresponding magnetic field. This section will briefly review the Earth's magnetic field models. The Earth's field can be crudely modeled in terms of a tilted (-11° from geographic north) magnetic dipole of magnitude $M = -8 \times 10^{25}$ G-cm^3 = -.31 G-R_E^3 (G is the magnetic unit Gauss; R_E is units of Earth radius). Ignoring the tilt for the moment, in the geomagnetic coordinate system, the magnetic field intensity induced by M at the point (r,q,f) is given by the expression:

$$B_i = (M/r^3)(3\cos\theta^2 + 1)^{0.5} \qquad (1)$$

where θ and ϕ are colatitude and longitude. In the Gaussian unit system, r is radius in cm, and B_i is in G. Given the above value for M, B_i is then found to have a maximum value of ~0.6 G near the polar cap and a minimum value of ~0.3 G near the equator at the Earth's surface. This simple model is important as it is often used to plot the radiation model results in terms of an "idealized dipole coordinate system" (see Fig. 1).

Eq. 1 is valid only for an idealized configuration of a centered dipole. In reality, large scale discrepancies (as high as ±25%) exist between the measured data and the ideal, dipole expression. Modifying the configuration from a centered dipole to an eccentric dipole reduces the discrepancies to about ~10%, but this is still unacceptably large. Instead, for most purposes, the International Geomagnetic Reference Field (IGRF) series of models is preferred. The latest version of the International Geomagnetic Reference Field, IGRF-87, is a computer model based on numerical fitting of measured data with a magnetic scalar potential expanded in terms of ten spherical harmonics[3]. The model calculates the seven magnetic elements of B_i for any given geographical location. Specifically, a scalar "potential" is found such that:

$$V(r,\theta,\phi) = a \sum_{n=1}^{N} \sum_{m=0}^{n} \left\{ \left[A_{n,m} \cos m\phi + B_{n,m} \sin m\phi \right] \left(\frac{a}{r} \right)^{n+1} + \left[C_{n,m} \cos m\phi + D_{n,m} \sin m\phi \right] \left(\frac{r}{a} \right)^{n} \right\} P_{n,m}(\cos \theta) \quad (2)$$

where: a = radius of Earth
r = radial distance in units of a
N = order of expansion
θ = colatitude
ϕ = east longitude
$A_{n,m}$, $B_{n,m}$ = constants for internal terms
$C_{n,m}$, $D_{n,m}$ = constants for external terms
$P_{n,m}$ = Legendre polynomials

The magnetic field components are then given by:

$$B_r = \frac{\partial V}{\partial r}$$
$$B_\theta = -\frac{1}{r}\frac{\partial V}{\partial \theta} \quad (3)$$
$$B_\phi = -\frac{1}{r \sin\theta}\frac{\partial V}{\partial \phi}$$

The epoch of the magnetic model is important and should correspond either to the same date as the date of the radiation model used or to a model epoch as close to the present as possible if only the current magnetic field value is desired (i.e., IGRF 1987 for 1993).

Figs. 2 and 3 show the three dimensional character of the Earth's magnetic field. Fig. 2 is a cross section of the Earth's magnetic field in the noon-midnight meridian showing the structure of the field lines and the plasma regions they contain. Fig. 3 illustrates the magnetic field amplitude over the northern hemisphere at a constant altitude of 400 km. The field amplitude varies from a minimum of 0.25 G near the equator to 0.5 G over the polar caps. Two peaks exist in the magnitude of the magnetic field over the north pole (if vector components are considered, the maximum at 270° east longitude is the true "dip" magnetic pole). Likewise, there are two minima near the equator—he largest of these is responsible for the so-called South Atlantic Anomaly, a region critical in determining radiation exposure in LEO. Finally, it should be noted that geomagnetic storm variations are superimposed on this main field. These are typically less that 0.01 G so that even during a severe geomagnetic storm, magnetic fluctuations are small at low altitudes compared to the average field (even though this is a very small change in the Earth's field, the effect of geomagnetic storms on particle fluxes in the polar ionosphere can be tremendous). Models of the external component of the geomagnetic field are available but are of limited importance to the trapped radiation belts given the great variability of the outer field.[4-6] They are critical, however, at geosynchronous orbit where the main magnetic field is of comparable strength to the external field. The external field dominates at higher altitudes.

Electron and Proton Belts

The use of standardized magnetic field models, adiabatic invariants, and the introduction of the McIlwain B-L coordinates have lead to standardized means of representing the time-averaged features of the trapped radiation environment. Until the recent CRRES (Combined Release and Radiation Effects Satellite) mission,[7] the AE/AP series of models developed by Vette and his colleagues at NASA Goddard have been the principle practical models of the Earth's trapped radiation environment. The AP/AE models are based on compiled data from many different satellites.[8-10] The P and E in the model names AP8 and AE8 refer to "Proton" and "Electron" and 8 is the version number of the models. For a given set of McIlwain B-L coordinates in the range from low Earth orbit to somewhat beyond geosynchronous, AP8 and AE8 provide estimates of the omnidirectional fluxes of

protons in the energy range of ~50 keV to 500 MeV and electrons in the energy range of ~50 keV to ~7 MeV. Time-dependent variations of the radiation fluxes such as those due to geomagnetic storms or short term solar modulations are not included in AP8/AE8. However, the models do differentiate between solar cycle maximum and minimum conditions. For protons, a larger flux is predicted at solar cycle minimum than solar cycle maximum. The situation is reversed for electrons with higher fluxes at solar maximum.

Although the use of the adiabatic invariants and B-L coordinates are very useful in simplifying this task, in reality, asymmetries in the Earth's magnetic and electric fields and their time variations introduce significant complications into the modeling process. In particular, "shell-splitting", distortions in the Earth's magnetosphere, and similar effects force the inclusion of temporal and local-time (or, less precisely, longitudinal) variables. The AE/AP model fluxes, for example, are parametrically represented by:[8]

$$I(>E,B,L,\tau,T) = N(>E,L)\Phi(>E,L,\tau)G(B,L) \quad (4)$$

where I is the integral omnidirectional flux, >E means for all energies above E, t is the local time, and T is the epoch (or date). Data from many different satellites are averaged in discrete B and L bins to determine the B-L variation G; in energy, L, and local time to determine the local time variation F; and in energy and L bins to determine the energy variations N. As many different satellites were used, it was important to know the efficiency and geometric factor for the different detectors. As discussed by Vette and his collaborators, there are many regions of spotty spatial coverage.[8] Likewise, short term temporal variations are not well represented. Basic uncertainty factors have been defined for the AP8/AE8 models. These are a factor of 2 for 5 to 10 year averages for both the AE8 and Ap8 models.

The environment predicted by these models below 1000 km is of particular interest for a number of missions. At low altitudes, the main trapped radiation environment consists of 2 components: the low altitude extension of the radiation belts (or "horns") at high latitudes and the low latitude South Atlantic (Magnetic) Anomaly. Figures 4 and 5 illustrate these regions for protons and electrons.[11] The units are particles/cm^2-s for E>30 MeV and E>0.5 MeV respectively. The lines represent isoflux contours at 296 km (Fig. 4) and 400 km (Fig. 5). High energy, trapped particles mirror at a characteristic constant magnetic field strength--thus particles that typically would mirror at higher altitudes above the atmosphere find themselves mirroring at much lower altitudes in this region thereby enhancing the background fluxes.

Model Difficulties

Figure 6 plots approximately one year's worth of hourly averages of the 1.9 MeV omnidirectional electron flux measured at midnight by the geosynchronous satellite ATS 1.[12] The daily sum of the geomagnetic index K_p (at the bottom of the figure) and the value predicted by the AE model (the horizontal line) are also plotted for comparison. This figure demonstrates two important points. First, the electron radiation flux at L=6.6 is highly variable on a daily time scale—some variations being on the order of 10 to 100. Secondly, the AE model is biased toward the few major geomagnetic storms. This biasing is to be expected as the model is derived by averaging the fluxes. Figure 7 demonstrates electron variations over a slightly longer time period for different L values. The data are 10 day averages of the electrons with energy greater than 0.28 MeV, taken on the 1963 38C spacecraft.[12] Inside of L=1.8 (generally referred to as the inner electron zone) the time variations are quite small, demonstrating the usefulness of an average model in this region. The steady decay of flux levels in the figure is due to the decay of the residue from the artificial Starfish injection event of July 1962. In contrast, outside L=1.8, the fluxes at L=2.2 vary greatly with time due to geomagnetic activity. The principle point to be made by this and the previous figure is, however, that large time variations are observed but that long term averages do indeed smooth out

these variations so that average models are useful in many applications.

Although a given AE/AP model may be accurate for the period of time for which the measurements were taken, it does not necessarily follow that it is accurate for another epoch. That is, there are long term variations such as the decay of the Starfish nuclear explosion radiation that change over much longer time scales than data exist. The solar cycle, for example, follows an irregular 11 year pattern and the level of geomagnetic activity at one solar minimum may differ substantially from that of the next. Thus, for a model to be appropriate for a given time interval, it should ideally include observations from that interval. As this is impossible in practical terms, the data base used should be as close in time as possible if accurate predictions are to be expected. The most recent observations for the AE models (and these are principally from one satellite) are over 15 years old whereas for the AP-8 model they are almost 20 years old!.

CRRES—The Next Generation

Given the many known uncertainities in the AE/AP models, the DoD (primarily the Air Force Phillips Laboratory) and NASA launched an agressive program in the 1980's to address many of their shortcomings. This resulted in the CRRES program. CRRES was launched on July 25, 1990 and ceased transmitting on 12 October 1991. It was placed in a 18.1°, 350 km by 33,000 km orbit with a period of 10 hours. The satellite carried perhaps the most complete complement of radiation environment sensors yet flown and was in a nearly ideal orbit for mapping the trapped radiation belts. Approximately 14 months of data during Solar Maximum were obtained before a battery failure terminated the mission. The data have been used to develop several new models of the trapped radiation environment and to test the AE/AP models. The results of these studies have been reported in a number of recent papers by the Phillips Laboratory (E.G. Mullen, M.S. Gussenhoven, et al.) and colleagues.[13-15] Here, two of the trapped radiation models developed by the Phillips Laboratory (CRRESRAD[13] and a quasi-static model of the the outer zone electrons[14]) will be briefly reviewed.

The CRRESRAD model[13] is a readily accessable PC-based software program that provides estimates of the dose behind four shielding thicknesses for a large range of satellite orbits. The model is based on the Space Dosimeter experiment[7] which returns dose data in the energy ranges 50 keV to 1 MeV (LOLET) and 1 to 10 MeV (HILET). The dose is measured behind four thicknesses of hemispherical aluminum shielding (0.57, 1.59, 3.14, and 6.08 gm/cm^2). These correspond to electrons with energy greater than 1, 2.5, 5, and 10 MeV and protons with energy greater than 20, 35, 52, and 75 MeV. To create a model, the data were divided into two parts: a "quiet period" before the March storm (27 July 1990-19 March 1991) and an "active one" after the storm (31 March 1991-8 October 1991). The data were then averaged in L and B/B_0 bins (where B_0 is the amplitude of B at the magnetic equator for the given value of L). Separate tables were then computed for the two time periods, the total period, for the LOLET and HILET and LOLET+HILET channels, and for the four shield thicknesses. This resulted in 36 dose tables. To determine the dosage expected for a specific satellite orbit, the code integrates the electron and proton dosage (interpolated from the appropriate tables for a given shielding) along the orbit for quiet, active, or average geomagnetic activity conditions.

Sample data for the CRRESRAD model are plotted in Figs. 8 and 9.[15] These results are for the dose rate, in Rad(Si)/s, as a function of L along the magnetic equator. The data are plotted in terms of HILET (for protons > 20 MeV) and LOLET (>2.5 MeV electrons and >135 MeV protons) for the quiet and active models and for a comparable calculation using the AE8 and AP8 models. The figures illustrate the differences between the CRRES and AE/AP models. Specifically, in Figure 8, there is relative agreement between the active CRRES model and the AP8 model for E>20 MeV protons whereas the low activity CRRES model is about an order of magnitude lower in dosage for L>2. At

higher energy cutoffs, this difference is reversed with the AP8 model agreeing more closely with the quiet model and being an order of magnitude lower than the active model for L>2. These differences are explainable in terms of a second, variable proton belt extending between L=1.8-4 present in the CRRES active model that is not present in the AE/AP models.

For Fig. 9, there are much larger differences between the models. In particular, the AE/AP model results exceed the CRRES models for L>3.5 (primarily because of the >2.5 MeV electrons) and is lower for L<2.5. There are in fact differences of three orders of magnitude between the active model and 1.5 orders between the quiet model and the AE/AP model in the so-called slot region near L=2.5. This is probably due to the absence of electrons above 5 MeV in the AE8 model and their presence in the CRRES models. There are other differences between the models, but these figures illustrate the major concerns—namely the extra proton belt in the CRRES active data and the lack of high energy electrons in the NASA models. The implications of these and other differences between the models for mission designers need to be carefully considered.[14, 15]

The second model to be discussed is the so-called quasi-static model.[14] In this model, data from the CRRES High Energy Electron Fluxmeter (HEEF), a particle detector which measures electrons in 10 different energies between 0.8 and 8 MeV, were used to construct a quasi-static model of the outer zone electrons based on the Ap index. The intent of the model is to provide a more accurate representation of the dynamic behavior of the outer zone. The CRRES spin axis points toward the Sun while the HEEF points perpendicular to the spin axis. Averaging over a satellite spin give an estimate of the unidirectional electron flux at a given L. Brautigam et al.[14] found that these fluxes were approximately correlated with the logarithm of a 15 day running average of the Ap index lagged by 1 day (called Ap_{15}). They then computed average radiation belt profiles as functions of L (between 2.4 and 6.6), energy (9 of the energy channels between 1 and 8 MeV), and for AP_{15} (8 intervals between 5 nT and 55 nT). A typical result for one of the energy channels (3.09 MeV) is presented in Fig. 10 and is compared with a corresponding prediction based on the AE8MAX model. The figure illustrates a basic conclusion of the Brautigam et al. study that the AE8 model is typically higher than the CRRES measurements at all L values above ~3.4.

Magnetospheric Heavy Ions

The next environment to be considered is the trapped heavy ion population. Low to moderate energy O^+ and He^{++} are typically observed throughout the magnetosphere but the sources of these particles are not entirely clear. The helium nuclei (mostly alpha particles) are possibly from the solar wind[16], while the O^+ may be primarily of ionospheric origin. In the case of the solar wind, particles probably enter the magnetosphere and are accelerated by radial diffusion. This process, described by Cornwall[17], adequately describes the magnetospheric helium ion population.[18, 19] The bulk of this helium population, however, is at energies too low to penetrate the walls of a spacecraft. C, N, and O ions have all been observed though it was not clear whether the particles were trapped in the magnetosphere (recent evidence supports the claim that the bulk of the lower energy O^+ at least is of ionospheric origin). Models by Adams and his colleagues[20] assume that there is a small flux of helium nuclei and a smaller flux of heavier nuclei in the magnetosphere above 10 MeV/nucleon. There are also reports of long-lasting enhancements of the low energy heavy ion fluxes after large solar flares. As yet, these ions are included in radiation dosage calculations in only very specialized applications although they are of concern for SEU effects.

Very recently, Grigorov et al.[21] and Cummings et al.[22] have presented evidence for an energetic ($\geq$15 MeV/nuc) trapped heavy ion component associated with the Galactic Cosmic Ray (GCR) anomalous component. Blake and Friesen[16] suggested that the anomalous cosmic ray (ACR) com-

ponent particles, which may be only singly ionized initially, can penetrate deeper into the magnetosphere than the normal GCR component which is typically fully ionized. The particles are then ionized near their geomagnetic cutoff and become trapped. This leads to a special trapped population of oxygen, nitrogen, neon, and other elements which may be the source of the observed heavy ion component. The SAMPEX spacecraft[22] recently (late 1992 and early 1993) observed $\geq$15 MeV/nuc trapped heavy ions with $Z \geq 2$. The trapped population includes He, N, O, and Ne and is located at L~2.[22] The population was seen to increase in intensity in concert with a similar increase in the ACR component.

The geographic distribution of the oxygen particles detected by SAMPEX (which is in an 82° inclination orbit with an apogee of ~670 km and a perigee of ~520 km) is illustrated in Fig. 11. Three distinct populations of oxygen ions are evident. For latitudes above 60°, there is a mixture of GCR and ACR which have directly penetrated the magnetic field. Between 50° and 60° there is a mid-latitude component composed of singly ionized (ACR) oxygen which has a lower latitude cutoff than that of the more highly ionized GCR oxygen. Below 50° there is a low-energy grouping near and below the estimated cutoff of singly-charged oxygen. The high-latitude and mid-latitude particle populations are present at all longitudes as would be expected for particles that are controlled by magnetic rigidity. The third population is concentrated in an ~8000 km long band southeast of the South Atlantic Anomaly. The L-shell for these particles corresponds to a trapped population at an L=2.04$\pm$0.26. Blake and Friesen[16] predicted that the trapped ACR oxygen would be located at L=2.5 to 3.5--near where it has now been observed. Thus the SAMPEX observations verify that the ACR mechanism predicted by Blake and Friesen is a source of trapped ions N, O, and Ne above 27, 21, and 14 MeV/nuc. Helium ions were also observed but this population is believed to have been trapped by another mechanism than that proposed by Blake and Friesen and may have another source.[22]

Neutral Particle Radiation

Although not a primary natural environment, neutrons are a potentially important source of the trapped charged particles in the Earth's belts. Neutrons (at rest) typically have a half-life of 11.7 minutes before they decay into an electron, proton, and anti-neutrino. As a result, all but the most energetic solar flare neutrons (and therefore extremely small fluences) will have decayed before they can reach the Earth's orbit. Likewise, there is no primary neutron component to the intergalactic cosmic rays. The observed neutron component is, instead, associated with secondary cosmic ray (both solar flare and intergalactic) processes. The neutrons produced by these processes are discussed in the following.[23]

A primary cosmic ray incident on the Earth's atmosphere will interact with air nuclei to produce a multitude of high energy secondary cosmic rays. These in turn will interact to produce additional particles in a "nuclear cascade". The production of these secondary particles becomes significant around 55 km reaching a maximum value at ~20 km (called the Pfotzer maximum). The intensity falls off below this altitude. At high energies, the so-called "knock-on" process dominates neutron production while at lower energies, "neutron evaporation"dominates. These neutrons interact with the atmosphere to produce various radioactive isotopes such as C^{14}. Representative differential energy spectra for neutrons at various depths in the atmosphere are presented in Fig. 12.[23]

About 10% of the secondary cosmic ray neutrons escape into space. Most of these neutrons (which are not controlled by the Earth's magnetic field) will decay (11.7 minute half-life) into electrons and protons which will be trapped in the Earth's radiation belts (these "cosmic ray albedo neutrons"-CRAN-are a major source of the high energy protons in the belts). A globally averaged albedo neutron spectrum is presented in Fig. 13.[23] Near the Earth, there is an approximate 1:7 ratio of albedo neutrons from the

equatorial atmosphere as compared with the polar atmosphere. Major flares and the corresponding ground-level measurements of the secondary neutron flux have been routinely measured for many decades. Significant ground level neutron events are relatively rare, however, and are normally observed only in conjunction with major solar flares.

Solar Flares
Solar Proton Events

A very energetic process, and potentially damaging situation, occurs when very strong magnetic fields in the solar photosphere reach a critical instability. On time scales of seconds, the strong fields are unstable enough to "snap", thereby adjusting and relaxing to remove the instability. A considerable amount of energy, up to 0.1% of the total solar energy output or about 10^{32} ergs, is released during this "flare". A solar flare typically lasts from a few minutes to a few hours and heats the surrounding corona to temperatures in excess of 2×10^7 K. Associated with the heating, large fluxes of atomic particles, primarily electrons and protons, are accelerated and expelled from the Sun. There are also substantial radio bursts and X-ray emissions. Many of the particles escape the Sun and into the interplanetary medium where they follow the solar wind magnetic field out through the ecliptic plane into interstellar space. As a result of the complexity of this field structure, both the intensity and the spectrum of the particles observed at Earth can vary significantly with position. These quantities depend critically on the positions of the Earth and the flare on the Sun relative to each other. Variations as large as 100 in the particle fluxes from the same flare at different points around the Earth's orbit have been observed. A schematic illustrating the time scales for the different solar flare events is presented in Fig. 14 (the 27 day period is the approximate rotation rate of the Sun as seen from the Earth).

The intensity and number of very large solar flares varies dramatically from solar cycle to solar cycle (Fig. 15). The lack of a clear correlation between sunspot number and frequency of proton events in Fig. 15 illustrates the difficulty in reliably predicting the level or frequency of proton events (see Feynman et al.[24, 25] for a detailed analysis of the solar proton fluence variations over a solar cycle). Adding to the problem is that most data on large solar flares are from only the last few cycles making statistical studies very difficult. One fact is clear, however, and that is that solar flare related effects occur more frequently during solar maximum. Although solar flares are less frequent during solar minima, these flare related effects can be greater in the terrestrial magnetosphere because the interplanetary fields, through which the flare particles travel, are less complicated and the particles can more easily gain access to the Earth's polar caps. As an example, even though the number of proton events goes down during minima in solar activity, the level of a given event, even during the lowest levels of solar activity, can be among the highest ever seen. A particularly good example was the great flare of 1972 which occurred nearly four years after the peak in solar activity.

The intense fluxes of high energy protons that are associated with the solar flares are very damaging to electronics both from the SEU and total dose standpoint (note: solar proton events are often referred to as solar flares; strictly speaking, a solar flare, which involves many processes, may or may not have a classifiable proton event). Hydrogen and heavy nuclei in the ~1 MeV/nucleon to ~10 GeV/nucleon energy range are ejected during solar proton events. Their intensities are generally a few to several orders of magnitude larger than those of GCR at these lower energies, depending obviously on the size of the solar flare. Adams and his collaborators at the Naval Research Laboratory (NRL) have developed several detailed models of the radiation environment associated with a flare.[20, 26-28] Typically, these and other flare models are based on the large proton event of 1972. These are com-bined with models of the mean abundances of the heavier ions relative to hydrogen to obtain a worst case model. Figure 16 presents Adam's characterizations of "typical",

"worst-case", and "anomalously large" (i.e., very rare) solar flare proton spectra for 1 AU. The worst-case solar flare proton flux is ~5 orders of magnitude larger than the GCR flux, but becomes "softer" above ~10 GeV.

For many years, there has been an ongoing controversy over how to model the probability of the occurrence of solar flare proton events and to estimate their radial variations. Recently, Feynman and colleagues have developed a comprehensive model of solar flares that largely replaces previous models.[24, 25] A major change has been the realization that instead of there being three types of flares (typical, worst-case, and anomalously large) in terms of energy output, there is indeed a continuum when the total output energy of the flares in an event series is integrated. In fact, when plotted in terms of the statistical occurrence frequency, it was found that the likelihood of the occurrence of a solar flare amplitude in a given time interval could be predicted. This new model, as represented in Figures 17 and 18[24, 25], has been used to estimate the likelihood of encountering a given mission-integrated fluence for various interplanetary spacecraft. Fig. 17 plots the cumulative probability of occurrence of a solar proton event fluence (for E>10 MeV) of the indicated level or less between 1963 and 1991. Fig. 18 uses these data to predict the probability of seeing a total proton dose (E>10 MeV) equal to or less than the graphed value for various mission lengths during solar maximum (the seven years centered around solar maximum–the other four years are assumed to have zero flux). Similar plots are available for other energy intervals and are currently being extended to other ions. Based on the recommendations of a workshop on the "Interplanetary Particle Environment"[29], the new model assumes a (conservative) radial dependence of r^{-3} for the flux inside 1 AU and a radial dependence of r^{-2} outside 1 AU. This implies that the fluence and dose will be trajectory dependent for interplanetary vehicles such as Galileo and Cassini.

Heavy Ions

In addition to intense proton fluxes, solar flare events also typically are accompanied by small but variable amounts of heavy ions. Again, the models typically utilized for this component are those of the NRL.[20] Tables 1 and 2[20] summarize the abundances of the heavy ions found in solar flare events relative to hydrogen. The abundance ratios from the tables are multiplied by the proton flare spectrum to get the individual ion spectra. For the NRL model, the worst-case composition for the elements from copper to uranium can be estimated by multiplying the abundance ratios of Table 2 by 1.92 exp $(z^{.79}/6.89)$. Although the solar heavy ions are usually assumed to be fully ionized, they may not be, particularly in the $0.5 \leq E \leq 2.5$ MeV/nucleon energy range.[30] Fischer et al.[31] (see also MeWaldt and Stone[32]) showed that solar energetic heavy ions in the energy range $5 \leq E \leq 20$ MeV/nucleon may also not be fully ionized and that the upper limits on the charge to mass ratio of the heavy ions may be as low as 0.1 (~0.5 for fully ionized heavy ions). Breneman and Stone[33] have indirect evidence that heavy ions in the energy range 3.5 to 50 MeV/nucleon may have the same distribution of charge states as for the 0.5 to 2.5 MeV/nucleon ions observed by Luhn et al.[30] The importance of the charge state of the ions is that it affects their entry into the Earth's magnetosphere–the higher the charge state of a given atomic species, the less likely it is to get through the Earth's magnetic field for the same energy.

Galactic Cosmic Rays (GCR)

The third background radiation environment is the Galactic Cosmic Rays or GCRs. Galactic Cosmic Rays are primarily interplanetary protons, electrons, and ionized heavy nuclei with energies ranging from ~1 MeV/nucleon to over $\sim 10^{10}$ eV/nucleon. Fig. 19 compares GCR proton and electron spectra while Fig. 20 displays the observed cosmic ray abundance distribution of the chemical elements in the energy range from ~100 MeV/nucleon to ~1 GeV/nucleon for hydrogen to the iron group.[34] For compari-

son, solar system abundances are also shown in the figure. Note that the two abundance distributions are strikingly similar. The major components are hydrogen (93.6 percent) and helium (6.3 percent). The remaining 0.14 percent includes all the rest of the elements. Observations indicate that outside the Earth's magnetosphere, the cosmic ray fluxes are isotropic to within about 10% over their entire energy range, suggesting that they are of galactic and/or extragalactic origin. Within the magnetosphere, however, they are not isotropic. That is, for the low Earth orbit environment, the geomagnetic field provides shielding against incident GCRs (and solar flare particles) as it can effectively deflect through the Lorentz force the lower energy particles. Because of the approximate dipole nature of the geomagnetic field, vertical particle velocities in the polar regions are essentially parallel to the magnetic field resulting in almost no Lorentz force so that the particles can gain direct access. At low inclinations, only particles with sufficiently high energy, or "rigidity", can penetrate through the magnetic shielding as the charged particles are forced into gyro loops by the magnetic field as they approach the Earth.

GCR Ion Spectra

The most abundant element in cosmic rays is hydrogen. Fig. 21[34] compares the differential energy spectrum of GCR hydrogen (primarily H^+) for solar maximum and solar minimum conditions with other GCR ion spectra. At very high energies, a power law with a spectral index of 2.75 is a good fit. The deviation below about 5 GeV/nucleon is thought to be due to solar modulation. As the amount of solar modulation depends on the general level of solar activity, there is a variation from solar minimum to solar maximum. Hydrogen, helium, carbon, oxygen, neon, magnesium, silicon, sulfur, calcium, and iron are assumed to be primarily primordial (that is, their flux consists of the originally created ions and has not been created by transmutation during transit across the galaxy).

NRL, in addition to its flare models, has created a family of GCR heavy ion model spectra corresponding to the curves shown in Fig. 21. The NRL models provide fits to the hydrogen, helium, and iron spectra along with a formula for scaling other elements to these three basic spectra. The differential energy spectra of hydrogen, helium, and iron nuclei are estimated for energies above 10 MeV/nucleon in the NRL models by functions of the form:

$$f(E,t) = A(E)\sin\{w(t-t_o)\} + B(E) \qquad (5)$$

where:

w	=	0.576 radians per year
t_o	=	1950.6 AD
t	=	date (in years)
E	=	particle energy in MeV/nucleon
A(E)	=	$0.5\,(F_{max} - F_{min})$
B(E)	=	$0.5\,(F_{min} + F_{max})$

The units of f are particles/m^2-ster-s-MeV/m. The functions F_{min} and F_{max} refer to solar minimum and solar maximum conditions for the following equation and differ by constants:

$$F = 10^{m}\left(\frac{E}{E_o}\right)^{a} \qquad (6)$$

where:

$$m = C_1 e^{-X_2\left[\log_{10} E\right]^2} - C_2 \qquad (7)$$

$$a = a_o\left\{1 - e^{-X_1\left(\log_{10} E\right)^b}\right\} \qquad (8)$$

Where a_o, b, C_1, C_2, E_o, X_1, and X_2 are fitted constants for the three elements, solar minumum, and solar maximum. Values for hydrogen, helium, and iron are given in Adams et al.[28] Using these three spectral shapes, the rest of the elements are then modeled using ratios to the three base functions. As lithium, beryllium, and boron are

assumed to be entirely composed of secondaries and nitrogen is assumed to be a mixture of primary and secondary particles, these elements have energy dependencies different from the three base species. The NRL models take these variations in lithium, beryllium, boron, and nitrogen into account by modifying the ratio of each element to either helium or iron as a function of energy.[28] The result of these procedures is an analytic model of the GCR ions capable of estimating their fluxes over solar cycle and a wide range of energies and elements.

GCR Variations

The flux of GCR increases radially with distance from the Sun. The magnitude of the radial gradient varies with both ion species and energy. For relativistic GCRs the radial gradient is <4%/AU while for GCR particles below 100 MeV/m the gradient is <10%/AU. The latitudinal gradient is small, under 1% per degree and may change sign each half solar cycle. The solar wind further modulates the GCR inversely with the 11 year cycle of solar activity. At the maximum of solar activity, GCR intensity is at a minimum and vice versa. The GCR intensity, at moderate energies, varies by a factor of 4 to 8 depending on the energy and ion.[20] The reason for the modulation of the GCR is apparently the solar wind magnetic field. As the GCR propagation is controlled by this field, any turbulence in the field (such as that associated with solar maximum) makes propagation of the GCR into the inner solar system more difficult–the particles are scattered more effectively. As the solar wind field relaxes during solar minimum, the GCR can more easily reach the inner solar system.

In addition to the temporal and spatial variations in the GCR, there is an occasional systematic change in the energy spectra for some ions. This so-called anomalous component appears as a flattening in the differential energy spectra of ions like helium, oxygen, nitrogen, and neon. The anomalous component may be singly ionized particles with an energy in the range from 1 to 200 MeV/m--a component which is not always present near the Earth.[20] The anomalous component varies by a factor of 100 to 1000 over the 11 year solar cycle—it appeared between 1971 and 1972 and disappeared again during the solar maximum of 1978. Jokipii et al.[35] have predicted that the anomalous component appears near the Earth only once every other solar minimum (i.e., it will appear again ~1994). The anomalous component seems to be more intense at greater distances from the Sun. Since the composition of the anomalous component suggests that it is interstellar gas accelerated by the solar wind, Fisk et al.[36] have predicted that only atoms with a first ionization potential higher than hydrogen will display anomalous spectra and that the ions will be singly ionized. If the anomalous component is indeed singly ionized, it can penetrate much more deeply into the Earth's magnetic field and may account for some of the measurements of heavy ions in the inner magnetosphere as mentioned earlier.

GCR Electrons

Although Galactic Cosmic Rays are primarily interplanetary protons and ionized heavy nuclei, electrons are also a component of the GCR. Their measured intensities at energies above ~100 MeV, however, are at least 1 order of magnitude smaller than that of the protons (Fig. 19). The model for GCR electrons presented here is taken from NASA SP-8118.[37] The integral intensity for galactic cosmic ray electrons, in units of (m^{-2}-s^{-1}-sr^{-1}), is given by:

$$I_{mean} = \frac{2000}{(\alpha E^6 + \beta E^3 + E^2 + \gamma)^{1/4}} + \frac{400}{E^{3/2}} \qquad (9)$$

where: $a = 10^{-12}$
$b = 10^{-3}$
$g = 6x10^4$
fluence = ÚÚI dW dt

Interplanetary e^- and H^+

Although the interplanetary proton and electron environments are of little impact on the radiation environment, they are included here for completeness. The models for in-

terplanetary electrons and protons are taken from NASA SP-8118.[37] These particles fall in the energy interval between the very low energy solar wind and the energetic solar protons (approximately 1 keV and 10 MeV). NASA SP-8118 gives the integral intensities (in units of $m^{-2}s^{-1}$ sr^{-1}) for these particles in terms of the following functions:

For intermediate energy (10^{-3} < E < 10 MeV) protons:

$$I_{ave} = \frac{1.0 \times 10^6}{r^2 E^{1.7}} \qquad (10)$$

For intermediate energy ($2x10^{-5}$ < E < 10 MeV) electrons:

$$I_{ave} = \frac{400}{r^2 E^2} \qquad (11)$$

where E is in MeV, r in AU, and the fluence = ÚÚI dW dt. The dose due to these particles is much smaller than that due to the typical solar flare environment and is thus ignored in most radiation calculations.

Extraterrestrial Trapped Radiation

As in the case of the Earth, many of the other planets in the solar system have been observed to have trapped radiation belts. The species, abundances, energies, and time variations of particles that are trapped in these radiation belts vary greatly depending upon the planet and its magnetic field. Planetary magnetic fields influence the particle spectrum that is observed near a planet in two ways—first, the magnetic field of the planet shields the planet from solar flare particles and from the GCR and, second, it allows particles to be trapped near the planet in radiation belts. Fig. 22[38] and Table 3[38] compare the magnetic fields and magnetospheres of the various planets. The Earth, for its size, has proportionally one of the most intense magnetic fields in the solar system. Jupiter and Saturn, like the Earth, should have (based on their magnetic fields) intense radiation belts. Subsequent flybys of Jupiter and Saturn have indeed bornethis out. Here, the discussion will concentrate on a model of the Jovian electron and proton radiation belts which, after the Earth's, are the best known and are by far the most intense in the solar system. A brief discussion of the Saturnian observations will also be presented (the Uranian and Neptunian belts are also of interest but are not as yet well modeled; Mercury, Mars, and Venus have very weak magnetic fields and therefore no radiation belts).

Jupiter

Jupiter has been known to have a magnetosphere since about 1960 when, in analogy with early spacecraft observations of the Earth's radiation belts, it was realized that the Jovian UHF radio emissions could be interpreted in terms of trapped energetic electrons.[39] The successful encounters of the Pioneer spacecraft with the Jovian magnetosphere gave rise to a number of quantitative models describing various aspects of the Jovian magnetosphere.[40, 41] In particular, magnetic field models by Smith et al.[42] and Acuna and Ness[43, 44] began to delineate the substantial differences that exist between the Jovian and terrestrial magnetospheres. Wave-like variations in the high energy particle fluxes led to the proposal that the Jovian magnetosphere was distorted into a thin disc—the so-called magnetodisc theory (Fig. 23[38, 45])—and that this thin disc was populated by a cold plasma consisting of heavy ions originating from Io. The passage of the Voyager 1 and 2 spacecraft, while failing to distinguish between the magnetic-anomaly and magnetodisc models, further refined the in-situ particle and field observations.

The in-situ observations verified that the strongest magnetic field in the solar system is that of Jupiter. Since the ability to trap particles magnetically is a function of the magnetic strength, it is little wonder then that it was also found to have the most intense radiation belts yet observed. These belts are so intense in fact that they rival the man-made saturated nuclear environment at the Earth—the most intense environment space systems will likely have to fly in. To

date (the model is currently undergoing revision to reflect the recent Ulysses flyby of Jupiter), the principle engineering model of these radiation belts is that of Divine and colleagues.[46] This model has many of the characteristics of the AE/AP radiation models and thus can be described in the same manner as the Earth's trapped radiation belts.

Jovian Radiation Models

In the Divine model[46], the independent variables used to define position for the magnetic field and charged particles are jovicentric distance r (commonly in m or R_J), latitude l (deg or rad), longitude l (deg in System III (1965)[47]), distance z=r sin l from the rotational equatorial plane (m or R_J), and distance R=r cos l from the rotation axis (m or R_J). The value of the Jovian equatorial radius is assumed to be 1 R_J =7.14 x 10^7 m. The common angular speed of rotation of Jupiter's internal magnetic field and of a meridian of constant longitude l in System III (1965) coordinates is assumed to be w=870.536 deg/day≈12.6 km/s R_J. In this system, l, the longitude, increases westward (opposite to the azimuthal angle in a system of spherical coordinates).

Of the encounters with Jupiter, the retrograde, highly inclined, small perijove trajectory flown by Pioneer 11 has been the most useful for modeling the moments of Jupiter's internal magnetic field. The detailed, 15-coefficient spherical harmonic magnetic field model "O4" derived from the fluxgate magnetometer on Pioneer 11[43, 44] was used in deriving the trapped radiation model presented here. In this jovian magnetic field model, the dipole moment was assumed to have the value M=1.535x10^{27} m^2A = 4.218 G-R_J^3 (for reference, this gives a value for the surface magnetic field of ~8 G at the jovian poles as compared to ~.6 G for the Earth). For each field line the magnetic shell parameter L has the constant value:

$$L = (M/B_e)^{1/3} R_J^{-1} \qquad (12)$$

where B_e represents the minimum field strength along the line. As in the case of the Earth, among all field lines having the same value of L, the smallest field strength for which Jupiter's atmosphere (equatorial radius 1 R_J, flattening 0.065) is encountered represents an upper cutoff field strength B_c for stable charged particle trajectories. The O4 model has been used to calculate B_c as a function of L and to analyze the energetic charged particle data in the development of the numerical models. Although the O4 magnetic field model was used in deriving the model parameters, the much simpler offset tilted dipole model D4 derived from the Pioneer helium vector magnetometer data[42] is sufficiently accurate for evaluating model parameters for many applications. The parameter values for this model are presented in Table 4.[46] The nearly equatorial offset of about 0.1 R_J suggests that L = 1.1 represents the smallest accessible value of L for the trapped particles (the O4 model yields minimum L = 1.089). A transformation of coordinates based on Table 4 allows derivation of distance r_m and latitude l_m in terms of r, l, and l. The vector components of the magnetic field may then be derived from the D4 model using standard dipole relations.[42] The magnetic field strength, as in Equation 1, is given by

$$B = (M/r_m^3)(3 \sin l_m^2 + 1)^{0.5} \qquad (13)$$

and the shape of a field line, along which the magnetic shell parameter L is constant, is given by

$$L = (r_m/R_J)(\cos l_m)^{-2} \qquad (14)$$

The dipole moment has the value M =1.538x10^{27} m^2A = 4.225 G-R_J^3 and the tilt colatitude of 10.77° equals the inclination between the rotational and magnetic equatorial planes represented by l=0° and l_m=0° respectively.

The principle radiation belt populations included in this model are, as in the case of the Earth, electrons (E>0.06 MeV) and protons (E>0.6 MeV). The range of applicability of the energetic electron model extends to the Jovian magnetopause while that of the protons out to L=12. The electron model in-

cludes a pitch angle dependency within L=16 but is considered isotropic beyond that point. The proton model includes a pitch angle dependency within L=12. The following paragraphs describe the model characteristics.

For the inner electron and proton models, the independent variables magnetic L shell, local field strength B, pitch angle a with respect to the field line, and particle kinetic energy E were utilized (B and L are of course functions of r, l, and I). The model populations are assumed independent of time, longitude, and direction azimuth about the field line, as appropriate for stably trapped populations. The mirror point field strength is given by:

$$B_m = B(\sin a)^{-2} \qquad (15)$$

and the requirement that the intensity vanish for $B_m > B_c$ insures that the drift loss cone is empty for a pitch angle a close to 0° or 180°.

At each value of L, analytic expressions have been developed (these values are tabulated in Divine and Garrett[46]), based on fits to the spacecraft and radio data, that allow evaluation of the particle integral and differential intensities I and i in terms of a, B, and E. That is, I has been fit to an analytic expression in a, B, and E at discrete values of L such that:

$$I_L = A_L(\alpha, B, E) \qquad (16)$$

Variations at other values of L are derived by interpolating between the relevant values. The corresponding differential intensity (in units of $cm^{-2}s^{-1}sr^{-1}MeV^{-1}$) is then given by:

$$i = -\frac{dI}{dE} \qquad (17)$$

Electron and proton omnidirectional fluxes are obtained by integration

$$J = 4\pi \int_0^{\pi/2} I(\sin\alpha)d\alpha \qquad (18)$$

The spectra represented by these equations were approximated by power laws. Values for the equations were obtained by minimizing the weighted root-mean-square residual in the logarithm of the ratios of the model-predicted count rates to the count rates observed from several detectors at the relevant L values. Improvements in the fits were derived by matching the model predictions to UHF radio observations from Earth.

In the middle and outer Jovian magnetosphere (i.e., beyond L=16), the energetic particle fluxes are extremely time-dependent and are, as a result, difficult to model. However, to adequately estimate radiation effects in the jovian environment, a simple, isotropic formula for the energetic electron fluxes, based on Pioneer 10 and 11 observations, has been included in the model for completeness. This formulation assumes that the peak equatorial fluxes can be described by a function of the form:

$$\log J_o = f(t) - 2.2 \log r - 0.7 \log (0.03 E + E^3/r) \qquad (19)$$

Here the electron kinetic energy E has units MeV, r has units R_J, and the omnidirectional integral flux J has units of $cm^{-2}s^{-1}$. The term f(t), which specifies the time dependence, is assumed to have an average value of 7.43. The maximum value given by equation 19 is assumed to occur along a disk surface at a height z_o (in R_J) above the jovian equatorial plane given by:[48]

$$z_o = r \tan a \cos (l - l_o) \qquad (20)$$

for L>16 and r<20 R_J, and, for r>20 R_J, by:

$$z_o = r_o \tan a \cos \{(l - l_o) - w (r - R_o)/V\} \qquad (21)$$

V_o, the "wave speed", is about 40 R_J/hr[48] which is, as might be expected, indistinguishable from the Alfven speed, V_A, in this regime. The values for l_o, r_o, w, and a (here a represents inclination of the magnetic axis, not pitch angle) are:

$l_o = 21°$ $\quad r_o = 20\ R_J$
$w = V_A \cdot 0.9°/R_J$ $\quad a = 10.77°$

The flux falls off away from this surface ex-

ponentially with a scale height of 2 R_J.[48]

$$J = J_o \exp\left(-\left|\frac{r\lambda - z_o}{2R_J}\right|\right) \qquad (22)$$

Figures 24 and 25[46] illustrate contours of constant omnidirectional integral flux for energies greater than 1 MeV for electrons and protons as predicted by the model. The fluxes can be compared with Fig. 6.

Saturn

Fig. 26[49] is a schematic illustration of the postulated Saturn magnetosphere. As in the case of Jupiter, Divine[50] has developed a first order radiation model for Saturn similar to that for Jupiter (this model, although unpublished, is available through JPL[50]). Based on high energy data from Pioneer 11, Voyager 1, and Voyager 2, the model covers the distance from 2.3 to 13 R_S. It describes the electron distribution at energies between 0.04 and 10 MeV and the proton distribution between 0.14 and 80 MeV. As in the Jupiter model, the first step in the model is to specify the Saturnian magnetic field. Estimates for this field and other relevant quantities are listed in Table 5. The magnetic dipole moment assumed is M = 4.3 x 10^{26} G-cm^3 = .195 G-R_S. For comparison with the Earth and Jupiter, the magnetic field amplitude at the saturnian surface over the poles is ~.4 G. Next, the integral and differential intensities for the electrons and protons, as functions of the magnetic field and L, are specified by algorithms very similar to those of the Jupiter model. The integral omnidirectional flux J is then calculated as before by Eq. 18.

The output of the model is presented in Figs. 27 and 28. The integral omnidirectional flux for the Saturn electron model at three energy thresholds are plotted in Fig. 27 (the dropouts are typically associated with the orbits of the Saturnian moons or rings). The fluxes at the magnetic equator (B_e/B=1.0) and at high magnetic latitude (B_e/B=0) are represented respectively by the solid and dashed lines. Similar plots for the protons are presented in Fig. 28 (for energies of 1, 10, and 100 MeV; solid, dashed, and solid).

Conclusions

The objective of this paper was to provide a review of the natural space radiation environment. The emphasis has been on the particulate environment and has covered the Earth's trapped environment, the solar flare environment, Cosmic Rays, and other interplanetary and extraterrestrial environ-ments. The Earth's trapped radiation environment and the solar flare environment are the two most critical environments for the designer. The models for each of these are currently undergoing substantial revision and should see significant improvements in the near future.

References

1 Van Allen, J.A., *Geomagnetically Trapped Radiation.* Space Science, 1963, New York-London: J. Wiley & Sons, Inc.

2 Daly, E.J., *The Evaluation of Space Radiation Environments for ESA Projects.* ESA Journal, 1988. **12**: p. 229-247.

3 Barraclough, D.R., *International Geomagnetic Reference Field: The 4th Generation.* Physics of the Earth and Planetary Interiors, 1987. **48**: p. 279.

4 Olson, W.P., and K.A. Pfitzer, *A Quantitative Model of the Magnetospheric Magnetic Field.* J. Geophys. Res., 1974. **79**: p. 3739.

5 Voigt, G.H., *A three dimensional, analytical magnetospheric model with defined magnetopause.* Z. Geophys., 1972. **38**: p. 319-346.

6 Tsyganenko, *Magnetosphere Model...* Annals. Geophys., 1976. **32**: p. 1.

7 Hardy, D.A., F. Hanser, and B. Sellers, *The Space Radiation Dosimeter (AFGL-701-2),* in *CRRES/SPACERAD Experiment Descriptions,* M.S. Gussenhoven, E.G. Mullen, andR.C. Sagalyn, Editor. 1985, AF Geophysics Laboratory: Hanscom AFB, MA.

8 Vette, J.I., M.J. Teague, D.M. Sawyer, and K.W. Chan. *Modeling the Earth's Radiation Belts.* in *Solar-Terrestrial Prediction Proceedings.* 1979. Boulder: NOAA.

9 Sawyer, D.M., and J.I. Vette. *AP-8 Trapped Proton Environment for Solar*

Maximum and Solar Minimum. 1976, NSSDC/WDC-A-R&S: 76-06.

[10] Vette, J.I. *The AE-8 Trapped Electron Model Environment*. November, 1991, NSSDC/WDC-A-R&S: 91-24.

[11] Smith, R.E., and G.S. West, ed. *Space and Planetary Environment Criteria Guidelines for Use in Space Vehicle Development, 1982 Revision*. Vol. 1. 1983, NASA:.

[12] Chan, K.L., and L. Colin, *Global Electron Density Distributions from Topside Soundings*. Proc. IEEE, 1969. **57**.

[13] Kerns, K.J., Capt., USAF, and M.S. Gussenhoven. *CRRESRAD Documentation*. 6 August, 1992, Phillips Laboratory, Directorate of Geophysics: PL-TR-92-2201.

[14] Brautigam, D.H., M.S. Gussenhoven, and E.G. Mullen, *Quasi-Static Model of Outer one Electrons*. submitted to IEEE Trans. Nucl. Sci., 1992. (December).

[15] Gussenhoven, M.S., E.G. Mullen, and D.H. Brautigam. *Near-Earth Radiation Model Deficiencies as seen on CRRES*. in *COSPAR 1993*. 1993.

[16] Blake, J.B., and L.M. Friesen. *A Technique to Determine the Charge State of the Anomalous Low Energy Cosmic Rays*. in *15th International Cosmic Ray Conference*. 1977. Plovdiv.

[17] Cornwall, J.M., *Radial Diffusion of Ionized Helium and Proton: A Probe for Magnetospheric Dynamics*. J. Geophy. Res., 1972. **77**: p. 1756.

[18] Spjeldvik, W.N., and T.A. Fritz, *Theory of Charge States of Energetic Oxygen Ions in the Earth's Radiation Belts*. J. Geophys. Res., 1978. **83**(A4): p. 1583.

[19] Fritz, T.A., and W.N. Spjeldvik, *Simultaneous Quiet Time Observations of Energetic Radiation Belt Protons and Helium Ions: the Equatorial a/p Ratio Near 1 MeV*. J. Geophys. Res., 1979. **84**: p. 2608-2618.

[20] Adams, J.H., Jr. , R. Silverberg, and C.H. Tsao. *Cosmic Ray Effects on Microelectronics, Part I: The Near-Earth Particle Environment*. August 25,1981, Naval Research Laboratory, Washington D.C.: NRL Memorandum Report 4506.

[21] Grigorov, N.L., and e. al., *Evidence for Anomalous Cosmic Ray Oxygen Ions in the Inner Magnetosphere*. Geo. Res. Ltrs., 1991. **18**: p. 1959.

[22] Cummings, J.R., A.C. Cummings, R.A. Mewaldt, R.S. Selesnick, E.C. Stone, and T.T. von Rosenvinge, *New Evidence for Geomagnetically Trapped Anomalous Cosmic Rays*. Geo. Res. Ltrs., 1993. **20**(18): p. 2003-2006.

[23] Smart, D.F., and M.A. Shea, *Galactic Cosmic Radiation and Solar Energetic Particles*, in *Handbook of Geophysics and the Space Environment*, A.S. Jursa, Editor. 1985, National Technical Information Service: Springfield, VA. Chapter 6.

[24] Feynman, J., T.P. Armstrong, L. Dao-Gibner, and S.M. Silverman, *A New Interplanetary Proton Fluence Model*. J. Spacecraft, 1990. **27**: p. 403.

[25] Feynman, J., G. Spitale, J. Wang, and S. Gabriel, *Interplanetary Proton Fluence Model: JPL 1991*. J. Geophys. Res., 1993. **98**(A8, August 1): p. 13,281-13,294.

[26] Adams, J.H., Jr. , J.R. Letaw, and D.F. Smart. *Cosmic Ray Effects on Microelectronics, Part II: The Geomagnetic Cutoff Effects*. May,1983, Naval Research Laboratory, Washington D.C.: NRL Memorandum Report 4506.

[27] Tsao, C.H., R. Silberberg, J.H. Adams Jr., and J.R. Letaw. *Cosmic Ray Effects on Microelectronics, Part III: Propagation of Cosmic Rays in the Atmosphere*. August 9,1984, Naval Research Laboratory, Washington D.C.: NRL Memorandum Report 4506.

[28] Adams, J.H., Jr. *Cosmic Ray Effects on Microelectronics, Part IV*. 1986, Naval Research Laboratory, Washington D.C.: NRL Memorandum Report 5901.

[29] Feynman, J., and S. Gabriel. *Interplanetary Particle Environment, Proceedings of a Conference*. 1988. Jet Propulsion Laboratory.

[30] Luhn, A., *et al.*, *Ionic Charge States of N, Ne, Mg, Si, S in Solar Particle Events*. Advances in Space Research, 1984. **4**: p. 161-164.

[31] Fischer, S., K. Vandas, B. Kuznetsov, and R. Ramatay, *Determination of the Effective Charge of Solar Cosmic Ray Nuclei Using the Earth's Magnetic Field*, in *Advances in Space Research*. 1984, p. 169-172.

[32] McWaldt, R.A., and E.C. Stone, *A*

Search for Deuterium Tritium and ^{3}He in Large Solar Flares. 1983, Bull. of the Am. Phys. Soc. p. 742.

[33] Breneman, H.H., and E.C. Stone, *Solar and Photospheric Abundance from Solar Energetic Particle Measurements.* Astrophys. J., 1985. **229**: p. L57-61.

[34] Meyer, P.R., R. Ramaty, and R. Webber, *Cosmic Rays - Astronomy with Energetic Particles,* in *Physics Today.* 1974.

[35] Jokipii, J.R., E.H. Levy, and W.B. Hubbard, *Effects of Particle Drift on Cosmic Ray Transport. I. General Properties.* Astrophys. J., 1977. **213**: p. 861.

[36] Fisk, L.A., B. Kpzlovsky, and R. Ramaty, Astrophys. J. (Lttrs.), 1974. **190**: p. 135-137.

[37] Divine, T.N. *Interplanetary Charged Particle Models*. March,1975, NASA: SP-8118.

[38] Garrett, H.B., and G.S. Spitale, *Effects of the Solar and Extra-Terrestrial Environment on Space Power Systems,* in *Space Power.* 1984, NASA: p. 225-249.

[39] Drake, F.D., and H. Havatum, *Non-thermal microwave radiation from Jupiter.* Astron. J., 1959. **64**: p. 329-330.

[40] Gehrels, N., ed. *Jupiter*. 1976, University of Arizona Press: Tucson, AZ.

[41] Dessler, A.J., ed. *Physics of the Jovian Magnetosphere*. Cambridge Planetary Science Series, ed. W.I. Axford, G.E. Hunt, andR. Greeley. 1983, Cambridge University Press: New York. 544.

[42] Smith, E.J., L. Davis Jr., and D.E. Jones, *Jupiter's magnetic field and magnetosphere,* in *Jupiter,* T. Gehrels, Editor. 1976, University of Arizona Press: Tucson, AZ. p. 788-829.

[43] Acuna, M.H., and N.F. Ness, *Results from the GSFC Fluxgate Magnetometer on Pioner 11,* in *Jupiter,* T. Gehrels, Editor. 1976, University of Arizona Press: Tucson, AZ. p. 1976.

[44] Acuna, M.H., and N.F. Ness, *The main magnetic field of Jupiter.* J. Geophys. Res., 1976. **81**: p. 2917-2922.

[45] Anon. *Physics of the Jovian and Saturnian Magnetospheres, Highlights of Conference.* in *Physics of the Jovian and Saturnian Magnetospheres*. 1981. John Hopkins University: John Hopkins University.

[46] Divine, T.N., and H.B. Garrett, *Charged particle distributions in Jupiter's magnetosphere.* J. Geophys. Res., 1983. **88**(Sept. 9): p. 6889-6903.

[47] Seidelmann, P.K., and T.N. Divine, *Evaluation of Jupiter longitudes in System III (1965).* Geophys. Res. Lett., 1977. **4**: p. 65-68.

[48] Carbary, J.F., *Periodicities in the Jovian magnetosphere: Magneto-disc models after Voyager.* Geophys. Res. Lett., 1980. **7**: p. 29-32.

[49] Krimigis, S.M., *et al., Low-energy charged particles in Saturn's magnetosphere: Results from Voyager 1.* Science, 1981. **212**(4491): p. 225-231.

[50] Divine, T.N. *Numerical Models for Electron and Proton Distributions in Saturn's Radiation Belts.* February 28, 1990, Jet Propulsion Laboratory: IOM 5217-90-029.

[51] Chan, K., M.J. Teague, N. Schofield, and J.I. Vette, *Modeling of electron time variations in the radiation belts,* in *Quantitative Modeling of Magnetospheric Processes,* W.P. Olson, Editor. 1979, American Geophysical Union: Washington, D.C. p. 121.

[52] Claflin, E.S., and R.S. White, *A study of equatorial inner belt protons from 2 to 200 MeV.* J. Geophys. Res., 1974. **79**: p. 959.

[53] Slavin, J., and e. al. *Planetary Mach Cones: Theory and Observation.* 1984, Jet Propulsion Laboratory.

TABLES

Table 1. Mean and Worst-Case Solar Particle Event Composition for Low Z Ions.[28]

Element	Mean	Worst	Element	Mean	Worst
H	1	1	P	2.3×10^{-7}	1.1×10^{-6}
He	1.0×10^{-2}	3.3×10^{-2}	S	8.0×10^{-6}	5.0×10^{-5}
Li	0	0	Cl	1.7×10^{-7}	8.0×10^{-7}
Be	0	0	Ar	3.3×10^{-6}	1.8×10^{-5}
B	0	0	K	1.3×10^{-7}	6.0×10^{-7}
C	1.6×10^{-4}	4.0×10^{-4}	Ca	3.2×10^{-6}	2.0×10^{-5}
N	3.8×10^{-5}	1.1×10^{-4}	Sc	0	0
O	3.2×10^{-4}	1.0×10^{-3}	Ti	1.0×10^{-7}	5.0×10^{-7}
F	0	0	V	0	0
Ne	5.1×10^{-5}	1.9×10^{-4}	Cr	5.7×10^{-7}	4.0×10^{-6}
Na	3.2×10^{-5}	1.3×10^{-5}	Mn	4.2×10^{-7}	2.3×10^{-6}
Mg	6.4×10^{-5}	2.5×10^{-4}	Fe	4.1×10^{-5}	4.0×10^{-4}
Al	3.5×10^{-6}	1.4×10^{-5}	Co	1.0×10^{-7}	5.5×10^{-7}
Si	5.8×10^{-5}	1.9×10^{-4}	Ni	2.2×10^{-6}	2.0×10^{-5}

Table 2. Mean Solar Particle Event Compositions for High Z Ions.[28]

Element	Mean	Element	Mean	Element	Mean
Cu	2.0×10^{-8}	Sn	2.0×10^{-10}	Lu	2.0×10^{-12}
Zn	6.0×10^{-8}	Sb	1.4×10^{-11}	Hf	8.0×10^{-12}
Ga	2.0×10^{-9}	Te	3.0×10^{-10}	Ta	9.0×10^{-13}
Ge	5.0×10^{-9}	I	6.0×10^{-11}	W	1.0×10^{-11}
As	3.0×10^{-10}	Xe	2.7×10^{-10}	Re	2.0×10^{-12}
Se	3.0×10^{-9}	Cs	2.0×10^{-11}	Os	3.0×10^{-11}
Br	4.0×10^{-10}	Ba	2.0×10^{-10}	Ir	3.0×10^{-11}
Kr	2.0×10^{-9}	La	2.0×10^{-11}	Pt	6.0×10^{-11}
Rb	3.0×10^{-10}	Ce	5.0×10^{-11}	Au	1.0×10^{-11}
Sr	1.0×10^{-9}	Pr	8.0×10^{-12}	Hg	1.0×10^{-11}
Y	2.0×10^{-10}	Nd	4.0×10^{-11}	Tl	9.0×10^{-12}
Zr	5.0×10^{-10}	Pm	0	Pb	1.0×10^{-10}
Nb	4.0×10^{-11}	Sm	1.0×10^{-11}	Bi	6.0×10^{-12}
Mo	2.0×10^{-10}	Eu	4.0×10^{-12}	Po	0
Tc	0	Gd	2.0×10^{-11}	At	0
Ru	9.0×10^{-11}	Tb	3.0×10^{-12}	Rn	0
Rh	2.0×10^{-11}	Dy	2.0×10^{-11}	Fr	0
Pd	6.0×10^{-11}	Ho	4.0×10^{-12}	Ac	0
Ag	2.0×10^{-11}	Er	1.0×10^{-11}	Th	2.0×10^{-12}
Cd	7.0×10^{-11}	Tm	2.0×10^{-12}	Pa	0
In	9.0×10^{-12}	Yb	9.0×10^{-12}	U	1.2×10^{-12}

Table 3. Physical Data on the Size and Magnetic Fields of the Planets and other Objects in the Solar System.

Object	Equatorial Radius (km)	Mass (kg)	Dipole Mag Moment (G-cm^3)	$\overline{E} = (10^{-8})(\overline{V}_s \times \overline{8})$ $\Downarrow$ Induced E-Field at Surface (V/cm)
Sun	6.960×10^5	1.991×10^{30}	$\sim 3.4 \times 10^{32}$	$\sim 4.4 \times 10^{-1}$
Mercury	2.439×10^3	3.303×10^{23}	5×10^{22}	1.0×10^{-5}
Venus	6.050×10^3	4.870×10^{24}	~0	—
Earth	6.378×10^3	5.976×10^{24}	8.1×10^{25}	2.5×10^{-3}
Moon	1.738×10^3	7.353×10^{22}	0	—
Mars	3.398×10^3	6.421×10^{23}	$<10^{22}$	$<10^{-6}$
Jupiter	7.14×10^4	1.899×10^{27}	1.59×10^{30}	1.84×10^{-1}
Io	1.82×10^3	8.916×10^{22}	$\sim 6.5 \times 10^{17}$	$\sim 2 \times 10^{-10}$
Saturn	6×10^4	5.686×10^{26}	4.3×10^{28}	5.0×10^{-3}
Titan	2.56×10^3	1.359×10^{23}	—	—
Uranus	2.6145×10^4	8.66×10^{25}	$\sim 1.9 \times 10^{28}$ (?)	$\sim 1.6 \times 10^{-2}$ (?)
Comets	~1-10	$\sim 10^{12}$ -10^{17}		

Table 4. Parameters of D4 Dipole, Based in System III(1965) Coordinates.

Dipole Offset Vector	Magnetic Moment Vector
Latitude $\lambda = 5.12^\circ$	tilt colatitude 10.77°
West longitude $l = 155.6^\circ$	west longitude $l = 200.8^\circ$
Magnitude $r = 0.1010\ R_J$	magnitude $M = 4.225\ \text{G}\ R_J^3$
Components $x = 10.0916\ R_J$ $y = -0.0416\ R_J$ $z = +00090\ R_J$	Components $M_x = -0.738\ \text{G}\ R_J^3$ $M_y = +0.280\ \text{G}R_J^3$ $M_z = +4.151\ \text{G}R_J^3$

Table 5. Parameter Values for Saturn used in the Model Calculations.

Quantity	Value
Radius	$R_S = 6.033 \times 10^7$ m
Gravitation	$GM_S = 3.794 \times 10^{16}\ \text{m}^3/\text{s}^2$
Rotation	$\omega = 810.76$ deg/day
Magnetic field coefficients	$g_1^0 = 0.21535G\ g_1^0 = 0.21535G$ $g_2^0 = 0.01642G\ g_2^0 = 0.01642G$ $g_3^0 = 0.02743G\ g_3^0 = 0.02743G$ $G_1^0 = 0.0001G\ \ G_1^0 = 0.0001G$ $G_1^1 = 0.00001G\ G_1^1 = 0.00001G$

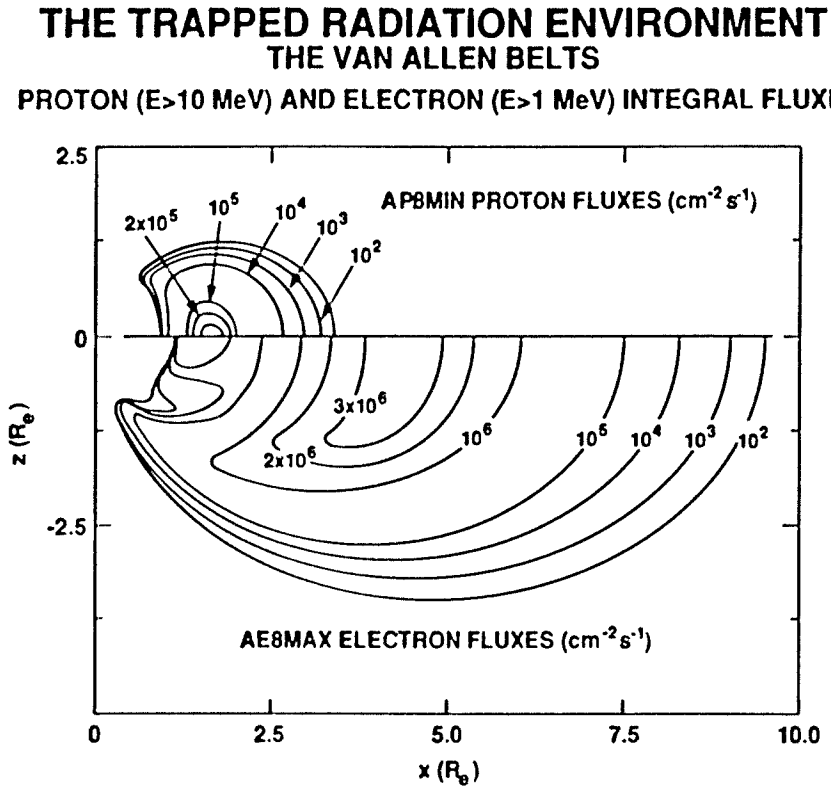

Fig. 1. The Earth's radiation belts in idealized dipole space, according to the AP8 and AE8 models. Average omnidirectional integral fluxes above energy thresholds are shown.[2]

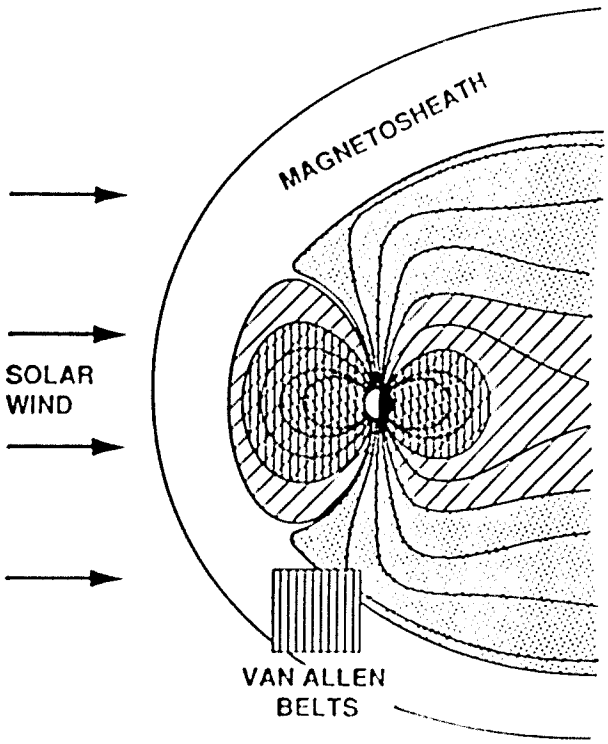

Fig. 2. Cross section of the Earth's magnetic field in the noon-midnight meridian showing the structure of the field lines and the plasma regions they contain.

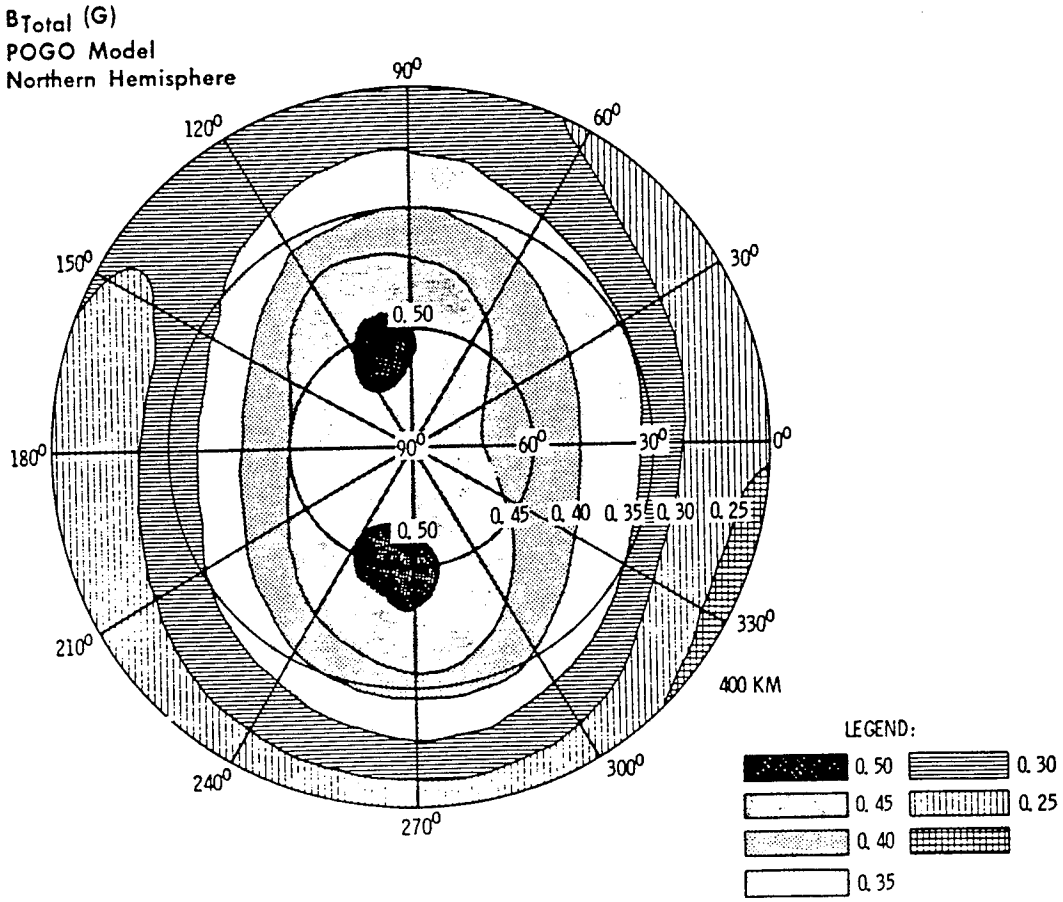

Fig. 3. Illustration of the magnetic field amplitude over the northern hemisphere at a constant altitude of 400 km. The field amplitude varies from a minimum of 0.25 G near the equator to 0.5 G over the polar caps.

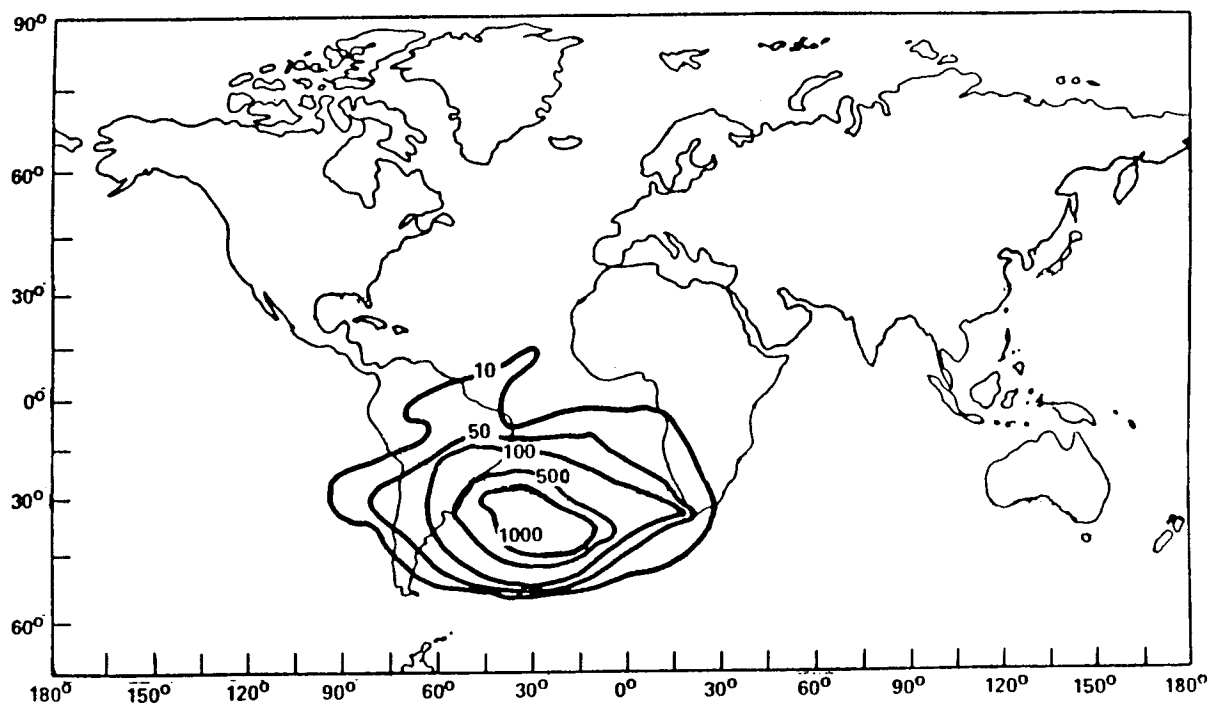

Fig. 4. Proton Flux Densities at 296 km Altitude.[11]

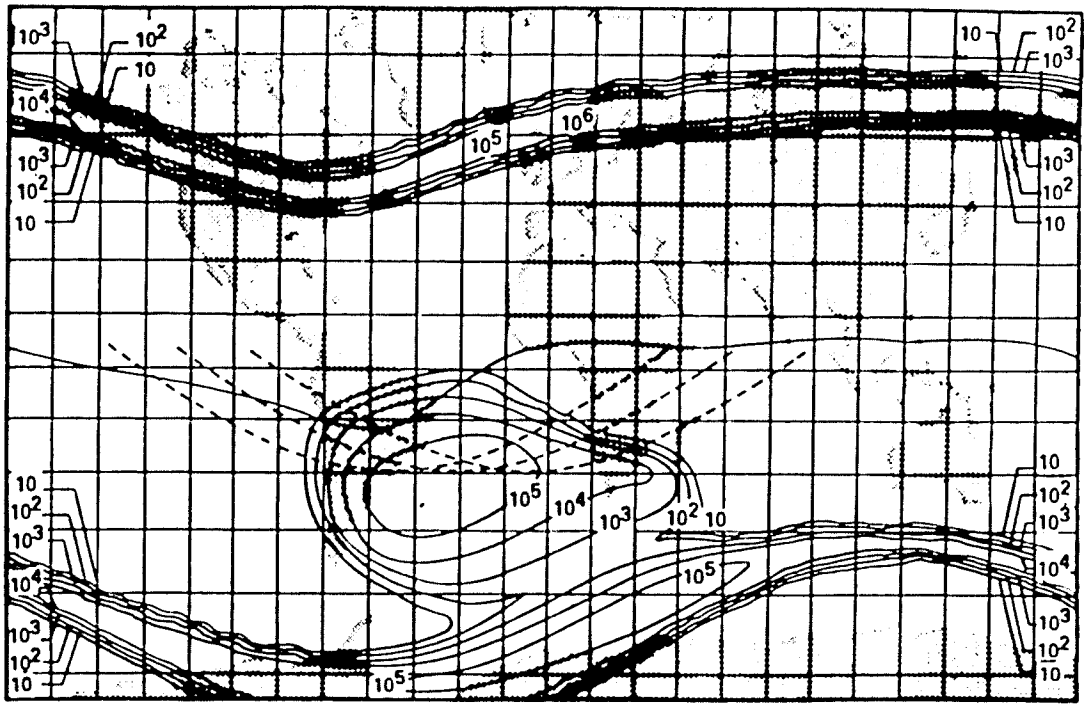

Fig. 5. Electron Constant Flux Contours at 400 km Alti-tude.(E>0.5 MeV)[11]

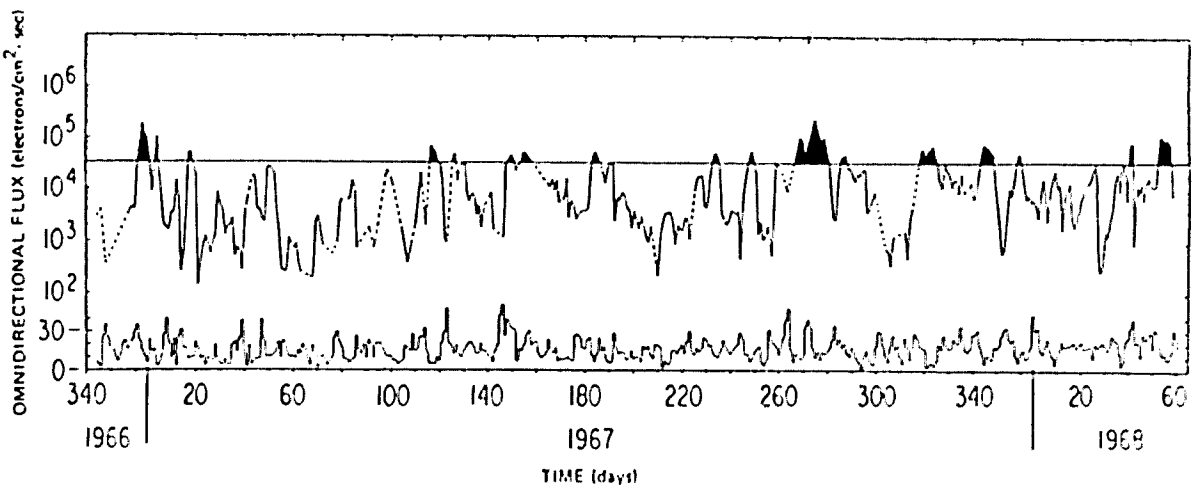

Fig. 6. Hourly averages of ATS1 1.9 MeV omnidirectional electron flux at local mid night.[51] Daily sum of K_p is plotted at the bottom of the figure. The horizontal line is the AEI-7 model equatorial flux at L = 6.6 and local midnight.

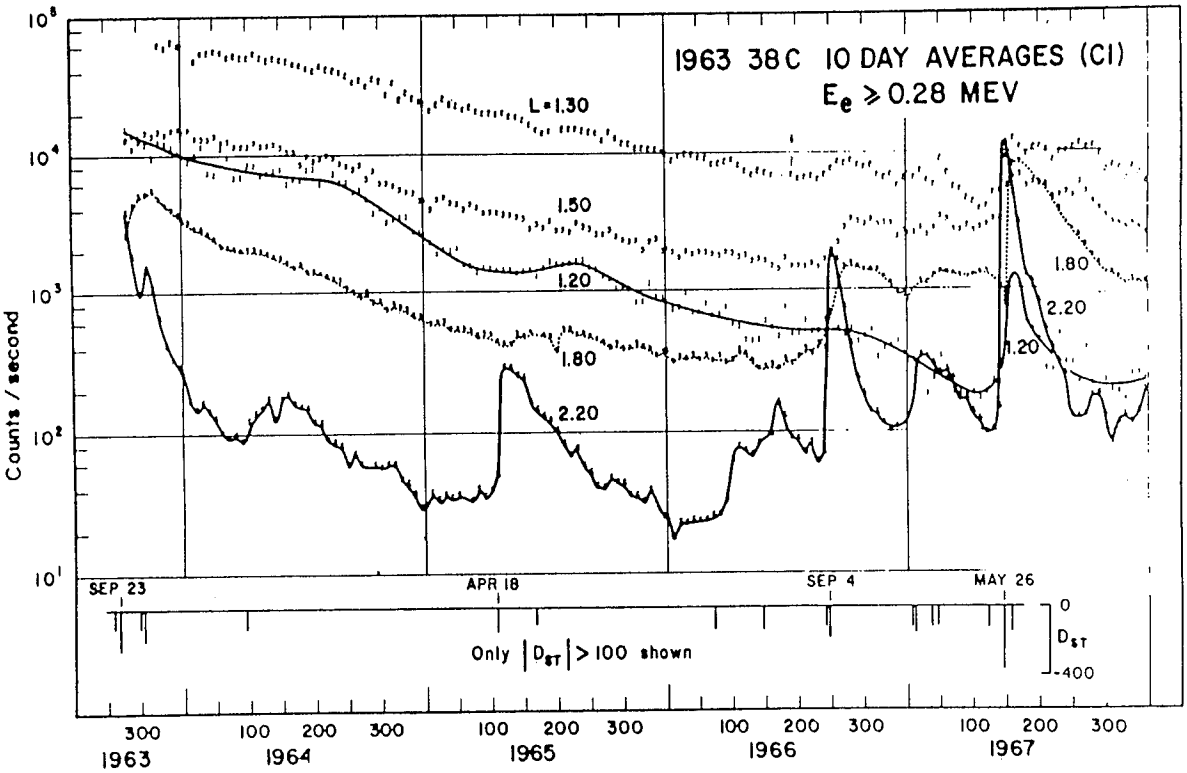

Fig. 7. 10 day averages of the inner zone electron fluxes greater than 0.28 MeV (in units of count rate) measured by the satellite 1963-38C. The effects of the decay of the Starfish nuclear debris and of the 4 major geomagnetic perturbations are evident.[51]

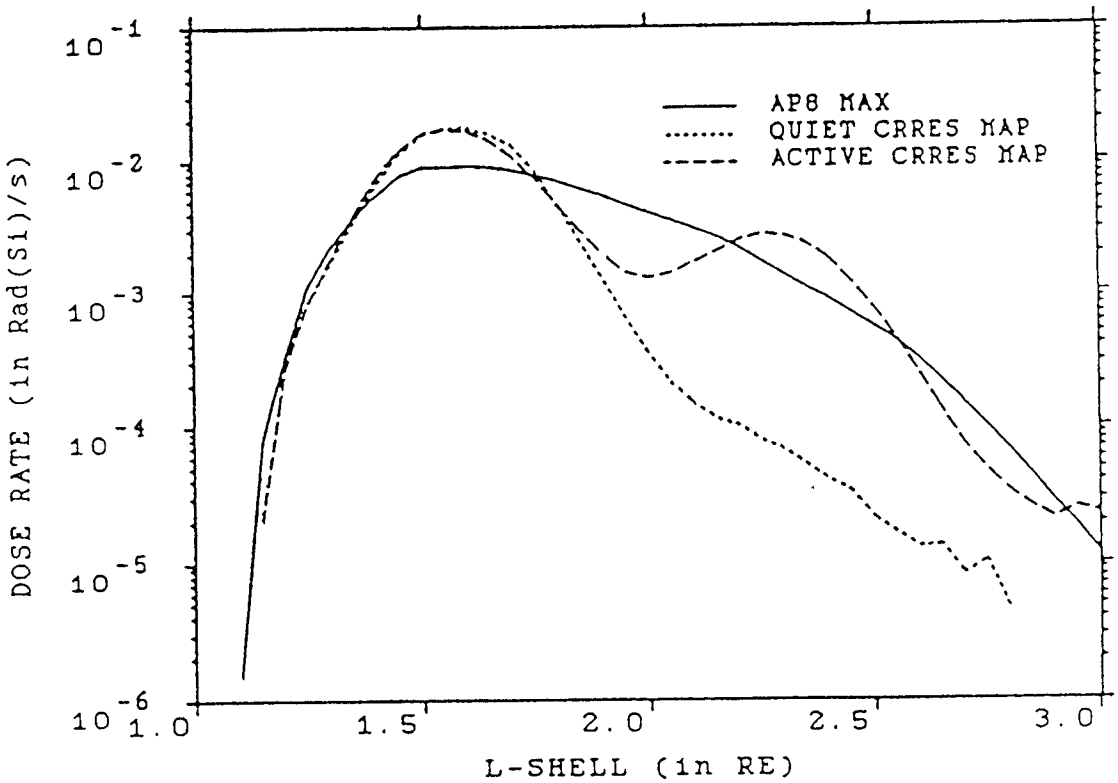

Fig. 8. Comparison of dose rate along magnetic equator as a function of L for quiet and active CRRES dose models and for AP8MAX. Dose rate is for E>20 MeV protons.[15]

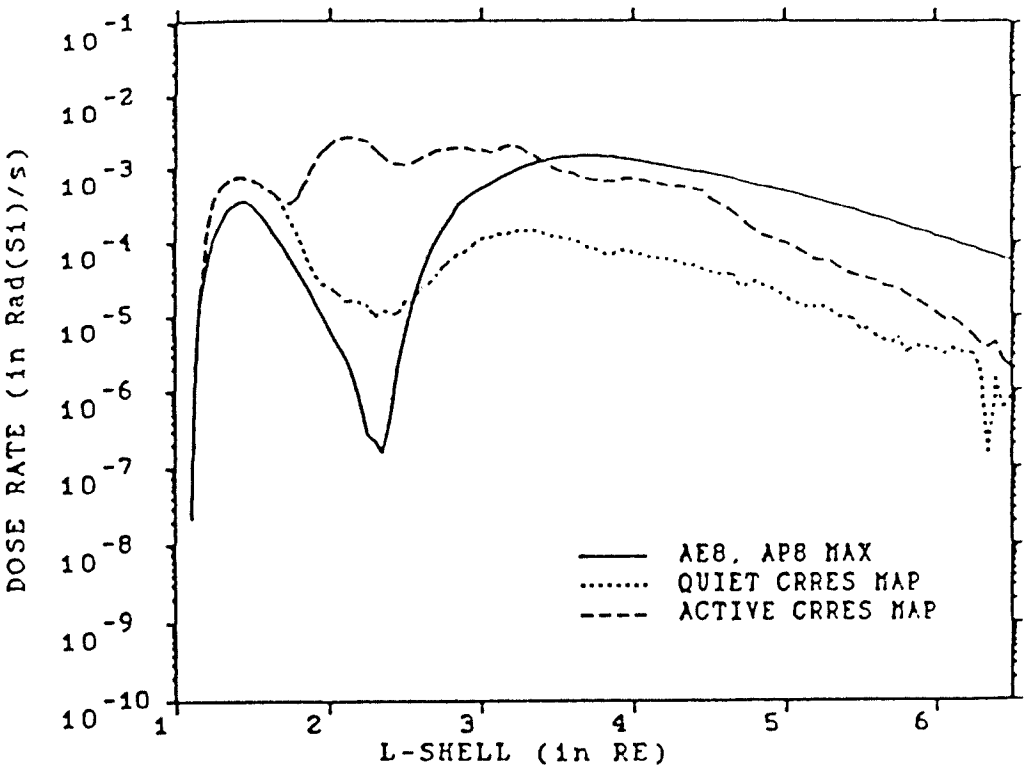

Fig. 9. Comparison of dose rate along magnetic equator as a function of L for quiet and active CRRES dose models and for AP8MAX/AE8MAX. Dose rate is for E>2.5 MeV electrons and E>135 MeV protons.[15]

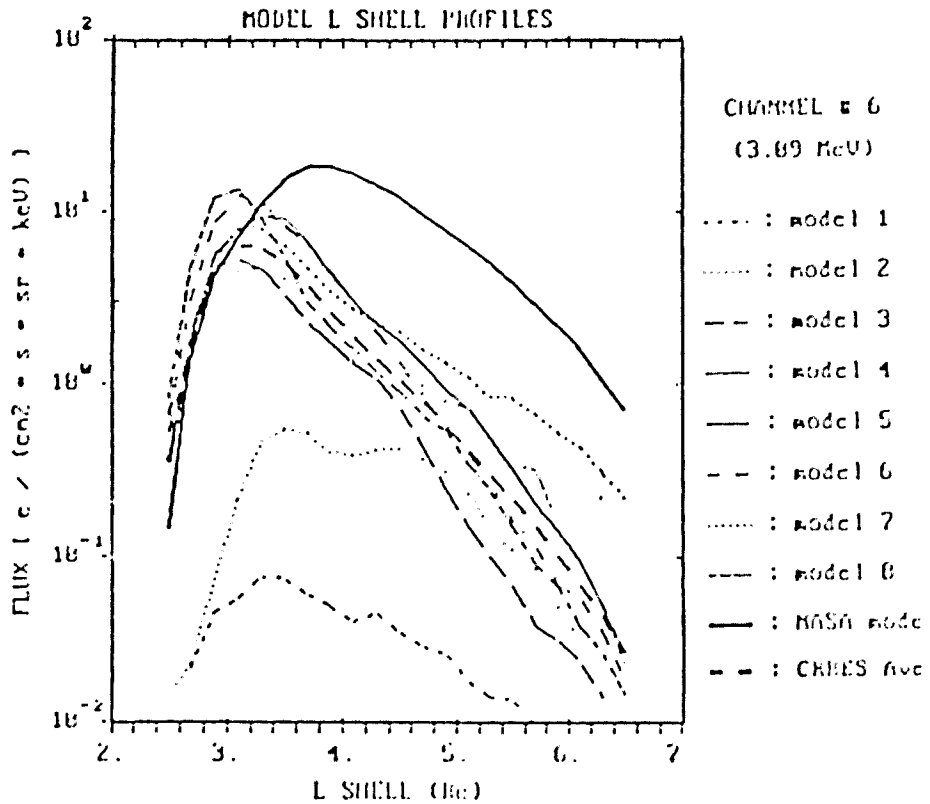

Fig. 10. Computed average radiation belt profiles as functions of L (between 2.4 and 6.6) for E>3.09 MeV and for 8 AP_{15} intervals between 5 nT and 55 nT. The individual interval results are compared with an overall average of the CRRES data and the corresponding prediction based on the AE8MAX model.[14]

SAMPEX OBSERVATIONS OF OXYGEN IONS

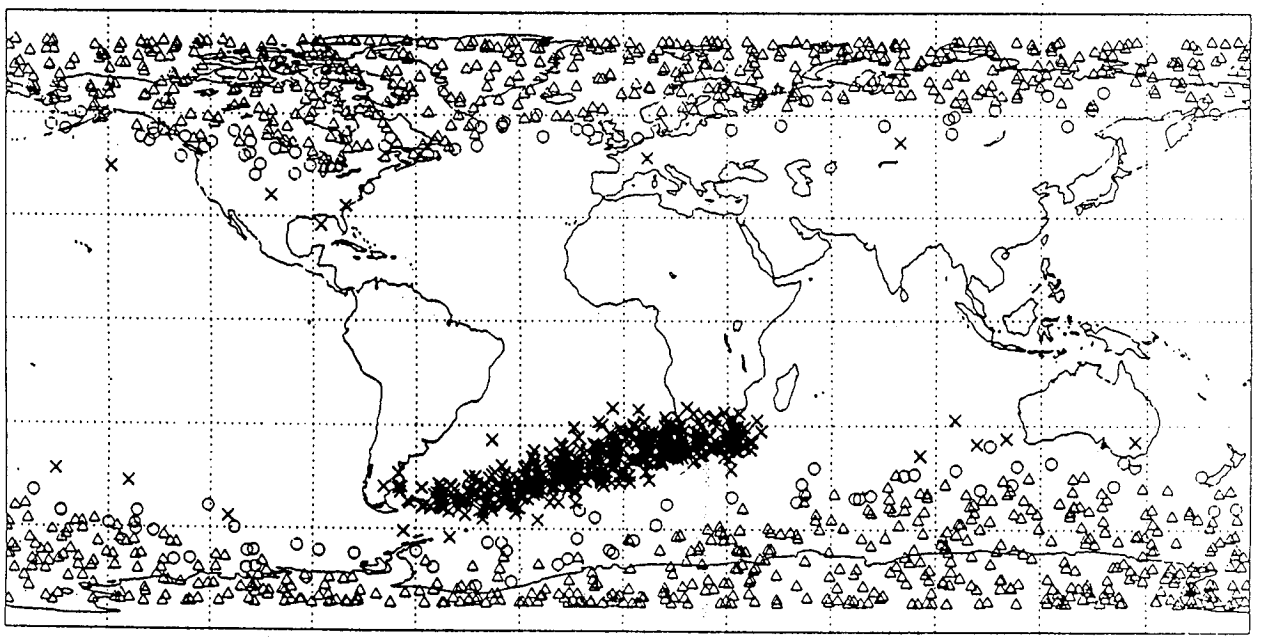

WHERE:

$\Delta = E_c > O^{+6}$

$\times = E_c < O^{+1.5}$

$O = O^{+6} > E_c > O^{+1.5}$

ORBIT:

520x670 KM; 82° inc; 1992-1993

Fig. 11. Geographic distribution of oxygen ions observed by SAMPEX between 1992 and 1993.[22] Triangles: events with cutoff energy above vertical O^{+6}; crosses: events with cutoff energy less than $O^{+1.5}$; and circles: events with intermediate cutoff energy.

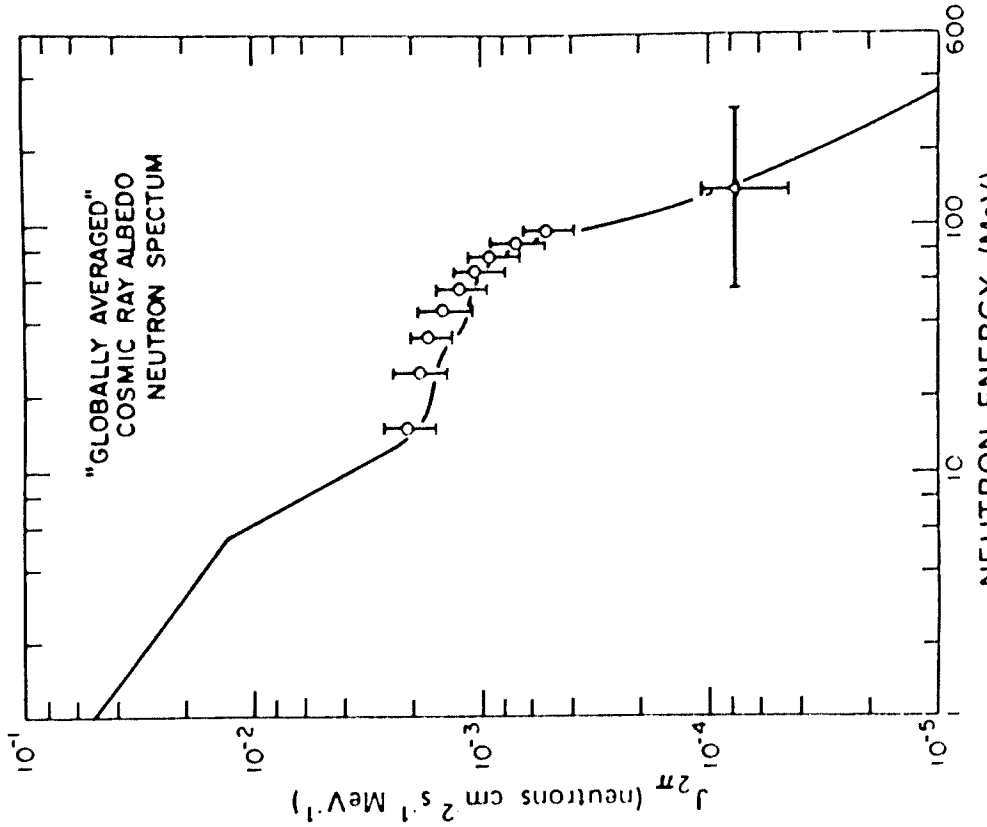

Fig. 13. A model "global averaged" albedo neutron spec-trum.[52]

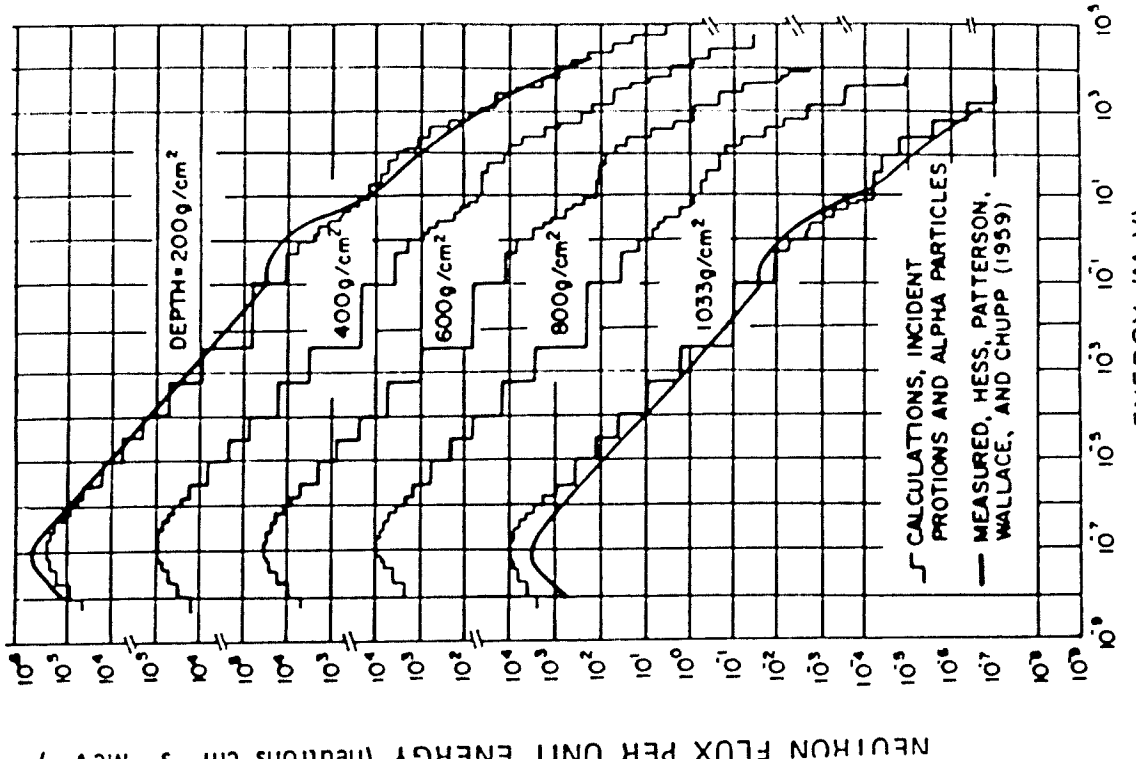

Fig. 12. Neutron spectra at various depths from top of the atmosphere. The data are adjusted to solar minimum conditions at the midlatitude geomagnetic latitude of ~42° (equivalent to a vertical cutoff rigidity of 4.5 GV).[23]

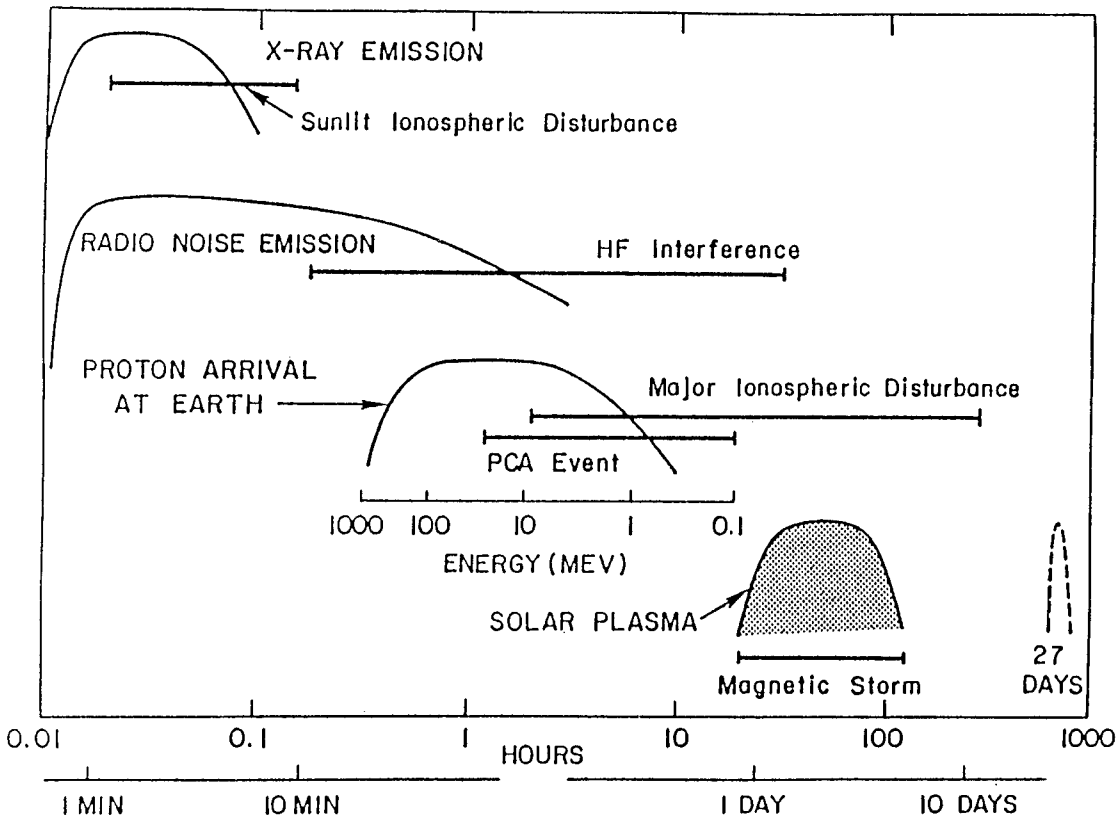

Fig. 14. Schematic plot of the relative variations in time of the amplitudes of the X-ray, radio noise, high energy particle, and solar plasma fluxes for a "typical" large solar flare.

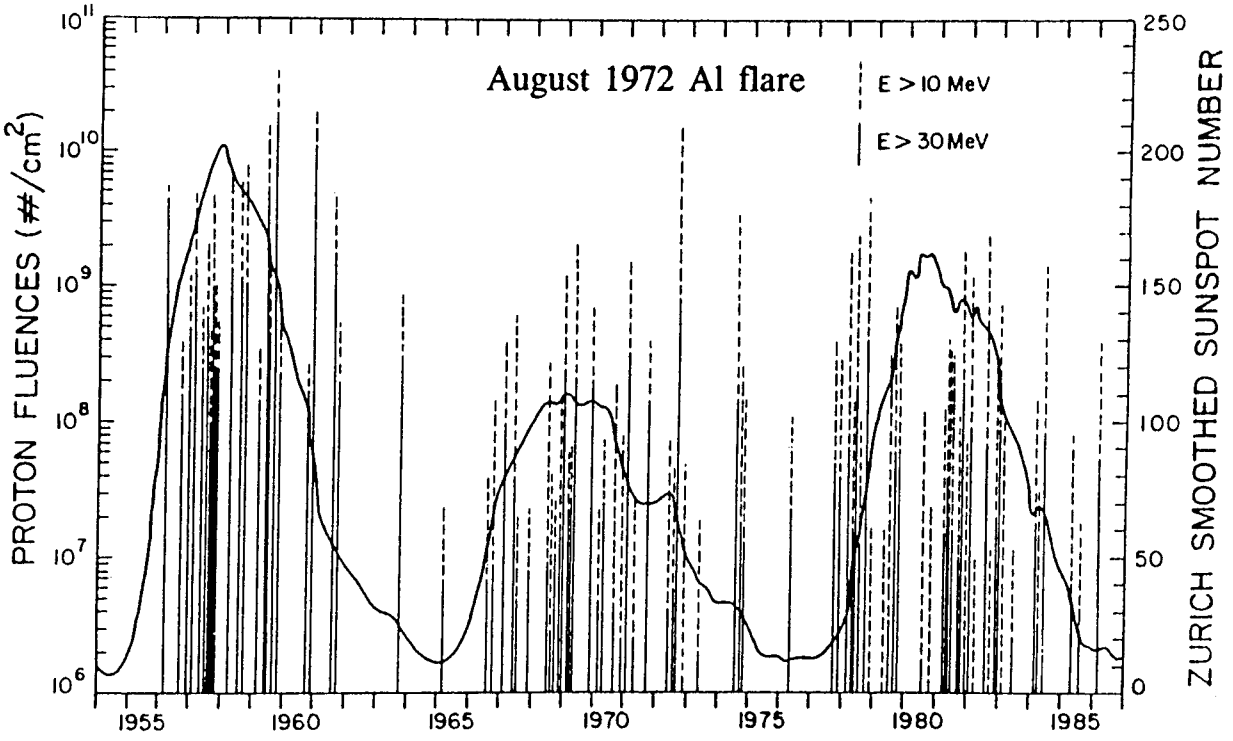

Fig. 15. Solar-flare proton fluences (vertical lines) super-imposed on the sunspot cycle (continuous curve). Solid lines correspond to E>3 MeV, dashed lines to E>1 MeV proton fluences.

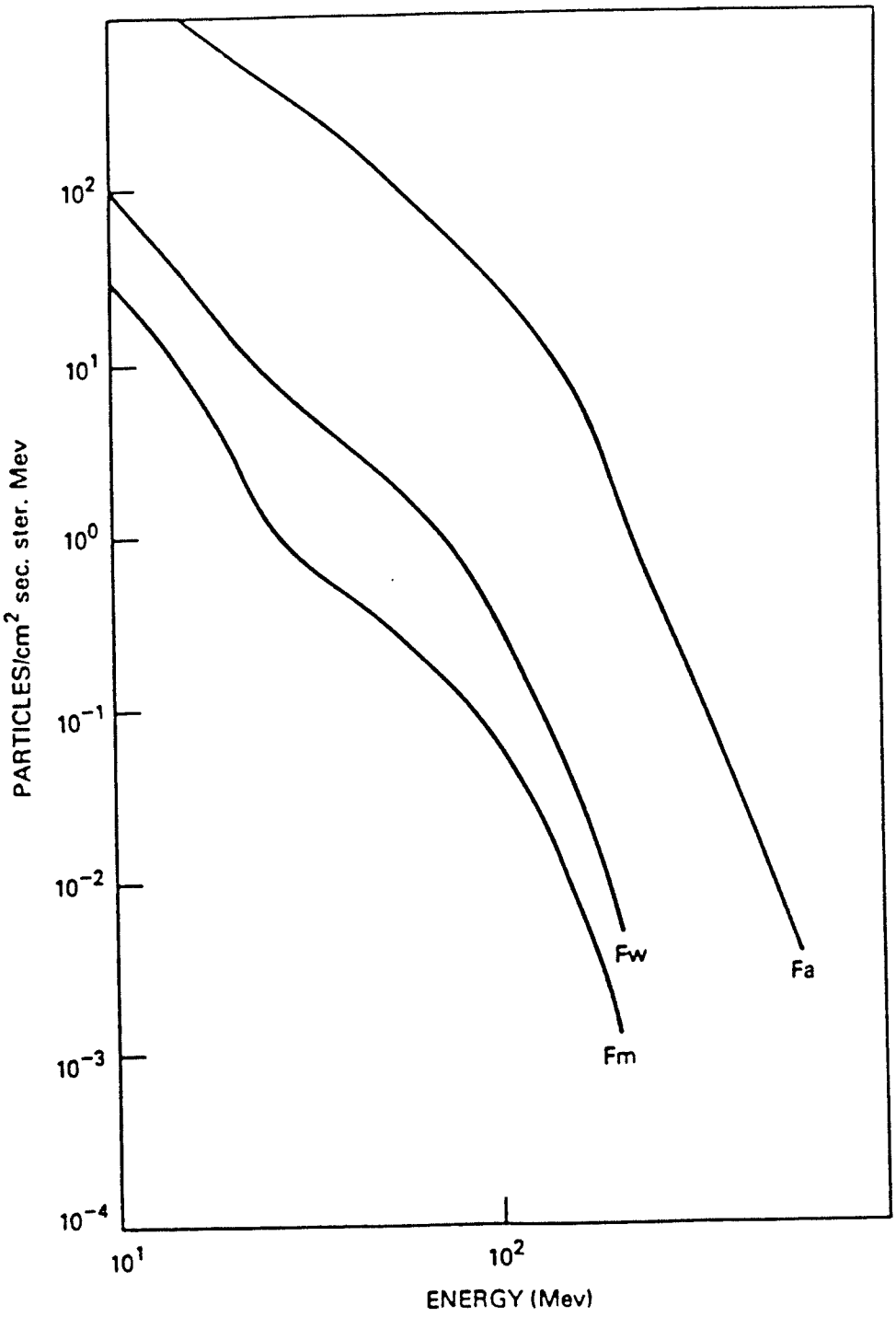

Fig. 16. The peak proton flux differential energy spectra for: F_m, a "typical" event; F_w, a "worst-case" event (90% confidence level); and F_a, an "anomalously large" event.[20]

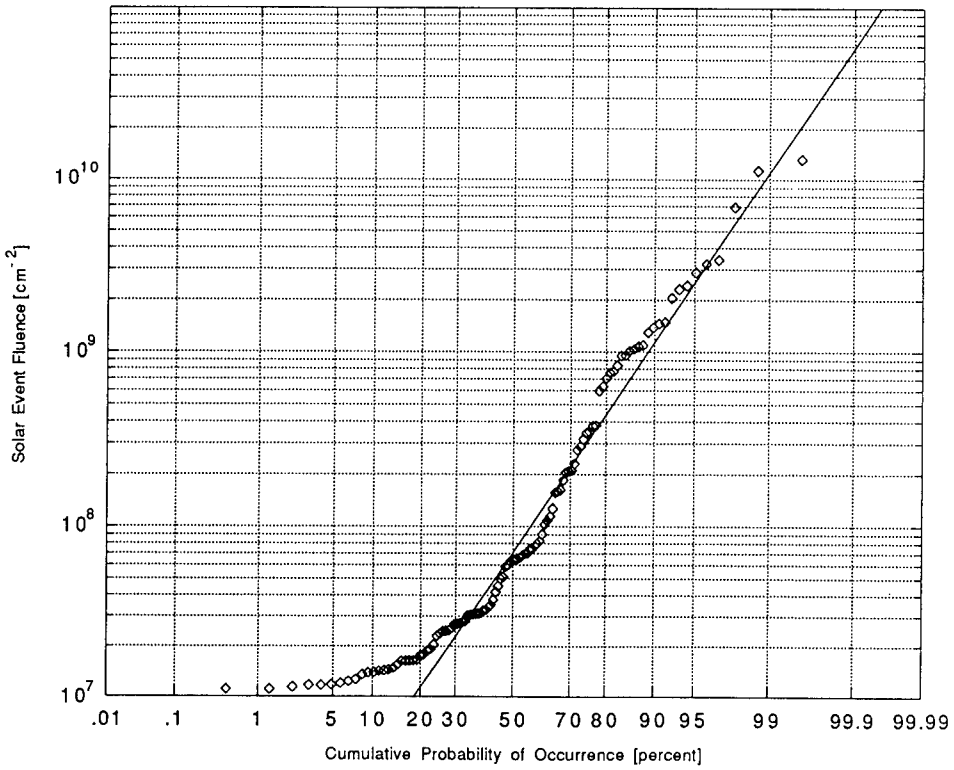

Fig. 17. Distribution of Solar Event Fluences for Solar Active Years between 1963 and 1991 for Protons of Energy > 10 MeV for which Daily Averaged Flux exceeds 1.0 cm^{-2}-s^{-1}-sr^{-1}. The straight line is the selected log normal distribution.[24]

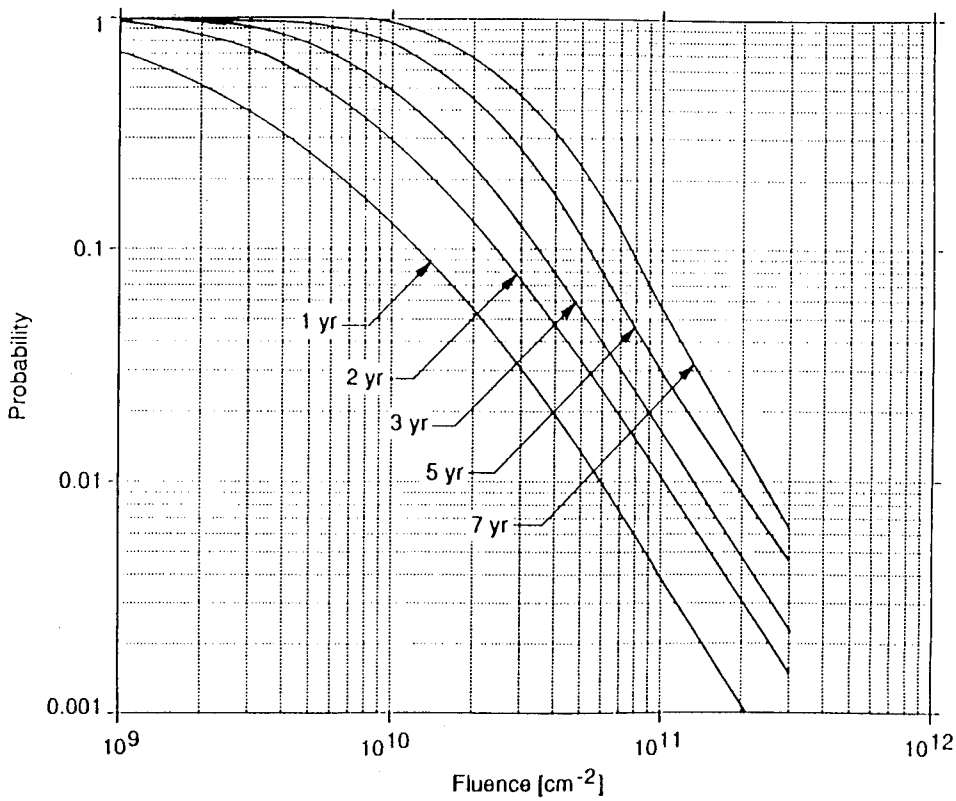

Fig. 18. Fluence Probability Curves for Protons of Energy Greater than 10 MeV for Various Mission Lengths.[24]

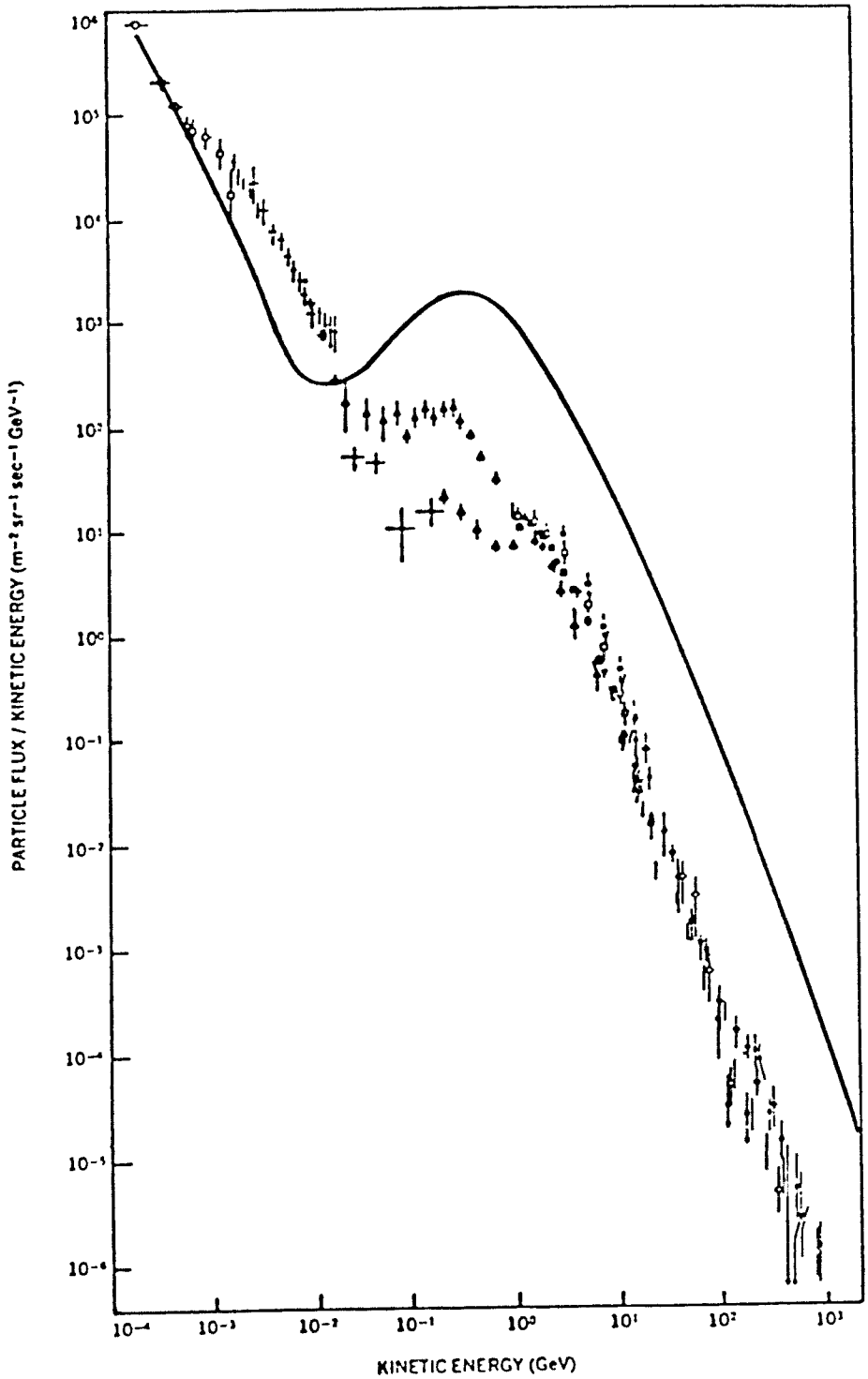

Fig. 19. The energy spectra of cosmic-ray protons (line) and electrons (points) as measured near Earth.[34] Below a few GeV, interstellar spectra are strongly influenced by the Sun.

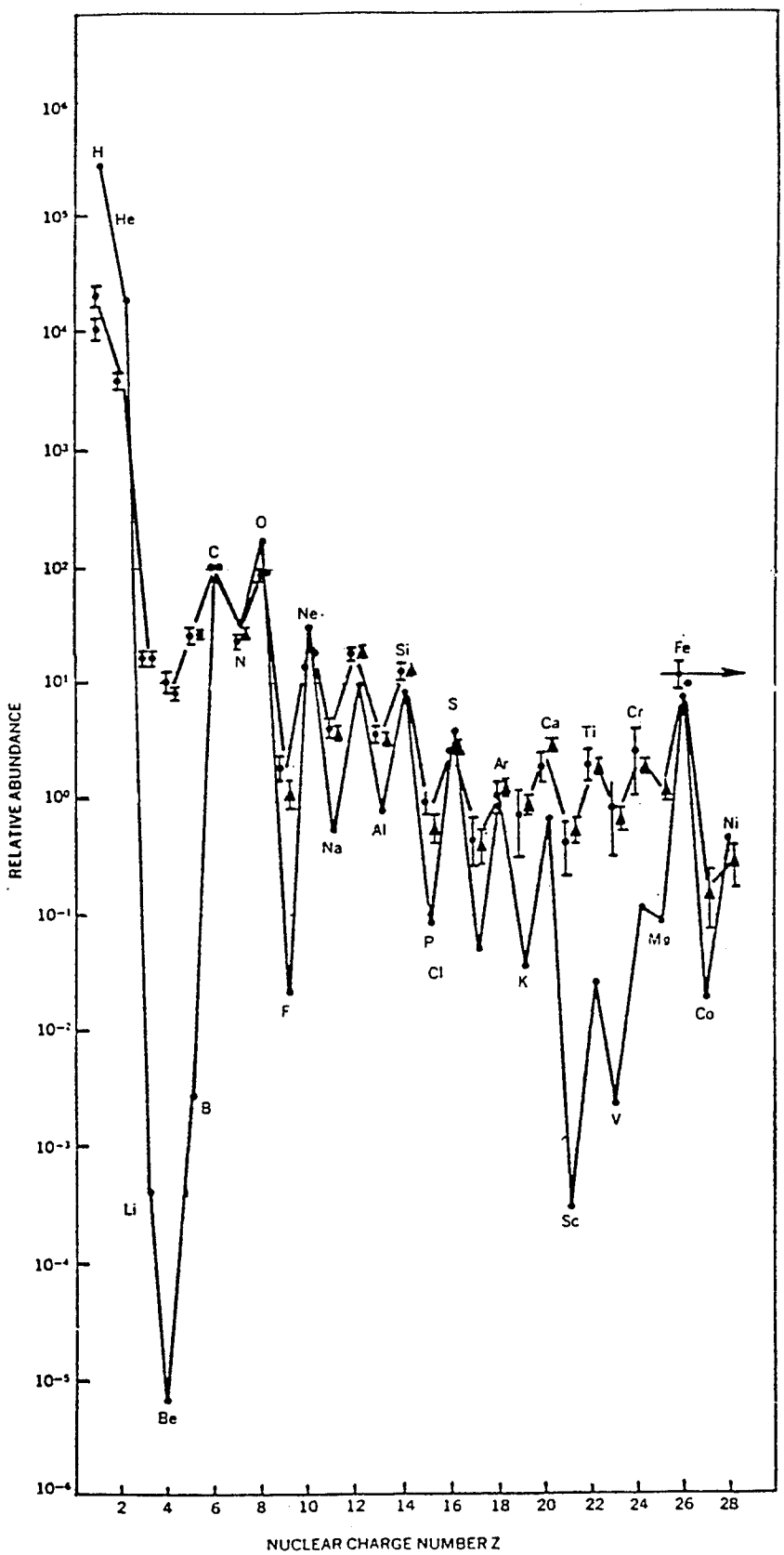

Fig. 20. Relative abundance of the elements from hydrogen to the iron group, normalized to that of carbon (C=100)[34]. The barred points represent the cosmic-ray abundances measured near Earth. The dots (without error bars) represent the elemental abundances in the solar system.

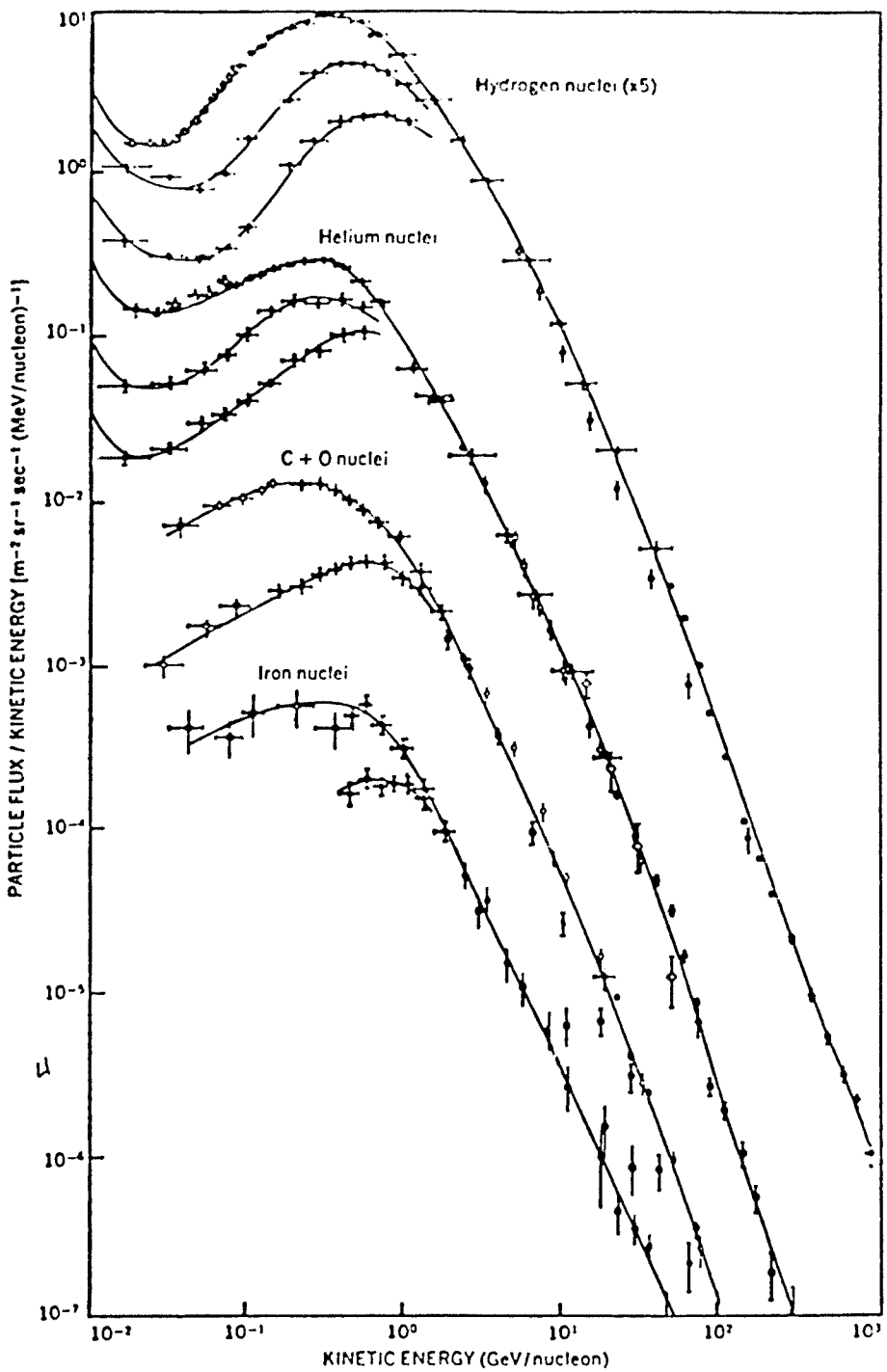

Fig. 21. Cosmic-ray energy spectra[34] of the more abundant nuclear species as measured near Earth. Below a few GeV/nucleon, these spectra are strongly influenced by modulation within the solar system. The different curves for the same species represent measurements at various levels of general solar activity, the lowest intensity being observed at the highest activity level.

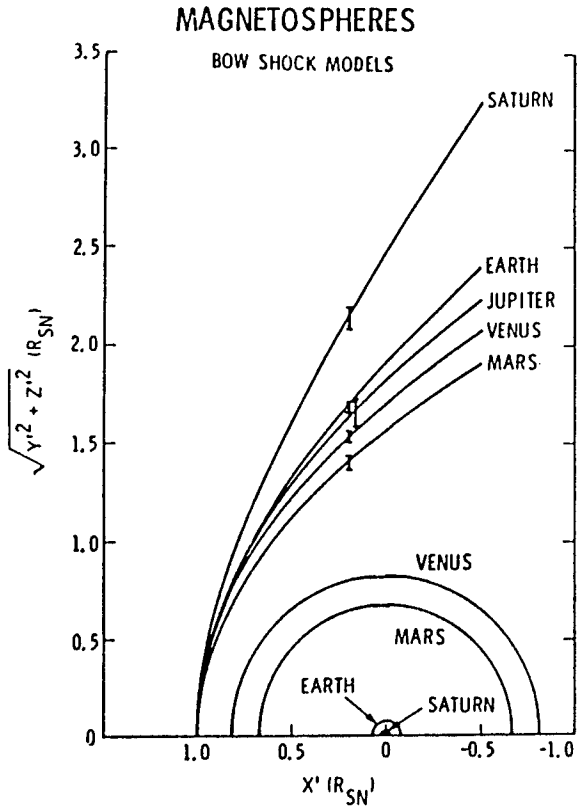

Fig. 22. Comparison of planetary-magnetospheres.[38, 53]

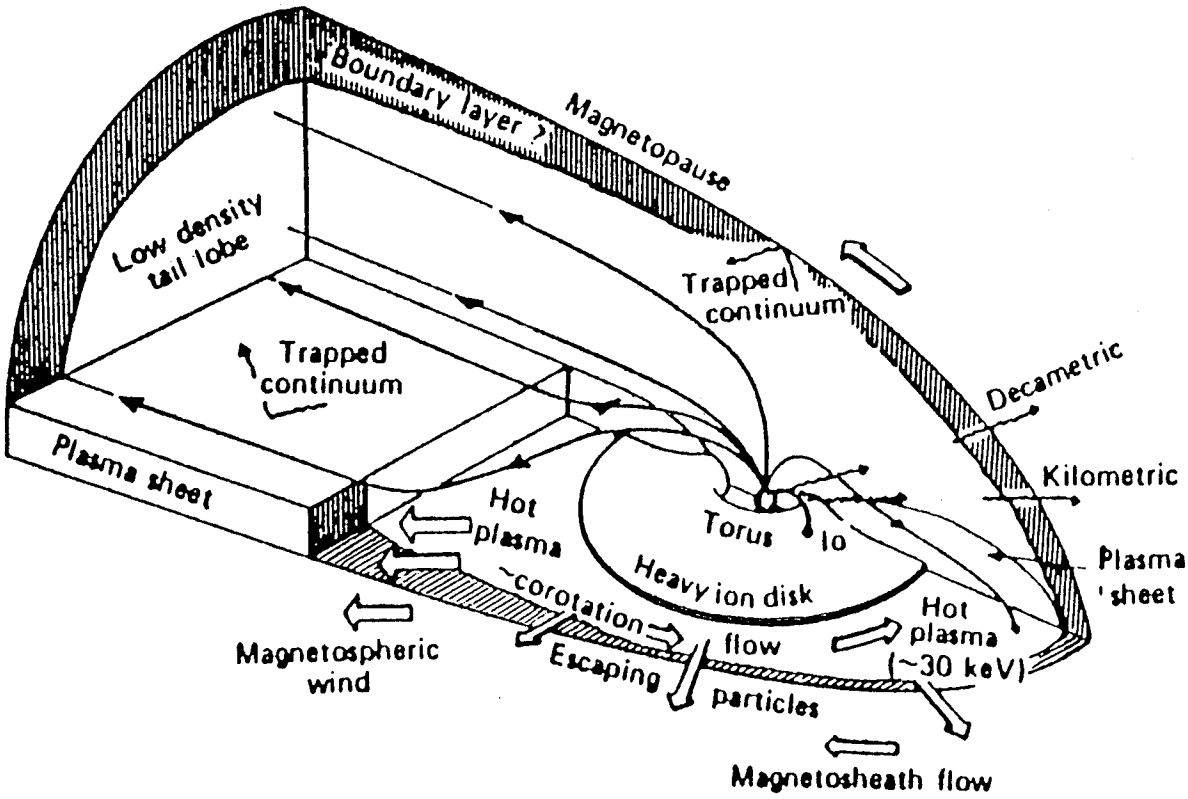

Fig. 23. Schematic representation of Jupiter's magnetosphere illustrating the various plasma regions and particle flows.[45]

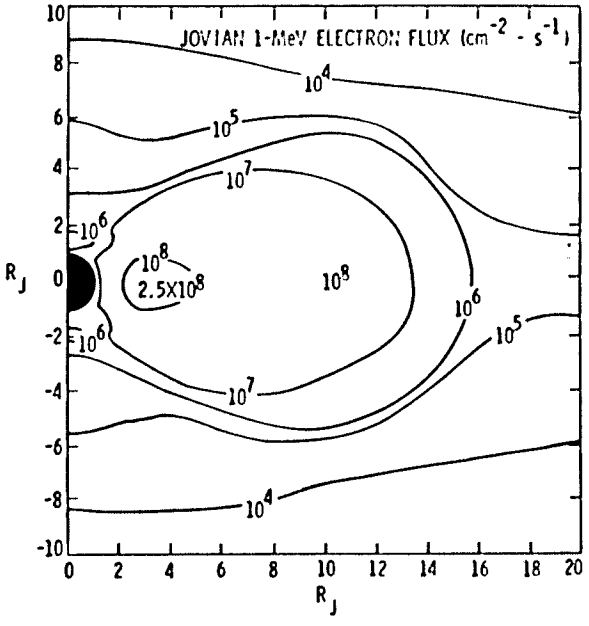

Fig. 24. Contours for electron fluxes above 1 MeV at Jupiter.[46]

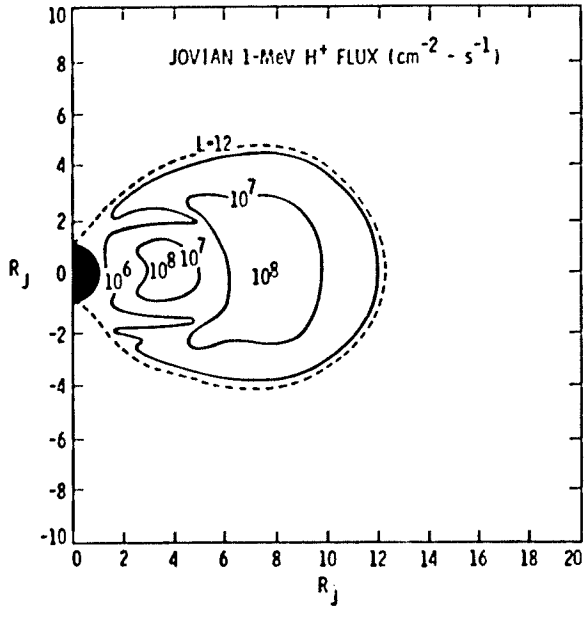

Fig. 25. Contours for proton fluxes above 1 MeV at Jupiter.[46]

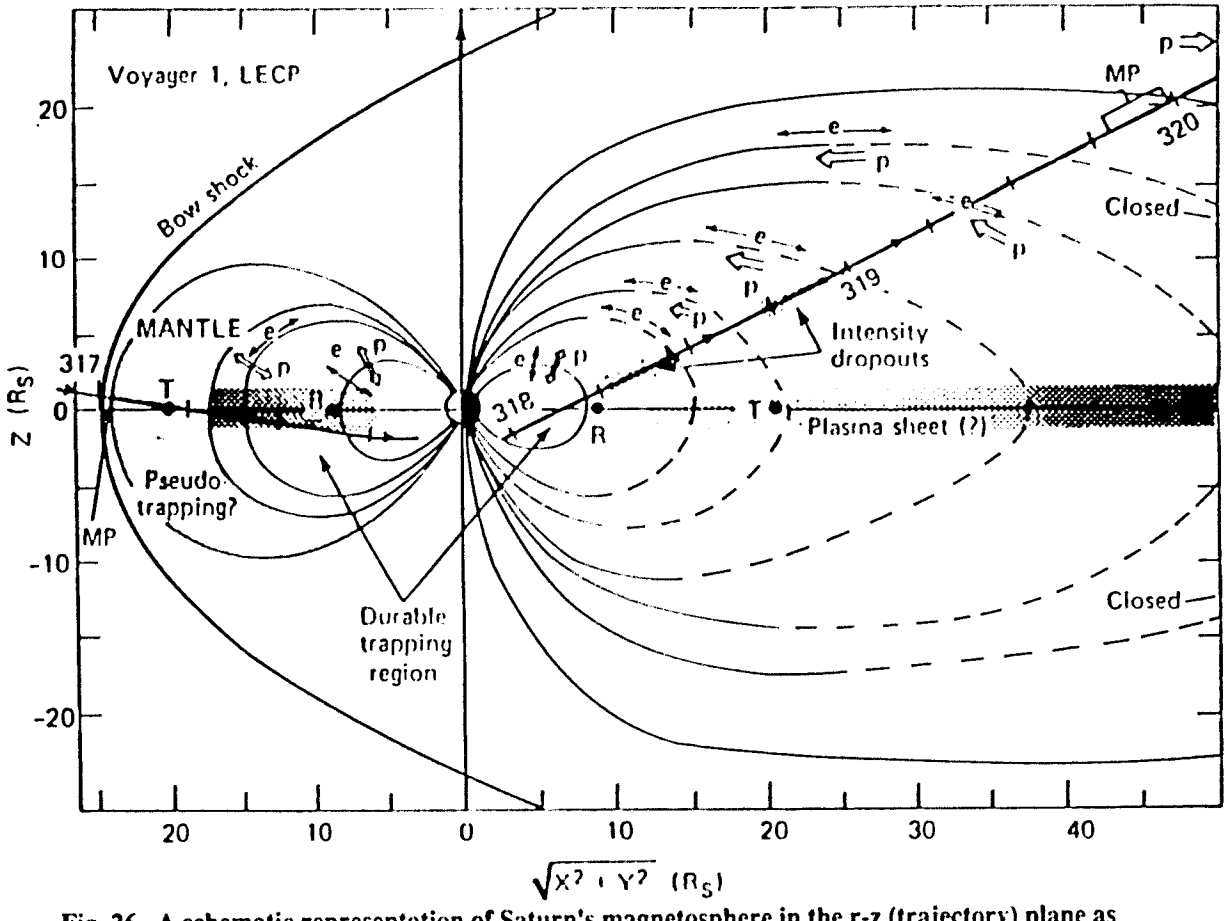

Fig. 26. A schematic representation of Saturn's magnetosphere in the r-z (trajectory) plane as revealed by the LECP data[49]. Tick marks on the trajectory are at 6-hour intervals from day 318 to 320. Note the Titan-associated mantle region outside ~ 17 R_S, and the presence of closed field lines in the tail lobe region. The phase of the second-order anisotropies relative to the magnetic field (B) is shown for both electron (e) and protons (p). R, Rhea: T., Titan: MP, magnetopause.

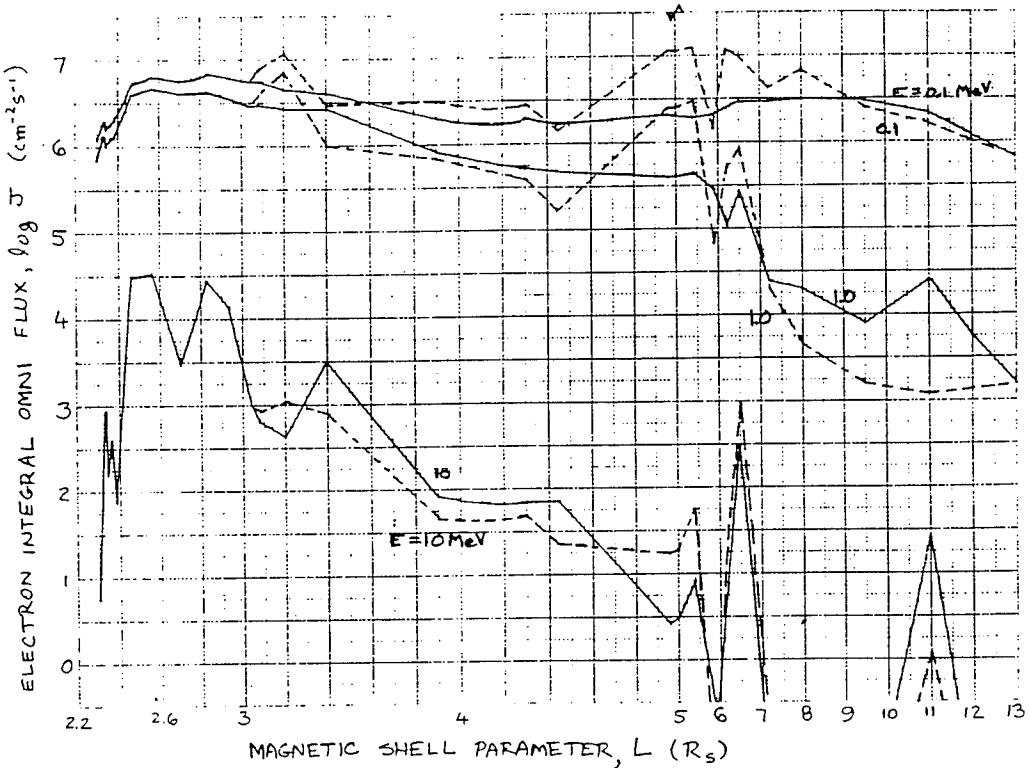

Fig. 27. Integral omnidirectional flux for the Saturn electron model[50] at three energy thresholds. The fluxes at the magnetic equator ($B_e/B=1.0$) and at high magnetic latitude ($B_e/B=0$) are represented respectively by the solid and dashed lines. The horizontal axis changes scale at L=5.

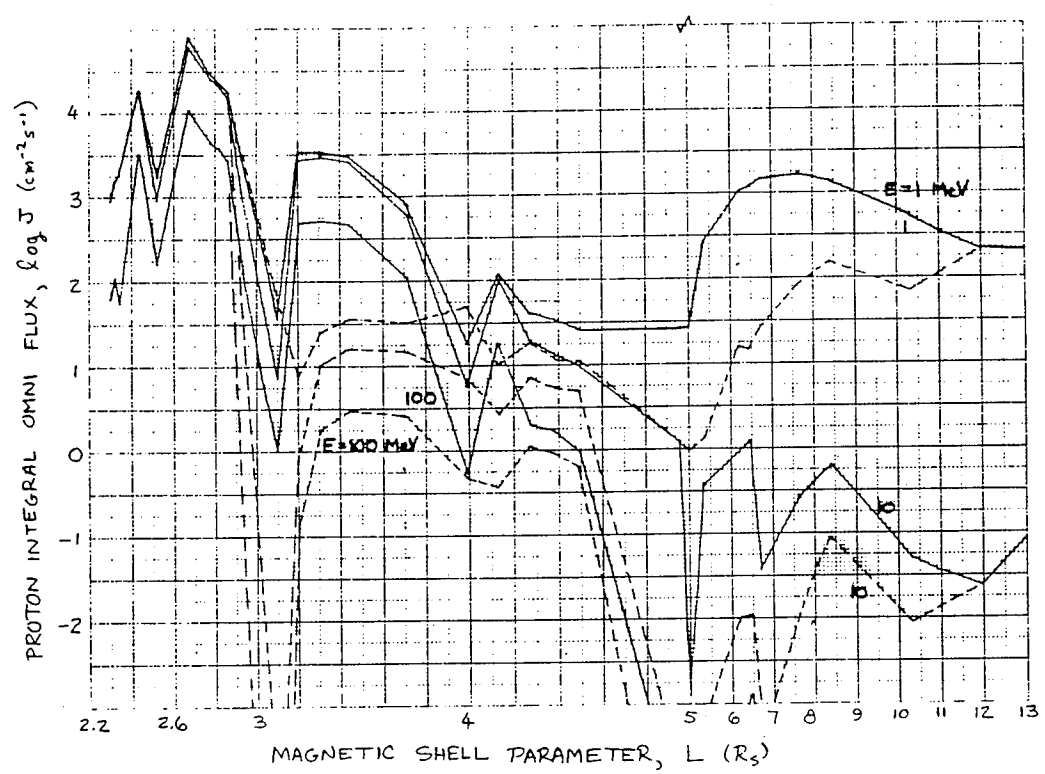

Fig. 28. Integral omnidirectional flux for the Saturn electron model[50] at three sample values of L (numbers adjacent to the curves). On the left the dependencies on local magnetic field strength B are shown for energy thresholds of 0.1, 1.0, and 10 MeV (solid, dashed, and solid lines) at each L. On the right, spectra are shown for the magnetic equator ($B_e/B=1.0$, solid lines) and for high magnetic latitude ($B_e/B=0$, dashed lines) at each L.

NEUTRAL DENSITY MODELS FOR AEROSPACE APPLICATIONS

F. A. Marcos
Geophysics Directorate
Phillips Laboratory
Hanscom AFB, MA

J. N. Bass
Radex, Inc.
Bedford, MA

C. R. Baker
Geophysics Directorate
Phillips Laboratory
Hanscom AFB, MA

W. S. Borer
Geophysics Directorate
Phillips Laboratory
Hanscom AFB, MA

Abstract

Aerodynamic drag is the major perturbation for low earth-orbiting spacecraft. Neutral density, winds and drag coefficient errors contribute to the satellite drag problem. A variety of empirical models have been developed to provide the engineering and science communities with a capability to specify and predict satellite drag. Empirical neutral density model accuracies have quantitatively improved little over the past 30 years. Physical models potentially circumvent many limitations of empirical models but their implementation requires new data on atmospheric heating and dynamics. Recent developments in both empirical and physical models for satellite drag are reviewed to provide an updated assessment of each approach. Forthcoming new modeling and measurement programs can lead to eventual significant improvements in operational satellite drag capabilities.

Introduction

Knowledge of satellite drag is important for practical aerospace applications including lifetime estimates, reentry prediction, orbit determination and tracking, and attitude dynamics. Orbital drag accelerations for a satellite in the earth's atmosphere depend on neutral density, winds and drag coefficient as given by:

$$a_D = 1/2 C_D A/M \rho V^2 \qquad (1)$$

where a_D is the drag acceleration, ρ is the atmospheric total mass density and A, M and C_D are the satellite's area, mass and drag coefficient respectively. The total atmospheric velocity relative to the satellite is: $V = - V_g + V_a + V_w$ and the components V_g, V_a and V_w are respectively the satellite's geocentric velocity, the earth rotational velocity and the wind contribution to atmospheric velocity.

This paper focusses on the earth's thermosphere at satellite altitudes, taken to be above about 150 km. The thermosphere is controlled by three highly variable energy sources: solar EUV and UV energy, auroral processes (Joule and particle heat-ing) and dynamical energy sources (tides and waves). Topics addressed are the processes that contribute to neutral upper atmosphere den-sity and wind variability, the accuracy and potential of both empirical and physical models to specify drag, a new technique for direct orbital measurement of satellite drag coefficients and forthcoming tools for improved modeling.

Neutral Density Variability

Solar EUV radiation is the main thermospheric heat source. This radiation originates in the solar chromosphere, transition region and corona. The EUV spectrum contains only about 10^{-5} of the energy in the visible spectrum. Earth's upper atmosphere completely absorbs the incident EUV. This leads to photoionization, photodissociation and subsequent chemical processes that release heat. Thermospheric temperature varies markedly with the EUV input. The main time scales for EUV variation are associated with the 11 year sunspot cycle, the 27 day solar rotation rate and shorter-term fluctuations. Figure 1 shows thermospheric temperature profiles corresponding to solar maximum and solar minimum conditions. Temperatures in the thermosphere increase with altitude to an asymptotic maximum value that varies between 700 K and 2000 K. Absorption of solar EUV by the atmosphere is also dependent upon the solar zenith angle, leading to additional dependencies of temperature on latitude, local time and season. Thermospheric temperatures maximize near the subsolar point. Dayside heating, maximizing near the sub-solar point, causes the atmo-

sphere to expand. The resulting pressure maximum at the sub-solar point also leads to a day-to-night wind flow. Winds flow from the high temperature, high pressure dayside over the poles and across the low pressure nightside. The global wind patterns are further modulated by collisions with the ionized constituents of the atmosphere. The increase in ion densities with solar activity tends to slow the winds at low latitudes due to ion drag.

The high latitude region receives additional energy and momentum sources, resulting in modulation of the solar EUV effects. The solar corona expands into space with a velocity of 200 -700 m/sec. This solar wind interacts with Earth's magnetized outer atmosphere, the magnetosphere, and creates geomagnetic disturbances. While it carries about a tenth of the power flux of the solar EUV spectrum, it is energized through complex interactions with the magnetosphere resulting in thermospheric heat-ing by energetic particles and joule heating. Auroral electric fields map down to thermospheric altitudes and drives non-divergent two-cell ion convection pattern. Figure 2 illustrates the interaction between EUV and solar wind processes. Consequent joule heating results from effects of frictional heating as the plasma is dragged through the neutral upper atmosphere. Localized Joule heating can be ten or more times as great as that due to EUV during magnetically disturbed times. This Joule heating in the auroral zone results in upwelling of nitrogen rich air, from altitudes near 130 km, to higher altitudes where atomic oxygen is dominant. Some of the heating is then advected away from the auroral zone by horizontal winds and gravity waves. The convecting ions also impart momentum to the neutral gases at high latitudes, driving a double vortex neutral wind system in the upper thermosphere. This interaction is most effective when the solar wind's Interplanetary Magnetic Field (IMF) has a southward component, merging efficiently with earth's geomagnetic field, and at high solar activity, when ion densities are high. The neutral atmosphere follows the ion convection cells resulting in an anti-sunward component of wind in the polar cap, augmenting that of the solar-EUV induced flow. During periods of northward IMF, the situation is more complicated: the winds may have an sunward direction in the polar cap, but only for cases where the northward component is greater than the east-west component of the IMF driving the neutral gas at auroral latitudes in the sunward direction in opposition to the thermal day to night pressure gradient. Enhanced joule heating during geomagnetic storms also result in pressure gradients that drive winds from high to low latitudes. Thus the two-cell convection pattern winds occur at auroral latitudes, while those due to joule heating affect the global temperature, density and composition. The response to geomagnetic activity therefore involves global-scale structure and dynamics changes including waves and winds propagating from high to low latitudes[1].

Figure 3 schematically describes the longitudinally averaged meridional circulation as a function of low, average and high geomagnetic conditions for equinox and solstice conditions. It demonstrates that the thermosphere is a dynamically active region with basic latitudinal structure controlled by the relative heating at low latitudes due to EUV and at high latitudes due to auroral processes. An example of thermospheric structure showing the difference between the quiet and disturbed conditions is given in Figure 4. Temperature and winds at 200 km altitude derived from a general circulation model simulation[2] are shown for northern hemisphere equinox conditions. For low geomagnetic conditions (Kp=1) the temperature maximizes in the early afternoon. Winds are small except at polar latitudes where they reach 300 m/sec. For the high geomagnetic case (Kp=6+) temperatures have increased globally, not just at high latitudes, and the maximum temperature now occurs at high latitudes. The temperature maximum, over Alaska, corresponds to a density enhancement of 65%. Winds are significantly enhanced, reaching 900 m/sec in the polar cap. The high latitude exhibits detailed structure rather than a continuous band of heated atmosphere.

Thermospheric wave sources include tides, gravity waves and planetary waves. Tides, or local time density variations, occur at periods

of one day or its subharmonics. The relative amplitudes of the diurnal and semi-diurnal tides are altitude dependent, with diurnal tides dominating at high altitudes and semi-diurnal components dominating at lower altitudes (typically below about 180 km). Detailed representation of the "tides' is complicated because they interact with other dynamical motions including gravity waves and the mean flow. As a result the tidal phases and amplitudes can vary unpredictably from day to day. Gravity waves have periods different from those of tidal waves and are not directly related to the earth-sun-moon geometry. These may be generated either locally in the thermosphere or at lower altitudes. Upward propagating gravity waves can be generated in the troposphere by processes including topography and storm fronts. These waves mainly affect the mesosphere and lower thermosphere. These waves are unpredictable and are not represented in empirical models. They typically have periods of minutes to hours and amplitudes of a few to several percent. Much larger amplitude gravity waves (up to 50 - 100%) are associated with large geomagnetic storms. At thermospheric altitudes wave generation is primarily due to auroral processes. Planetary waves are oscillations with a period greater than one day are associated with large-scale planetary waves whose primary restoring mechanism is due to the Coriolis force. While radar wind measurements have shown the existence of these waves at altitudes below 100 km, their effects on the thermosphere have only recently been inferred. Density variations withannual and sub-annual periodicities are also a regular feature of the upper atmosphere. The "semi-annual" variation is generally characterized in current models by maxima near equinox and minima near solstice. Experimental data show that the phase and amplitude are not constant from year to year. There is presently no accepted mechanism explaining the semi-annual variation, although explanations involving EUV, high latitude heating and upward propagating gravity waves have been advanced. Longitudinal variations are also a feature of the neutral atmosphere. Satellite composition measurements have shown that density maxima occur for heavy constituents at the longitude of the north and south magnetic poles. The behavior of the lighter constituents is negatively correlated. This behavior is related to plasma density and motion influenced by earth's magnetic field. Ion-neutral coupling is therefore involved in determining the longitudinal distribution of the neutral density.

Qualitatively, uncertainties in thermospheric processes and environmental parameters lead to uncertainties in satellite drag. Long-term satellite drag predictions are mainly due to inability to forecast the solar cycle. Geomagnetic storms can cause major errors in short-term drag predictions; others contributing sources are short-term EUV variations and dynamics.

Thermospheric Models

Overview

A graphical summary of the evolution of neutral atmospheric models is shown in Figure 5 (adapted from Hedin[3]). Empirical models are generally based on satellite tracking data or on direct measurements of thermospheric composition and temperature. An excellent overview of many of these empirical thermospheric models has been prepared by the AIAA[4]. General circulation models, described later in this paper, are also shown ion the chart. The known thermospheric density variations at satellite altitudes represented in all recent empirical models are: (1) solar flux (solar cycle and daily component), (2) geomagnetic activity, (3) local time, (4) day of year, (5) latitude, (6) longitude and (7) waves. Empirical models represent the solar electromagnetic and auroral heating inputs by proxy indices $F_{10.7}$ and Kp respectively. $F_{10.7}$ radiation is generated in the sun's atmosphere by different mechanisms than those that generate EUV. Thus, $F_{10.7}$, which is not absorbed in the earth's atmosphere is a readily available but approximate indicator of solar activity. indicator of solar activity. Geomagnetic indices Kp and ap used to represent global changes in geomagnetism are based on a network of mid-latitude magnetometer stations monitoring variations in Earth's magnetic field. Table 1 summarizes the approximate magnitude and time scale for density changes at various altitudes between

200 and 800 km generated using the MSISE-90 model for fixed values of local time = noon, day of year = 81, latitude = equator (except 60° north for the geomagnetic activity and longitude variations). Gravity and planetary waves are not included in these models. For lower thermospheric altitudes, below about 110 - 120 km, solar EUV flux and geomagnetic forcings are small and the major variations are due to tides, gravity waves, season and latitude.

Direct comparison, for low and high solar flux conditions, of typical models derived from drag and from in-situ data is shown in Figure 6. The ratio of the J70[5] to MSISE90[6], is shown as a function of altitude and latitude for fixed conditions of local time (noon), geomagnetic activity (ap=4) and day of year (equinox). J70 is used by AF Space Command and NASA MSFC in the GRAM model, MSISE-90 and the most recent of the MSIS series of models. J70 has a lower boundary of 90 km whereas MSISE-90 extends to the earth's surface. The global densities derived from these two models based on different techniques agree very well, being generally within 10 - 15%. The J70 model is used in a more computationally efficient manner with density look-up tables. Since it is based on composition measurements, the MSIS series of models are superior for applications requiring knowledge of atmospheric constituents.

Empirical Model Status

Significant advances in understanding the morphology of drag variations have not resulted in commensurate quantitative improvements in satellite drag modeling. Figure 7 provides a comprehensive assessment of the capability of several empirical models to specify density[7]. The study used Satellite Electrostatic Triaxial Accelerometer (SETA) density measurements obtained below 250 km altitude during the period 1974-1984. This figure shows the typical 15% error (increasing with altitude due mainly to a lack of data for model development there). At altitudesabove 400 km, the errors tend to be 25% or greater while at lower thermospheric altitudes, near 100 km, models errors deduced from limited data sets also show standard deviations of 15-20%[6].

The general trend of standard deviations (expressed as one-sigma errors) with geomagnetic activity and latitude, obtained from SETA-1 and -2 satellite accelerometer drag measurements near 200 km altitude, is shown in Figures 8a (for SETA-1, March-April 1979, maximum Kp of 7-) and 8b (for SETA-2, July 1982, maximum Kp of 9). The MSISE90 model is used for these analyses, although J70 was found to give similar results. Data are in latitude, local time and Kp bins. Since the SETA data are from sun-synchronous satellites there are no local time variations in a specific bin. Further, the data in each latitude bin are for essentially the same altitude. As a result the errors are generally less than the 15% shown in Fig 7. At low latitudes the standard deviation is 5-6%, while for the low-latitude inclination AE-E a 12-13% standard deviation was derived. Since the majordifference between the SETA and AE-E data are in altitude, season and local time coverage, these errors appear to contribute about 6-7% to the standard deviation. Conversely, the SETA low latitude errors are attributed mainly to intrinsic variations, including waves and possible ion-neutral interactions, and possibly EUV fluctuations. Model accuracy deteriorates rapidly with latitude above 50 degrees and with increasing geomagnetic activity. The high latitude errors maximize near the geomagnetic pole, demonstrating increased gravity wave activity due to geomagnetic storms. Analysis of SETA data-to-model errors in latitude-longitude bins showed a tendency for higher errors on the nightside near the geomagnetic pole, consistent with an auroral source for gravity waves and greater wave propagation on the nightside due to reduced ion drag.

Ratios of mean values of data-to-model vs latitude and Kp shown in Figures 8c and 8d to demonstrate that there may be systematic unmodeled variations to be revealed by new measurements. Both data sets show maxima at low latitudes on the dayside and nightside and at dayside auroral latitudes.

From Eq. 1, a wind directed along the satel-

lite velocity vector, changes the drag by about 5% per 200 m/sec[2]. During large geomagnetic storms the maximum wind value can exceed 1 km/sec, (REF 1,2) equivalent to about a ±25% density change depending on whether the wind is in the same or opposite direction as the satellite velocity vector. Wind effects may tend to largely average out when their effect is integrated over a satellite orbit. However, there will be some orbital configurations for which winds are significant, particularly during storms, e.g. a high inclination satellite in an elliptical orbit. An important consideration for spacecraft design is the maximum cross-track winds to be encountered in orbit. Cross-track winds of 300-600 m/sec were measured at high latitudes over a 21 day period of low to moderately high geomagnetic activity[8]. Winds of 1.4 km/sec were inferred[9] from spacecraft attitude control thrusters during extreme geomagnetic activity (Kp = 9) Neutral wind fields are generated self-consistently in the first-principles models. Empirical global wind models have also been developed using similar techniques as developed for MSIS. The HWM90[10] (Horizontal Wind Model) applicability extends down to 100 km. The empirical neutral density and wind models are separate and are not self-consistent. Both approaches need to be fully validated to determine their relative applicability to reducing existing satellite drag errors. An analysis of SETA cross-track winds over a 21 day period was compared to TIGCM and HWM wind predictions. Both models generally predicted variations of winds increasing with geomagnetic activity and showed latitudinal dependencies consistent with a two-cell convection pattern.[11]

Empirical Model Prospects

Part of the difficulty in reducing empirical model errors is that the primary variations in the thermosphere were already accounted for in the early Jacchia models. Recognized limitations of empirical models include (1) the use of proxy indicators $F_{10.7}$ and Kp to represent solar and geophysical influences on the atmosphere, (2) relatively coarse spatial resolution, (3) simplified physics, (4) lack of time-dependent waves and neutral winds and (5) limitations of accuracy and extent of the data base and on the extrapolation procedures to extend the model to data-sparse regions.

The widespread occurrence of wavelike features in the observed thermospheric density has implications for how well models of any description can predict atmospheric densities and satellite drag. Since overall model errors are about 15% for quiet conditions, and low latitude variations are of the order of 5 - 6% when local time, altitude and latitude are not varying, this study demonstrated that the stochastic nature of shorter scale gravity waves limit the ultimate accuracy that can be achieved but are not the limiting factor in the capability of models to fit or predict satellite drag. Since semi-empirical models are based on mean climatology, they could benefit from higher resolution; they cannot, however, be expected to predict time-dependent traveling waves. Further progress in empirical modeling is expected in areas where there are insufficient data and where more accurate measurements come available (10% errors in models will require at least measurements with only 10% errors).

General Circulation Modeling

The continued development of physical models leads to another prospect for improved accuracy for satellite drag specification and prediction. The governing (or "primitive") equations of the thermosphere are given by appropriate expressions for the conservation of mass, momentum, and energy for the gas as a whole, as well as for the individual species within the gas. The conservation equations are coupled and require appropriate boundary conditions and information on a number of transport parameters (such as coefficients of viscosity, thermal conduction, and eddy diffusion) for their solution. The transport parameters are obtained either experimentally or from gas kinetic theory considerations. This paper focuses on the three-dimensional, time dependent Thermosphere-Ionosphere General Circulation Model[12] (TIGCM). The TIGCM advantages respond to empirical model limitations and include (1) use of actual thermospheric forcing parameters rather than proxy indices (2)

higher spatial resolution (5°), (3) incorporation of dynamics, chemistry and energetics processes, based on first-principles, to deduce variability, rather than strictly empirical data, (4) time dependent wave propagation and self-consistent winds, and (5) extrapolation of data based on physics. Inputs are solar EUV and UV radiation, magnetospheric convection and auroral particle precipitation, and structure of upward propagating tides from the middle atmosphere. Parameterizations of various input fields are necessary for the specifications of the three-dimensional time-dependent physical processes described in these models. Outputs include composition, density (from composition data), winds, temperatures and ionospheric parameters.

The simulation capabilities demonstrated in Figure 9 showed temperature structures at high latitudes in response to geomagnetic heating. The existence of these features have been confirmed through analyses of satellite drag measurements and demonstrate the advantage of General Circulation Models to predict new phenomena. Direct use of solar EUV eliminates the need for the forecasting involved in determining a 90 day mean solar flux in empirical models. Recent refinements now take into account interactions between the neutral atmosphere/ionosphere coupled system and electrodynamics[13]. Current activity is focussed on lowering its boundary and incorporating upward propagating waves more realistically.

Due to the use of heating and cooling rates as well as other coefficients, the TIGCM does not always give more accurate absolute density values and simulations are normalized to MSIS mean values. Currently, the model derives the solar EUV inputs from a relation with $F_{10.7}$ and the auroral inputs are derived from a NOAA-TIROS activity index. Lower boundary tides are given by a model. Further, since the mechanism for the semi-annual variation remains undetermined, this variation is not included in the TIGCM. The present model upper boundary is near 500 km. Continued improvements will rely heavily on determining smaller scale and time-dependent structure and on obtaining improved three-dimensional time-dependent heating parameters.

VSH Model

The VSH[14] model is a semi-empirical approach based on numerous TIGCM simulations for a wide range of solar and geophysical conditions. It combines these outputs, in a parameterized form to run on a small computer. This parameterized technique was adopted to combine benefits of two approaches; empirical modeling to establish mean values of the upper atmosphere and physical modeling to determine the local variations about the mean value. Spectral coefficient libraries are obtained by applying spectral fits to truncate the output fields from TIGCM runs, while maintaining 99% accuracy. Using these libraries, VSH performs the inverse operation of synthesizing the desired fields from the spectral coefficients. A preliminary comparison of an independent set of SETA-2 data to the MSIS 90 model and to the latest VSH version shows that VSH is generally a modest improvement over MSIS particularly at high latitudes and during geomagnetic storm conditions. This result is encouraging and more extensive validations are planned.

Drag Coefficient Determination

In deducing neutral density from drag measurements, whether using low-resolution orbital tracking techniques or high resolution satellite accelerometer data, the drag is proportional to the product of ambient density and spacecraft drag coefficient. Accurate measurements of C_D are essential for tying down absolute density values from satellite drag measurements. Uncertainties in drag coefficients for low altitude satellites have recently been reviewed by Herrero[15]. The drag coefficient is defined from Eq. (1):

$$C_D = 2\, a_D M/(A\rho V^2) \qquad (2)$$

Thus if it were possible to simultaneously measure satellite drag, neutral density and ambient winds, for a satellite with known area-to mass ratio, the drag coefficient could be derived directly. The Air Force ADS[16] (Atmo-spheric Density Specification) comple-

ment of experiments makes possible the direct measurement of drag coefficient. ADS sensors are an accelerometer and two mass spectrometers. The goal of the PL (Phillips Laboratory) ADMS (Absolute Density Mass Spectrometer) sensor is to measure the absolute density to 5%. The SETA accelerometer measures satellite drag to within 1%. In addition, the goal of the Aerospace Corporation CADS (Composition and Density Spectrometer) mass spectrometer is to measure in-track winds to 5%. Thus, in principle C_D can be measured with an error of slightly more than 5% for the spacecraft carrying this complement of sensors. ADS is scheduled for launch in early 1994 into a polar orbit with initial perigee and apogee of 175 km and 1500 km, respectively. Since the mass spectrometers also measure the neutral composition, variations of C_D with composition and altitude can be determined. With accurate attitude determination, the degree of accommodation can also be derived. This experiment complement could be flown on orbital experiments specifically designed to examine drag coefficients as a function of geometry or spacecraft materials.

New Programs Supporting Satellite Drag Capabilities

New measurements are expected throughout the middle and end of this decade, although budgetary constraints are already threatening or stretching out many programs. ADS is scheduled for launch in FY94 and will provide the most accurate density data set yet achieved. The Navy RAIDS (Remote Atmospheric and Ionospheric Detection) instrument objectives are to remotely measure ionospheric constituents and neutral density from 90-600 km. This is a new technique and the potential density accuracy is presently not established. Follow-on sensors (designated SSULI) are planned for operational use on the DMSP satellites. The Midcourse Sensors (MSX), designed to study earthlimb backgrounds, will also provide information on atmospheric dynamics in the lower thermosphere. The new NASA TIMED mission plans systematic measurements of the atmosphere from 60-180 km to understand the physical and chemical processes in the mesosphere-lower thermosphere region and to understand gravity waves, tides and planetary waves and large-scale circulation affecting this region. Studies of thisregion are augmented by the NSF ground-based CEDAR (Coupled Energetics and Dynamics of Atmospheric Regions) program and the PL high altitude lidar.

New phenomena may also be derived from historical and current tracking data. Systematic variations were found in the ballistic coefficients of four satellites studied[17] by AF Space Command during the rising portion of Solar Cycle 22. These data will be studied to determine existence of unmodeled systematic variations in the thermosphere. Analyses are planned to exploit tracking data to provide near real time densities for use in orbit determination. Also, tracking data from high altitude satellites are being examined[18] for the potential of developing additional data bases to improve the MSIS model in the 800-1000 km region.

The solar EUV, auroral particle and electric field inputs will also be addressed by proposed programs. Potential solar EUV programs are the PL ACES (Auto-Calibration EUV Spectrometer) experiment, the GOES/EUV instrument for future launch on a TIROS-NOAA satellite; and the TIMED solar EUV monitor. Auroral inputs can be much more quantitatively and qualitatively defined from the PL AURA (Atmospheric Ultraviolet Radiance Analyzer) remote sensing technique. A follow-on of AURA is planned for operational use on DMSP as the SSUSI instrument. DMSP also carries the SSIES instrument which permits in-situ measurements of electric fields. High-latitude ionospheric convection can be better specified with AMIE (Assimilative Mapping of Ionospheric Electrodynamics) techniques[19], an evolving approach that integrates measurements from radars, ground magnetometers and satellites to provide the best estimate of ionospheric convection patterns. Pl is also investigating a capability to derive IMF data from ground-based measurements of ionospheric convection patterns.

The implementation of a new generation of space weather models, is planned for the AF

Space Forecast Center. Individual physically based, not climatological, models will specify and forecast the solar wind, magnetosheath, magnetosphere, ionosphere and neutral atmosphere. The system is designed to provide high-accuracy predictions of the near-Earth space environment on the time scale of an hour or two and general warnings of geomagnetic disturbance on the time scale of a few days.

Figure 10 summarizes the tools utilizing realistic measurements of the atmosphere and its heating sources to lead to improved specification and forecasting of satellite drag. Based on forthcoming data sources and anticipated modeling achievements, there are promising prospects for eventually significantly reducing model errors.

Summary

The current limits to operational empirical models arise from use of proxy indicators for solar and geomagnetic variations, need for predicted values of solar flux, unmodeled systematic variations, unpredictable natural variability, variations with scale sizes less than model resolution and accuracy of thermospheric measurements. Since most of the major variations have already been incorporated, improvements are likely to come in increments rather than through breakthroughs. The TIGCM technique has evolved to the point where it is now achieving accuracies of empirical models. VSH was a first step in implementing a general circulation model operationally. In order to achieve the capabilities inherent in General Circulation Models, extensive monitoring of solar and magnetospheric heat sources and boundary conditions for upward propagating waves are essential. New data sources being planned from ground-based and spacecraft platforms will provide improved knowledge of the critical inputs needed for further validating, upgrading and implementing these models. The AF Space Forecast Center will have the capability to integrate these data. The extension and expansion of existing pro-grams provides a solid basis for progress lead-ing to a superior capability for satellite drag forecasting.

References

[1] R. G. Roble, The Thermosphere, *The Upper Atmosphere and Magnetosphere,* National Academy of Sciences, Washington, DC, 1977.

[2] R. E. Dickinson, E. C. Ridley and R. G. Roble, A three-dimensional general circulation model of the thermosphere, *J. Geophys. Res.*, Vol. 86, p. 1499.

[3] A. E. Hedin, "MSIS-86 Empirical model status and future directions", *Atmospheric density and aerodynamic drag models for Air Force operations,* GL-TR-90-0033 (II), F. Marcos, ed., 13 Feb, 1990.

[4] AIAA, Guide to Reference and Standard Atmosphere Models, ANSI/AIAA, G-003-1990, Washington, D.C, 1990.

[5] L. G. Jacchia, *Revised static models of the thermosphere and Exosphere with empirical temperature profiles*, SAO Special Report No. 313, 1970.

[6] A. E. Hedin, "Extension of the MSIS thermosphere model into the middle and lower atmosphere", *J. Geophys. Res.*, Vol. 96, 1991, p. 1159

[7] F. A. Marcos, "Accuracy of atmospheric drag models at low satellite altitudes", *Adv. Space Res.*, Vol 10, 1990, p. (3) 417.

[8] F. A. Marcos and J. M. Forbes, "Thermospheric winds from the satellite electrostatic triaxial accelerometer system", *J. Geophys. Res.*, Vol. 90, 1985, p. 6543.

[9] J. A. Pearson, *The Low-G accelerometer calibration orbital accelerometer experiment,* Aerospace Report No. TR-0074(4260-10)-1, Vol II, July 1973.

[10] A. E. Hedin, M. A. Biondi, R. G. Burnside, G. Hernandez, R. M. Johnson, T. L. Killeen, C. Mazaudier, J. W. Meriwether, J. E. Salah, R. J. Sica, R. W. Smith, N. W. Spencer, V. B. Wickwar and T. S. Virdi, "Revised global model of thermosphere winds using satellite and ground-based observations", *J. Geophys. Res.*, Vol 96, 1991, p. 7657.

[11] J. M. Forbes and R. G. Roble and F. A. Marcos, "Magnetic activity dependence of high-latitude thermospheric winds and densities below 200 km", *J. Geophys. Res.*, Vol. 98, 1993, p. 13,693.

[12] R. G. Roble, E. C. Ridley and A. D. Richmond, "A coupled thermosphere-iono-

sphere general circulation model", *Geophys. Res. Lett.*, Vol. 15, 1988, p. 1325.

[13] A. D. Richmond, E. C. Ridley and R. G. Roble, "A thermosphere/ionosphere general circulation model with coupled electrodynamics", *Geophys Res Lett.*, Vol. 19, 1992, p. 601.

[14] T. L. Killeen and R. G. Roble, *Development of a Vector Spherical Harmonic (VSH) model of the thermosphere,* GL-TR-90-0145, March, 1990.

[15] F.A. Herrero, The lateral surface drag coefficient of cylindrical spacecraft in a rarefied finite temperature atmosphere, AIAA Jnl, Vol 23, June, 1985, p. 862

[16] F. A. Marcos, C. R. Baker, J.N.Bass, T. L. Killeen and R. G. Roble, Satellite drag models: Current status and prospects, AAS93-621, Victoria, B. C., Canada,1993.

[17] D. E. Snow and J.J. F. Liu, "Atmospheric variations observed from orbit determination", AAS 91-492, 1991, Durango, CO.

[18] W.J. Cunningham, R.S. Nerem and A. E. Hedin, Improvement of the MSIS86 model using medium altitude satellite tracking data, *EOS Transactions A.G.U.*, 1993, p.102.

[19] A.D. Richmond and Y.A. Kamide, "Mapping electrodynamic features of the high-latitude ionosphere from localized observations: Technique", *J.Geophys. Res.*, Vol. 93, 1988, p. 5741.

Table 1. Thermospheric density variability as a function of altitude

	Δρ (%)				
Effect	150 km	200 km	400 km	800 km	Time Scale
1. Flux (Solar Cycle)	25	110	1165	3800	Years
2. Flux (Daily)	0	1	5	15	Day
3. Geomagnetic Activity	25	35	60	100	Hours
4. Local Time	10	25	115	230	Hours
5. Semi-Annual	15	15	50	80	Months
6. Latitude	10	15	60	90	Months
7. Longitude	2	2	5	15	Day

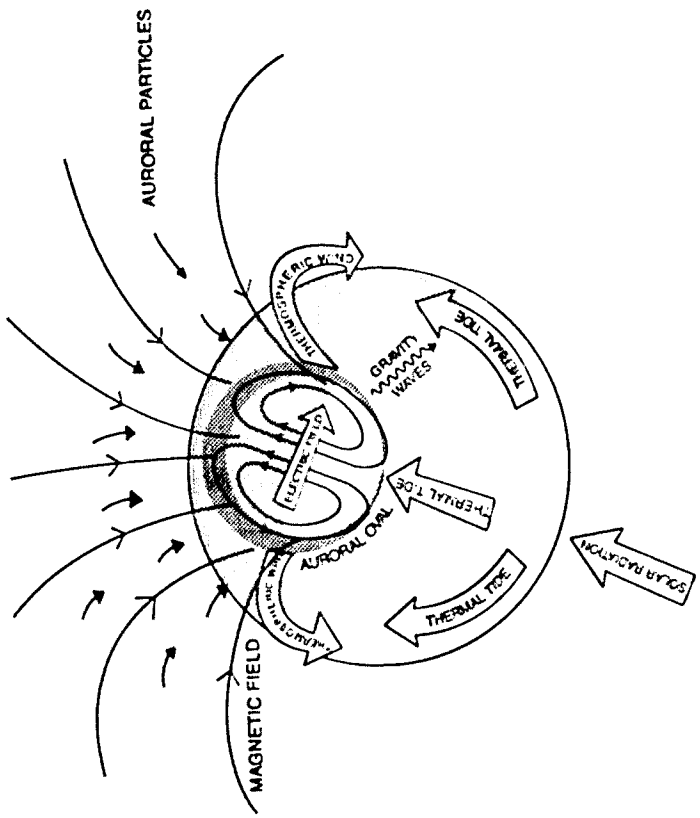

Figure 2. Schematic Representation of the Global View of Thermospheric Dynamics

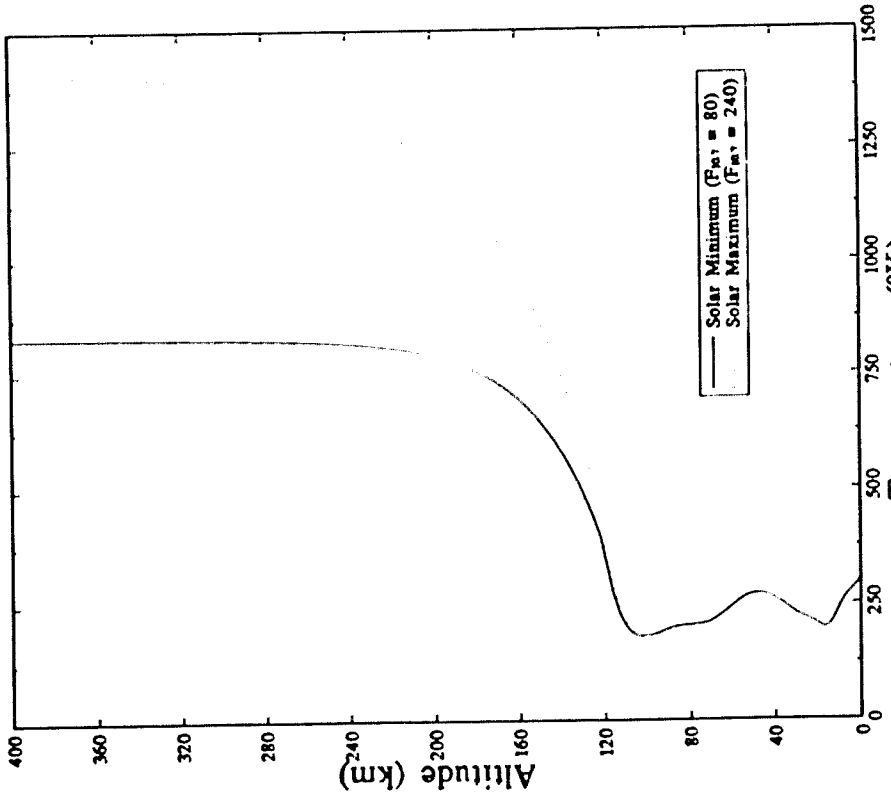

Figure 1. Variation of Temperature with Altitude in Earth's Atmosphere (Thermospheric temperatures are shown for solar miximum and minimum conditions.)

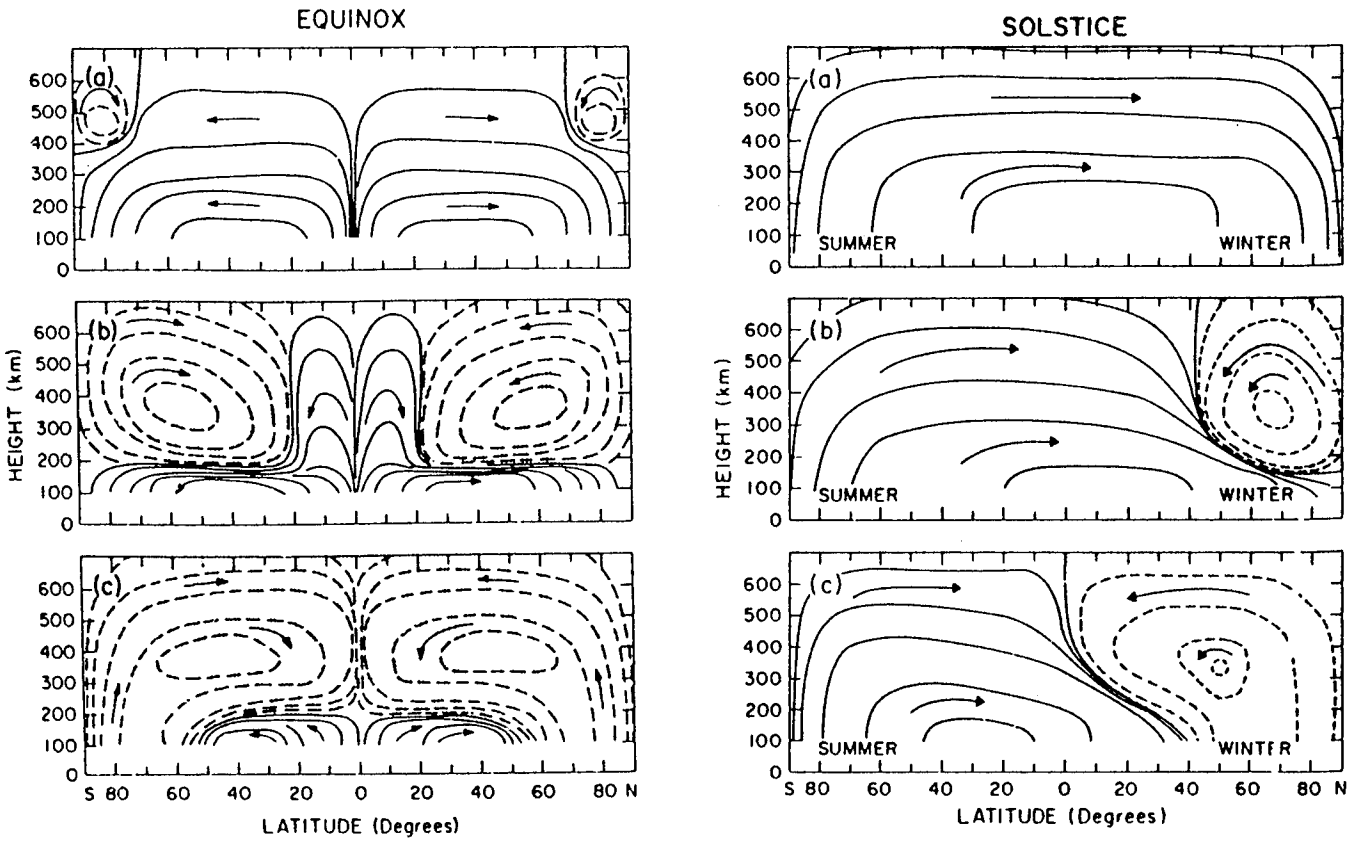

Figure 3. Schematic Representation of Thermospheric Circulation during Equinox (left) and Solstice (right) for (a) low, (b) moderate, and (c) high geomagnetic conditions

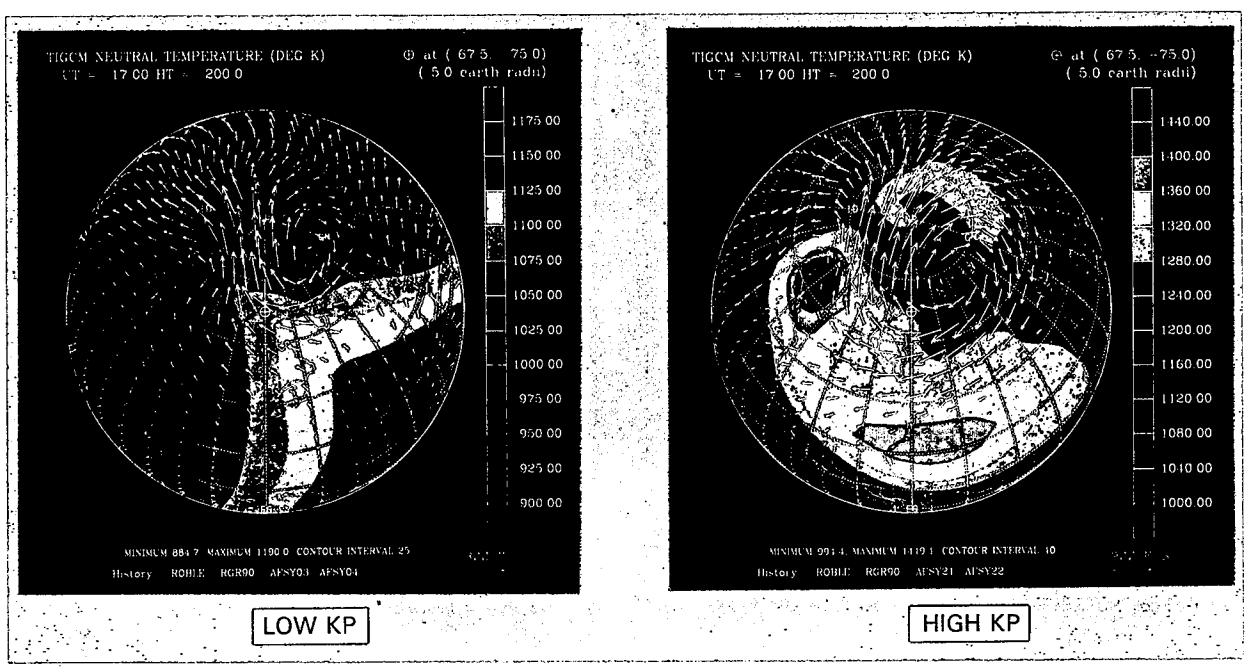

Figure 4. TIGCM Representation of Neutral Winds and Temperatures for Low (left) and High (right) Geomagnetic Conditions

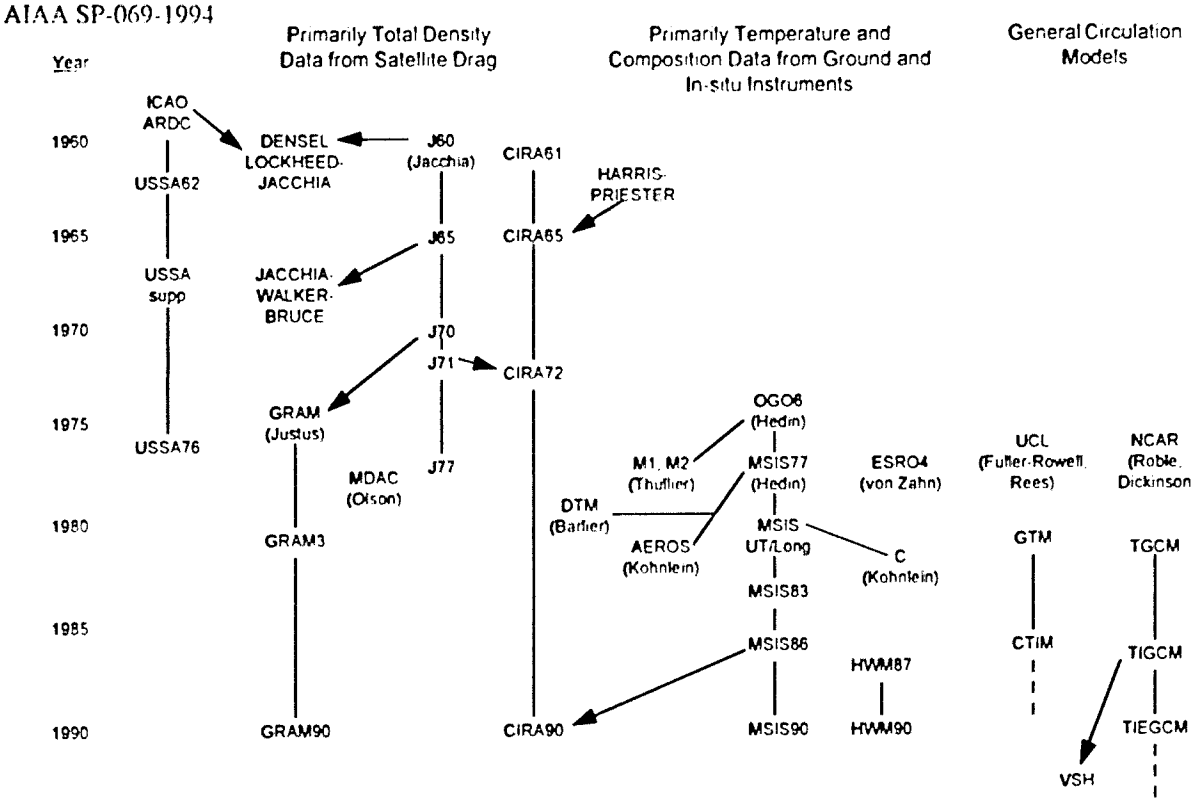

Figure 5. Historical Development of Thermospheric Models

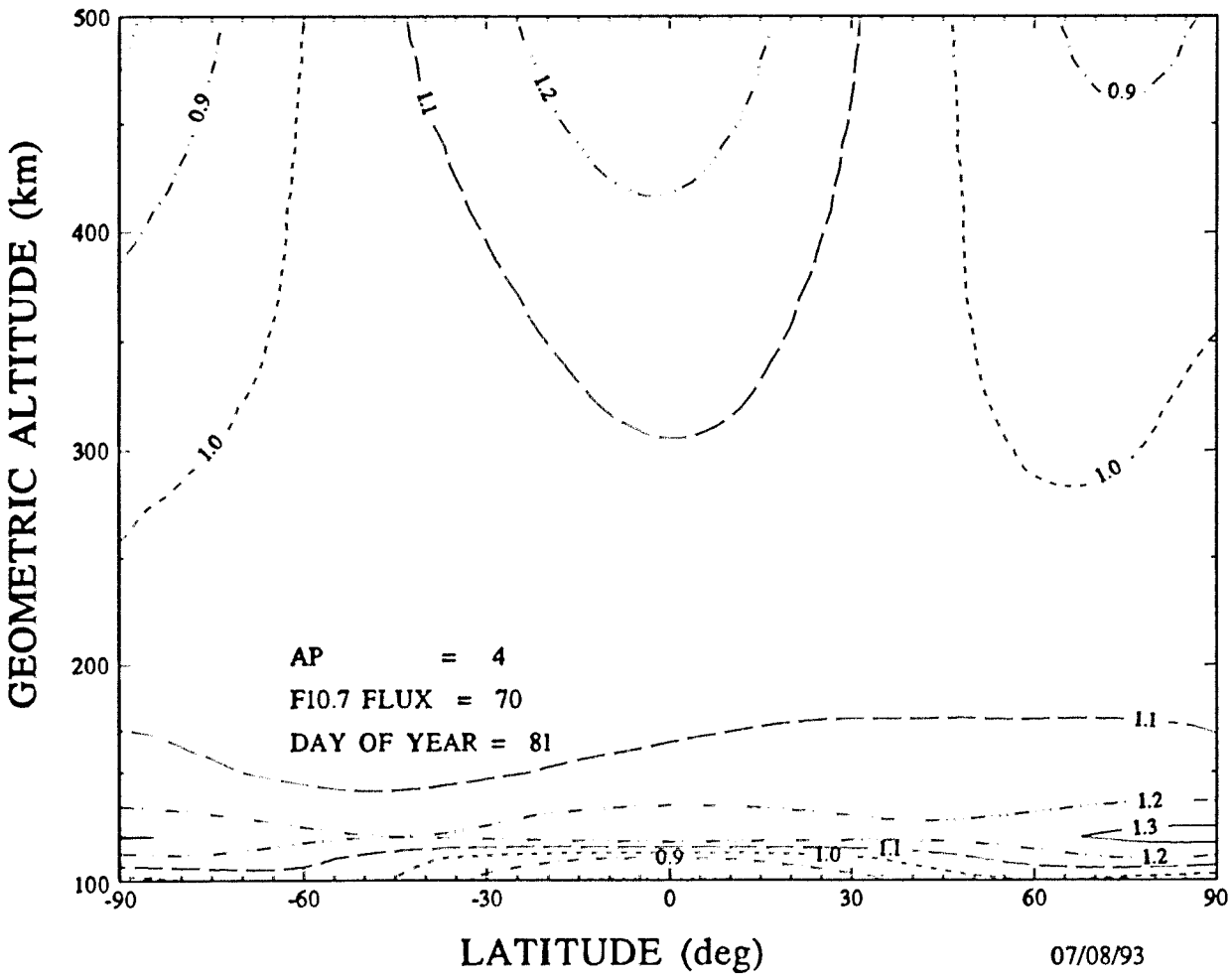

Figure 6. Ratio of Jacchia 1970 Model Densities to MSIS E90 Model Densities as a Function of Latitude and Altitude for Equinoctial, Low Geomagnetic Activity and Low and High Solar Flux Conditions

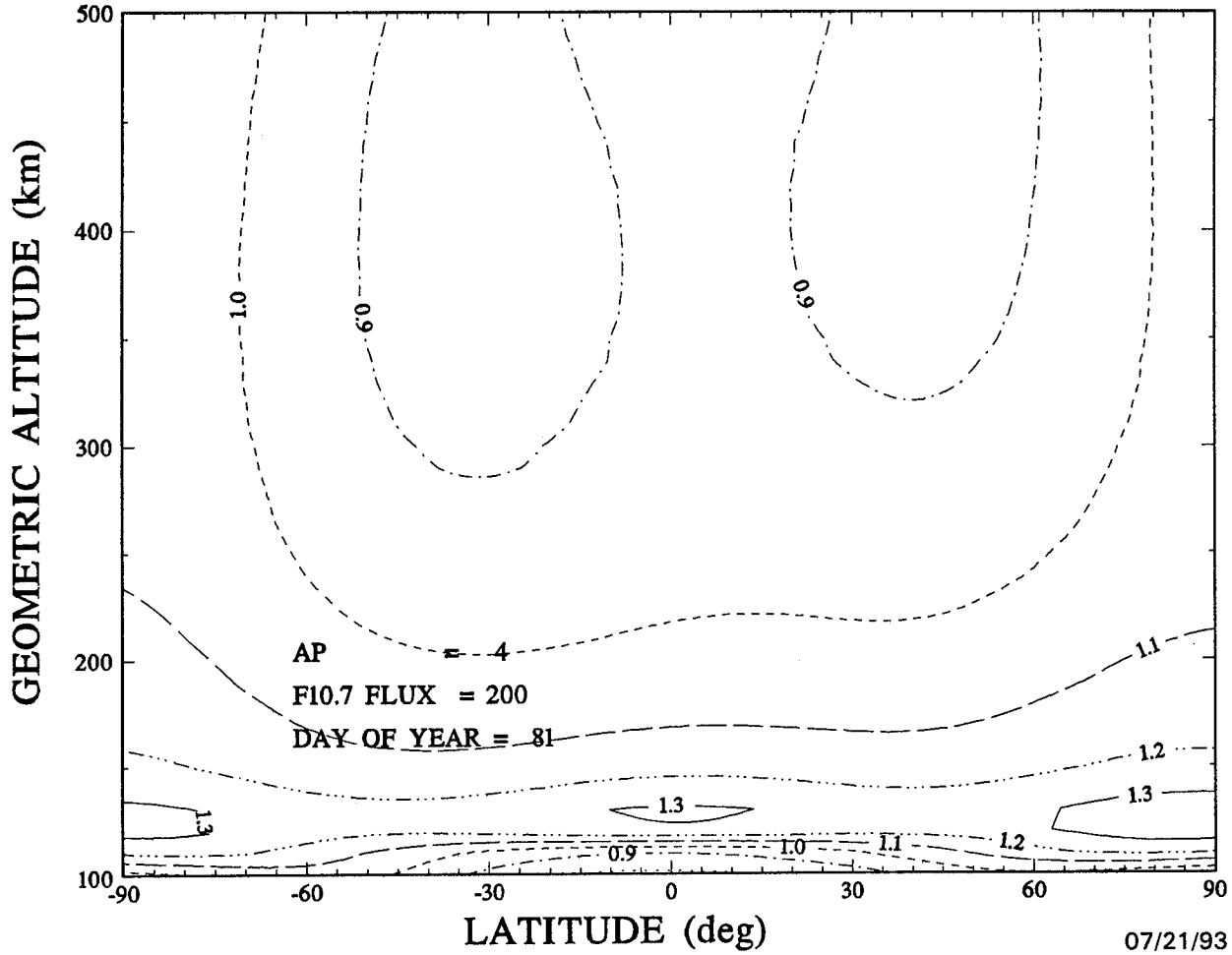

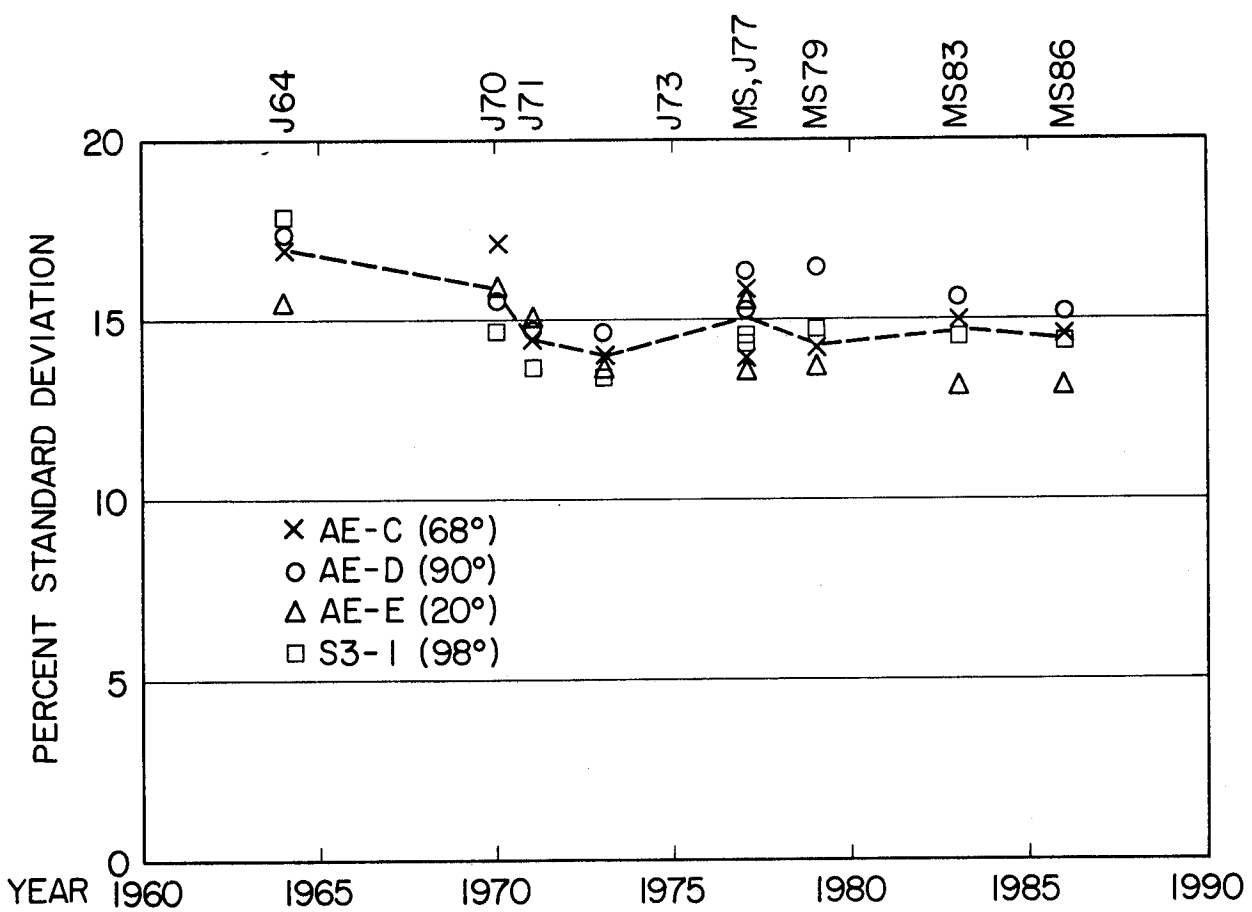

Figure 7. Statistical Evaluation of Empirical Thermospheric Neutral Density Models

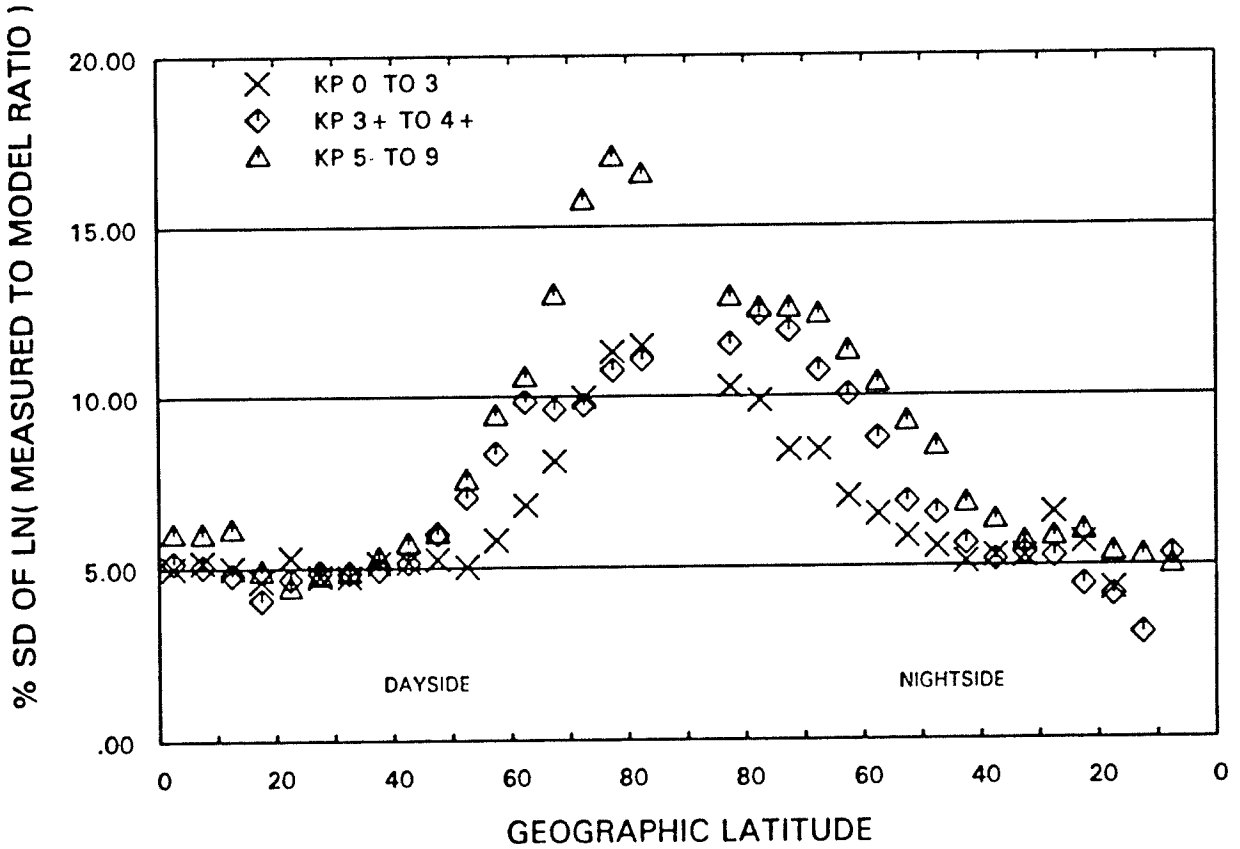
% SD OF LN(MEASURED TO MODEL RATIO)
20.00
15.00
10.00
5.00
.00
KP 0 TO 3
KP 3+ TO 4+
KP 5- TO 9
DAYSIDE
NIGHTSIDE
0
20
40
60
80
80
60
40
20
0
GEOGRAPHIC LATITUDE

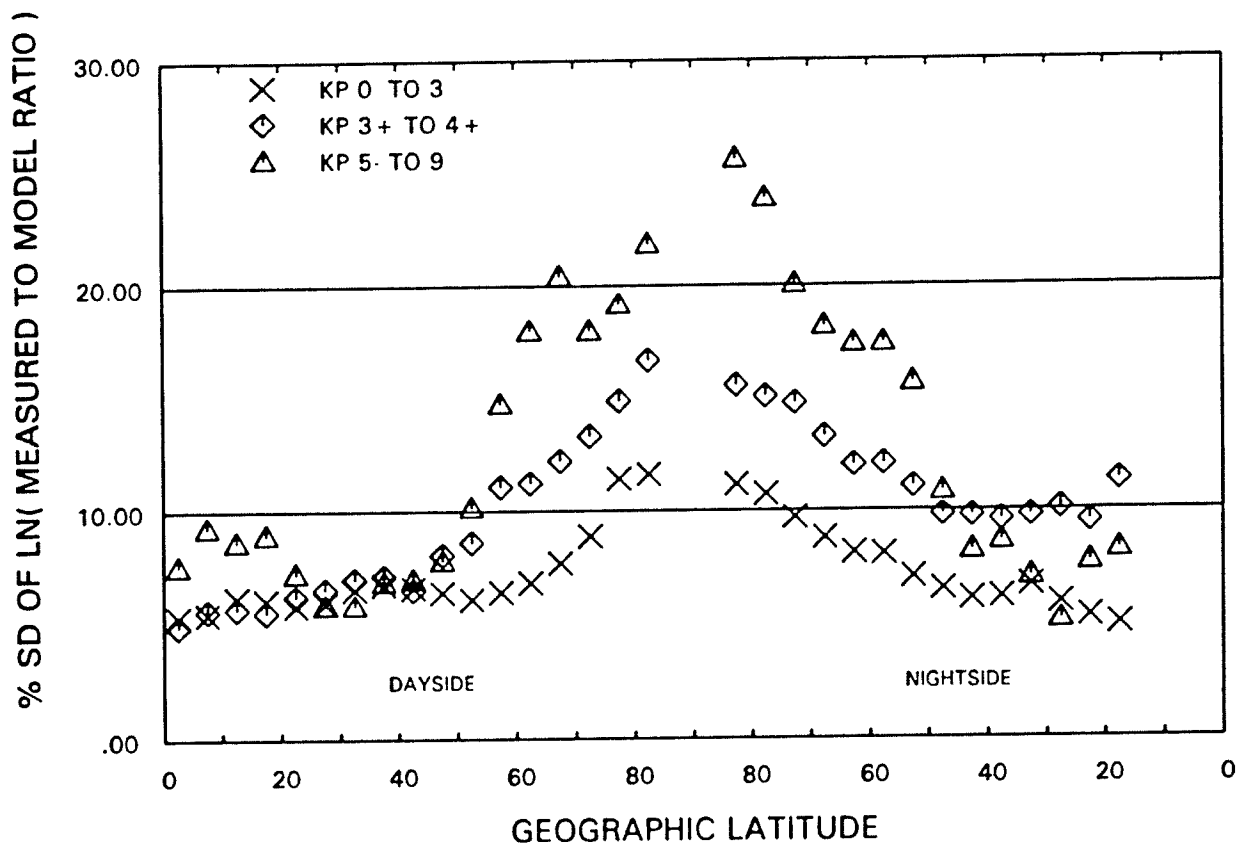
% SD OF LN(MEASURED TO MODEL RATIO)
30.00
20.00
10.00
.00
KP 0 TO 3
KP 3+ TO 4+
KP 5- TO 9
DAYSIDE
NIGHTSIDE
0
20
40
60
80
80
60
40
20
0
GEOGRAPHIC LATITUDE

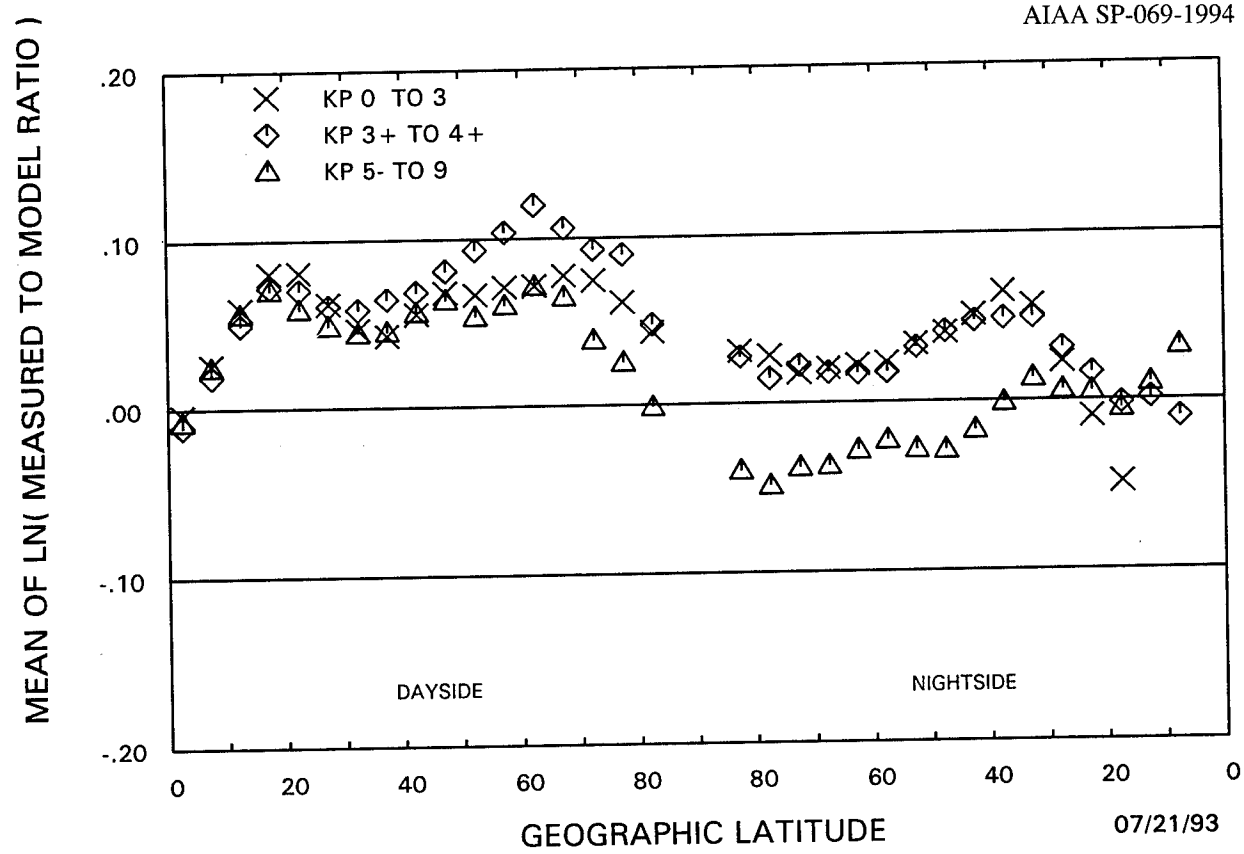

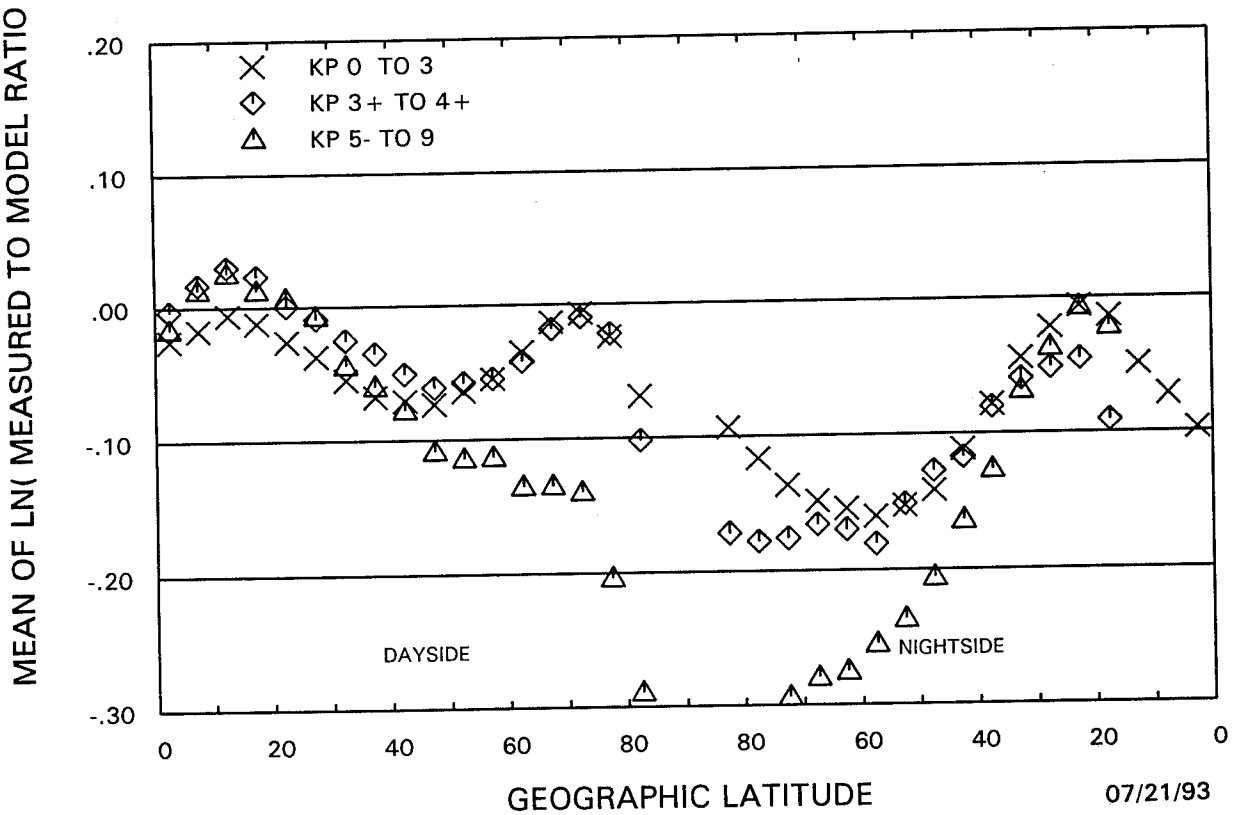

Fiogure 8. (a) and (b). Standard Deviations fo Ratios of (a) SETA-1 Mar-Apr 1979 and (b) SETA-2 Jul 1982 Density Data to MSISE90 Model vs Geographic Latitude;
(c) and (d). Mean Values of Ratios of SETA-1 and (d) SETA-2 Density Data to MSISE90 Model vs Geographic Latitude (in Kp and local time bins)

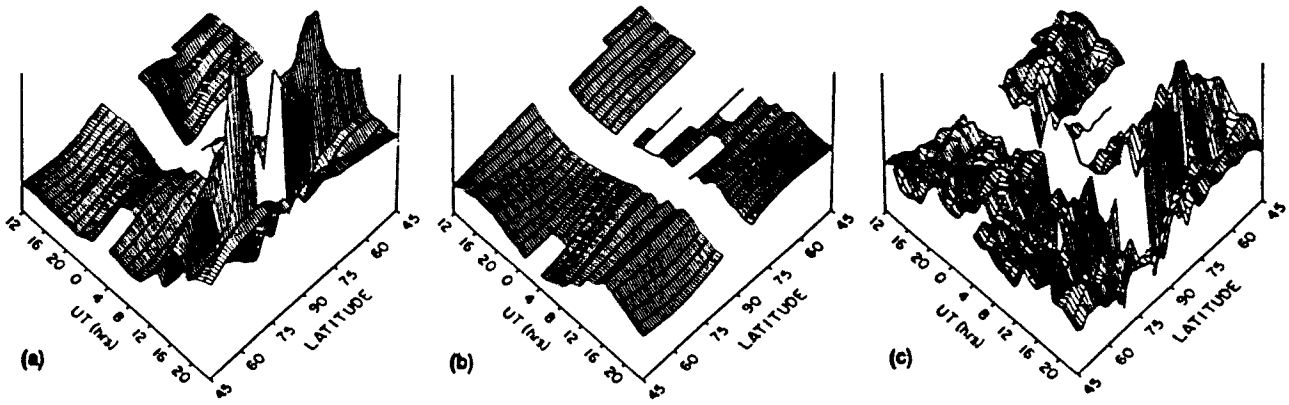

Figure 9. Three-dimensional Depictions of Density (normalized to 200 km) from (a) TGCM, (b) MSIS86, and (c) Satellite Accelerometer Measurements

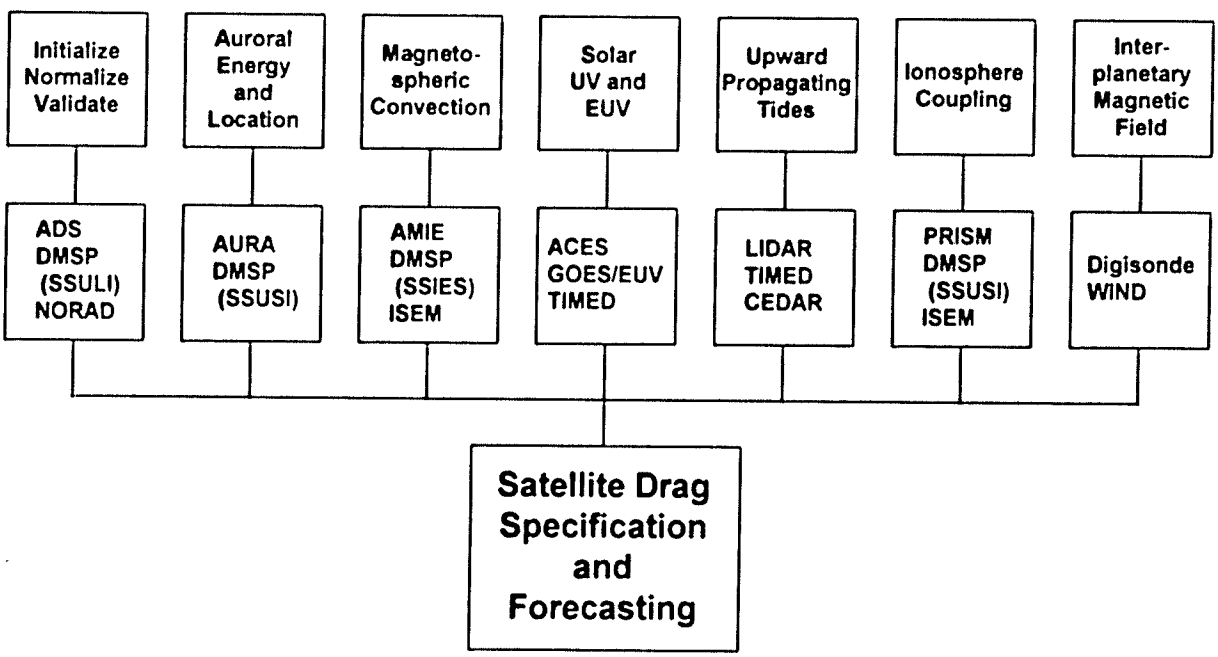

Figure 10. Forthcoming Programs that Support Improved Satellite Drag Capability

ORBITAL DEBRIS ENVIRONMENT: AN UPDATE

Phan D. Dao
Phillips Laboratory
Geophysics Directorate
Hanscom AFB, MA

Abstract

To properly assess the space environment and model the risk posed by collisions between space assets and man-made space debris, new sources of data have been planned and recently obtained. Critical measurements of the population to cm sizes are being made by the National Aeronautics and Space Administration (NASA) and the Department of Defense (DoD) in this area lacking in data. Two questions to be answered by these efforts are: what is the size of the debris population and how does it impact the operational and planned space programs. The number of small sized debris obviously needed quantification because it is expected to contribute the most to the total population of space objects in Earth orbits. The Air Force Phillips Laboratory (PL) is undertaking a concerted effort to assess the debris environment by optical measurement and modeling. Debris measurements with optical telescopes operated by the MIT / Lincoln Laboratory in Socorro, New Mexico, and the PL Laser and Imaging Directorate, in Maui, Hawaii and the NASA-sponsored debris Haystack radar have resulted in new data on observed detection rates, and measured or estimated eccentricity, semi-major axis and inclination distributions. In this paper, the problem of collisions is studied as a statistical assessment and hazard will be reported as a probability of collision or collision rate. Expectations of detection rate are computed for each debris observing session and compared with actual rates. Differences in rate are used to update the size of the population. From the updated number of objects and listing of their fundamental orbital parameters, one can compute spatial density and collision flux. A collision flux model is then used to compute the flux associated with a spacecraft in a 28 degree inclination and 500 km altitude orbit. Results will be compared with NASA reported values of flux for radar sensitive objects.

Introduction

The level of public awareness about space debris has steadily increased the last 10 years and particularly after the inclusion of a statement on space debris in the President's National Space Policy in 1988 which immediately prompted a series of initiatives and studies by various government agencies [1]. Department of Defense's (DoD) interest was expressed with the 1983 USAF Scientific Advisory Board study and again more pronounced after USAF anti-satellite test in 1985. There are currently over 6500 objects with radar cross section large enough to be tracked by the US Space Command space surveillance sensor network and about half of that could be classified as debris. The number of smaller objects not catalogable but still considered hazardous to orbiting assets could be much higher. While in the even smaller size regime below 0.5 mm, meteors dominate the collision flux (encounters per unit area per unit time) experienced by spacecraft, for objects larger than 1 mm, collision probability is dominated by orbital debris which are confined to a much smaller volume near earth. The need to define, monitor and mitigate the debris problem in this size regime has been recognized and related research work is being conducted and supported by NASA and DoD.

Up to 1990, there were insufficient data to bound the threat of collision with debris in near Earth environment with acceptable uncertainties. Due to aggressive measurement programs recently executed, there is now new data to update earlier assessments and models. The goal of this paper is to present a current assessment of the collision threat based on work done in the last 3 years (1990 - 1993) at the Phillips Laboratory (PL). It has been recognized that the Space Command catalog is a reliable source of information for

objects down to approximately 10 cm and constitutes the basis of this study. The catalog lists each object with its deterministic orbit allowing us to follow it deterministically and definitively identify it. It is assumed in this analysis that the population of catalog objects is a good representation of space objects in Earth orbits. The catalog however, is not inclusive enough to completely assess the debris flux to a smaller yet significant size limit. The current best estimate of its limiting size is about 10-20 cm. For smaller objects, augmentation of non-deterministic measurements can be used to estimate the collision flux. There are a number of measurements organized in the 1990-1993 window to study this small size range. NASA sponsored a series of radar campaigns (X and Ku bands) to measure debris flux down to 0.5 cm range and AF supported a measurement program based on optical sensors. There are fundamental differences between these two important measurement programs. The NASA radar measurement is a statistical survey of space to determine debris flux. In comparison, the optical sensors not only survey space but whenever possible track the detected object for a more exact orbit determination[2]. Additional orbital information is an important ingredient for the calculations of flux and could offer an alternative to the catalog representation. Both catalog and optical sensor orbital descriptions are used in the study and a comparison will be provided. Using commonly adopted relationships linking physical size to cross section, NASA-sponsored radar is currently pushing the measurement to sub-cm regime while PL-supported optical sensors are limited to approximately 5 cm. This report is about the analysis of optical data acquired by PL from the following sites: MIT Lincoln Laboratory's (MIT/LL) Experimental Test System (ETS) and the PL Air Force Maui Optical Site (AMOS) telescopes. Comparisons with radar results will also be presented.

Telescopes

Since the 1980's, MIT/LL has participated in optical measurement of space debris with the (ETS) telescopes in Socorro, New Mexico. In the effort funded by PL, both ETS 31 inch telescopes were used for debris observations. In 1990, a staring survey campaign was conducted at the request of PL. In this effort, the telescopes are aimed at a selected field near zenith. A total of 32 hours of dual telescope data was acquired in that period. In May 1991, MIT/LL began the current debris measurement program under the direction of PL and coordination of the AF Space Command. In addition to staring, telescopes were used for the first time to track detected objects to better characterize their orbital element sets. The search and track method has been used since February 1992. One telescope offers one- degree field of view and the other approximately two degrees. In the AMOS debris program the main and auxiliary GEODSS telescopes, located on Mt. Haleakala, Maui, are used for debris measurements. AMOS is also capable of IR imaging which in tandem with data in the visible allows their scientists to study debris albedo.

Observations for both sites are typically scheduled for the twilight periods when objects between above 300-400 km are illuminated by sunlight but observed against a dark sky. Each session lasts about one hour corresponding to solar depression angles from 12 degrees. to about 24 degrees. Most observations are done with the telescope parked near zenith but there are elevations reported away from zenith. Look angles and telescope motion are documented in *coverage* files which are prepared and submitted for analysis at PL/GP.

Detection Rate Calculations

For an ensemble of objects uniformly distributed in space and all traveling with a constant velocity, the detection rate could be estimated by the product of the detection cross section A, the object velocity v relative to the detection volume and the spatial density of objects n.

$$\text{Detection Rate} = A \cdot v \cdot n \qquad (1)$$

For an ensemble of objects of different altitudes and inclinations, the resulting

density is the sum Σn with the individual spatial density n computed as follows

$$n = \left(4\pi^2 r\sqrt{(r-a+ae)(a+ae-r)}\right)^{-1} \quad (2)$$

$$a - ae \le r \le a + ae \text{ and } i > \beta \quad (3)$$

where r is the geocenter distance, a the orbit's semi-major axis, i the inclination, and β the site's latitude. Outside the limits specified in Equation 3, density is zero as indicated in the expression of spatial density published by Kessler[3]. Object's inclination, i is used to determine whether the object is detectable from the location site. This corrects for the bias introduced by the site latitudes. There is however a second order residual bias in the averaging. It is conceivable that objects with inclination smaller than the site latitude could be observed if the telescope is allowed to point South. In most sessions, however, the telescopes have been parked near zenith. For the remaining sessions the number of south pointing sessions is probably balanced out by the north pointing sessions. This residual bias could be ignored in practice.

Previous studies of optical data did not take into consideration the ever changing performance of the detector. Detector sensitivity is a function of many factors related to atmospheric conditions, phase of the Moon, photometric background, and detector noise. We attempt to account for these effects by using the limiting magnitude recorded by the site. When possible, the limiting magnitude is reported continuously. Without continuously monitored information, the average limiting magnitude could also be used to estimate the detection rate. With the population increasing with decreasing limiting size, which in turn is determined by the limiting magnitude, the use of *best* or *average* value of limiting magnitude is not always justified. For that reason, correction based on limiting magnitude is most critical to remove any bias in the calculation of detection rate.

It is typical that the detection of low Earth orbit objects is more difficult than for nearly stationary objects such as stars. For objects at 500 km altitude, the limiting magnitude is typically 2.1 magnitudes lower than the stationary limit (requiring higher brightness). This limitation will of course be relaxed for objects at higher altitudes moving slower with the overall magnitude correction composed of the reported stationary magnitude and the motion degradation which is 2.1-1.25 (log (500 km/h)), where h is altitude. The dependence of the limiting size on altitude manifests itself twice: first as the ρ^{-2} (where ρ is range) dependence and again in the motion dependence.

During the session, typically 45-60 minutes long, the Earth's shadow varies in height and the contribution of each altitude bin to the session obviously depends on the sun zenith angle during the session. In practice, objects in low altitudes spend less time in the sun than those at higher orbits. If uncorrected, this situation would result in overestimating detection rate. If the observed population is proportional to the ratio of observed to estimated detection rate, that would also lead to underestimating debris population. For each session, the coverage of each of the ten altitude bins is computed based on the amount of time the bin spends in the illumination range. For a high altitude bin, the coverage could be as high as 1 because it stays illuminated during most of the session. Again, for these calculations, the average telescope direction near zenith is used. This approximation is justified for the range of solar depression angles in question and the purpose of obtaining an average coverage factor for each altitude.

As discussed above, the initial population is assumed to be the Space Command catalog (Sept. 1991) population. The list of semi-major axis and inclination for the 6687 objects is used to compute the debris flux through the detection volume. This choice only implies that the measured population is similar to the catalog in terms of inclination and altitude distributions. The ratio of observed rate to estimated rate (O/E) will eventually determine the observed population size. For comparison, the inclination and altitude distributions of debris tracked and

provided to us by ETS are also used to estimate detection rates. Estimates of the measured population based on this initial population will also be presented.

As implied by (1), not only does the detection rate depend on the total spatial density, it also depends on the motion of the debris swarm through the detection volume. Note that this is not the only place motion affects the detection rate. As previously pointed out, it also affects the detectable spatial density through the sensor limiting size. To compute the motion of the swarm relative to the telescope, reported slew rates of the telescope and individual orbit inclinations are reported by the sites in the *coverage* files. Almost all sessions are collected with the field of view fixed at a location near zenith where there are photometrically calibrated stars. The motion of each potential object of the debris swarm in the field of view could easily be calculated for this simple case by assuming near zenith detections.

For optical sensors, it is a fairly good approximation that detection sensitivity is fairly efficient in the field of view, except for the outer edges. Therefore, the detection volume is the conic volume defined by its field of view (FOV). FOV is chosen as the geometric mean of the angular distances subtended by the imager. Most objects would traverse the volume in the direction of the local tangent and the cross section for an incremental altitude bin dρ would be

$$dA = FOV \cdot \rho \cdot d\rho \qquad (4)$$

It was agreed with the optical sites that for each report of coverage (constituting a line in the coverage file), telescope right ascension and declination are not allowed to change substantially. It is expected that telescope altitude could change during the time interval represented by the line but could be approximated by its value at median time. For that situation, one could compute the expected rate of detection without having to integrate over time. Therefore we only need to perform two summations: one for range and the other for inclination for each reported scan segment.

$$N = \sum dA\left(\sum v(\rho,i) f_i(i) n(h(\rho), d(\rho,v))\right)$$

Figure 1 shows the geometry of the detection volume. As shown, the rate results from the summation over the altitude/distance range and the inclination range. Spatial density as a function of size, altitude and inclination is used. Limiting size is allow ed to depend on motion. Relative motion is calculated based on inclination, altitude and telescope slew rate. For each session, the expected rate (E) is used to compute the O/E ratio. The campaign ratio is obtained by averaging the session ratios.

Results on Population and Collision Flux

Results are grouped in campaigns. Grouping results by campaign seems to make sense for the following reasons. For each site / campaign, the limiting magnitudes do not change substantially from its average value. Large fluctuations of limiting sizes could bias the averaged result because detection rates would be dominated by the most sensitive sessions. A total of 198 hours have been analyzed with this methodology. There is a total of 860 hours of optical data collected in the PL program. While there is some correlation between physical size and RCS or optical cross section, the correlation between RCS and optical cross section has a wide spread. It is therefore expected that there exists a large population of objects with large albedos but negligible RCS and vice versa. Except for the undefined overlap, the flux reported in this paper could be considered above and beyond the contribution of radar measurements. The 1990-91 ETS data campaign is consistent with a population 3.3 times larger than the catalog for optical objects with sizes larger than 5.3 cm. Population correction is equal to the O/E ratio. The size-adjusted population is then used to compute the collision flux for a 500 km altitude and 28 degree inclination orbit. The characteristics of the initial population are assumed to follow the eccentricity, semi-major axis, and inclination distributions of catalogued objects. As an alternative, the

optically observed distributions are also used to give an independent set of estimates. Analysis of the ETS June 1993 data campaign indicates quite a small population of optical objects with sizes larger than 7.6 cm. Since all 27 hours of data were taken in June, seasonal effects have not had a chance to average out the results. This might contribute to a relatively small O/E ratio and small population estimate. AMOS has provided 136 hours of data which have been analyzed. Since limiting magnitude is not monitored continuously during the observation sessions, the reported magnitudes are estimated by the operator for the entire session. Observed detection rates are consistent with a population of 4500 objects with diameters larger than 13 cm. Collision flux is computed for the adjusted populations for an orbit at 500 km and 28 degree inclination. The adjustment factor is simply the O/E ratio of the set of data. The flux curves are shown in Figure 2a and 2b. The solid triangles are the results of GP analysis and the hollow triangles are estimates based on correlation with the catalog provided by the sites. The flux curve for the 1991 catalog objects computed with the GP Flux model is also shown for reference. In Figure 2b, the data points are compared with radar results from the NASA Haystack Experiment. The Haystack curves at 500 km and Space Station heights are computed from a NASA debris model which is consistent with Haystack measurements. The empirical Engineering model published by NASA[4] is also shown for comparison. The optical data points indicate a power law dependence of the form

$$N(d>d_0) \alpha d_0^{-1.5}$$

in the range from 5 to 12 cm. This power law is consistent with the reported result by Henize et al.[5]. It has been suggested that this dependence is consistent with the mass distribution of explosions in the transition regime from small sizes dominated by high intensity explosions and large sizes dominated by low intensity explosions. Experimental data has suggested that high intensity explosions can be described by $N \sim d^{-2}$ and low intensity explosions by $N \sim d^{-1.5}$ [6]. Using the d^{-2} power dependence of N, the flux could be estimated to be 6×10^{-5} m^{-2} yr^{-1} for $d > 1$ cm and at the altitudes of maximum flux about 1000 km.

Conclusions

The results of this analysis is consistent with a moderate flux at all altitudes. With this flux, the probability of collision for a spacecraft* of cross section $45/\sigma 4$ and an operational lifetime $4/\tau 4$ is estimated as

$$P = 1 - \exp(-\text{Flux}\ \sigma\ \tau) \sim \text{Flux}\ \sigma\ \tau$$

and projected to be quite small for a cross section of 10 m^{-2} and operational life of 10 years, $P \sim 6 \times 10^{-3}$. In other words, the $d > 1$ cm collision lifetime of such vehicle is 1700 years, much longer than the realistic operational lifetime. For unmanned spacecraft, it is sufficient to design the satellite with collision probability much smaller than failure probability. For manned platforms, the situation is complicated by the public expectation of absolute safety and should involve arguments beyond the technical contents of this paper.

In the follow up effort, we will work on the uncertainties associated with these flux values. The remaining 500 hours of data will be processed. All data will incorporated to provide a unified flux curve. It has been suggested that the orbits of smaller objects have characteristics not resembling the catalogue and future efforts will be focused on assessing the impact on flux levels.

We wish to thank Capt. Al Reinhardt for pulling the Phillips Laboratory team together and supporting this effort. We are also grateful to John Lambert, John Africano, Eric Pearce, David Gibson and Paul Kervin for sharing their data with PL/GPIM. The technical contribution from Ron Siewert is also acknowledged. Fruitful discussions with Bill Borer on debris fragmentation relationships are appreciated. Lt. Scott Maethner's critical review of the manuscript is appreciated.

* 28 degree inclination and 1000 km altitude

References

[1] Interagency Group report on Orbital Debris for the National Security Council, February 1989.

[2] E. Pearce, M. Blythe, D. Gibson and P. Trujillo, *Recent Results of Reacquisitioning Debris Search, AIAA 93-0161*, 31st Aerospace Sciences Meeting, Reno, NV, Jan. 11-14, 1993.

[3] Kessler, D., Icarus 48, 39 (1981).

[4] NASA Technical Memorandum, No. TM 100 471.

[5] K. Henize, J. Stanley, C. O'Neill and B. Nowakowski, *Detection of Orbital Debris with GEODSS Telescopes*, SPIE Conference on Space Debris Detection and Mitigation, April 1993, Orlando.

[6] P. Dao and R. McNutt, *Space Debris Measurement and Modeling, AAS 91-371*, Astrodynamics Specialist Conference, August 1991, Durango, Colorado; D. McKnight, *Determination of Breakup Initial Conditions*, 29th Aerospace Sciences Meeting, January 1991, Reno, Nevada.

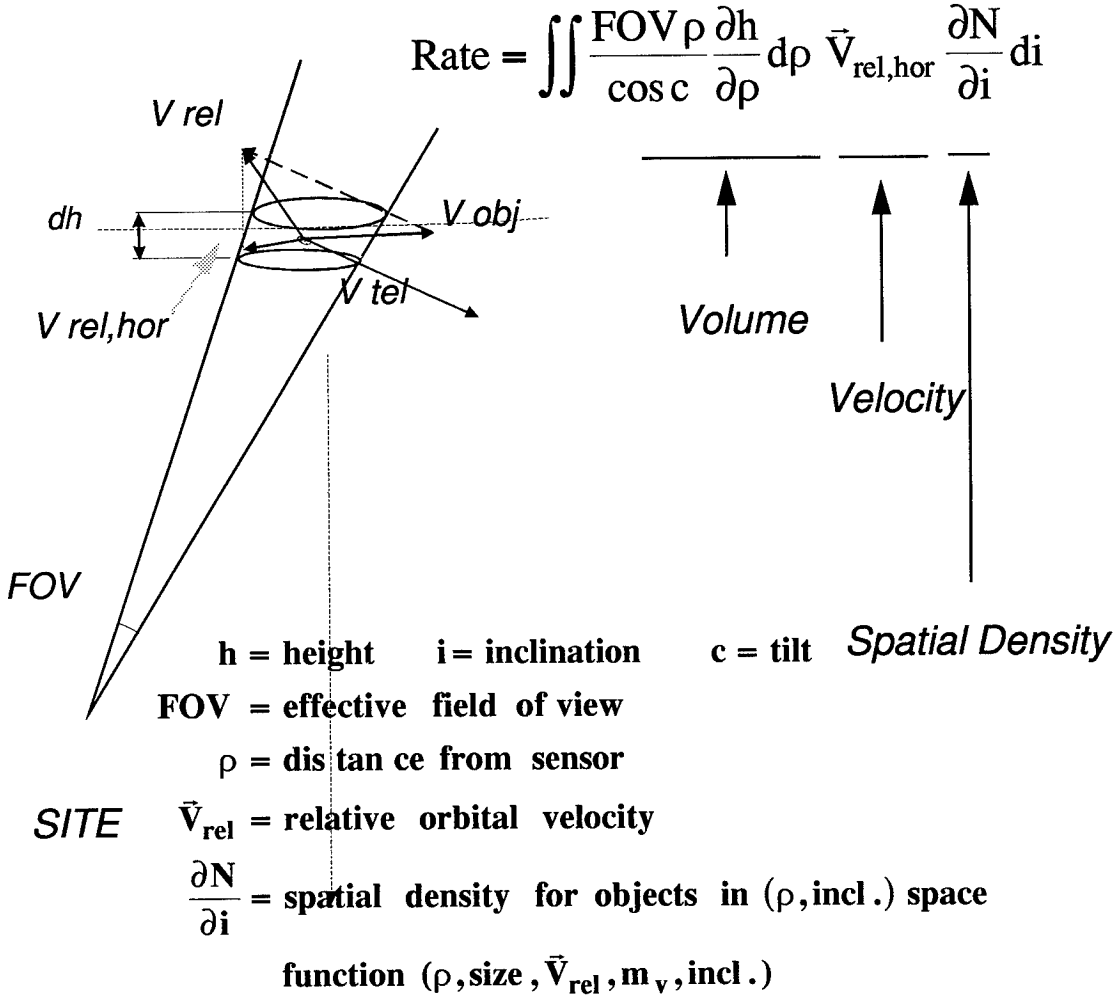

Figure 1. Geometry of Detection Volume

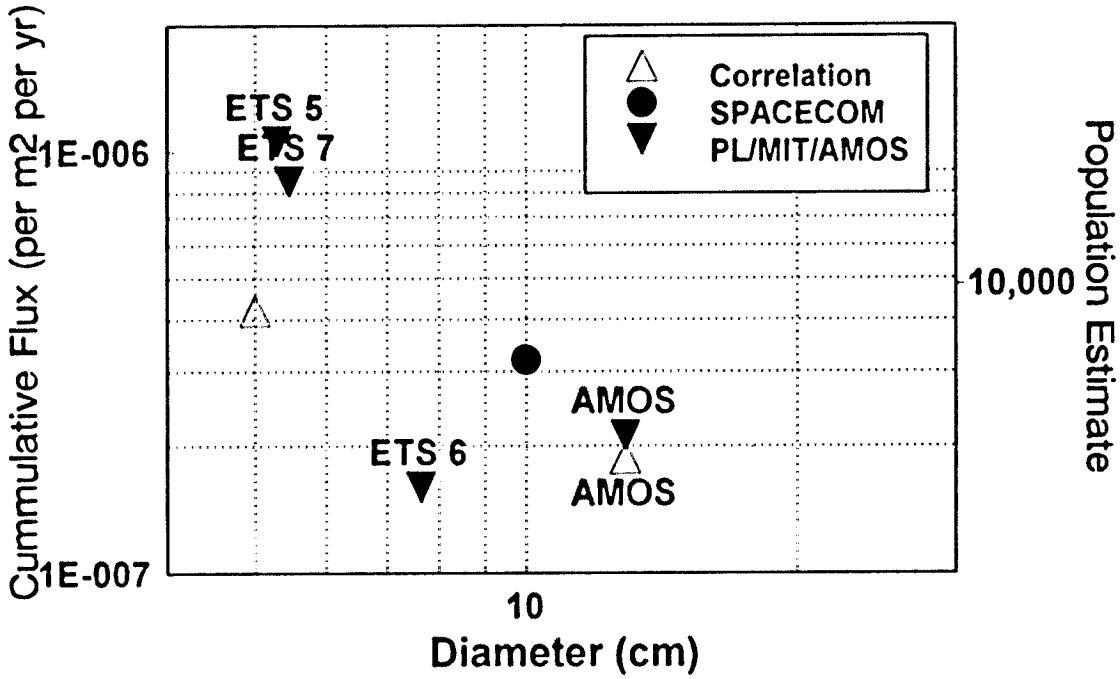

Figure 2a. Estimates of population and flux of optically detected objects (radar not included) Flux at 500 km and 28 degree inclination

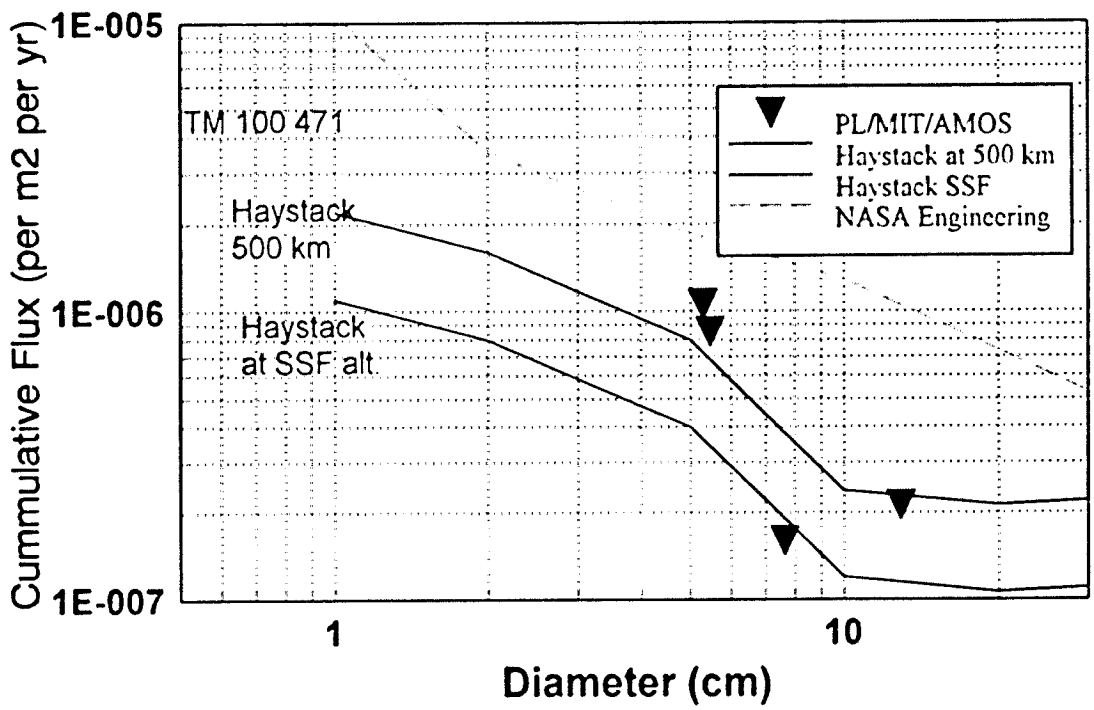

Figure 2b. Comparison of optically detected flux with radar detected flux (NASA Haystack result) The dashed line is shown for the NASA Engineering Model (TM 100471) prediction.

SPACE DEBRIS REENTRY RISK ANALYSIS

Stanley A. Bouslog
Lockheed Engineering & Sciences Company
Houston, Texas

Brian P. Ross and Christopher B. Madden
NASA Johnson Space Center
Houston, Texas

Abstract

A model to evaluate the survivability of space hardware reentering the Earth's atmosphere is described, and a method for evaluating the risk to Earth's population due to impact of surviving pieces is presented in this paper. The reentry survivability model has been verified with flight data. The model has been used to provide estimates of the mass of a material required to survive reentry and to evaluate the effect of object characteristics on reentry survivability. The reentry survivability of the SPARTAN spacecraft is evaluated and 6 to 9 major pieces are predicted to impact the Earth. The risk of injury or death associated with this event has been determined to be between 8.4×10^{-5} and 1.4×10^{-4}.

Nomenclature

A_{ref}	Object reference area
C_D	Drag coefficient
D	Drag force or diameter
E	Probability of human injury
f	Heating factor due to dynamic motion
g_0	Sea level acceleration of gravity
h	Altitude above sea level
h_s	Stagnation enthalpy
Kn	Knudsen number
L	Length
m	Object mass
q_{cw}	Cold wall average convective heating rate
q_{net}	Net heating rate to surface
q_{ox}	Heating rate due to material oxidation
q_{rr}	Radiative cooling rate
q_{st}	Stagnation point heating rate
r	Object radius
r_0	Radius of spherical Earth
R	Effective radius used in heating rate calculation
t	Material thickness
T_w	Wall temperature
V	Relative velocity of object
V_{circ}	Circular velocity at 122 km. altitude (7,803 m/s)
ε	Material Emissivity
σ	Stefan-Boltzmann constant
γ	Relative flight path angle
ρ	Atmospheric density
ρ_{sl}	Sea level atmospheric density
τ	Efficiency of heat transfer to wall due to oxidation
ω_e	Angular velocity of the Earth
χ	Longitude, measured in the orbital plane
φ_e	Inclination of orbital plane with respect to the Earth's equator
ΔH_{ox}	Heat of formation of the material oxide considered per unit mass of oxygen
$\dot{V}$	Time rate of change of relative velocity
$\dot{h}$	Time rate of change of altitude
$\dot{\gamma}$	Time rate of change of relative flight path angle
$\dot{\chi}$	Time rate of change of longitude

Introduction

The increasing commercialization and international use of space is resulting in an increase of debris in Earth orbit. The presence of debris from space hardware poses a risk to spacecraft due to an increasing chance of debris impact. This increase in risk will result in the need to incorporate debris impact protection into the spacecraft design and will therefore increase spacecraft cost. Space program costs will also increase due to the probable increase in spacecraft insurance premiums. Therefore,

the National Aeronautics and Space Administration (NASA) has initiated an effort to define policy that will limit the generation of debris in Earth orbit. Planned removal of non-functioning space structures from the Earth orbit environment may be required. One of the most desirable means of space hardware debris removal from Earth orbit is to rely on hardware disposal by atmospheric reentry. The thermal environment associated with Earth entry is severe enough to provide the means to force the breakup and demise of the hardware. However, portions of the spacecraft may survive entry and pose a risk to human life and property on the ground. Space hardware reentry survivability must be evaluated in order to assess this risk.

The analysis of reentry object survivability requires the integrated evaluation of the reentry aerodynamics, the aerothermodynamic environment, and the thermal response of the hardware during a simulated reentry trajectory. The analytical models must be simple enough to permit evaluation within a reasonable time span and yet the physics of the problem must be modeled sufficiently. Analytical procedures for evaluating the reentry survivability of spacecraft nuclear reactors were developed by Sandia Corporation[1] in the early 1960's as part of the Aerospace Nuclear Safety Program. Computer codes for evaluating NASA spacecraft and rocket upper stage reentry breakup and survivability, and the risk to human life, were developed by Lockheed Missiles & Space Company[2-8] in the late 1960's and early 1970's. The reentry breakup of spacecraft with radioisotope thermoelectric generators (RTG) have been evaluated by TRW[9, 10], Aerospace Corp.[11], and Jet Propulsion Laboratory.[12, 13] Aerospace Corp.[14] has also provided a review of the methods used to predict the hazard associated with space hardware that survives reentry and impacts the Earth.

Models are being developed at NASA Johnson Space Center to evaluate space hardware reentry breakup and survivability and to evaluate the risk to people on Earth due to impacting debris. These tools can be used to establish policies to limit the risks associated with planned removal of space hardware from Earth orbit by atmospheric reentry. This paper presents a description of the tool being developed to model reentry breakup and survivability, the results of an effort to validate the tool with flight data, the results of parametric studies to better understand the trends of object reentry survival, and describes the application of this tool to pieces of space hardware. The paper will also include a description of the methods used to evaluate the risk to people on Earth due to those pieces of debris that survive reentry.

Overview of Risk Analysis Process

The first step in the process to assess the risks associated with reentering space debris is to determine which pieces of debris survive reentry and impact Earth. As space structures encounter the atmosphere, they experience aerodynamic heating and pressure loads. For larger objects, the structural temperature may increase to the point of structural failure at which time the structure breaks into smaller components. Each of these smaller components must be analyzed to determine if they survive reentry heating. Once it is determined which components sur-vive reentry and impact the Earth, the probability of casualties due to this event may be determined using the size of the surviving ob-jects, the probable impact footprint, and information about the population density within the footprint. For space hardware that reenters from a naturally decaying orbit, the point of reentry is uncertain and the reentry debris could impact anywhere within a latitude band corresponding to the orbital inclination. If the reentry point is known, a more localized impact footprint can be determined using knowledge of the range of ballistic coefficients for the surviving components. For controlled or targeted reentries, the impact footprint can be positioned over unpopulated portions of the Earth; therefore, risk of casualties can be minimized.

Obviously, the determination of which pieces survive reentry is a very important step in the process of analyzing the risk of

space structure disposal by atmospheric reentry. The next sec-tion provides a description of a tool that can be used to evaluate reentry breakup and survivability of space structures during reentry.

Reentry Breakup and Survivability Analysis

Tool Overview and Assumptions

The Object Reentry Survival Analysis Tool (ORSAT) is a FORTRAN computer code that consists of several routines to determine the ballistic coefficient, average heating rates, and temperatures of an object at each time point in a simulated Earth reentry trajectory. The aero-dynamics, aerothermodynamics, and thermal model routines provide the object ballistic coefficient, heating rates, and temperatures, re-spectively. The routines are executed to deter-mine the temperature history of the object structure. If the space structure is a large com-plex one, such as most satellites, the object structural temperature can be monitored during a simulated reentry until it attains a preset value at which failure is expected. The breakup conditions can then be used to initialize the reentry of smaller components of the spacecraft. The melting and removal of material from the reentering objects are also modeled by ORSAT. The object structure is modeled by dividing it into layers (see Figure 1) and it is assumed that the outer layer is stripped away due to aero-dynamic shear once it has completely melted. Logic is provided to change the object mass and size due to ablation, i.e. material removal. At present, only solid and hollow spheres and cylinders can be modeled. To simplify the problem, the objects have been assumed to be rotating rapidly enough to use average values for the drag coefficient and the aerodynamic heating rates. This analytical procedure is based upon that developed by Cropp.[1] Figure 2 provides a flow chart of the tool.

Trajectory Simulation

The trajectory simulation routine computes a 3-degree-of-freedom (point mass) trajectory using equations derived in an Earth-fixed reference frame which are simplified for flight in a great circle plane.[15] There are four equations which are derived assuming a spherical, rotating Earth.

$$\dot{h} = V\sin\gamma$$

$$\dot{\chi} = \frac{V\cos(\gamma)}{r_0 + h}$$

$$\dot{V} = -\frac{D}{m} - g_0\left(\frac{r_0}{r_0+h}\right)^2\sin(\gamma) - r_0\omega_e{}^2\sin(\chi-\gamma) + \left(p_{ew}{}^2 + r_{ew}^2\right)\left[r_0\sin(\chi-\gamma) + (r_0+h)\sin(\gamma)\right] - \left(r_{ew}q_{ew}\right)\left[r_0\cos(\chi-\gamma) - (r_0+h)\cos(\gamma)\right]$$

$$\dot{\gamma} = \frac{V\cos\gamma}{r_0+h} - \frac{g_0}{V}\left(\frac{r_0}{r_0+h}\right)^2\cos\gamma + 2\omega_e\cos\varphi_e + \frac{r_0\omega_e{}^2}{V}\cos(\chi-\gamma) - \frac{\left(p_{ew}^2 + q_{ew}^2\right)}{V}\left[r_0\cos(\chi-\gamma) - (r_0+h)\cos(\gamma)\right] + \frac{q_{ew}r_{ew}}{V}\left[r_0\sin(\chi-\gamma) + (r_0+h)\sin(\gamma)\right]$$

where,

$$p_{ew} = \omega_e\cos(\varphi_e)$$
$$q_{ew} = \omega_e\sin(\varphi_e)\cos(\chi-\gamma)$$
$$r_{ew} = -\omega_e\sin(\varphi_e)\sin(\chi-\gamma)$$

The terms p_{ew}, q_{ew}, and r_{ew} are the components of the Earth's angular velocity expressed in the wind axis system. The simulation uses a 1976 Standard atmosphere model and a fourth order Runga-Kutta numerical integration routine.

Aerodynamics

The average drag coefficient of spheres and cylinders are computed for free molecular, transitional, and continuum flow regimes as a function of Knudsen number, Kn. Cropp[1] presents the drag coefficient as a function of Kn for a sphere and a cylinder in a cross-flow. For spinning cylinders that enter end-on, tumbling end-over-end, or random tumbling, Klett[16] has provided relations for

the continuum and free molecular drag coefficients as a function of the length to diameter ratio of the cylinder. In the transitional flow regime, Cropp[1] suggests that the average drag coefficient for tumbling cylinders be scaled to the variation of C_D with Knudsen number for a sphere. For the end-on cylinder, C_D is varied linearly with Knudsen number from the continuum to the free molecular value. The reference areas for the drag coefficients are based upon the projected areas - πr^2 for spheres and LD (length x diameter) for cylinders. Figure 3 provides a sample of the drag coefficients used by ORSAT.

Aerothermodynamics

The net heating to the reentering object is computed by the sum of the convective and chemical heating and the radiative cooling of the outer surface.

$$q_{net} = q_{cw} + q_{ox} - q_{rr}$$

Average cold-wall convective heating rates, q_{cw}, are computed based upon fractions of the stagnation point heating rates using the Detra, Kemp, and Riddell[17] relation for continuum flow

$$q_{st} = \frac{19,976}{\sqrt{R}}\left(\frac{\rho}{\rho_{sl}}\right)^{0.5}\left(\frac{V}{V_{circ}}\right)^{3.15} \text{(Watts/cm}^2\text{)}$$

and the following relation for free molecular heating.

$$q_{st} = \frac{0.9\rho V^3}{2}$$

A free molecular thermal accommodation coefficient of 0.9 has been assumed. These two relations are multiplied by factors, f, to provide the average heating to the body.

$$q_{cw} = f\, q_{st}$$

These factors are based upon assumed distributions of heating to spheres and cylinders and then integrated over the angular range of motion assumed. The factors, as presented by Cropp[1], for spinning spheres in continuum and free molecular flows are 0.275 and 0.25, respectively. Klett[16] has developed the factors for spinning cylinders that enter broadside, end-on, tumbling end-over-end, and tumbling randomly, and the relations for defining these factors have been incorporated into ORSAT. To model the transition regime between free molecular and continuum flow regimes, the variation of Stanton number versus Knudsen number for a sphere, as presented by Cropp[1], has been used.

The model for heating due to material oxidation presented by Cropp[1] has also been incorporated into ORSAT. This model assumes that the oxidation process is diffusion limited and that a fraction of the heat produced by the predominant reaction is absorbed by the wall. The amount of oxygen that has diffused to the wall and is available for the reaction has been related to the Stanton number. The final relation obtained by Cropp is

$$q_{ox} = \frac{0.215\, q_{cw} \Delta H_{ox} \tau}{h_s}$$

where t is the efficiency of the heat transfer to the wall due to oxidation. This value can be varied parametrically to evaluate the effects of material oxidation. ΔH_{ox} is the heat of formation of the material oxide considered per unit mass of oxygen.

The radiative cooling term, q_{rr}, accounts for the reradiation of heat away from the hot outer surface.

$$q_{rr} = \varepsilon \sigma T_w^4$$

where e is the material emissivity and s is the Stefan-Boltzmann constant (5.67×10^{-8} W/m^2-K^4).

Thermal Model

The aerothermodynamic heating during reentry will raise the temperature of the object, and if the imposed heating is of sufficient duration and magnitude, the object is likely to completely melt and be

destroyed, or demised. Since some materials have a low thermal conductivity and maintain a temperature gradient within the material, a thermal conduction analysis is required to determine the appropriate temperature re-sponse of the object.

The temperature response is determined by using a Forward Time Central Space (FTCS) finite difference solution for either a hollow or solid spherical or cylindrical object in one space dimension. The 1-D heat equation is solved in the appropriate spherical or cylindrical coordinate system. The boundary condition at the surface includes terms for the convective aerothermodynamic heating, the heat of oxidation, and re-radiation from the surface. On the inside of a hollow object the surface is treated as adiabatic. For the solid sphere and cylinder, the center response is estimated by using the approach by Özisik.[18]

As the temperature of the object rises, the outer layers will eventually reach the melting temperature of the material under consideration. At that point, the temperatures are fixed at the melting temperature and the net heat into each layer is tracked with time. Eventually, the net heat absorbed into the outer layer will meet or exceed the heat of fusion for the material and the layer is removed. The simulation proceeds as before except the boundary conditions are now applied to the new surface. This method assumes that the molten material is immediately removed from the surface of the object by aerodynamic shear forces. It is also assumed that the material does not produce gases which might affect the aerothermodynamic heating to the surface.

Tool Verification

The verification of a tool that is used to evaluate the reentry survivability of space hardware is best accomplished by comparison to flight data in which the reentry behavior of an object has been monitored. Sandia Corporation, in the 1960s, conducted flight tests to evaluate the reentry behavior of spacecraft nuclear reactors. Of special concern to the Aerospace Nuclear Safety Department was the reentry ablation of nuclear fuel rods. Therefore, a sub-orbital test was conducted in which fuel rod models were ejected from a reentry vehicle after being launched into a sub-orbital trajectory with a NASA Scout rocket.[19] The simulated fuel rods consisted of cylinders with walls of various thicknesses and an optical tracer material in the cylinder core. See Figure 4. During entry the fuel rods were tracked by optical instruments and the time at which the tracer material was observed was identified. These data provide an indication of the altitude at which the cylinder walls have ablated and the tracer material was exposed. Reference 20 provides a detailed description of the flight test and the optical data.

ORSAT was exercised for the simulated fuel rods and the predicted demise altitudes were compared to the test data. Each of the fuel rods was modeled as a tumbling hollow cylinder. The assumption that the cylinder was hollow results in an adiabatic wall condition which is appropriate since the rod walls were separated from the tracer material by insulation. Figure 5 presents a comparison of a fuel rod trajectory predicted by ORSAT and that determined from the flight data. The point at which the rod ablated and exposed the tracer is identified as the actual demise point. ORSAT predicts this to be a few seconds earlier than the actual event. This reasonably close agreement with flight data provides confidence that ORSAT models reentry survivability reasonably well.

Results of Parametric Studies

Two parametric studies have been conducted using ORSAT to evaluate the trends of object survival during Earth atmospheric entry from low Earth orbit. The first study modeled the reentry of solid spheres of four materials - stainless steel, aluminum, titanium, and beryllium. For each material, the size, and therefore the mass, of the sphere was varied until it was large enough to survive entry and impact the ground. This study considered a single relative entry

velocity of 7350 m/s and entry flight path angles ranging from -0.05 to -2.0 degrees. Results of this study are summarized in Figure 6 and two trends are apparent. First, shallow entries (small flight path angles) require a larger mass to survive entry due to the longer exposure time to entry heating. Figure 7 provides a comparison of the average heating rates to a steel sphere for flight path angles of -0.05 and -2.0 degrees. The second trend reveals that materials with a high heat of ablation, such as beryllium and titanium, require little solid-sphere mass to survive entry. These results are due to the difference in material properties such as density, melt temperature, specific heat capacity, and heat of fusion. Beryllium has the highest heat of ablation and therefore it has the lowest survivable mass. The low density results in a small entry ballistic coefficient and reduced peak heating rates. The high heat of fusion requires a much higher heat load to melt the material.

A second parametric study has been conducted in which the effect of ballistic coefficient on demise altitudes of hollow spheres has been evaluated. The spheres were assumed to be hollow shells in which the mass of the sphere could be changed by adding ballast inside the sphere. The spherical shell maintained a constant thermal mass to which heating would be applied. Each run of ORSAT determined the altitude at which the shell would be destroyed due to reentry heating. The results of this study are presented in Figure 8 and clearly show the trend that the demise altitude decreases as the ballistic coefficient decreases. These results are consistent with observations of reentry debris that has survived reentry, impacted Earth, and then was recovered.[14] Space structures with low ballistic coefficients are more likely to survive reentry.

Ground Impact Risk Analysis

The risk to the world's population from space debris reentering from a decaying orbit is evaluated by a method similar to one used by the Aerospace Corp..[14] The risk is a function of the size and number of surviving pieces, the inclination of the orbit, and the land area and population of the latitude band traversed by the orbit. The actual calculation computes the expected number of casualties using the equation

$$E = P\left[\frac{N}{A}\right]L$$

where

P = the probability of impact in the area of interest

A = area of interest, the land area in the latitude band

N = number of people in area of interest, population of latitude band

$$L = \sum_{\#Objects} \left(0.6 + \sqrt{A_{ref}}\right)^2 (m^2)$$

The area of interest here is the land area within the latitude band defined as ± the orbital inclination. Figure 9 presents a plot of the probability, P, of impacting land as a function of inclination angle. The debris area is the area on the surface of the Earth that is affected by the impacting object to the extent that if a person were inside this area, he/she would be injured or killed by it. This area is determined by taking the maximum cross-sectional area, A_{ref}, of an object and adding a 0.3 meter border around it. L is the summation of these areas for all of the impacting pieces. The equation for computing the risk, E, is based on two assumptions for a random reentry.

1. It is equally likely that the ascending node of the final orbital revolution will be anywhere on the equator.
2. It is equally likely that the start of the final plunge to earth will be anywhere along the final orbital revolution.

This computation of risk does not account for that part of the population which will be sheltered by buildings and other structures. In this respect, the equation is conservative in its risk prediction.

Population Model

To determine A and N, it is necessary to

know population and land area for countries as a function of latitude. The actual and projected total populations of each country, for the years 1950-2025, were obtained from the Population Division of the United Nations.[21] Total land areas for each country were obtained from The World Almanac.[22] The percentage of total land area within a latitude band was then calculated by hand using an equal area projection world map. This was done for each country at 5 de-gree band increments. The percentages for each band were then used to determine the population within each latitude band by assuming a uniform population distribution within each country.

Applications to Space Hardware

Orbital DEbris RAdar Calibration Spheres (ODERACS)

The Orbital DEbris RAdar Calibration Spheres (ODERACS) experiment is a joint effort of NASA/JSC, NASA/GSFC, N. Carolina State Univ., DoD, Phillips Labs, and the U.S. Air Force. The purpose of the experiment is to release spheres of known physical size and albedo into orbit in order to calibrate the ground-based radars and optical telescopes. This experiment will provide a means for end-to-end radar and optical calibration necessary for precision measurements of small orbital debris. Six spheres of three different types will be ejected into orbit on Space Shuttle flight STS-60.

The ORSAT code provided a simulation of the flight and eventual demise of the spheres in the Earth atmosphere. In Figure 10, the altitude and velocity histories of a 10 cm (4.0 inch) diameter stainless steel sphere are presented. The ORSAT code predicts the demise of this sphere at an altitude just below 60 km.

SPARTAN Spacecraft Reentry

The Shuttle Point Autonomous Research Tool for AstroNomy (SPARTAN) is an autonomous spacecraft (see Fig. 11) that provides data about solar winds and the sun's corona. After being released from the Space Shuttle Orbiter payload bay, SPARTAN free-flies during a data collection period, and then is retrieved by the Orbiter. Since it is possible that this spacecraft may not be retrieved, a reentry breakup and survivability analysis was conducted to determine which pieces of the spacecraft may survive reentry and impact the Earth. For the STS-63 SPARTAN mission, the spacecraft would reenter from a decaying orbit of 57° inclination, and the surviving pieces could impact anywhere within a ±57° latitude band.

The first step of the process to evaluate the risk associated with a spacecraft reentry is to determine the point in the reentry at which the spacecraft breaks into smaller components. The SPARTAN spacecraft was modeled as an equivalent hollow aluminum cylinder with a diameter of 0.762 m and a length of 3.3 m. The total weight of the spacecraft is 1289 kg. To determine the breakup point, the ORSAT code was run for the equivalent hollow cylinder entering the Earth's atmosphere broadside and spinning. When sufficient heat had been absorbed to completely melt the equivalent cylinder skin, it was assumed the spacecraft would break into smaller components. The thickness of the cylinder was sized to ensure that the equivalent cylinder weight and the sum of the weights of the components released at spacecraft breakup equaled the total weight. This assumption re-sulted in the requirement that 457 kgs (35% of the total weight) of aluminum melted to achieve breakup. A temperature history of the cylindrical model skin is provided in Figure 12. Given this model, the spacecraft was predicted to breakup at an altitude of 72 km. Observations by Aerospace Corp.[14] indicate that most monocoque structure spacecraft breakup near an altitude of 78 km. Therefore, the component survivability analysis was conducted using both breakup altitudes.

The SPARTAN spacecraft consists of multiple components as shown in Figure 13. It has been postulated that at reentry breakup

the spacecraft would breakup into seventeen types of com-ponents as identified in Table 1. Each of these components are modeled as equivalent spheres or cylinders, and then, the ORSAT code was used to determine if the component demised or survived reentry. The initial conditions for both the 72 and 78 km breakup conditions were evaluated. As summarized in Table 2, six components survive the reentry for a 78 km breakup and nine components survive reentry for a 72 km breakup. Since considerable uncertainty in the breakup altitude exists, the total debris area, L, of components surviving reentry is predicted to be between 6.6 and 11 m^2. Using these values, the risk associated with the reentry of SPARTAN spacecraft from a 57° orbit would be between 8.4×10^{-5} and 1.4×10^{-4} that a person would be injured or killed.

Summary and Conclusions

A method for predicting the risk associated with reentering space debris has been presented. A key feature of this method is the tool and procedures used to determine which pieces of a spacecraft survive atmospheric reentry and impact the ground. Given the surviving pieces, the risk of death or injury to a human due to the reentry event can be determined. Predictions of reentry survivability using the ORSAT compare reasonably well to flight test results. The reentry breakup and the component survivability of the SPARTAN spacecraft has been evaluated using the methods and tools presented in this paper. The SPARTAN spacecraft has been predicted to breakup at an altitude between 78 and 72 km. For lower breakup altitudes, more components of the spacecraft survive reentry and impact the Earth which increases the risk of human casualty. The risk of human casualty for the SPARTAN reentry is predicted to be between 8.4×10^{-5} and 1.4×10^{-4} depending upon the breakup altitude.

Acknowledgments

The authors would like to thank Mark Behnke/ Interstel, Inc. and Craig Tooley/NASA-Goddard for providing information about the SPARTAN spacecraft.

References

[1] Cropp, L. O.,"Analytical Methods used in Predicting the Re-entry Ablation of Spherical and Cylindrical Bodies," SC-RR-65-187, Sandia Corporation, Sept. 1965.

[2] Sullivan, W. D., Gilbreath, G. L., and O'Neill, M. J.,"Survival Analysis of Skylab Program Vehicles," LMSC/HREC D162374, Lockheed Missiles & Space Company, Huntsville, Alabama, July 1970.

[3] McCormick, P. O., Hedden, R. O., and Bhadsavle, A.,"A Study of Saturn Debris Risk Hazard Analyses," LMSC/HREC D225218, Lockheed Missiles & Space Company, Huntsville, Alabama, July 1971.

[4] McCormick, P. O. and Hedden, R. O.,"Apollo-Soyuz Docking Module Breakup, Survival and Risk Hazard Analyses," LMSC/HREC TR D390052, Lockheed Missiles & Space Company, Huntsville, Alabama, Feb. 1974.

[5] McCormick, P. O. and Hedden, R. O.,"Earth Resources Technology Satellite Breakup, Survival and Risk Hazard Analyses," LMSC/HREC TR D390133, Lockheed Missiles & Space Company, Huntsville, Alabama, April 1974.

[6] Derrick, J. N. and McCormick, P. O.,"Centaur Breakup, Survival and Risk Hazard Analyses," LMSC/HREC TR D390182, Lockheed Missiles & Space Company, Huntsville, Alabama, May 1974.

[7] McCormick, P. O. and Hedden, R. O.,"Apollo-Soyuz Test Project Service Module Breakup, Survival, Dispersion and Risk Hazard Analyses," LMSC/HREC TR D390557, Lockheed Missiles & Space Company, Huntsville, Alabama, Oct. 1974.

[8] McCormick, P. O. and Hedden, R. O.,"High Energy Astronomy Observatory Breakup, Survival and Risk Hazard Analyses," LMSC/HREC TR D390552, Lockheed Missiles & Space Company, Huntsville, Alabama, Oct. 1974.

[9] Bell, J. M.,"Pioneer F & G Spacecraft/RTG Reentry Breakup Study," NASA-CR-162891, July 1970.

[10] Bell, J. M.,"Orbital Reentry Breakup Analysis Report P74-1 Payload System," TRW Systems Group, No. D00604, Nov.

1974.
11 Ailor, W. H. et al,"Analysis of SP-100 Reentry," AFWL-TR-84-80, Aerospace Corp., Oct. 1984.
12 McRonald, A.,"Galileo RTG Reentry Breakup Analysis," NASA/JPL 1625-228.
13 Jaffe, P., Diner, A., McRonald, A., Tenn, I.,"Ulysses: Breakup Analysis Final Report," NASA/JPL 1628-54.
14 Refling, O., Stern, R., Potz, C.,"Review of Orbital Reentry Risk Predictions," Aerospace Corp., ATR-92(2835)-1, July 1992.
15 Miele, A.,Flight Mechanics, Vol. 1, Theory of Flight Paths, Addison-Wesley Publishing Co., Inc., 1962.
16 Klett, R. D.,"Drag Coefficients and Heating Ratios for Right Circular Cylinders in Free-Molecular and Continuum Flow from Mach 10 to 30," SC-RR-64-2141, Sandia Corp., Dec. 1964.
17 Detra, R. W., Kemp, N. H., Riddell, F. R.,"Addendum to 'Heat Transfer to Satellite Vehicles Re-entering the Atmosphere'," Jet Propulsion, Vol. 27, No. 12, Dec. 1957.
18 Özisik, M. Necati, Heat Conduction, John Wiley & Sons, New York, 1980.
19 Erickson, C. E. et al,"Re-entry Flight Demonstration Number One (RFD-1): Design, Development, and Performance of the Reentry Vehicle," SC-RR-64-511, Sandia Corp., May 1964.
20 White, I. B. et al,"Re-entry Flight Demonstration Number One (RFD-1): Optical Data and Fuel Element Experiment," SC-RR-64-516, Sandia Corp., Oct. 1964.
21 Interpolated National Populations 1950-2025 from World Population Prospects: The 1992 Revision, United Nations, New York, New York, 1992.
22 The World Almanac and Book of Facts 1991, Pharos Books, 1991.

Table 1 - SPARTAN Components and Reentry Models.

Component	Mass (kgs)	Reentry Model	Material
HAO Experiment	40.8	Hollow Cylinder D=0.279 m; L=2.64 m; t=0.0064 m	Aluminum
SAO Experiment (includes Invar box)	72.6	Hollow Cylinder D=0.305 m; L=2.59 m; t=0.0075 m	Aluminum
Arc Door	37.6	Solid Sphere D=0.295 m	Aluminum
Grapple Fixture	19.1	Hollow Sphere D= 0.413 m; t=0.0085 m	Titanium
ACS Bottles (2 each)	12.5	Hollow Cylinder D= 0.254 m; L =0.762 m $t_{layer\ 1}$=0.0095 m; $t_{layer\ 2}$=0.00343 m	Layer 1: Kevlar Layer 2: Aluminum
Battery Boxes (2 each)	161.9	Hollow Cylinder D=0.424 m; L=0.830 m; t=0.0233 m	Aluminum
Gyro	6.4	Hollow Cylinder D=0.152 m; L=0.254 m; t=0.0218 m	Aluminum
LR40 Battery	24.9	Hollow Cylinder D= 0.290 m; L=0.316 m; t=0.0207 m	Aluminum
Kinematic Mounts (3 each)	4.5	Solid Sphere D=0.146 m	Aluminum
Data Handling Elecs. Assembly	106.1	Hollow Cylinder D=0.736 m; L=1.09 m; t=0.0153 m	Aluminum Elec. Components
ACS Elecs. Assembly	69.9	Hollow Cylinder D=0.739 m; L=1.09 m; t=0.0100 m	Aluminum Elec. Components
REM Adapter Piece	12.7	Hollow Cylinder D=0.635 m; L=1.09 m; t=0.00209 m	Aluminum
Experiment Elecs. Box Pieces (2 each)	5.9	Hollow Cylinder D=0.508 m; L=0.533 m; t=0.0025 m	Aluminum
Cross Beam Bulkhead	13.2	Hollow Cylinder D=0.660 m; L=1.07 m; t=0.00254 m	Aluminum
HAO Electronics	34.0	Hollow Sphere D=0.5 m; t=0.0165 m	Aluminum Elec. components
SAO Electronics	20.4	Hollow Sphere D=0.5 m; t=0.0096 m	Aluminum Elec. components
Invar Box	22.7	Solid Sphere D=0.177 m	Invar

Table 2 - Summary of Survivability of SPARTAN Spacecraft Components.

Component	78 km Breakup		72 km Breakup	
	Survivability	**Debris Area** (m^2)	**Survivability**	**Debris Area** (m^2)
HAO Experiment	Demise at 71.4 km	0	Demise at 66.4 km	0
SAO Experiment	Demise at 71.0 km	0	Demise at 65.9 km	0
Arc Door	6 kg Survives	0.74	11 kg Survives	0.74
Grapple Fixture	Survives	0.93	Survives	0.93
ACS Bottles (2 each)	Survives	2.16	Survives	2.16
Battery Boxes	Demise at 62.7 km	0	Demise at 55.5 km	0
Gyro	Demise at 66.4 km	0	Demise at 62.7 km	0
LR40 Battery	Demise at 67.2 km	0	Demise at 62.4 km	0
Kinematic Mounts	Demise at 62.8 km	0	Demise at 59.1 km	0
Data Elecs. Assy.	12 kg Survive	2.24	35 kg Survive	2.24
ACS Elecs. Assy.	Demise at 64.1 km	0	15 kg Survive	2.24
REM Piece	Demise at 75.7 km	0	Demise at 69.7 km	0
Exp. Elecs. Box	Demise at 75.8 km	0	Demise at 70.2 km	0
Cross Beam	Demise at 75.1 km	0	Demise at 68.9 km	0
HAO Elecs.	Demise at 58.1 km	0	7 kg Survives	1.09
SAO Elecs.	Demise at 67.0 km	0	2 kg Survives	1.09
Invar Box	Survives	0.57	Survives	0.57
	Total	6.64	Total	11.06

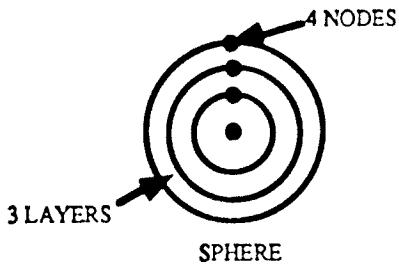

Figure 1 - Example of a Spherical Object Model with Three Layers.

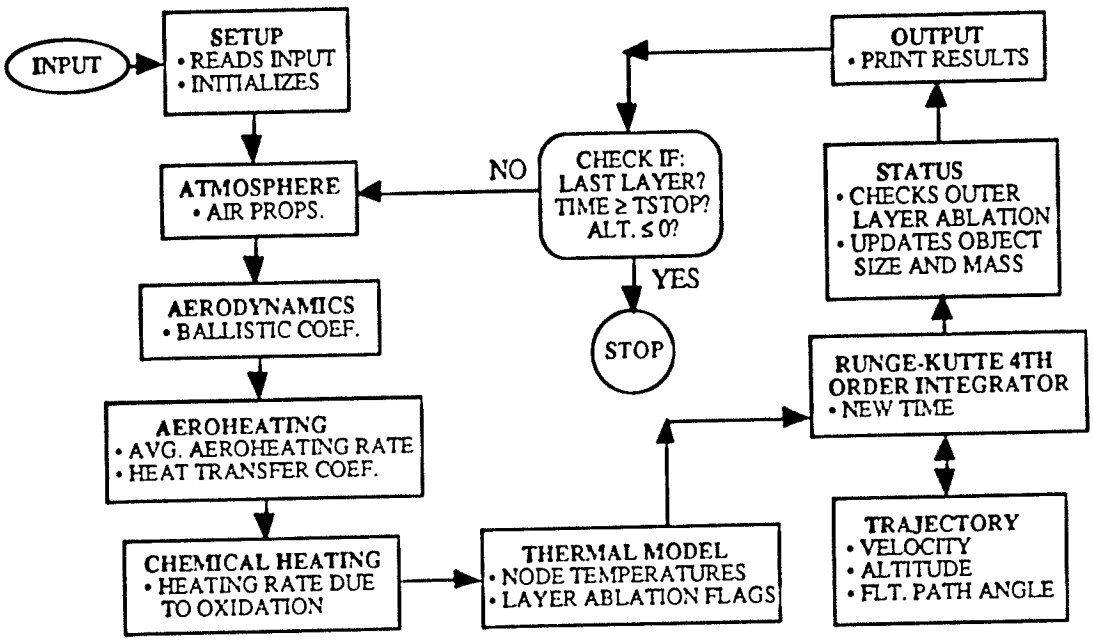

Figure 2 - Flow Chart of ORSAT Computer Code.

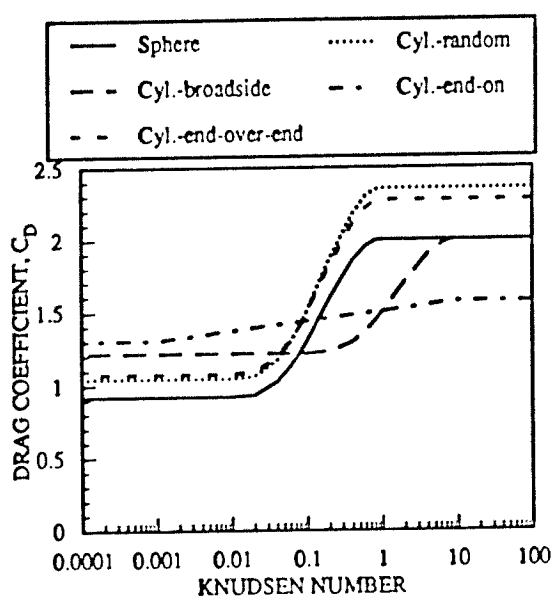

Figure 3 - Sphere and Cylinder (L/D=1) Drag Coefficients.

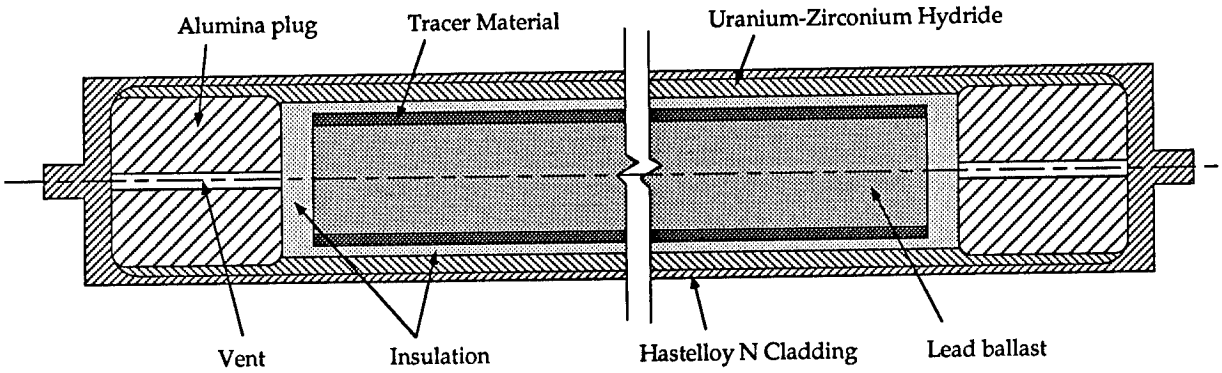

Figure 4 - Sketch of a Sandia Flight Test Model Fuel Rod.

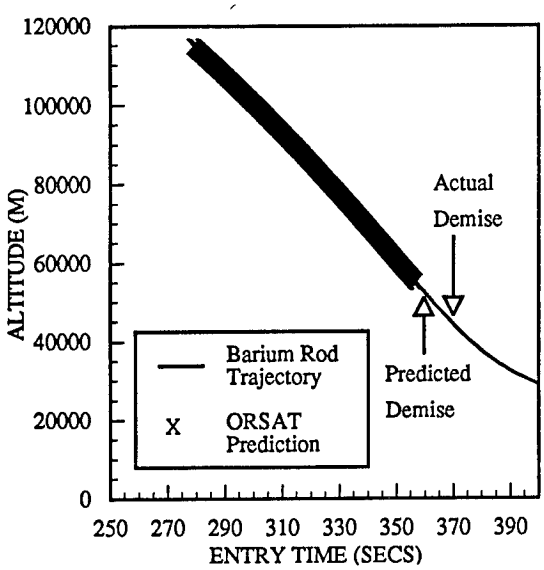

Figure 5 - Comparison of Predicted and Actual Trajectories for Sandia Fuel Rod.

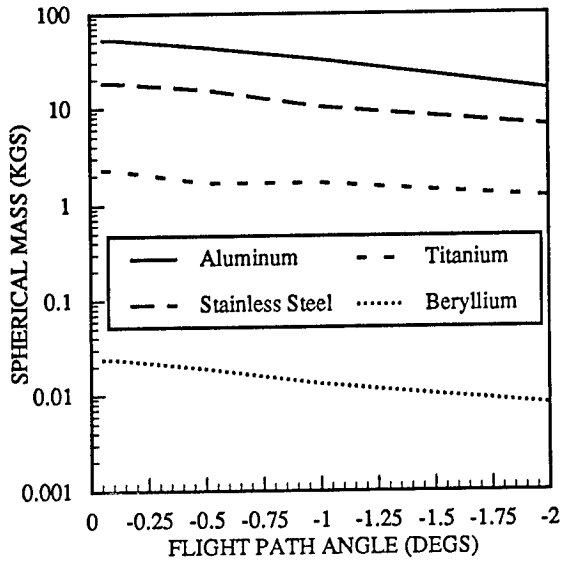

Figure 6 - Spherical Mass Required to Survive Entry, V_{entry} = 7350 m/s.

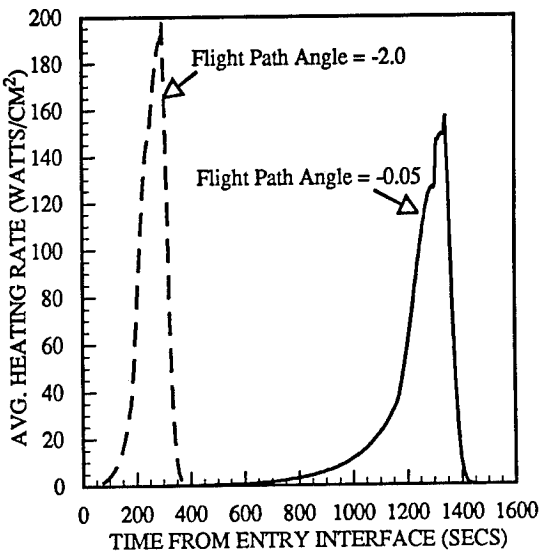

Figure 7 - History of Average Heating Rates to a Solid Steel Sphere, V_{entry} = 7350 m/s.

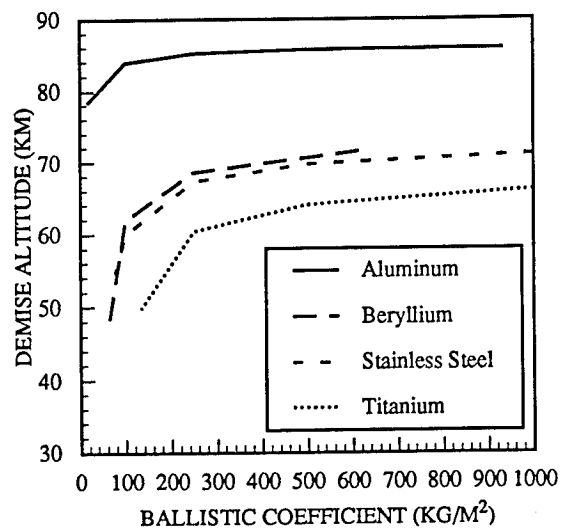

Figure 8 - Effect of Ballistic Coefficient on Demise Altitude for a 1.0 m Diameter Sphere with a 3 mm wall; V_{entry} = 7350 m/s; g = -0.1 degs.

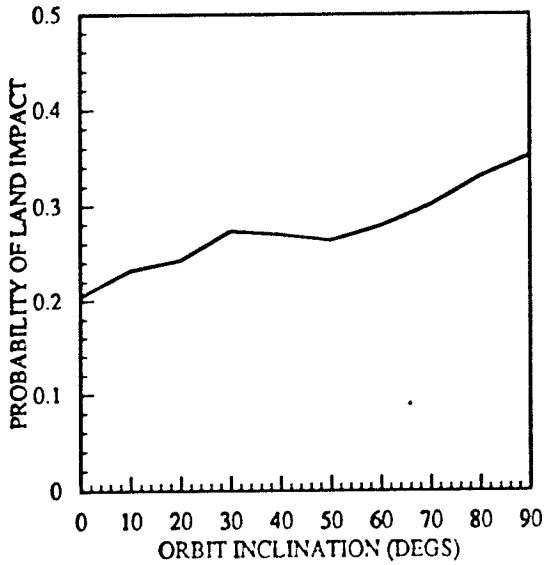

Figure 9 - Probability of Impact on Land vs. Inclination Angle.

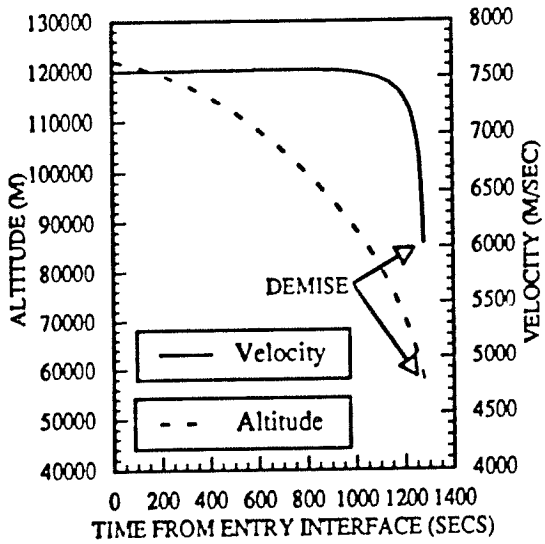

Figure 10 - Reentry of 10 cm ODERACS Stainless Steel Sphere.

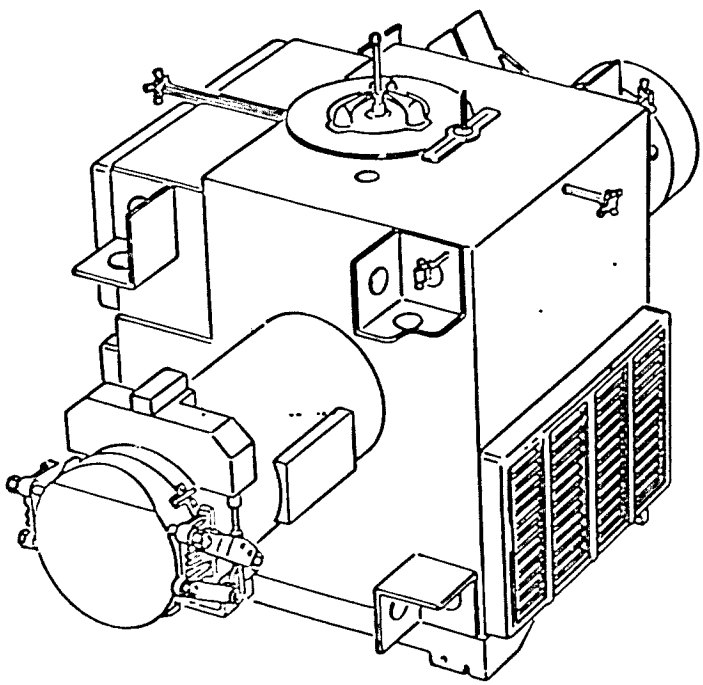

Figure 11 - Sketch of SPARTAN Spacecraft.

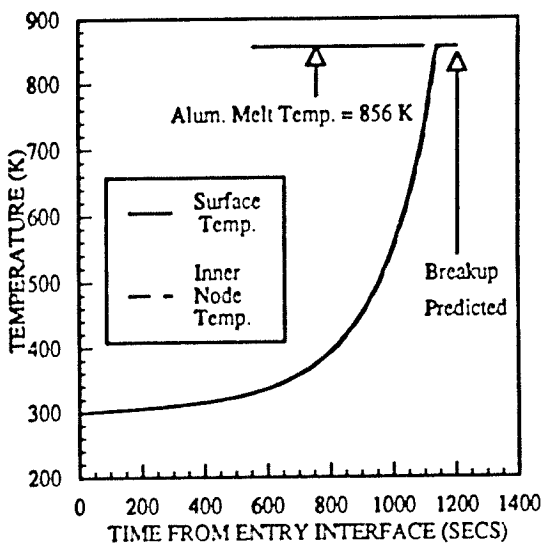

Figure 12 - Temperature History of SPARTAN Hollow Cylinder Model.

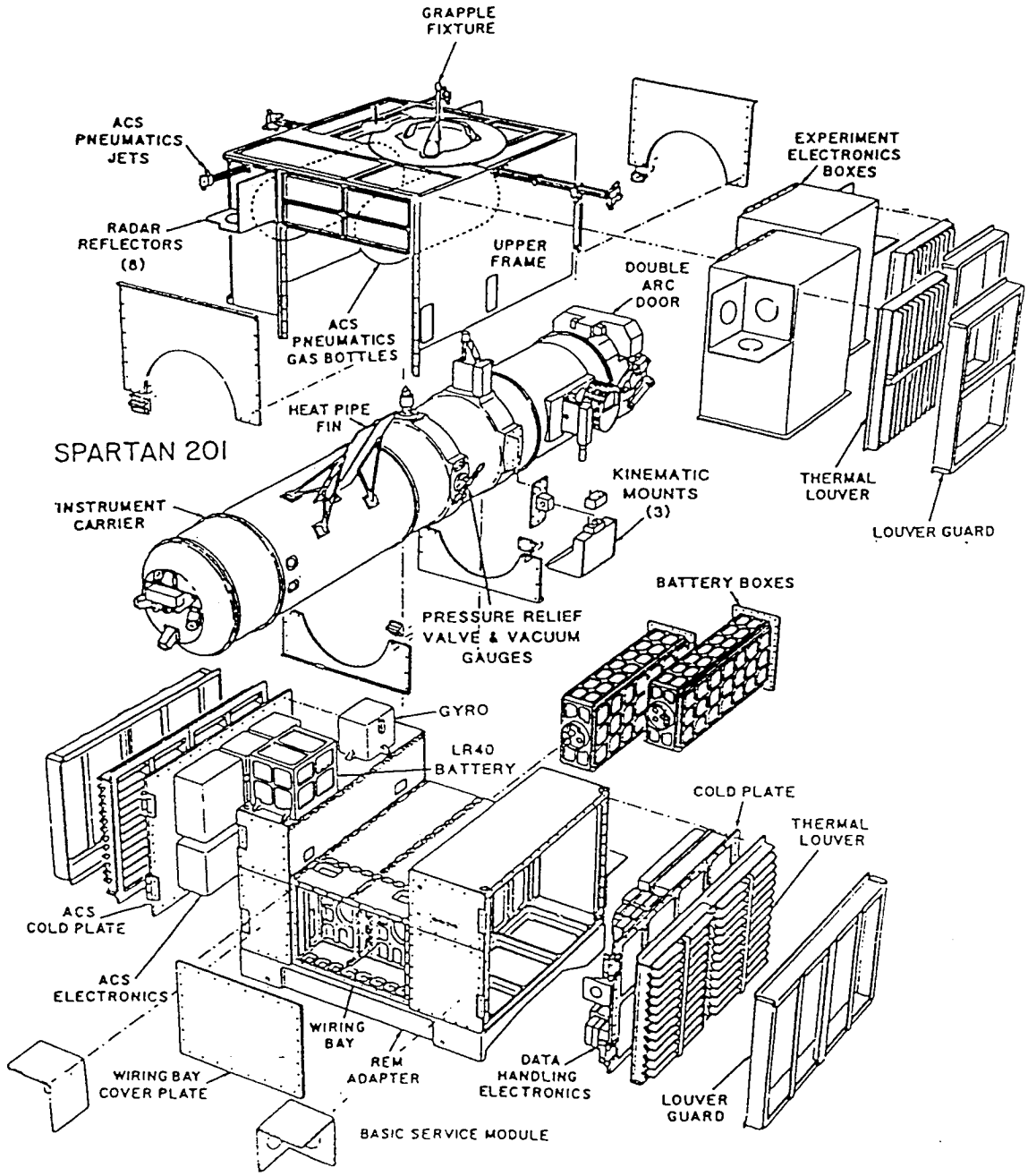

Figure 13 - Exploded View of SPARTAN Spacecraft.

THERMAL ENVIRONMENT IN SPACE FOR ENGINEERING APPLICATIONS

Glen W. Batts
Senior Staff Scientist
New Technology, Inc.
Huntsville, Alabama 35802

Abstract

Correct definition of the orbital thermal environment is an integral part of an effective spacecraft thermal design. The orbital thermal environment varies significantly over orbits and over mission lifetime. Temperature control requirements for spacecraft components normally are for a pre-determined temperature range. Therefore, temperature fluctuations need to be minimized to prevent system fatigue. One of the most frequently encountered concerns is the ability to provide adequate heat rejection to cold sensitive electronic systems. Fluctuations in the temperature can fatigue any one of the different components of the system which promotes system failures. Another major concern is the possibility of excessive freeze-thaw cycling of thermal control fluids caused by abrupt changes in the thermal environment which may require oversizing of radiators or permanent radiator freezing. Thus, the thermal environment is an important factor in the design of spacecraft.

Introduction

Spacecraft receives radiant thermal energy from three sources and radiate or reflect it to the cold sink of space. The three primary sources are: incoming solar radiation (from which the solar constant is derived), reflected solar energy (albedo), and outgoing longwave radiation (OLR) which is emitted by the Earth and atmosphere. When one considers the Earth and its atmosphere as a whole and averages over long time periods, the incoming solar energy and outgoing longwave radiant energy are essentially in balance. However, it is not in balance everywhere on the globe and there are variations with respect to local time, geography, and atmospheric conditions. A spacecraft's motion with respect to the Earth results in its viewing a very small swath across the full global thermal profile variations as functions of time in accord with the thermal time constants of the hardware systems. The analysis presented in this paper shows the thermal variations for two spacecraft orbit inclinations, a thirty (30) degree inclination orbit and a ninety (90) degree inclination orbit.

Thermal Environment Description

The incoming energy that originates at the Sun has the overall spectral shape of the radiation from a blackbody at a temperature of 5762 K. This energy is called the solar constant and the value given to it, even though measurements have shown that it is not constant but varies on the order of one percent with time, is valid only at 1 Astronomical Unit (AU). Even this small variation may be of importance to thermal analyses of space vehicle elements, subsystems and/or systems. Since the amount of energy leaving the Sun decreases as the square of the distance from the Sun increases, the annual variation of the Earth's distance from the Sun must also be considered in thermal analyses of orbiting space vehicles.

That portion of the incoming solar radiation that is reflected back to space by the Earth-atmosphere system is called the albedo radiation and it has approximately the same spectral shape as the Sun's radiation. Since the albedo is the ratio of the backscattered radiation to the incoming solar radiation, the absolute value of the albedo radiation must be indexed to the value of the incoming radiation. This radiation is highly dependent upon the characteristics of the surfaces that are causing the incoming radiation to be reflected back to space. The albedo radiation at any one location is a combination of that reflected by the surface of the Earth and that reflected by the clouds. Both of these surfaces may be highly variable, both spatially and temporally, with the result that the absolute value to be used in any spacecraft thermal analysis is highly dependent upon its application.

The Earth-atmosphere system itself emits longwave radiation that will affect the space-

craft. Globally this longwave radiation has approximately the spectral shape of the radiation emitted by a blackbody at a temperature of 288 K. Since the amount of this radiation affecting a spacecraft is also dependent upon the surface characteristics as well as the properties of the intervening medium, it is also highly variable, both spatially and temporally, and once again the absolute value to be used in any thermal analysis is highly dependent upon its application.

Since all three of these radiations can only be adequately measured from space, the amount of data available for use in establishing absolute values to be used in thermal analyses is very small for the best applications and completely inadequate for a large number of cases, especially those requiring detailed knowledge of their variability over short time periods.

Description of Available Data

Primarily, all of the available data were measured under the auspices of the Earth Radiation Budget Experiment (ERBE). See References for details of this experiment and the data it has obtained. Of the entire dataset obtained by the experiment, the S-4 and S-7 data subsets were the only ones that could possibly provide the data required to provide answers to questions by the Space Station thermal design engineers. Before discussing the analysis of the available data, a discussion of the parameters provided in these two data sets is appropriate.

The next five paragraphs are direct quotes from the S-4 and S-7 User's Guides; ERBE 3-3-12-3-85-1-10, June 1985 and ERBE 3-3-12-5-85-8-0, August 1985.

"The ERBE is a multisatellite system designed to measure the Earth's radiation budget. The ERBE instruments fly on low inclination NASA satellites and two sunsynchronous NOAA satellites. Each satellite carries both a scanner and a nonscanner instrument.

The scanner instrument package contains three detectors to measure shortwave (0.2 to 5 um), longwave (5 to 200 um) and total wave band radiation (0.2 to 200 um). Each detector scans the Earth perpendicular to the satellite groundtrack from horizon-to-horizon. The detectors are thermistors that use space on every scan as a reference point to guard against drift. They are located at the focal point of an f/1.84 Cassegrain telescope whose aluminum-coated mirrors have been overcoated to enhance ultraviolet reflectivity. The total channel has no filter and absorbs all wavelengths. The shortwave channel has a fused silica filter that transmits only shortwave radiation. The longwave channel has a multilayer filter on a diamond substrate to reject shortwave energy and accept longwave. To enhance the spectral flatness of the detectors, each thermistor chip is coated with a thin layer of black paint. The instantaneous field-of-view (FOV) of each channel is hexagonal, with angular size of 3 deg by 4.5 deg; the longer dimension being along the satellite groundtrack.

The nonscanner instrument package contains four Earth-viewing channels and a solar monitor. The Earth-viewing channels have two spatial resolutions: a horizon-to-horizon view of the Earth, and a field-of-view limited to about 1000 km in diameter. The former are often called the wide field-of-view (WFOV) and the latter the medium field-of-view (MFOV) channels. For each of the two fields of view there is a total spectral channel that is sensitive to all wavelengths and a shortwave channel that uses a high purity, fused silica filter dome to transmit only the shortwave radiation from 0.2 to 5 um. The solar monitor is a direct descendant of the Solar Maximum Mission's (SMM) ACRIM detector and is expected to have similar capabilities. Because of the concern for spectral flatness and high accuracy, all five of the channels on the nonscanner package are active cavity radiometers.

There are two fixed wide-angle channels continously viewing the Earth disc. The measurements are continous over the entire globe for NOAA-9 and NOAA-10, and between 57 deg N and S latitudes for ERBS that precessed 4.95 deg west per day. There are two fixed medium-angle channels continously viewing a circle of nominally 5 deg radius at the top of the atmosphere. The measurements are continous over the entire globe for NOAA-9 and NOAA-10, between 57 deg N and S latitude for ERBS. There are three scanning narrow-angle channels continously viewing small areas over the entire Earth. The cross-track scan width is approxi-

mately 40 km at nadir, and there is a 35% field-of-view overlap along-track at nadir for ERBS.

The wide angle channels on the ERBS spacecraft have a FOV of 136 deg while those on the NOAA spacecrafts have a FOV of 126 deg. The medium-angle channels have footprints of approximately 5 deg radius or 1000 km at the top of the atmosphere. The narrow-channels have a common hexagonal FOV of about 3 x 4.5 deg, which is equivalent to a 31 km x 47 km footprint at nadir for ERBS and 44 km x 65 km for NOAA. The solar channel has an unencumbered FOV that observes the entire solar disk and measures 20 minutes of usable data about twice per month during solar calibration periods. The solar channel's shutter cycles every 32 seconds during a solar calibration. For the nonscanner, five channels provide 125 samples per second with an accuracy of approximately 1%. The scanner channels are sampled every 0.033 seconds."

S-4 Data Subset

The S-4 Output Product System produces the time and space averages of all the individual estimates of radiant exitance at the top of the atmosphere for each month and each each spacecraft using data from the Monthly Time/Space Averaging Subsystem. The basic structure of the ERBE grid system (D. Brooks, 1981) lends itself to calculating several types of averages. There are six different sets of estimates. The first set uses all scanner (SCAN) measurements. The second set uses only those scanner measurements identified as viewing clear sky (CS) areas. The medium and wide field-of-view (MFOV and WFOV) measurements are reduced to estimates with both the shape factor (SF) and the numerical filter (NF) techniques that produce four more sets of estimates. There are three different time periods of averaging: daily, monthly, and monthly hourly. The monthly hourly mean corresponds to estimates for one specific local hour that are averaged over the total number of days in the month. All of these averages make use of diurnal models.

The first type of average is on a regional level. Data values from higher resolution regions can be 'nested' into lower spatial resolution regions namely, 2.5 deg and 5.0 deg regions which are nested into 10 deg regions. The next level of averaging occurs across latitudinal bands. Data from all regions in a 2.5 deg, 5.0 deg, to 10.0 deg latitudinal band can be accumulated to produce zonal average. The final type of average is on a global level. Several global averages were produced for each satellite or combination of satellites.

For each of the three ERBE spacecraft (ERBS, NOAA 9, NOAA 10), there are three instruments (scanner, nonscanner, MFOV and nonscanner WFOV) and two data reduction techniques (SF and NF). Processing is controlled by the lower resolution region numbers. The colatitude index is used to obtain the correct area weight value and to distinguish between polar and non-polar latitudinal bands. The 2.5 deg products are used to nest to the 5.0 deg products that are then used to nest to the 10.0 deg products. Separate zonal and global products are produced for each resolution and for each data reduction technique. Thus, for each satellite and combination of satellites, there are potentially nine different global (monthly) averages of each calculated quantity.

S-7 Data Subset

This product contains a condensed version of the nonscanner data that are found on a monthly set of Processed Archival Tapes, except that the shortwave estimates of the radiant exitance at the top of the atmosphere (TOA) are based on the mostly-cloudy over ocean bidirectional model. The product then provides a consistent data set of nonscanner TOA estimates that are not dependent on scene type and, therefore, not dependent on the operational status of the ERBE scanner instruments. The filtered nonscanner radiometric values are 4-second averages as opposed to the 0.8-second measurement values on the Processed Archival Tapes. This product contains no scanner data and each tape contains data for one month from one spacecraft. The month is divided into daily files, each of which are divided into 16-second records.

This subset contains monthly information from the MFOV and WFOV nonscanner instrument package. TOA estimates in this data subset are calculated with the Inversion Subsystem dead scanner software. A single file on tape contains

information for a single 24-hour (one day) time period. There may be up to 31 daily files on one monthly tape. All information on the tape is from the same satellite. Thus, there may be three tapes for the same month, one for each satellite.

The data for a daily file starts at Greenwich midnight {zero Universal Time (UT)} and continues for 24 hours. This period is divided into 16-second intervals which gives a maximum of 5400 data records on a file. As long as there is one valid nonscanner measurement within a 16-second interval, a full data record is written and default values are used to flag invalid data. Each record is indexed to an approximate Earth-sun distance in AUs and an x,y,z location in an Earth-fixed coordinate system.

In addition to the navigation and housekeeping data, filtered MFOV and WFOV total and shortwave radiometric measurements are recorded on the tape every 0.8-seconds so there are 20 entries per 16-second record. Each measurement value is an average over seconds of a 16-second time period. From these filtered measurements, estimates of the unfiltered MFOV, the WFOV, and shortwave radiation are derived and recorded on the tape. The unfiltered nonscanner measurements are recorded on the data tape every 4 seconds so that there are four measurements per 16-second record.

TOA estimates of the radiant exitance (SW or LW) are based on the nonscanner unfiltered measurements averaged over 32 seconds. All TOA estimates contained in the S-7 subset are independent of the actual underlying scene type. The S-7 TOA estimates assume the scene is mostly cloudy over ocean everywhere, which is the best single scene to use. Using a single scene type to derive the numerical filter and shape factor is felt to improve the long-term consistency of the TOA estimates. As in the S-4 subset, there are two data reduction techniques used, a numerical filter method and a shape factor method. A single estimate using the numerical filter method is affected by measurements over a 416-second time interval. The average measurement derived using the shape factor technique combines 32 seconds of nonscanner unfiltered measurements.

S-7 Data Analysis

Albedo/Solar Zenith Angle Dependence

Albedo may be assumed to be independent of the solar zenith angle (SZA) to a first approximation; the scattering is "Lambertian" or equal in all directions. This approximation has been assumed for most engineering applications in the past. However, the improved data quality and the capability of current engineering analysis methods warrant an improved approach. Treatment of this topic in the scientific literature is generally "scene specific", e.g., it depends on the geographic features in the field-of-view, data which is not generally available to the design engineer, and the algorithms tested did not fully remove the zenith angle dependence from this data set. Therefore, a zenith angle correction was derived specific for the data used in the Space Station and AXAF-S analyses. The correction is significant, especially for the AXAF-S orbit which always sees high solar zenith angles. The correction is specifically tuned to the analysis tools most commonly used for engineering analysis, Thermal Radiation Analysis System (TRASYS) and Thermal Synthesizer System (TSS). When used with this correction and the proper thermal definition parameters, these thermal analyses tools should reproduce the ERBE measurements.

The albedo/SZA correction was derived using four months of data, representative of all seasons, restricted to the -30 to +30 latitude band. Verification was made by testing four other months of data and testing wider latitude bands. This correction removes the albedo parameter's solar zenith angle dependence to within +0.04. The correction is as follows:

$$Alb(SZA) = Alb(SZA=0) + Corr$$

$$Corr = [C4(SZA)^4 + C3(SZA)^3 + C2(SZA)^2 + C1(SZA)]/100$$

where SZA is the Solar Zenith Angle in degrees and the albedo is expressed as a fraction.

C4 = +1.8556 E-6
C3 = -1.9114 E-4
C2 = +6.5970 E-3
C1 = +1.5034 E-2

Figure 1 illustrates the correction. This term must be added to the albedo given in Tables 1

and 2 which are shown graphically in Figures 2 and 4.

Running Mean Analysis

For any satellite system having any complexity, different portions of the hardware will have different thermal response times ranging from less than a minute to hours. To enable analysis of the thermal response to variations the satellite will encounter as it moves along its orbit track, a running mean analysis of albedo and OLR was done. Running means were computed for averaging time ranging from a few seconds to one and one-half hours. Since these parameters vary systematically with latitude, corrections are applied to account for the differences in orbit inclinations between the ERBE measuring satellites and the satellite being designed. Cumulative Percentage Frequencies (CPFs) of the running means give the low extreme (1st, 3rd, and 5th percentiles) and high extreme values (95th, 97th, and 99th percentiles) and the expectation value (50th percentile) for both albedo and OLR for various averaging time periods along an orbit track. Table 1 shows the final results for -30 to +30 latitude orbit and Table 2 shows the final results for -90 to +90 latitude orbit. Figures 2 and 3 illustrate Table 1 and Figures 4 and 5 illustrate Table 2. Based on the thermal time constant of the system, subsystem or component being analysed, albedo and OLR values can be estimated from the figures for various percentile levels.

Albedo/OLR Correlation

There tends to be a general misconception that when albedo is low the OLR is high and vice versa. However, when one analyses albedo and OLR along orbits, this is not always the case. Figures 6,7, and 8 illustrate the correlation of albedo vs. OLR for the running mean time average of 16 seconds, 15 minutes, and 90 minutes for the latitude band -30 to +30. Figures 9, 10, and 11 illustrate the correlation of albedo vs. OLR for the running mean time average of 16 seconds, 15 minutes, and 90 minutes for the latitude band -90 to +90. As illustrated by these figures, no general statement can be made as to the correlation between albedo and OLR for all satellite systems, subsystems, or components.

Summary

Heretofore, the engineering community has used annual global averages of albedo and OLR in satellite design. With the advent of newer, lighter composite materials brought about by payload weight concerns, this concept is no longer feasible. The ERBE satellites have been measuring thermal parameters since 1984 and most of the usage has been science based. Emphasis is now being placed on using this data in the engineering community for space vehicle design, especially the Space Station which has so many subsystems and components all of which have their own thermal responses. Comprehensive analysis of the ERBE data from the engineering point of view is needed to assist in the development of models which can be used by the engineering community in the design of space vehicles.

Acknowledgments

This work was accomplished under NASA MSFC contract with appreciation to Dr. C.K. Hill, MSFC-ES44; Dr. B.J. Anderson, Ms. B.F. James, MSFC-EL54; Dr. Robert Smith, Physitron; Ms. Sandy Nolan, LARC-LESC.

REFERENCES

Satellite/Instrument/Data Processing Documentation

NASA/LARC "Earth Radiation Budget Experiment (ERBE) Data Management System Raw Archival Tape (S-1), (S-2), (S-4), (S-6), (S-7), (S-8), (S-9), and (S-10) User's Guides" Hampton, VA

MSFC-DOC-2253 "Advanced X-Ray Astrophysics Facility - Spectroscopy (AXAF-S) Natural Space Environment: Definition and Requirements (Level III)

Journal Articles and Study Reports

Barkstrom, B.R., 1984. "The Earth Radiation Budget Experiment (ERBE)." Bull. Amer. Meteor. Soc., 65: 1170-1185.

Barkstrom, B.R., and G.L. Smith, 1986. "The Earth Radiation Budget Experiment: Science and Implications." Rev. of Geophys. and Sp. Phys., 24:379-390.

Brooks, D., 1981. "Grid System for Earth

Radiation Budget Experiment." NASA Technical Memorandum 83233.

ERBE Science Team, 1986. "First Data from the Earth Radiation Experiment (ERBE)." Bull. Amer. Meteor. Soc., 67:818-824.

Kopia, L., 1986. "Earth Radiation Budget Experiment Scanner Instrument." Rev. of Geophys., 24: 400-406.

Luther, M.R., 1986. "The Earth Radiation Budget Experiment Nonscanner Instrument." Rev. of Geophys., 24: 391-399

Schiffer, R.A. and W.B. Rossow, 1985. "The International Satellite Cloud Climatology Project (ISCCP) global radiance data set: A new resource for climate research." Bull. Amer. Meteor. Soc., 66: 1498-1505.

Seze, G. and W.B. Rossow, 1991. "Time-cumulated visible and infrared radiance histograms used as descriptor of surface and cloud variations." Int. J. Remote Sensing.

Smith, G.L., R.N. Green, E. Raschke, L.M. Avis, B.A. Wielicki, and R.

Davies, 1986. "Inversion Methods for Satellite Studies of the Earth's Radiation Budget: Development of Algorithms for the ERBE Missions." Rev. of Geophys., 24: 407-421.

WCP. 1986b. "Report of the Workshop on Surface Radiation Budget for Climate Applications." Columbia, Maryland, 18-21 June 1985. WCP-115, World Meteorological Organization, Geneva, 144pp.

Table 1. Latitudes -30° to +30°

Albedo

secs	hrs	0%L	1%L	3%L	5%L	50%	95%H	97% H	99%H	100% H
16	.0044	.066	.079	.087	.093	.165	.299	.318	.354	.513
64	.0178	.066	.080	.088	.093	.166	.297	.315	.350	.490
128	.0356	.068	.081	.089	.095	.167	.292	.31	.343	.477
256	.0711	.071	.085	.094	.099	.169	.282	.297	.327	.441
512	.1422	.077	.094	.104	.110	.172	.264	.276	.300	.394
896	.2489	.086	.103	.114	.119	.175	.245	.256	.276	.373
344	.3733	.093	.110	.120	.126	.176	.235	.244	.263	.330
1800	.5000	.096	.114	.124	.130	.176	.230	.237	.253	.31
2688	.7467	.104	.122	.132	.137	.176	.221	.228	.242	.295
3600	1.0000	.110	.128	.138	.142	.176	.216	.222	.233	.288
5400	1.5000	.124	.139	.145	.149	.176	.211	.216	.225	.258

OLR

secs	hrs	0%L	1%L	3%L	5%L	50%	95%H	97% H	99%H	100% H
16	.0044	151	174	187	194	249	285	291	303	345
64	.0178	152	175	187	195	249	285	290	302	343
128	.0356	154	177	189	196	249	284	289	301	342
256	.0711	160	182	193	200	248	282	287	296	334
512	.1422	174	193	202	208	247	277	281	288	313
896.	.2489	89	204	212	216	247	272	276	282	297
1344	.3733	194	209	215	219	246	270	273	279	296
1800	.5000	199	212	218	221	246	269	272	277	294
2688	.7467	206	216	221	224	246	267	270	274	289
3600	1.0000	210	219	223	226	246	265	268	272	283
5400	1.5000	217	223	227	229	246	263	265	269	277

Table 2. Latitudes -90° to + 90°

Albedo

secs	hrs	0%L	1%L	3%L	5%L	50%	95%H	97%H	99%H	100%H
16	.0044	.070	.089	.102	.112	.258	.407	.424	.462	.535
64	.0178	.070	.089	.103	.113	.258	.404	.421	.459	.531
128	.0356	.071	.091	.105	.115	.258	.400	.416	.452	.527
256	.0711	.075	.095	.110	.121	.259	.391	.406	.439	.522
512	.1422	.083	.108	.124	.134	.258	.377	.391	.416	.481
896	.2489	.095	.123	.141	.152	.256	.362	.373	.394	.455
1344	.3733	.119	.146	.162	.171	.254	.348	.358	.375	.426
1800	.5000	.138	.163	.176	.183	.253	.340	.349	.363	.418
2688	.7467	.145	.167	.179	.186	.253	.337	.345	.360	.416
3600	1.0000	.154	.173	.184	.190	.253	.333	.340	.353	.401
5400	1.5000	.162	.179	.188	.193	.253	.329	.335	.345	.391

OLR

secs	hrs	0%L	1%L	3%L	5%L	50%	95%H	97%H	99%H	100%H
16	.0044	157	178	186	190	223	276	283	300	349
64	.0178	157	179	187	191	223	276	283	300	348
28	.0356	160	181	188	192	223	275	282	299	347
256	.0711	166	184	191	194	223	273	279	295	342
512	.1422	177	189	194	197	225	267	273	286	332
896	.2489	184	194	199	201	226	260	265	275	315
1344	.3733	188	198	202	204	226	254	258	267	304
1800	.5000	191	200	204	206	227	250	254	261	295
2688	.7467	194	200	204	206	227	250	253	260	280
3600	1.0000	196	201	205	207	227	248	252	259	280
5400	1.5000	198	202	205	208	227	247	250	257	276

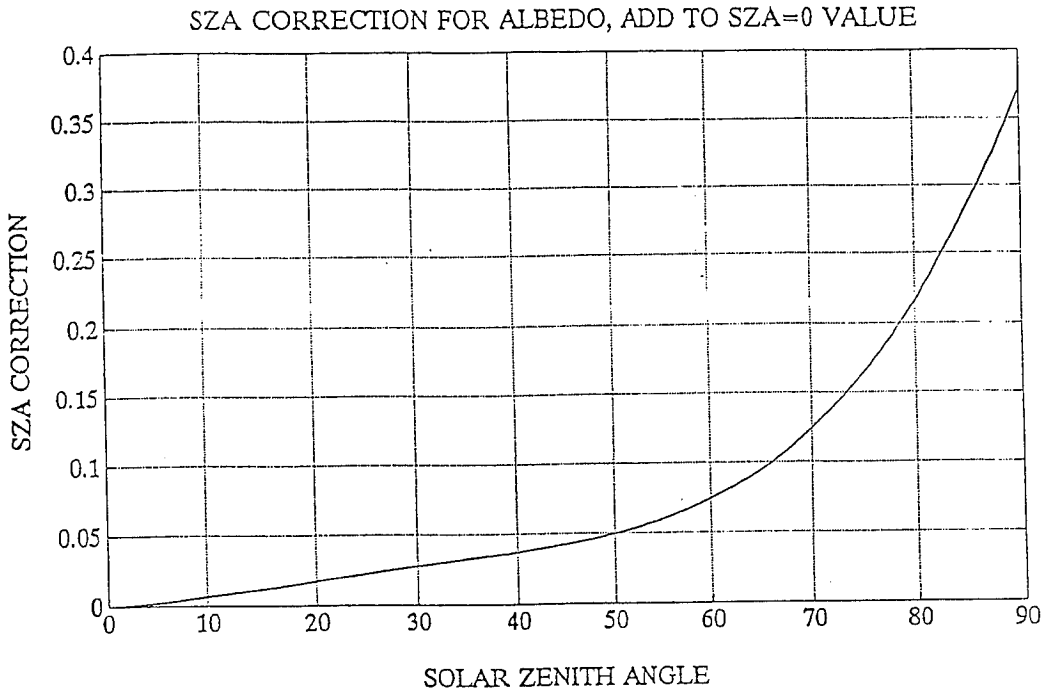

Figure 1. SZA Correction for Albedo

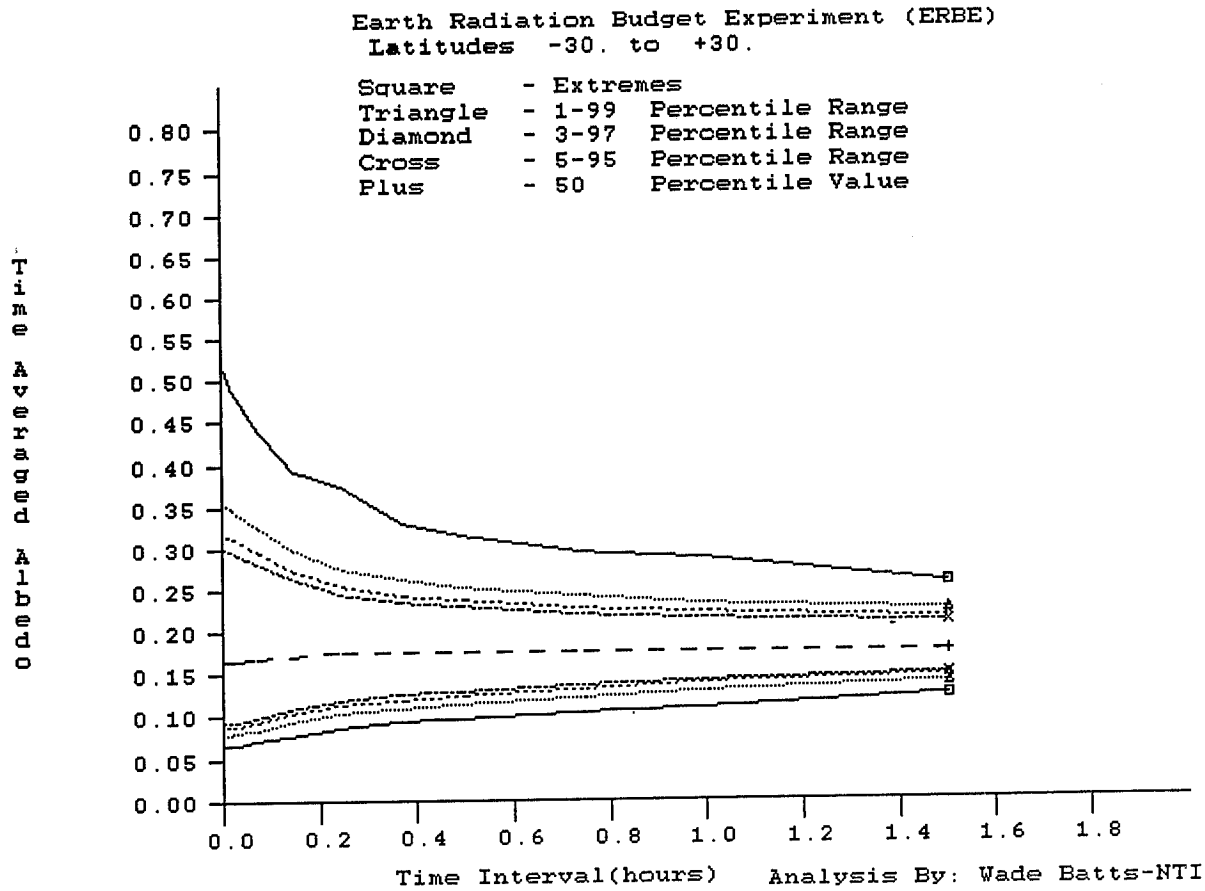

Figure 2. Time Averaged Albedo Percentiles for Latitudes -30° to +30°

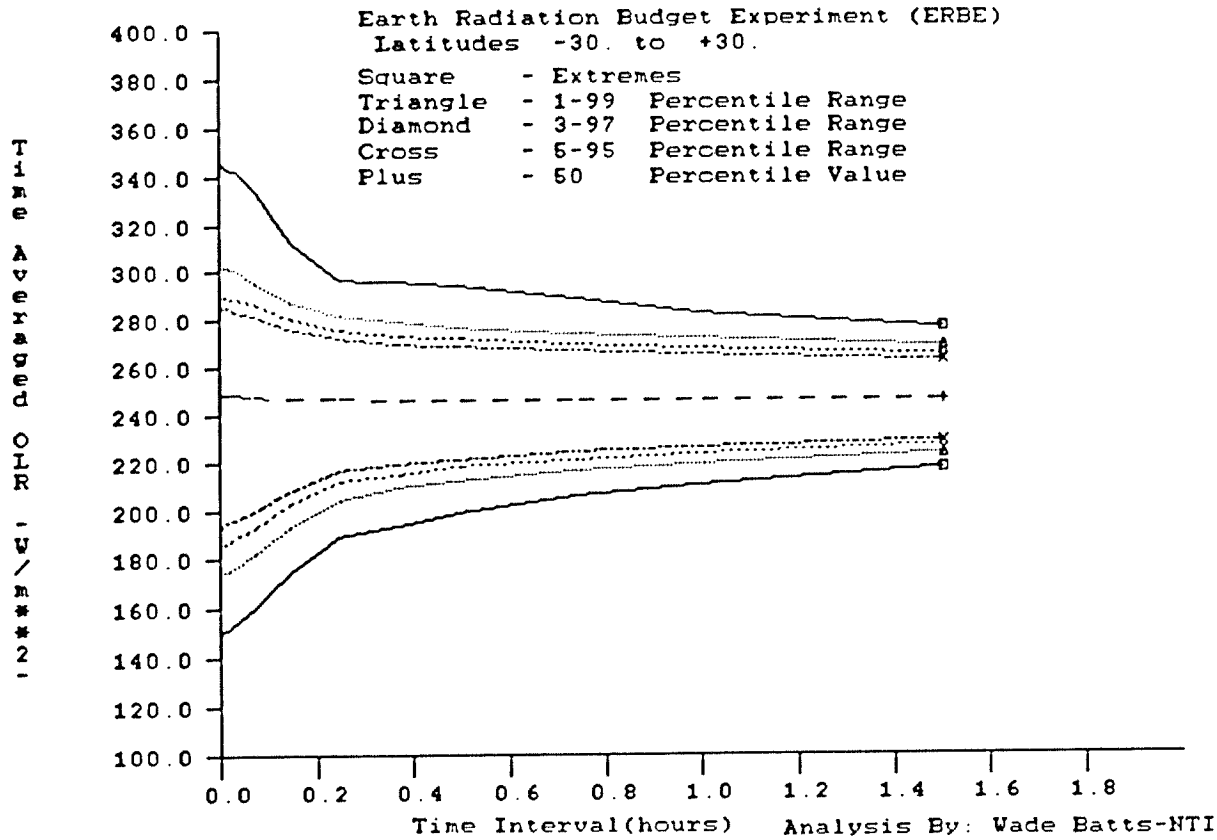

Figure 3. Time Averaged OLR Percentiles for Latitudes -30° to +30°

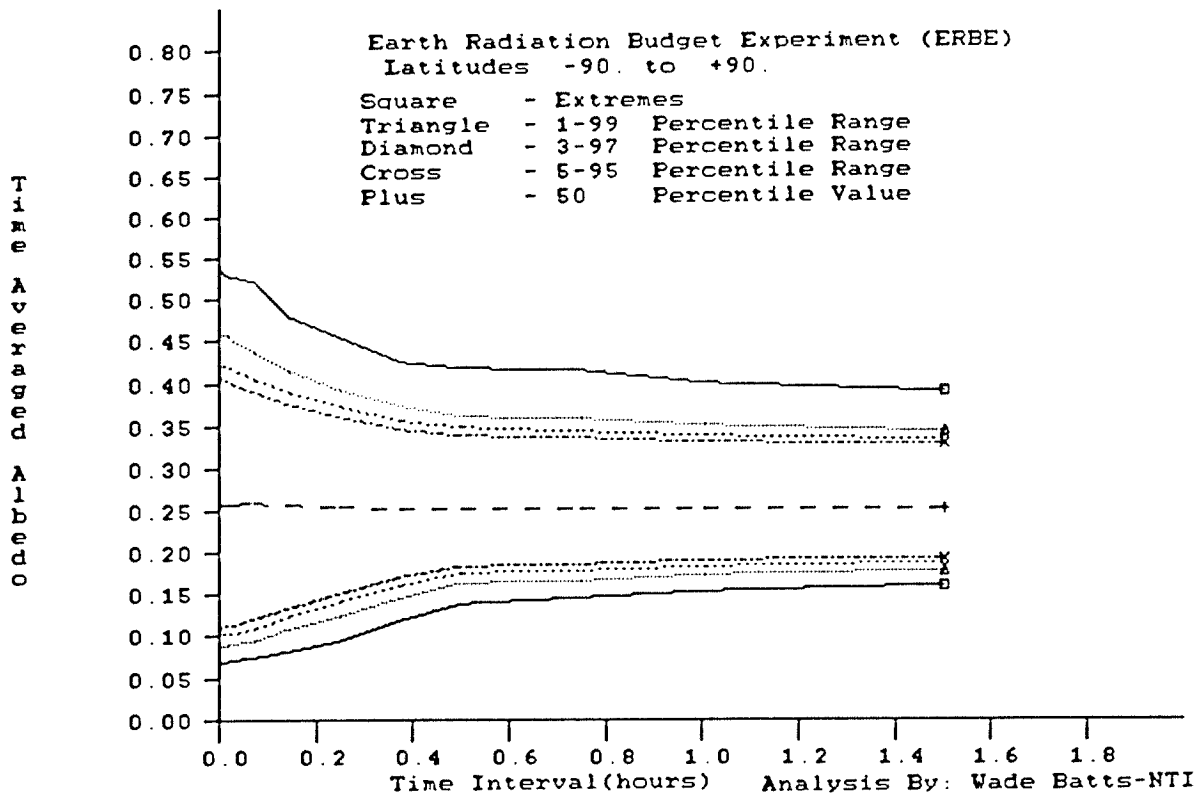

Figure 4. Time Averaged Albedo Percentiles for Latitudes -90° to +90°\

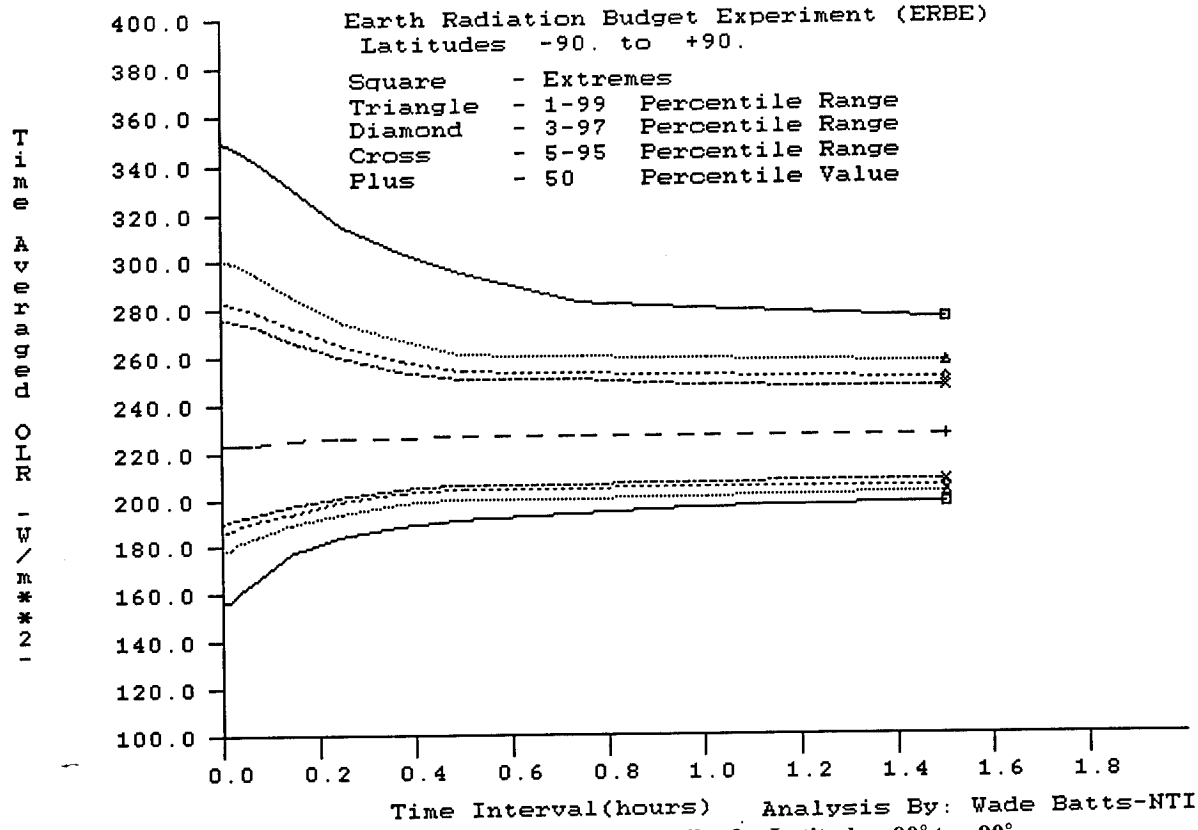

Figure 5. Time Averaged OLR Percentiles for Latitudes -90° to +90°

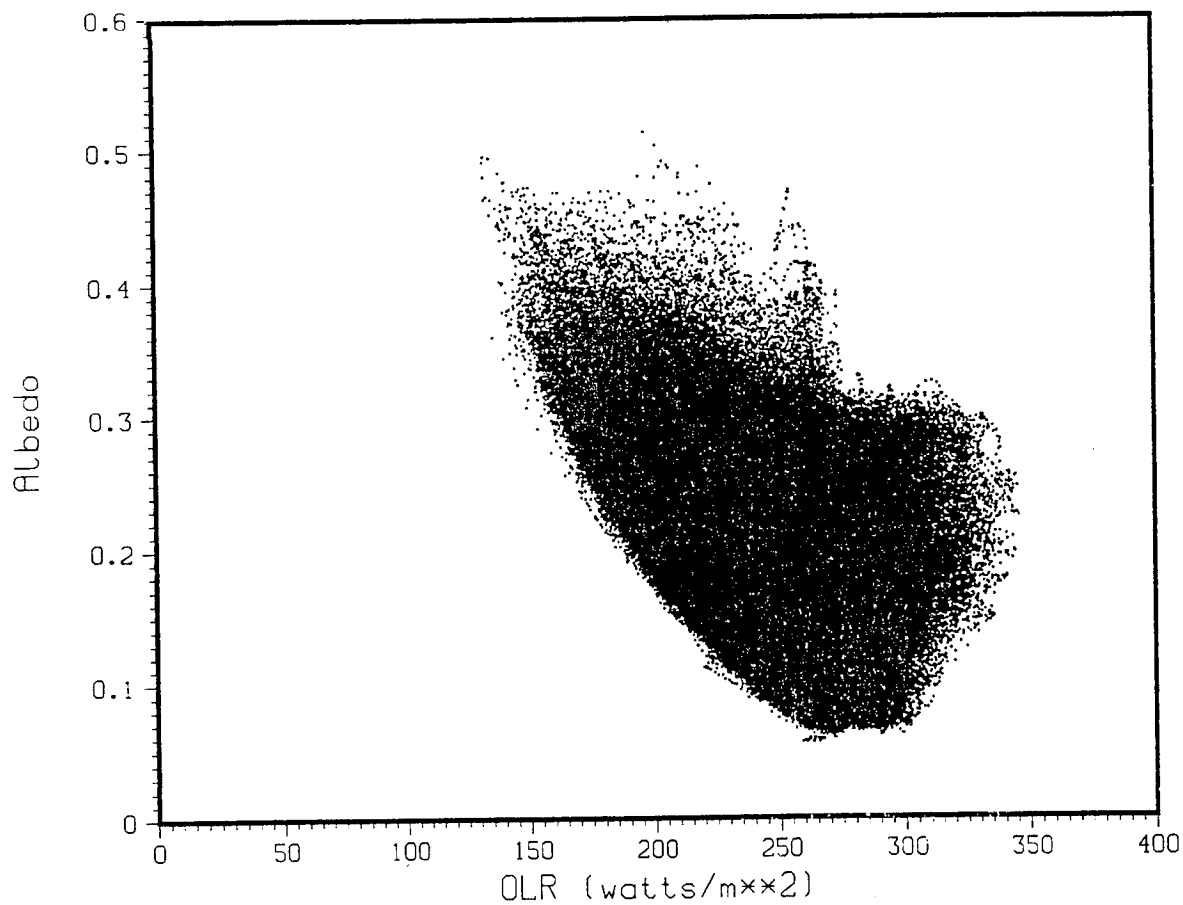

Figure 6. Albedo vs. OLR for Latitudes -30° to +30° for 16 sec. Time Averaging

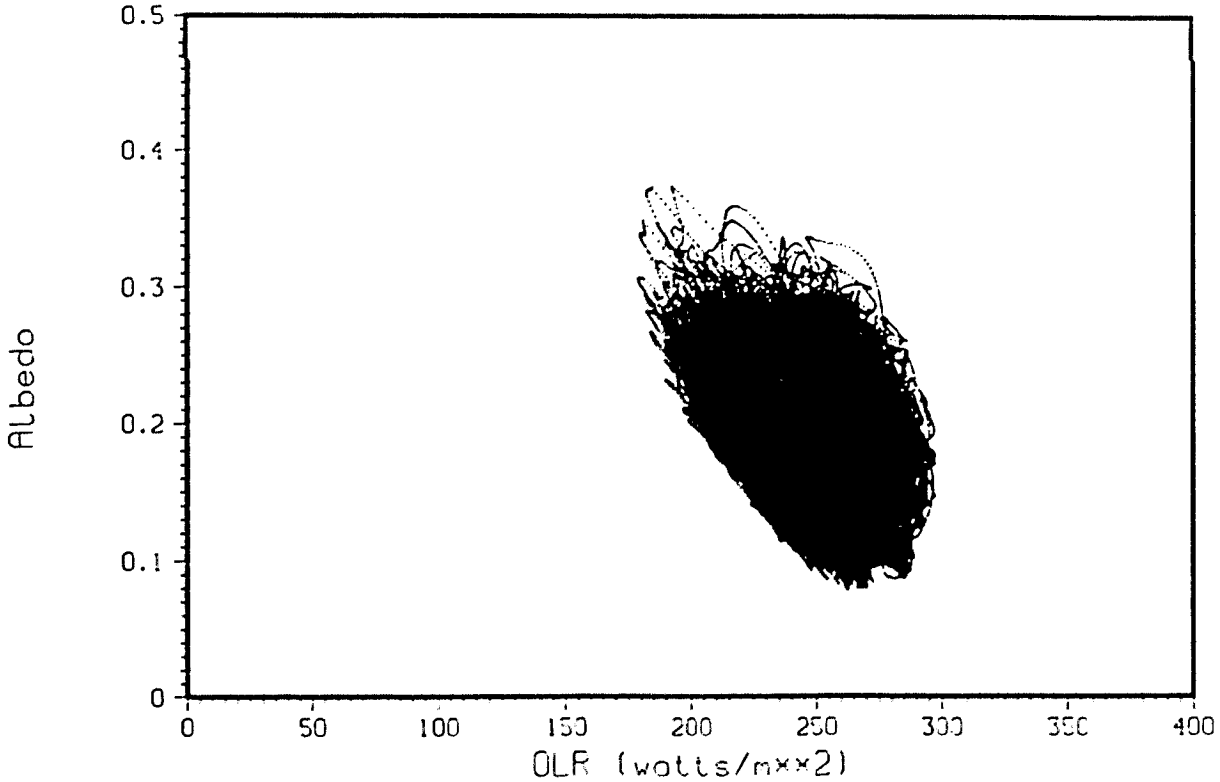

Figure 7. Albedo vs. OLR for Latitudes -30° to +30° for 15 min. Time Averaging

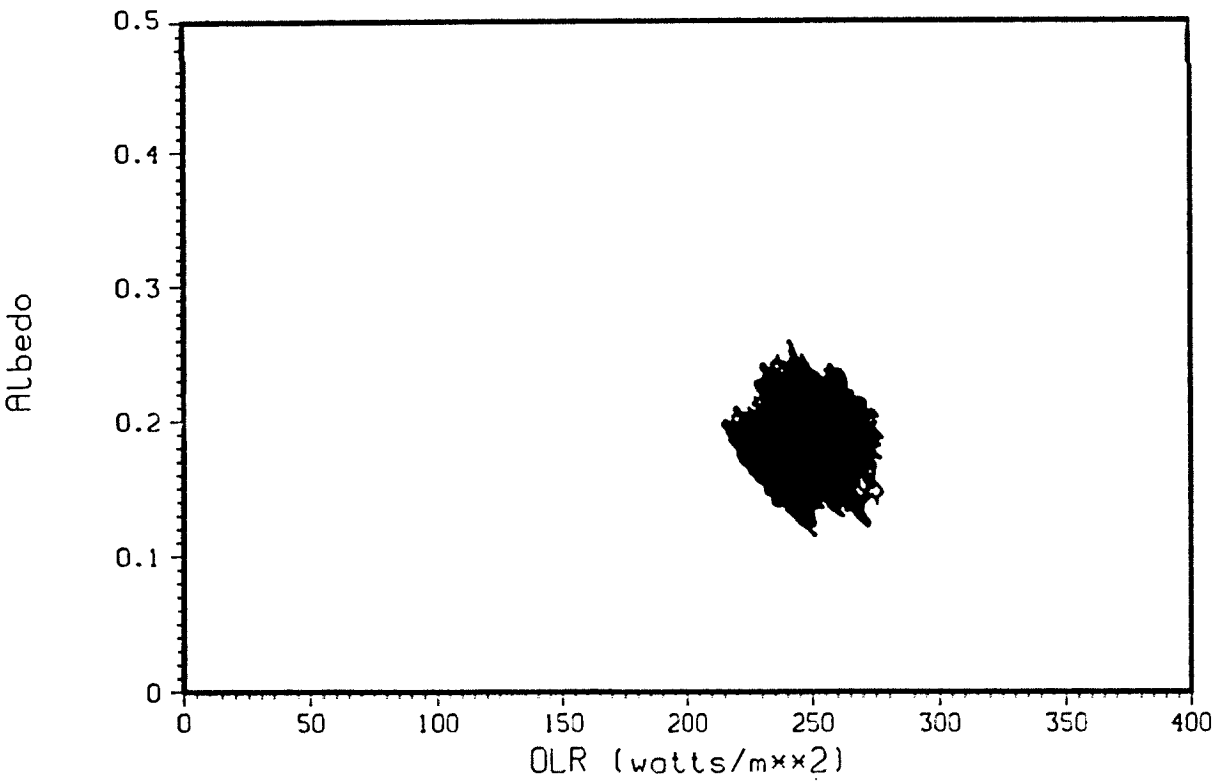

Figure 8. Albedo vs. OLR for Latitudes -30° to +30° for 90 min. Time Averaging

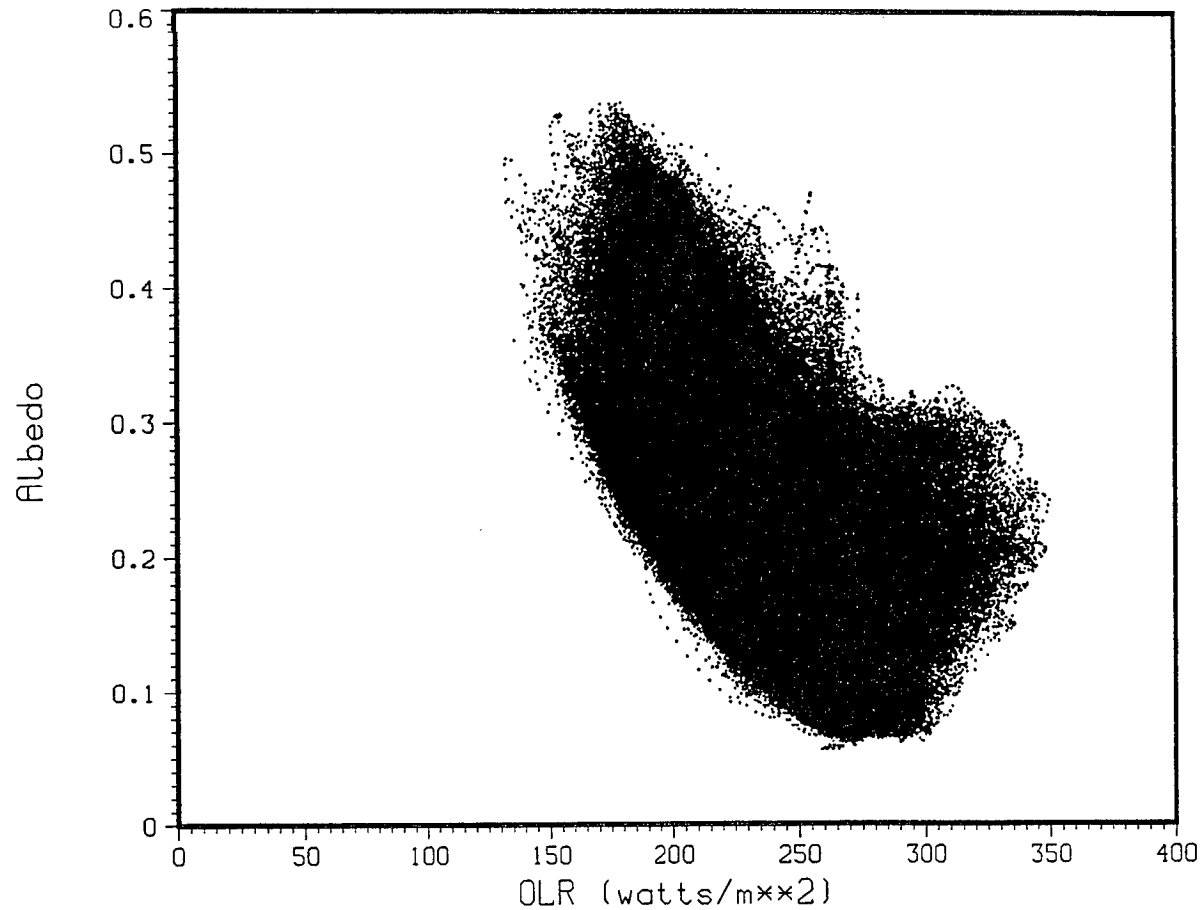

Figure 9. Albedo vs. OLR for Latitudes -90° to +90° for 16 sec. Time Averaging

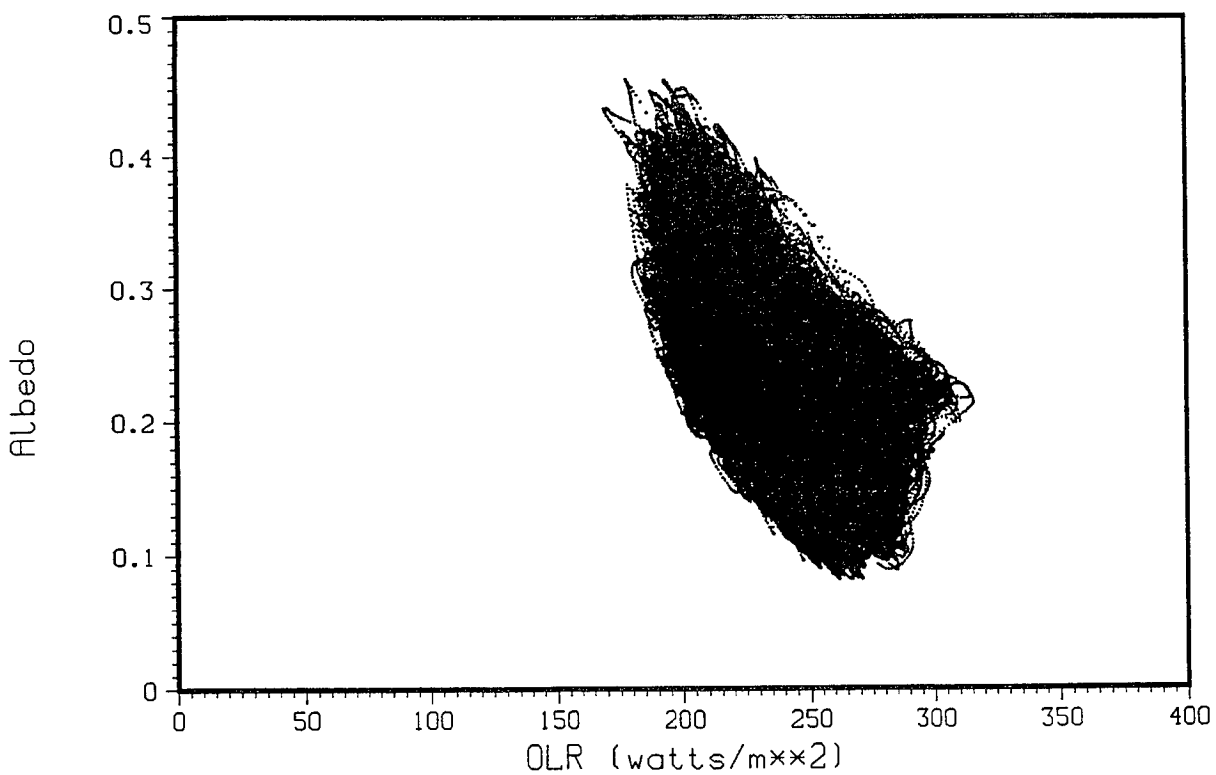

Figure 10. Albedo vs. OLR for Latitudes -90° to +90° for 15 min. Time Averaging

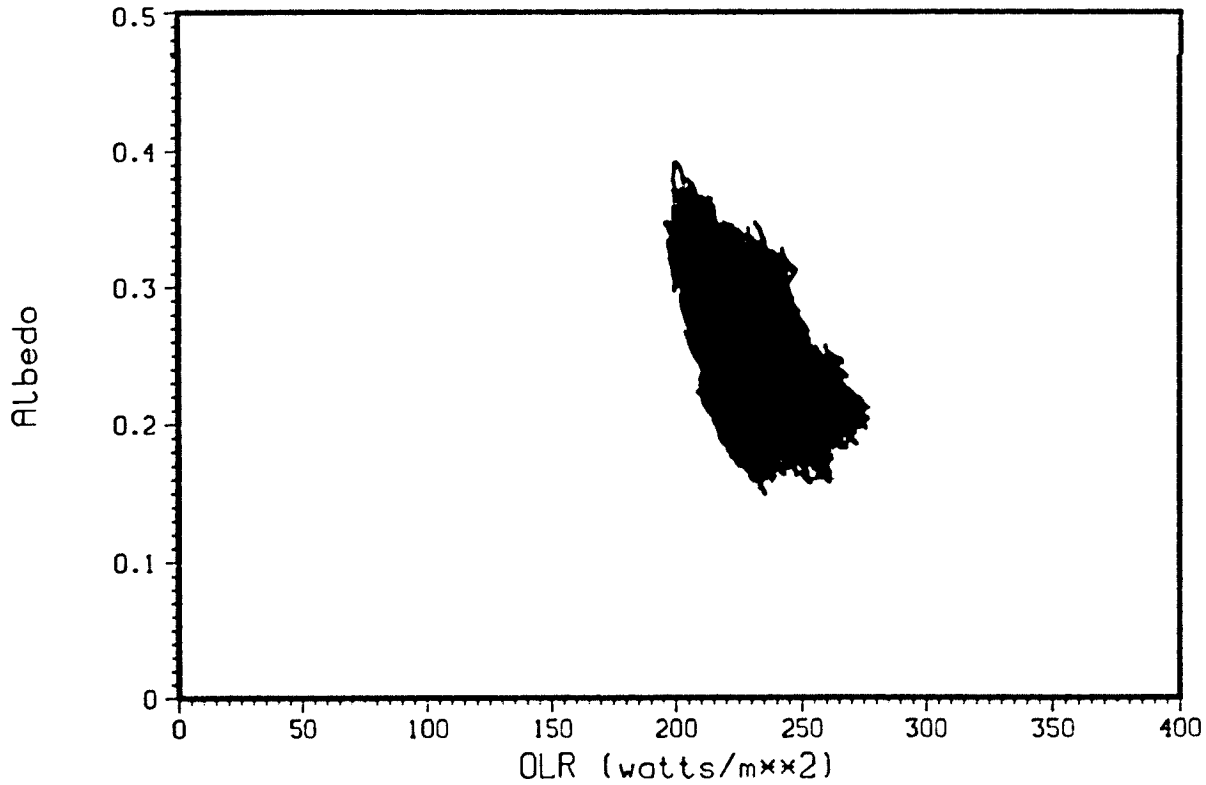

Figure 11. Albedo vs. OLR for Latitudes -90° to +90° for 90 min. Time Averaging

American Institute of Aeronautics and Astronautics
1801 Alexander Bell Drive, Suite 500
Reston, VA 20191-4344

ISBN 1-56347-423-9